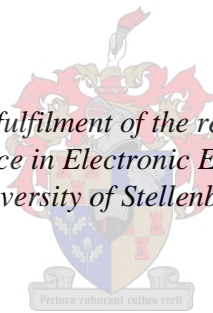


THE DESIGN, IMPLEMENTATION AND TESTING OF A MOVING PLATFORM LANDING ALGORITHM FOR AN UNMANNED AUTONOMOUS HELICOPTER

by

Philip Bellstedt

*Thesis presented in partial fulfilment of the requirements for the degree of
Master of Science in Electronic Engineering at the
University of Stellenbosch*



Supervisor: Prof T. Jones

Faculty of Engineering
Department Electrical and Electronic Engineering

March 2015

DECLARATION

By submitting this thesis electronically, I declare that the entirety of the work contained therein is my own, original work, that I am the owner of the copyright thereof (unless to the extent explicitly otherwise stated) and that I have not previously in its entirety or in part submitted it for obtaining any qualification.

Signature:

P. Bellstedt

Date:

Copyright © 2015 Stellenbosch University

All rights reserved.

ABSTRACT

With a view to future ship deck landings, a moving platform landing algorithm for an unmanned autonomous helicopter was successfully designed and a number of systems were developed in order to implement the landing algorithm.

Through a combination of an MCA-based ship motion prediction algorithm and the appropriate analysis of platform motion criteria, a system was developed which can identify valid landing opportunities in real ship motion data recorded at sea state 4 for up to 5 s into the future with a 75% success rate.

The bandwidth of the heave motion estimator and controller of the helicopter were increased by the implementation of GPS latency compensation, and velocity and acceleration feed forward terms respectively. The resulting bandwidth of at least 0.2 Hz is sufficient to track the heave motion of a platform which is simulating the motion of a ship at sea state 4 or lower.

After the various systems were integrated they were coordinated in a landing state machine. A stationary platform landing was demonstrated successfully during flight tests, verifying the functionality of the landing state machine and the integration of the system. Landings on a platform simulating the motion of a ship at sea state 4 were demonstrated successfully in hardware-in-the-loop simulations.

OPSOMMING

Met die oog op toekomstige skip dek landings, is 'n bewegende platformlandingsalgoritme vir 'n onbemande outonome helikopter suksesvol ontwerp en 'n aantal stelsels ontwikkel om die landingsalgoritme te implementeer.

Deur 'n kombinasie van 'n MCA-gebaseerde skipbewegingvoorspellingsalgoritme en die toepaslike ontleding van platformbewegingskriteria, is 'n stelsel ontwikkel wat geldige landingsgeleenthede in realskipbewegingsdata kan identifiseer. Vir skipbewegingsdata wat by seetoestand 4 opgeneem is kan landingsgeleenthede 5 s in die toekoms met 'n 75% sekerheid identifiseer word.

Die bandwydte van die afgeebewegingafskatter en beheerder van die helikopter is deur die implementering van GPS vertragingkompensasie, en snelheid en versnelling vorentoe-voer terme onderskeidelik verhoog. Die gevolglike bandwydte van minstens 0.2 Hz is voldoende om die afgeebeweging van 'n platform te volg wat die beweging van 'n skip by seetoestand 4 of laer simuleer.

Nadat die stelsels geïntegreer is is hulle gekoördineer in 'n landingtoestandsmasjien. 'n Stilstaande platform landing is suksesvol gedemonstreer tydens vlugtoetse, wat die funksionaliteit van die landingtoestandsmasjien en die integrasie van die stelsel bewys. Landings op 'n platform wat die beweging van 'n skip by seetoestand 4 simuleer is suksesvol in hardeware-in-die-lus simulاسies gedemonstreer.

ACKNOWLEDGEMENTS

A number of people deserve credit for helping me to complete this chapter of my life:

- **Armcor** for funding this project.
- **Prof Jones** for allowing me the freedom to realise my dreams throughout this project.
- My colleagues at the ESL, but especially: **Willem** for proofreading some of the early chapters and for helping me with the structure of this thesis; **Ger** for always being willing to help; the “**astrology**” **department** at the ESL for the interesting conversations and technical advice; and **Wiaan** and **Nico** for their patience, advice, assistance, early mornings, late afternoons and for the great work they are doing to improve the quality of the ESL’s hardware.
- All my friends who supported me along the way, but especially: **Lisa** for showing me what it means to be a friend; **Wouter** for always being there for me; **Gulu** for the Neelsie soup days; **Nadia** for the valuable thesis writing advice; **Jacobie** for the support towards the end of this project; **Lindsay** for proof reading parts of this thesis; and my “**kleingroepe**” for their prayers.
- My family which supported me, but especially: **Lizzy** for providing a lot of assistance with proofreading and for all the Mc D’s trips; **Marianne** for always offering to help and for talking nonsense with me when I needed it most; **Neni** for being there for me throughout my life; **Lissi** and **Großmammi** for also being there for me and for the much needed Johannesburg breakaway; **Großpappi** for all the aviation stories and for always coming along to the flying field; **Hati** for all the interesting technical discussions over the years which no one else wanted to listen to; and **my parents...**

Special thanks must go to **my parents**: Thank you for your unwavering support throughout this project and throughout my life in everything I have undertaken; for your trust; for providing me with a solid foundation from which I could build myself up; for teaching me to work with my hands; for letting me disassemble appliances and build crazy gadgets as a young boy; and for proofreading parts of this thesis. For these things and everything else I have forgotten to mention I am eternally grateful! **Mams and Paps**, I dedicate this project to you.

CONTENTS

Declaration	i
Abstract	ii
Opsomming	iii
Acknowledgements	iv
Contents	v
List of Figures	xii
List of Tables	xviii
Nomenclature	xix
1. Introduction	1
1.1 Related Projects	1
1.1.1 Helicopter	1
1.1.2 3-DOF Platform	3
1.2 Project Objectives	4
1.3 Contributions	4
1.4 Thesis Outline	5
2. Ship Deck Landing Algorithms	7
2.1 Introduction	7
2.2 Approach	7
2.2.1 Fore/Aft Approach	8
2.2.2 Relative-Wind Approach	9
2.2.3 Cross-Deck Approach	10
2.3 Landing Opportunity Identification	11
2.3.1 Ship Motion Prediction	11
2.3.2 Landing Criteria Analysis	14
2.4 Descent	18
2.4.1 Absolute Velocity Descent	19
2.4.2 Deck Heave Motion Tracking Descent	19

2.5	Touchdown.....	20
2.6	3-DOF Platform Landing Algorithm.....	21
2.7	Summary.....	22
3.	Ship Motion Prediction.....	24
3.1	Introduction	24
3.2	Minor Component Analysis	24
3.2.1	Input Data	25
3.2.2	Minor and Principal Component Extraction.....	25
3.2.3	Minor Component Selection.....	28
3.2.4	Prediction.....	29
3.3	Implementation.....	29
3.4	Testing	31
3.4.1	Roll Angle	32
3.4.2	Pitch Angle	34
3.4.3	Heave Position.....	35
3.4.4	Heave Rate.....	36
3.5	Summary.....	37
4.	Landing Criteria Analysis.....	38
4.1	Introduction	38
4.2	Environmental Criteria Analysis	38
4.3	Platform Motion Criteria Analysis	38
4.3.1	Theory.....	38
4.3.2	Implementation.....	40
4.3.3	Testing	40
4.4	Helicopter Motion Criteria Analysis	46
4.5	Summary.....	46
5.	Kinematic Estimator.....	47
5.1	Introduction	47
5.2	Helicopter Position and Velocity Estimation	47

5.2.1	Complementary Filter.....	47
5.2.2	GPS Measurement Errors	49
5.2.3	GPS Measurement Latency Compensation	51
5.3	Helicopter Attitude Estimation.....	52
5.3.1	Tilt-Compensated Magnetometer Heading Measurement.....	52
5.3.2	Magnetic Interference.....	54
5.3.3	Magnetometer Calibration.....	56
5.4	Platform Heave Estimation.....	57
5.4.1	Target Landing Point.....	57
5.4.2	Platform Point Under Helicopter.....	58
5.5	Implementation.....	62
5.6	Summary.....	63
6.	Low-level Controllers.....	64
6.1	Introduction	64
6.2	Inertial Position Control	64
6.2.1	Transformation	65
6.2.2	Command Limits	65
6.3	Longitudinal Control	65
6.3.1	Pitch Rate Loop	66
6.3.2	Longitudinal Velocity Control Integrator.....	66
6.3.3	Command Limits	66
6.4	Lateral Control.....	67
6.4.1	Roll Rate Loop	67
6.4.2	Lateral Velocity Control Integrator	68
6.4.3	Command Limits	68
6.5	Heave Control.....	68
6.5.1	Original System.....	68
6.5.2	Velocity and Acceleration Feed Forward.....	72
6.5.3	Command Limits	74

6.6	Heading Control	74
6.6.1	Model Derivation.....	75
6.6.2	Collective to Tail Rotor Pitch Mixing	76
6.6.3	Command Limits	77
6.7	Implementation.....	77
6.8	Summary.....	77
7.	High-level Controllers	78
7.1	Introduction	78
7.2	Timed Deck Landing Descent Controller.....	78
7.3	Landing State Machine.....	80
7.3.1	Start.....	82
7.3.2	Approach	82
7.3.3	Descent	86
7.3.4	Touchdown.....	88
7.3.5	Aborts	88
7.3.6	Virtual Landing Mode	88
7.4	Implementation.....	89
7.5	Summary.....	89
8.	System Integration.....	90
8.1	Introduction	90
8.2	3-DOF Platform - SMPLCA.....	92
8.2.1	Interfacing.....	92
8.2.2	Data Exchange.....	93
8.2.3	Fail Safe.....	94
8.3	3-DOF Platform & SMPLCA – Helicopter OBC.....	94
8.3.1	Interfacing.....	94
8.3.2	Data Exchange.....	97
8.3.3	Fail Safe.....	99
8.4	Summary.....	100

9.	Practical Testing: Low-level Systems	101
9.1	Introduction	101
9.2	Initial Heave Controller Tuning	101
9.2.1	Flight 1 (2013-02-22)	101
9.3	Basic System Verification	106
9.3.1	HIL Simulation	106
9.3.2	Flight 1 (2013-10-03)	107
9.3.3	Magnetometer Calibration (2013-11-04)	112
9.3.4	HILS: Effect of Magnetometer Calibration Error	115
9.3.5	Flight 3 (2013-11-05)	116
9.4	GPS Latency Compensation	117
9.4.1	Flights: Initial Latency Determination (2013-11-05; 2014-01-29)	118
9.4.2	HILS: Latency Effect and Compensation Tuning	119
9.4.3	Flight: Compensation Tuning (2014-04-17)	123
9.5	Heave Controller Tuning Verification	125
9.5.1	Flight (2014-04-17)	125
9.5.2	HIL Simulation	128
9.6	Proposed Heave Controller	130
9.6.1	HILS: Original Controller & Feed Forward Tuning	131
9.6.2	Flight: Feed Forward Tuning (2014-04-17)	134
9.7	Sine Tracking	136
9.7.1	HIL Simulation	137
9.7.2	Flights (2014-04-17)	139
9.8	Summary	141
10.	Practical Testing: High-level Control	142
10.1	Introduction	142
10.2	Virtual Landing - Sinusoidal Ship Data	142
10.2.1	Flights (2014-04-17)	142
10.3	Actual Landing - Stationary Ship Data	144

10.3.1	Flights (2014-05-01).....	144
10.4	Actual Landing - Sinusoidal Ship Data	146
10.4.1	HIL Simulation.....	146
10.5	Actual Landing - Real Ship Data.....	148
10.5.1	HIL Simulation.....	148
10.6	Summary.....	150
11.	Conclusions & Recommendations.....	151
11.1	Conclusions	151
11.2	Recommendations	152
11.2.1	Prediction.....	152
11.2.2	Landing Criteria.....	152
11.2.3	Estimator.....	152
11.2.4	Magnetometer.....	152
11.2.5	Controllers	152
11.2.6	RF Link.....	153
11.2.7	HILS	154
A.	3-DOF Platform.....	155
A.1	Introduction	155
A.2	Original system.....	155
A.3	Modifications.....	158
A.3.1	Mechanical	158
A.3.2	Safety.....	161
A.3.3	Control.....	163
A.3.4	Ground Station.....	165
A.4	Testing	167
A.5	Summary.....	171
B.	Sea States.....	172
C.	Lateral, Longitudinal & Heading Control	173
C.1	Initial Controller Tuning Tests	173

C.1.1	Flight 2: Heading Controller Verification (2013-02-22)	173
C.1.2	Flight 3: Inertial East & Lateral Controllers Tuning (2013-02-22)	175
C.1.3	Flight 4: Inertial North & Longitudinal Controllers Tuning (2013-02-22) ...	180
C.2	Further Controller Tuning Tests	184
C.2.1	Flights (2013-11-05; 2014-01-29; 2014-04-17)	184
D.	Additional Control Tuning Data	191
D.1	Heave	191
D.1.1	Initial Tuning	191
D.1.2	Tuning Verification	192
D.1.3	HIL Comparison	194
D.2	Lateral	195
D.2.1	Initial Tuning	195
D.2.2	Further Tuning	198
D.3	Longitudinal	200
D.3.1	Initial Tuning	200
D.3.2	Further Tuning	203
	Bibliography	206

LIST OF FIGURES

Figure 1.1 - ESL's X-Cell helicopter test bed	3
Figure 1.2 - Main mechanical system of the ESL's modified 3-DOF motion simulation platform	3
Figure 2.1 - Flow characteristics for a rotor in hover taxi forward flight near the ground [10]	7
Figure 2.2 - Streamlines coloured by instantaneous velocity magnitude over a Royal Navy Type 45 Destroyer in a headwind derived from CFD simulations [11]	8
Figure 2.3 - Top view of ship section with helicopter performing F/A landing approach	9
Figure 2.4 - Top view of ship section with helicopter performing RW landing approach	10
Figure 2.5 - Top view of ship section with helicopter performing XD landing approach	11
Figure 2.6 - Example ship pitch and roll amplitudes vs. ship speed and heading [12]	14
Figure 2.7 - Safe and unsafe wave directions and corresponding ship speeds for an unrestrained UAV [31]	15
Figure 2.8 - Example SHOLs [29]	16
Figure 2.9 - Deck availability and rise time determined by EI [33]	18
Figure 2.10 - Flow over main rotor during VRS [37]	19
Figure 2.11 - Safe and unsafe wave directions and corresponding ship speeds for a restrained UAV [31]	21
Figure 2.12 - Flowchart of the designed 3-DOF platform landing algorithm	23
Figure 3.1 - SMPLCA application during simulation	30
Figure 3.2 - Roll angle predictions with $\alpha=0.1$	32
Figure 3.3 - Pitch angle predictions with $\alpha=0.1$	34
Figure 3.4 - Heave position predictions with $\alpha=0.1$	35
Figure 3.5 - Heave rate predictions with $\alpha=0.1$	36
Figure 4.1 - Results of landing criteria analysis with static bounds on 5 s roll angle predictions	41
Figure 4.2 - Results of landing criteria analysis with static bounds on 1 s roll angle predictions	41
Figure 4.3 - Results of landing criteria analysis with dynamic bounds on 5 s roll angle predictions	42
Figure 4.4 - Results of landing criteria analysis with dynamic bounds on 1 s roll angle predictions	42
Figure 4.5 - Results of landing criteria analysis with dynamic bounds on 5 s pitch angle predictions	43

Figure 4.6 - Results of landing criteria analysis with dynamic bounds on 1 s pitch angle predictions	44
Figure 4.7 - Results of landing criteria analysis with dynamic bounds on 5 s heave position predictions	44
Figure 4.8 - Results of landing criteria analysis with dynamic bounds on 1 s heave position predictions	45
Figure 5.1 - Bode magnitude plot of low- and high-pass filter pair	48
Figure 5.2 - Block diagram of complementary filter	48
Figure 5.3 - Block diagram of complementary filter with GPS measurement latency	50
Figure 5.4 - Bode plot of complementary filter transfer function with GPS measurement latency	51
Figure 5.5 - Bode plot of complementary filter transfer function with GPS measurement latency compensation	52
Figure 5.6 - Magnetometer measurements without interference (blue) and magnetometer measurements with interference (red) (axes represent x-, y- and z-axis magnetometer measurements in μT) [63]	54
Figure 5.7 – Model of the magnetic field of three permanent magnets in the absence of an external magnetic field (left) and within a uniform magnetic field (right) [62]	55
Figure 5.8 - Model of the magnetic field of three unmagnetised ferromagnetic bars in the absence of an external magnetic field (left) and within a uniform magnetic field (right) [62]	56
Figure 5.9 - Platform and helicopter system.....	59
Figure 6.1 - Block diagram of inertial position controller.....	64
Figure 6.2 - Block diagram of longitudinal controller.....	66
Figure 6.3 - Block diagram of lateral controller.....	67
Figure 6.4 - Block diagram of original heave controller	68
Figure 6.5 - Block diagram of original combined heave controller during approximately level flight	69
Figure 6.6 - Bode plot of heave controller with original gains.....	71
Figure 6.7 - Bode plot of heave controller with modified gains.....	72
Figure 6.8 - Block diagram of proposed combined heave controller during approximately level flight.....	72
Figure 6.9 - Bode plot of heave controller with modified gains and velocity and acceleration feed forward	74
Figure 6.10 - Block diagram of heading controller	75
Figure 6.11 - Block diagram of existing heading model	75
Figure 6.12 - Block diagram of the existing heading model revealing effect of gyro.....	76
Figure 7.1 - Landing descent in platform relative frame (top) and inertial frame (bottom)	79

Figure 7.2 - State machine for landing on a platform.....	81
Figure 7.3 - Top view of platform and helicopter during <i>rotate</i> state	82
Figure 7.4 - Top view of platform and helicopter during <i>move</i> state	85
Figure 7.5 - Top view of platform and helicopter upon completion of the approach.....	85
Figure 8.1 - Integrated system	91
Figure 8.2 – RF transmission cycle	98
Figure 8.3 - RF transmission slot mainly containing DGPS correction data.....	99
Figure 8.4 – RF transmission slot mainly containing telemetry data	99
Figure 9.1 - Block diagram of original combined heave controller	102
Figure 9.2 - Collective command responses.....	103
Figure 9.3 - Heave velocity responses.....	104
Figure 9.4 – Inertial down position responses.....	104
Figure 9.5 - Aerial plan (initial HIL simulation)	107
Figure 9.6 - RF transmission latency estimates.....	108
Figure 9.7 - RF platform data sample period.....	109
Figure 9.8 - True vs. raw RF platform jerk	109
Figure 9.9 - True vs. estimated platform acceleration	110
Figure 9.10 - True vs. estimated platform velocity	110
Figure 9.11 - True vs. estimated platform position	111
Figure 9.12 - Aerial plan (flight; problematic spiral motion).....	111
Figure 9.13 - 3D locus of uncalibrated magnetometer measurements as recorded during calibration.....	113
Figure 9.14 – 2D loci of uncalibrated magnetometer measurements as recorded during calibration.....	113
Figure 9.15 - 2D loci of calibrated magnetometer measurements.....	114
Figure 9.16 - Aerial plan (HIL simulation; uncalibrated magnetometer).....	116
Figure 9.17 - Aerial plan (flight; calibrated magnetometer).....	117
Figure 9.18 - GPS vs. accelerometer response instants	118
Figure 9.19 - GPS latency effect on heave velocity estimates (HILS).....	120
Figure 9.20 - GPS latency effect on heave position estimates (HILS).....	121
Figure 9.21 - GPS latency compensated heave velocity estimates (HILS)	121
Figure 9.22 - GPS latency compensated heave position estimates (HILS)	122
Figure 9.23 - GPS latency compensated heave velocity estimates (flight)	124
Figure 9.24 - GPS latency compensated heave position estimates (flight)	124
Figure 9.25 - Collective command responses.....	126
Figure 9.26 - Heave velocity responses.....	127
Figure 9.27 - Inertial down position responses.....	127

Figure 9.28 - Collective command responses.....	129
Figure 9.29 - Heave velocity responses.....	129
Figure 9.30 - Inertial down position responses.....	130
Figure 9.31 - Block diagram of proposed combined heave controller during approximately level flight.....	130
Figure 9.32 - Velocity response (HILS; no feed forwards).....	132
Figure 9.33 - Position tracking response (HILS; no feed forwards).....	132
Figure 9.34 - Velocity response (HILS; optimal feed forward gains).....	133
Figure 9.35 - Position tracking response (HILS; optimal feed forward gains).....	133
Figure 9.36 - Velocity response (flight; 0.20 Hz reference; optimal feed forward gains).....	135
Figure 9.37 - Position tracking response (flight; 0.20 Hz reference; optimal feed forward gains).....	136
Figure 9.38 - Velocity response (HILS; 0.30 Hz reference).....	137
Figure 9.39 - Position tracking response (HILS; 0.30 Hz reference).....	138
Figure 9.40 - Velocity response (flight; 0.10 Hz reference).....	140
Figure 9.41 - Position tracking response (flight; 0.10 Hz reference).....	140
Figure 10.1 - Position response during landing (flight; 0.10 Hz platform reference).....	143
Figure 10.2 - Position response during landing (flight; stationary platform).....	145
Figure 10.3 - Aerial plan during landing (flight; stationary platform).....	145
Figure 10.4 - Position response during landing (HILS; 0.20 Hz platform motion).....	147
Figure 10.5 - Aerial plan during landing (HILS; 0.20 Hz platform motion).....	147
Figure 10.6 - Position response during landing (HILS; real ship platform landing).....	149
Figure 10.7 - Aerial plan during landing (HILS; real ship platform landing).....	149
Figure A.1 - Main mechanical system of the original 3-DOF platform [7].....	155
Figure A.2 - Orthographic drawing of base-piston-valve-platform assembly [7].....	156
Figure A.3 - Target ship.....	157
Figure A.4 - Platform system aligned with target ship axis system [7].....	157
Figure A.5 - Landing arrestor near worst case (attachment points indicated by yellow arrows).....	159
Figure A.6 - Modified mechanical system.....	161
Figure A.7 – Helicopter and platform.....	161
Figure A.8 - Ship axis system [7].....	163
Figure A.9 - Platform heave response.....	167
Figure A.10 - Platform pitch response.....	168
Figure A.11 - Platform roll response.....	168
Figure A.12 - Platform heave response (time shifted 0.2 Hz references).....	169
Figure A.13 - Platform heave response (time shifted 0.1 Hz references).....	170

Figure C.1 - Block diagram of heading controller.....	173
Figure C.2 - Tail rotor pitch command response.....	174
Figure C.3 - Yaw rate response	174
Figure C.4 - Heading angle response.....	175
Figure C.5 - Block diagram of combined inertial east and lateral controller during near-north heading flight.....	176
Figure C.6 - Lateral cyclic command	177
Figure C.7 - Roll rate response.....	178
Figure C.8 - Roll angle response	178
Figure C.9 - Lateral velocity response.....	179
Figure C.10 - East position response	179
Figure C.11 - Block diagram of combined inertial north and longitudinal controller during near-north heading flight	180
Figure C.12 - Longitudinal cyclic command response.....	182
Figure C.13 - Pitch rate response	182
Figure C.14 - Pitch angle response	183
Figure C.15 - Longitudinal velocity response	183
Figure C.16 - North position response	184
Figure C.17 - Longitudinal cyclic command response.....	186
Figure C.18 - Pitch rate response	186
Figure C.19 - Pitch angle response.....	187
Figure C.20 - Longitudinal velocity response.....	187
Figure C.21 - Longitudinal position response	188
Figure C.22 - Lateral cyclic command response	188
Figure C.23 - Roll rate response.....	189
Figure C.24 - Roll angle response	189
Figure C.25 - Lateral velocity response.....	189
Figure C.26 - Lateral position response.....	190
Figure D.1 - Collective command response	191
Figure D.2 - Heave velocity response	191
Figure D.3 - Down position response.....	192
Figure D.4 - Collective command response	192
Figure D.5 - Heave velocity response	193
Figure D.6 - Down position response.....	193
Figure D.7 - Collective command response	194
Figure D.8 - Heave velocity response	194
Figure D.9 - Down position response.....	195

Figure D.10 - Lateral cyclic command response.....	195
Figure D.11 - Roll rate response.....	196
Figure D.12 - Roll angle response.....	196
Figure D.13 - Lateral velocity response	197
Figure D.14 - East position response.....	197
Figure D.15 - Lateral cyclic command response.....	198
Figure D.16 - Roll rate response.....	198
Figure D.17 - Roll angle response.....	199
Figure D.18 - Lateral velocity response	199
Figure D.19 - Lateral position response	200
Figure D.20 - Longitudinal cyclic command response.....	200
Figure D.21 - Pitch rate response	201
Figure D.22 - Pitch angle response.....	201
Figure D.23 - Longitudinal velocity command	202
Figure D.24 - North position response	202
Figure D.25 - Longitudinal cyclic command response.....	203
Figure D.26 - Pitch rate response	203
Figure D.27 - Pitch angle response.....	204
Figure D.28 - Longitudinal velocity response.....	204
Figure D.29 - Longitudinal position response.....	205

LIST OF TABLES

Table 2.1 - Ship motion prediction algorithm summary.....	14
Table 3.1 - Roll angle prediction performance.....	33
Table 3.2 - Pitch angle prediction performance	35
Table 3.3 – Heave position prediction performance.....	36
Table 3.4 – Heave rate prediction performance	37
Table 4.1 - Landing criteria analysis performance comparison	45
Table 6.1 - Original heave controller gains (G1).....	70
Table 6.2 - Modified heave controller gains (G2/G3/G4/G5)	71
Table 9.1 - Heave control gains for tuning flight	103
Table 9.2 - GPS latency figures from test data.....	119
Table 9.3 - GPS latency compensation time vs. heave motion estimation errors (HIL)	122
Table 9.4 - GPS latency compensation time vs. heave motion estimation errors (flight)	125
Table 9.5 – Velocity and acceleration feed forward gains vs. heave tracking errors (HIL)..	134
Table 9.6 - Acceleration feed forward gains vs. heave tracking errors (flight).....	136
Table 9.7 - Reference frequencies vs. heave tracking errors (HILS)	138
Table 9.8 - Reference frequencies vs. heave tracking errors (flight).....	141
Table A.1 - Platform performance indicators.....	157
Table A.2 - Platform motion limits	162
Table A.3 - Platform reference limits.....	162
Table A.4 – Modified platform performance indicators.....	169
Table A.5 - Modified platform performance indicators (time shifted references)	170
Table B.1 - NATO North Atlantic Sea State Definitions [22]	172
Table C.1 - Heading control gains for tuning flight	173
Table C.2 – Inertial east and lateral control gains for initial tuning flight	177
Table C.3 – Inertial north and longitudinal control gains for initial tuning flight.....	181
Table C.4 – Inertial, lateral and longitudinal control gains for verification flight 1	185

NOMENCLATURE

Notational convention

\dot{a}	Rate or velocity
\ddot{a}	Acceleration
A	Matrix
\mathbf{a}	Vector
\bar{a}	Mean
$A_{i,j}$	Matrix element at row i and column j
\hat{a}	Estimated or predicted state
a_i	Vector element i

Letters

A	Number of aborted landing attempts
B	Magnetometer measurement
C	Matrix of minor components
D	Inertial down position
d	Subset size
E	Inertial east position
$E(s)$	Error signal in the s-domain
$\%E$	Fraction of the total energy of the input data
E	Diagonal matrix containing the eigenvalues of R
e	Error
f	Scaling factor

G	Transfer function
$G1$	Set of control gains used on original helicopter system
$G2-G5$	Sets of control gains used on modified helicopter system
g	Gravity
k	Controller gain
L	Input vector length
M	Number of minor components
m	Offset vector
N	Inertial north position
P	Number of input vectors
p, q, r	Roll, pitch and yaw rates
R	Autocovariance matrix
T	Sample period
t	Time
w	Exponential weight
u, v, w	Body frame velocities
V	Number of valid safe landing opportunities identified
V	Column matrix containing the eigenvectors of R
X	Input matrix
x	Input vector
x, y, z	Body frame positions

Greek symbols

α	Exponential decay factor
----------	--------------------------

δ	Actuator command
θ	Pitch
ϕ	Roll
ψ	Yaw or heading
Σ	Diagonal matrix containing the square root of R
σ	Standard deviations
τ	Delay
τ_a	Absolute latency of GPS position measurements
τ_b	Relative latency between GPS position and velocity measurements

Subscripts

1	Related to starting point
a	Related to lateral cyclic
aff	Acceleration feed forward
b	Related to longitudinal cyclic
c	Related to collective
cal	Calibrated measurement
cmd	Command
$declination$	Declination
ff	Feed forward
GPS	GPS related
H	Related to helicopter
h	In the horizontal plane
I	Intermediate step input data

<i>l</i>	Related to tracked landing opportunity
<i>lp</i>	Related to landing point
<i>lat</i>	Related to latency
<i>level</i>	When level
<i>mag</i>	Related to the magnetometer
<i>off</i>	Offset
<i>O</i>	Raw input data
<i>P</i>	Related to platform point under helicopter
<i>r</i>	Related to tail rotor
<i>ref</i>	Reference
<i>raw</i>	Raw measurement
<i>ss</i>	Steady state
<i>T</i>	Related to target landing point
<i>trans</i>	Related to transmission
<i>vff</i>	Velocity feed forward

Superscripts

<i>T</i>	Transpose
----------	-----------

Abbreviations and Acronyms

3-DOF	3-degree of freedom
ACK	Acknowledgement
AR	Auto-regressive
DCM	Direction cosine matrix
CC	Correlation coefficient

DGPS	Differential Global Positioning System
EI	Energy Index
EPI	Error prediction interval
ESL	Electronic Systems Laboratory
F/A	Fore/aft
FDO	Flight Deck Officer
FFRLS	Forgetting factor recursive least squares
FPGA	Field-programmable gate array
GPS	Global Positioning System
HIL	Hardware-in-the-loop
HILS	Hardware-in-the-loop simulation
IDE	Integrated development environment
IMU	Inertial measurement unit
LAPACK	Linear Algebra Package
LSM	Landing state machine
LSO	Landing Safety Officer
MCA	Minor component analysis
MSA	Minor subspace analysis
NATO	North Atlantic Treaty Organization
NED	North-east-down
NN	Neural network
OBC	Onboard computer
OEM	Original equipment manufacturer
OpenCV	Open Source Computer Vision

P	Proportional
PI	Proportional integral
PCA	Principal component analysis
QWT	Qt Widgets for Technical Applications
RF	Radio frequency
RMS	Root mean square
RMSE	Root mean square error
RTK	Real-time kinematic
RW	Relative-wind
SHOL	Ship-Helicopter Operating Limit
SLC	Successive loop closure
SMPLCA	Ship motion prediction landing criteria analysis
SNR	Signal-to-noise ratio
SR	Success rate
SVD	Singular value decomposition
SWP	Settling with power
TCP	Transmission Control Protocol
UAV	Unmanned aerial vehicle
UDP	User Datagram Protocol
VRS	Vortex ring state
XD	Cross-deck

1. INTRODUCTION

The dynamic environment of a ship's deck poses many challenges to a landing helicopter. Other than simply removing the need for a manual pilot, an autonomous landing system can take up some of these challenges to improve landing accuracy and safety. The long term goal of the overarching unmanned helicopter project of the Electronic Systems Laboratory (ESL) at Stellenbosch University is to develop an autonomous take-off and landing system which enables an unmanned helicopter to take-off from and land on the deck of a moving ship. To this end, a number of sub-projects focused on various aspects of the problem were completed. After the successful completion of automated stationary platform landings, the focus of the overarching project moved to automated moving platform landings. As practical testing on the flight deck of a ship at sea is risky, difficult to schedule and expensive, the short term goal of the overarching project is to land an unmanned helicopter on a 3-degree of freedom (3-DOF) motion simulation platform.

1.1 RELATED PROJECTS

1.1.1 HELICOPTER

Carstens developed a control system for a small, unmanned, electrically powered helicopter [1]. Due to payload restrictions, sensor data was sent via an RF link to a ground station computer which returned appropriate control commands.

Groenewald addressed the payload problem by developing a test bed based on a larger, unmanned, internal combustion engine powered, X-Cell aerobatic helicopter [2]. The helicopter was equipped with a Pentium III based onboard computer (OBC) and an appropriate sensor suite. A dynamic model was derived for the helicopter and a hardware-in-the-loop simulation (HILS) environment was developed.

Rossouw developed controllers and Borland C++ ground station software for the ESL's X-Cell helicopter test bed [3]. After an appropriate dynamic model was derived for the helicopter, controllers were developed using a classical successive loop closure approach. A higher level waypoint navigation controller was also developed. The control system was implemented on the Pentium III based OBC and flight tested.

Van Schalkwyk developed an adaptive full state controller [4]. A non-linear helicopter model was presented for a generic helicopter. The model was customised for the ESL's X-Cell helicopter test bed, linearised, and used to design the controller. The developed controller was

compared with a non-adaptive classical controller. The controllers were implemented and flight tested.

After completion of their Master's theses, Rossouw and Van Schalkwyk were tasked with the further development of the ESL's X-Cell helicopter test bed. The OBC was migrated to the ESL's dsPIC 6014A based system. The estimator was modified and new controllers were developed for near-hover flight using a classical successive loop closure approach. This work was completed on a contract basis and much of it was not documented.

De Jager designed a monocular vision system and implemented it on an FPGA computer [5]. The high accuracy measurements obtained from the vision system were combined with low accuracy GPS and IMU measurements in a kinematic estimator. Stationary platform landings were tested on the fully integrated system during HIL simulations.

After completion of their Master's theses, De Jager and Basson (another previous ESL student) equipped the ESL's X-Cell helicopter test bed with a NovAtel differential GPS system and demonstrated stationary platform landings during practical flight tests. This work was completed on a contract basis and much of it is undocumented.

Swart developed a monocular vision system for the estimation of ship motion states and an adaptive ship motion prediction algorithm [6]. The developed systems were implemented on a Gumstix computer and integrated with the ESL's X-Cell helicopter test bed's existing systems. Practical flight tests demonstrated the ability to perform stationary platform landings. Moving platform landings were demonstrated in HIL simulations.

Irwin is in the process of completing an analysis of various sensors which might be used on a helicopter system as well as completing the design of a new Kalman filter-based kinematic estimator. The Kalman filter was implemented on a Gumstix computer, integrated with the ESL's X-Cell helicopter test bed and verified through practical flight tests.

Fourie is deriving an improved dynamic model for the ESL's X-Cell helicopter test bed and designing classical controllers based on theoretical analyses and practical flight tests. A ship motion prediction algorithm is also being considered. The project's goal is to perform a landing on a platform which is translating laterally and longitudinally.

A photograph of the ESL's X-Cell helicopter test bed is provided in Figure 1.1. It has a main rotor blade diameter of 1.55 m, a no-fuel mass of 7.20 kg and a fuelled-up mass of 7.67 kg.



Figure 1.1 - ESL's X-Cell helicopter test bed

1.1.2 3-DOF PLATFORM

Smit developed the ESL's original 3-DOF motion simulation platform [7]. The purpose of the system was to simulate ship motion for take-off and landing tests of aircraft.

Alberts, Basson, Beeton, Runhaar, De Jager (all previous ESL students working on a contract basis) and the author modified the 3-DOF motion simulation platform to improve its ability to simulate ship motion and to make it suitable for small helicopter landings. This included the development of a landing arrestor system. These modifications are documented in Appendix A. The modified system's heave motion tracking bandwidth is 0.2 Hz. A photograph of the main mechanical system of the modified platform system is shown in Figure 1.2. The landing surface is 2.5×2.5 m in size and the stroke of the linear pneumatic actuators is 1.2 m.

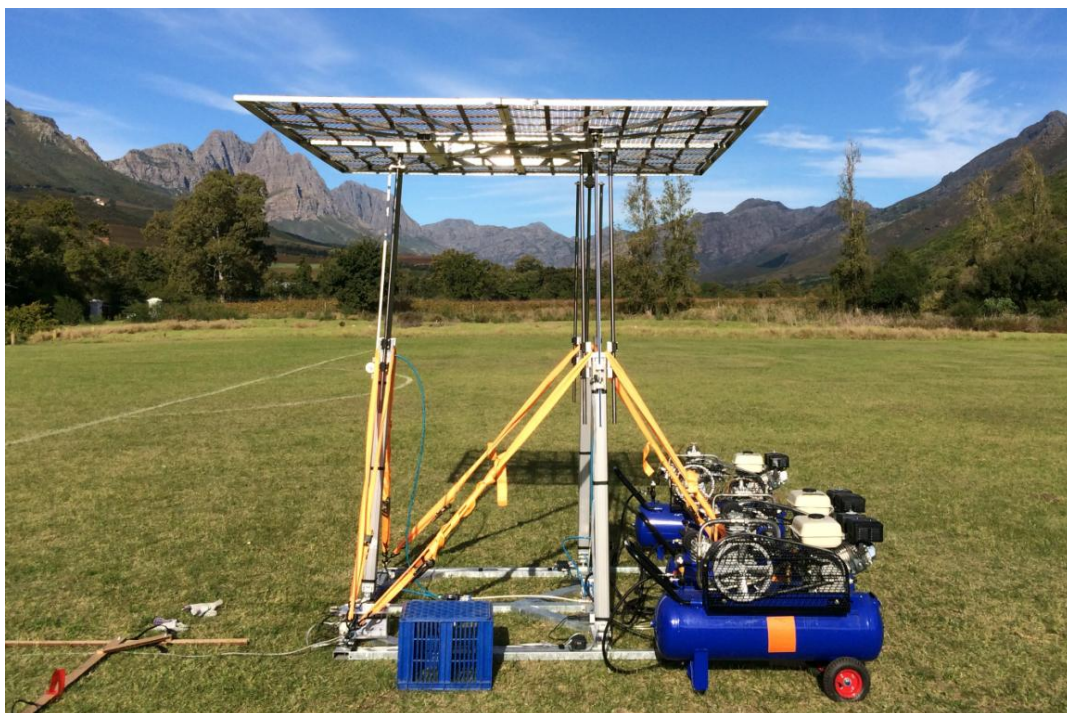


Figure 1.2 - Main mechanical system of the ESL's modified 3-DOF motion simulation platform

1.2 PROJECT OBJECTIVES

The main objective of the project which is the topic of this thesis was to design, implement and test an algorithm for landing a controllable unmanned helicopter autonomously on a platform which is simulating the rolling, pitching and heaving motion of a ship. Such a landing algorithm is a sequence which is followed to progress from a state of general waypoint navigation flight until engine stop on the platform. The main objective was split into the following objectives:

- Research ship deck landing algorithms and design a platform landing algorithm on the basis of the research.
- Design and implement the systems required to execute the designed landing algorithm.
- Test the landing algorithm in simulations and through practical flight tests.

The ESL's X-Cell helicopter test bed was the vehicle given for this project and was assumed to be controllable under near-hover flight conditions. The vehicle was supplied with the hardware and software used by De Jager and Basson as discussed in Section 1.1.1. The ESL's 3-DOF motion simulation platform was the platform given for this project.

Much of the literature on the topic of moving platform landings is concerned with the estimation of platform motion states [8, 9]. As accurate motion states are available from the platform's ground station software, the plan for this project was to send the platform motion states available on the ground station to the helicopter via its RF link so that more attention could be given to other important aspects of moving platform landings.

For the purposes of this project the north-east-down Earth frame is considered to be an inertial frame.

1.3 CONTRIBUTIONS

With a view to the overarching project's long term goal of developing an autonomous take-off and landing system which enables an unmanned helicopter to take-off from and land on the deck of a moving ship, various aspects of ship deck landing algorithms were considered in the literature. Based on these considerations a moving platform landing algorithm was designed.

In order to implement the designed moving platform landing algorithm on the ESL's X-Cell helicopter test bed and the ESL's 3-DOF motion simulation platform, a number of systems were implemented or modified:

- An MCA-based ship motion prediction algorithm was implemented and software was developed for the real-time execution thereof.
- Environmental, platform and helicopter landing criteria limits were determined and systems and methods were developed for the real-time analysis thereof for landing opportunity identification.
- The helicopter's heave motion estimator's bandwidth was increased for platform tracking purposes by GPS latency compensation.
- A platform heave motion estimator was implemented for the helicopter.
- The helicopter's heave controller was modified by the addition of velocity and acceleration feed forward terms to enable the helicopter to track the heave motion of a platform simulating the motion at the flight deck of a ship.
- A timed deck landing descent controller was designed to allow for a relative descent to a landing opportunity specified by time.
- The helicopter's landing state machine was adapted to allow for safe platform landing operations in the sequence suggested by the designed landing algorithm.
- The helicopter system, the platform system, and prediction and landing criteria analysis systems were integrated via TCP and a more efficient RF link configuration.

Upon completion of the development of the systems, practical testing commenced and provided the following contributions:

- Stationary platform landings were achieved during flight tests.
- Landings on a moving platform which is simulating the real motion of a ship at sea state 4 were achieved during hardware-in-the-loop simulations.

1.4 THESIS OUTLINE

The literature on various aspects of ship deck landing algorithms is considered in Chapter 2 and moving platform landing algorithm design choices are made based on those considerations. The development of the systems required to implement the landing algorithm on ESL hardware is the topic of chapters 3 to 8:

- Chapter 3 deals with the development of a ship motion prediction algorithm and software which can execute such an algorithm.
- Chapter 4 describes appropriate landing criteria and details the development of methods and systems for landing criteria analysis.

- Chapter 5 provides a brief overview of the previously undocumented estimator of the helicopter, highlights some problems associated with it for the project at hand, and describes how the problems were addressed.
- Chapter 6 provides an overview of the previously undocumented low-level controllers of the helicopter, points out shortcomings of the heave controller for the current project, and describes how those shortcomings were addressed.
- Chapter 7 is a detailed description of the high-level controllers designed and implemented for the execution of the proposed landing algorithm.
- Chapter 8 details the integration process, various problems experienced, and ways in which the problems were addressed.

HIL simulations and practical flight testing are the topics of chapters 9 and 10. The testing of the low-level systems discussed in chapters 5 and 6 is discussed in Chapter 9. The testing of the high-level controller and system integration discussed in chapters 7 and 8 is discussed in Chapter 10.

Conclusions and recommendations are provided in Chapter 11.

2. SHIP DECK LANDING ALGORITHMS

2.1 INTRODUCTION

A ship deck landing algorithm is a sequence which is followed by a helicopter to progress from a state of general waypoint navigation flight until engine stop on the flight deck of a ship. Such an algorithm can be broken into the following components: approach, landing opportunity identification, descent and touchdown. These aspects are considered in the literature for a generic helicopter and ship and, based on the findings, the design of an algorithm for landing a helicopter on a moving platform which is simulating ship flight deck motion is detailed.

2.2 APPROACH

The approach is the route which must be followed by the helicopter from a point during general waypoint navigation flight to a stable lateral and longitudinal position and heading over the flight deck of the ship. Various aerodynamic challenges are faced throughout the approach. Approach altitudes, lateral and longitudinal paths, and heading angles are considered to deal with these challenges.

Throughout the approach enough vertical separation should be allowed between the helicopter and the ship, not only to avoid a collision, but also to avoid momentary partial ground effect when crossing the edge of the deck. Ground effect is the increased lift generated by the main rotor of a helicopter when close to a surface [10]. This is due to an increase in effective angle of attack caused by a decrease in the velocity of the air flow induced by the main rotor, as illustrated in Figure 2.1. While this effect is most pronounced when hovering, ground effect is also observed during forward flight. Significant ground effect is only observed below an altitude of approximately one main rotor blade length above a surface, but an altitude of at least two main rotor blade lengths above a surface is required to ensure that the helicopter is ground effect free.



Figure 2.1 - Flow characteristics for a rotor in hover taxi forward flight near the ground [10]

If only part of the main rotor experiences ground effect while crossing the edge of the deck, a lift imbalance will be experienced resulting in undesirable rolling and/or pitching of the

helicopter. To avoid this, the vertical separation between the helicopter and the ship should be at least two main rotor blade lengths on approach.

The lateral and longitudinal path and the heading angle are chosen to reduce the effect on the helicopter of the wind relative to the flight deck as well as the aerodynamic wake turbulence behind the superstructure of the ship. The wind relative to the flight deck is the vector sum of the local wind velocity and the ship's velocity. A visualisation of the air flowing over a ship best illustrates the aerodynamic wake turbulence experienced at the flight deck. Such a visualisation is shown in Figure 2.2 for headwind conditions.

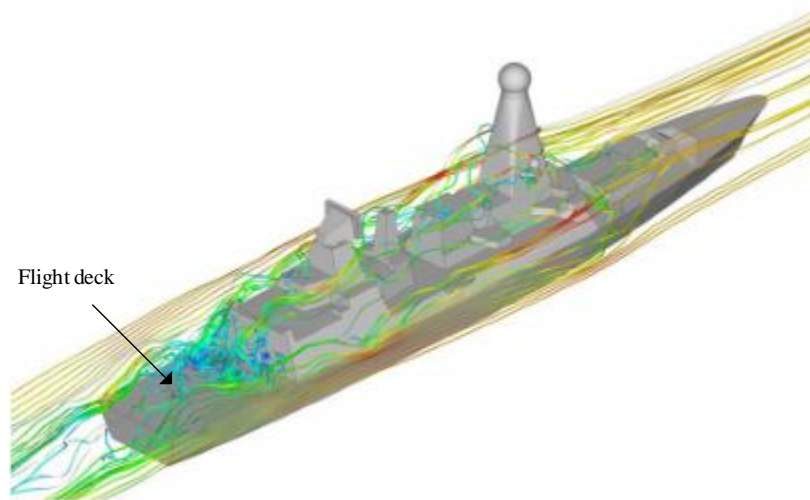


Figure 2.2 - Streamlines coloured by instantaneous velocity magnitude over a Royal Navy Type 45 Destroyer in a headwind derived from CFD simulations [11]

The relative wind and the aerodynamic wake turbulence make it more challenging to control the helicopter when flying over the flight deck. An appropriately chosen lateral and longitudinal path and heading angle can reduce this challenge. The three most common approaches used in the Netherlands and in the United Kingdom are the fore/aft, relative-wind and cross-deck approaches [12].

2.2.1 FORE/AFT APPROACH

The fore/aft (F/A), or forward facing approach, starts with the helicopter at an altitude of at least two main rotor blade lengths above the ship's deck at a hover wait position alongside the port side of the ship, in-line with the landing point, with a heading matching the ship's heading as illustrated in Figure 2.3. A lateral position manoeuvre is executed to reach a hover position above the landing point. Once this position is reached, lateral position, longitudinal position and heading angle relative to the flight deck are maintained for the remainder of the landing procedure.

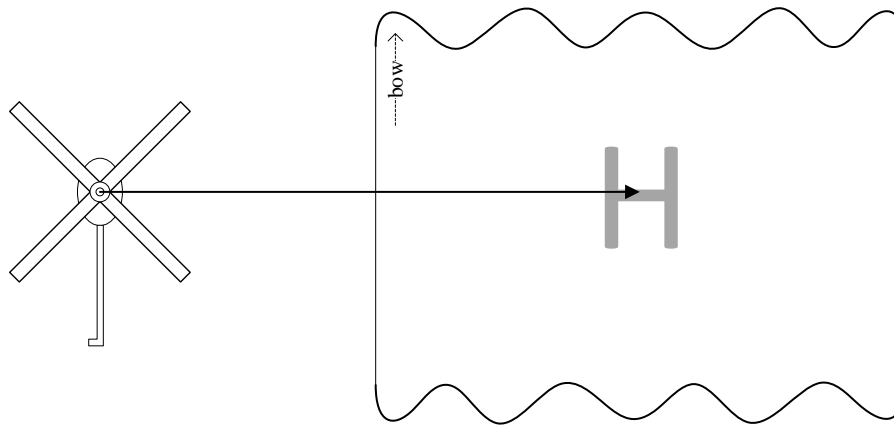


Figure 2.3 - Top view of ship section with helicopter performing F/A landing approach

While the official F/A approach calls for a starting position on the port side of the ship, this is merely to improve the flight deck view of a pilot of a manned helicopter [12]. For an unmanned aerial vehicle (UAV), the starting point should be chosen on the leeward side (downwind) of the ship, be it port or starboard.

The advantage of the F/A approach is that it minimises the time spent in the aerodynamic wake of the ship's superstructure [13]. The disadvantage is that the helicopter becomes more sensitive to the cross-wind component of the wind relative to the deck due to its ship-aligned heading [12]. In addition to the demand placed on the helicopter's lateral and longitudinal controllers to maintain position control, the heading controller is constantly required to counter the yawing moment induced by the wind. The resulting increase in lateral force and rolling moment, due to the increased tail rotor force, places greater demands on the lateral controller. Care must be taken to ensure that the capabilities of the lateral, longitudinal and heading controllers are not exceeded.

2.2.2 RELATIVE-WIND APPROACH

The relative-wind (RW), or into wind approach, starts with the helicopter at an altitude of at least two main rotor blade lengths above the ship's deck at a hover wait position alongside the ship, directly downwind from the landing point, with a heading matching the direction of the wind relative to the deck as illustrated in Figure 2.4. A longitudinal position manoeuvre is executed to reach a hover position above the landing point. The lateral position, longitudinal position and heading angle are maintained for the remainder of the landing procedure.

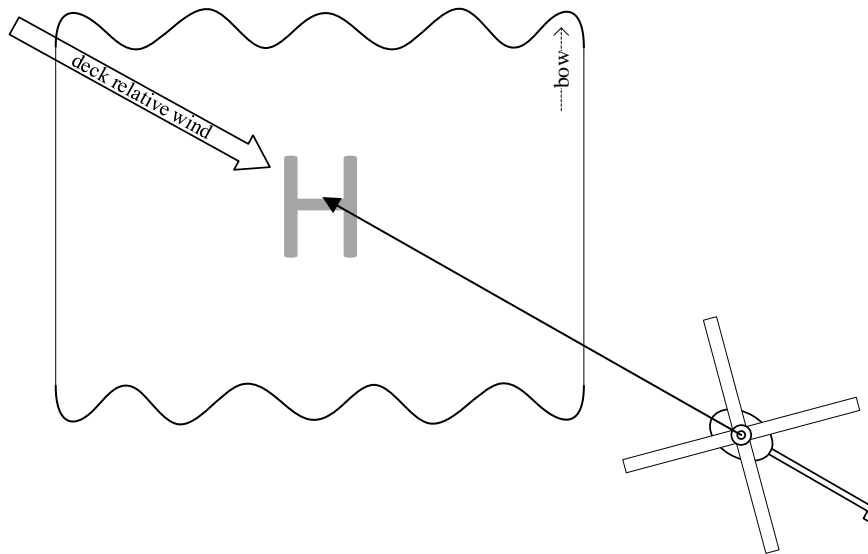


Figure 2.4 - Top view of ship section with helicopter performing RW landing approach

The advantage of the RW approach is that it minimises the surface area of the helicopter with respect to the wind relative to the deck and therefore reduces the effect of the wind on the helicopter. This reduces the demand on the heading and lateral controllers when compared to the F/A approach as the heading controller only needs to reject small, random disturbances (in addition to countering main rotor torque). The disadvantage of the RW approach for UAVs is that, in order to maintain a heading into the wind, the UAV must either be able to measure the relative wind direction or must obtain relative wind information from the flight deck. For manned flight the RW approach limits the pilot's view of the flight deck. As a result, lower wind speed limits are typically used during RW approaches when compared with F/A approaches, but this is not applicable to UAVs.

2.2.3 CROSS-DECK APPROACH

The cross-deck (XD) approach starts with the helicopter at an altitude of at least two main rotor blade lengths above the ship's deck at a hover wait position alongside the leeward side (downwind) of the ship, in-line with the landing point, with the heading perpendicular the ship's heading as illustrated in Figure 2.5. A longitudinal position manoeuvre is executed to reach a hover position above the landing point. Once this position is reached, lateral position, longitudinal position and heading angle relative to the flight deck are maintained for the remainder of the landing procedure.

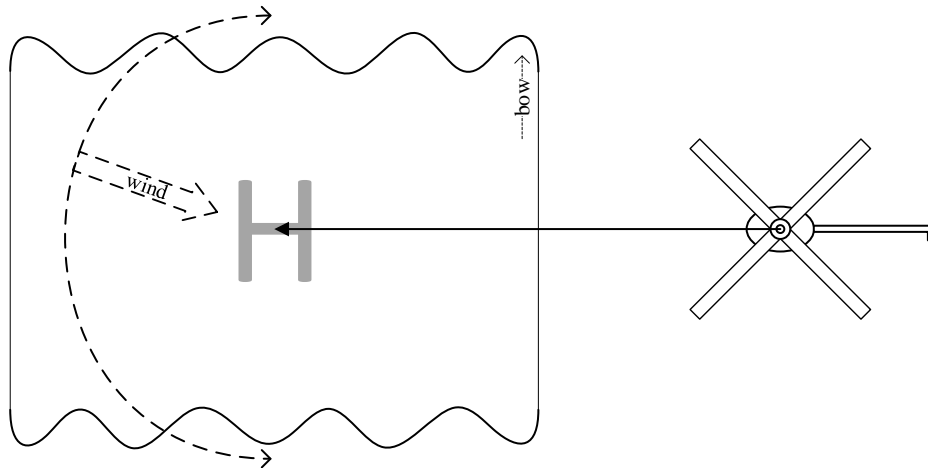


Figure 2.5 - Top view of ship section with helicopter performing XD landing approach

The advantages and disadvantages of the XD approach are quite similar to the F/A approach discussed in Section 2.2.1 except that the helicopter becomes more sensitive to the head or tail wind component (instead of the cross-wind component) of the wind relative to the deck. For manned flight the XD approach limits the pilot's view of the flight deck even more than the RW approach. As a result, lower wind speed limits are typically used during XD approaches when compared with F/A and RW approaches, but this is not applicable to UAVs.

2.3 LANDING OPPORTUNITY IDENTIFICATION

Once the approach has been completed, safe landing opportunities must be identified. For UAVs, a safe landing is defined as a landing which is completed without damaging the helicopter or ship and without injuring ground personnel. For manned flight, the passengers and crew must also be uninjured for a landing to be considered safe. The relative motion between the helicopter and the ship at touchdown determines the outcome of the landing. Ship and helicopter states of motion at landing time can therefore be analysed to determine whether a landing opportunity has presented itself.

2.3.1 SHIP MOTION PREDICTION

If ship motions can be predicted, landing opportunities can be identified longer before they are realised, which allows more time to execute a landing. During manned flight, if no predictive aids are available, the pilot and Landing Safety Officer (LSO) attempt to make very short term manual predictions of what the ship is likely to do next [13], but the stochastic nature of the forces which act on ships makes the task of predicting ship motion difficult [14]. Longer term automated predictions (also suitable for use with UAV systems) can be produced with suitable prediction algorithms.

Two main prediction approaches appear in the literature: (1) making predictions based on past ship motion data and (2) making predictions based on a ship model driven by various inputs such as actuator inputs and wave motion data from a suitable sensor (e.g. radar). While the latter approach has been shown to provide prediction horizons of 2 minutes [15], it requires a complex model for every ship which it is used on and also requires expensive wave motion sensors. In recent literature some prediction algorithms based on the former prediction approach have been shown to provide prediction horizons of up to 20 s [16], sufficient for most helicopter landing systems.

Many publications on the topic of ship motion prediction use computer generated data (combinations of noisy sine waves or simulated wave data) to test prediction algorithm performance [16, 17, 18, 19]. Due to the stochastic nature of the sea surface waves typically experienced by a ship, this is not an adequate performance indicator [14]. Tests on empirical ship motion data provide a much better idea of the performance of a prediction algorithm. It is therefore important to take note of the type of input data used when comparing publications on the topic of ship motion prediction. The sea state at the time when the ship motion data was captured also greatly affects ship motion prediction performance [14, 19]. Therefore the sea state should also be noted when comparing publications on the topic of ship motion prediction. “Sea state” is defined as follows: “A description of the properties of sea surface waves at a given time and place. This might be given in terms of the wave spectrum, or more simply in terms of the significant wave height and some measure of the wave period.” [20]. Sea states are classified from 0 to 9, where 0 is described as “calm” and 9 is described as “phenomenal” [21]. Sea state 4, with 1.25 m to 2.5 m waves with a period of 6.1 s to 15.2 s, is the most common sea state [22] and can be described as “moderate” [21]. A table specifying the metrics associated with all the NATO North Atlantic sea states is provided in Appendix B. In addition to noting the type of input data and the sea state when comparing publications on the topic of ship motion prediction, the size and mass of the ship used should be noted as they affect the dynamics of the ship [14].

2.3.1.1 AUTO-REGRESSION

From *et al.* [14] proposed an auto-regressive (AR) predictor and compared it to the predictor proposed by Chung *et al.* [23] which finds a superposition of sinusoidal waves to represent past ship motion data and propagates that representation into the future. Real ship motion data of a 96 ton, 20.4 metre long Emmy Dyvi class ship recorded at sea state 3 was used to test and compare the predictors. The AR predictor was found to be more accurate than the superposition of sinusoidal waves, except for prediction horizons of 0.2 s or less. The predictions produced by the AR predictor for a prediction horizon of up to 3 s were described

as reasonable (approximately in phase) and without large errors in magnitude (standard deviation of 0.3 m/s).

2.3.1.2 FORGETTING FACTOR RECURSIVE LEAST SQUARES

Yang *et al.* [17, 18, 19] proposed a predictor based on an adaptive order time series model, solved by the forgetting factor recursive least squares (FFRLS) method, and compared it to an AR predictor. Computer generated ship motion data of an 8534 ton, 159 metre long [24] Kanimbla class Landing Platform Amphibious ship simulated by the FREYDYN 8.0 software package at sea state 3 was used to test and compare the predictors. Predictions produced by the AR predictor were slightly more accurate in magnitude than those produced by the FFRLS predictor, but the FFRLS predictor offered better phase accuracy and lower memory requirements. The FFRLS predictor produced 12.5 s predictions with a 10% error.

2.3.1.3 NEURAL NETWORKS

Kahn *et al.* [25, 26] proposed a predictor based on an artificial neural network (NN) trained using singular value decomposition (SVD) and genetic algorithms. Real ship motion data of a cruiser-size vessel operating in sea states 5 to 6 was used to test the predictor. The 7 s predictions produced by the predictor were described as accurate.

2.3.1.4 MINOR COMPONENT ANALYSIS

Zhao *et al.* [16] proposed a predictor based on minor component analysis (MCA) and compared it to NN, AR and Weiner predictors. Computer generated ship motion data of an 8362 ton, 154 metre long [27] DDG-51 destroyer simulated by John J. McMullen Associates, Incorporated at sea state 3 was used to test and compare the predictors. The MCA predictor was shown to predict ship motion 5 s and 20 s into the future with a smaller error and with lower computational demands than any of the other predictors in the comparison. For a prediction horizon of 20 s, the MCA predictor was shown to predict ship motion very accurately (root mean square error (RMSE) of 0.05 m).

Mok [28] also proposed a predictor based on MCA. Real ship motion data recorded at sea state 4 was used to test the predictor. The physical specifications of the ship used were not specified. For a prediction horizon of 5 s, the predictor's performance was described as reasonable (RMSE of 1.5° and correlation coefficient of 0.78).

2.3.1.5 SUMMARY

The various ship motion prediction algorithms considered above are summarised in the following table:

Researcher	Method	Data source	Sea state	Prediction horizon
From <i>et al.</i>	AR	Real ship: 96 t, 20.4 m	3	3 s
Yang <i>et al.</i>	FFRLS	Sim ship: 8534 t, 159 m	3	12.5 s
Kahn <i>et al.</i>	NN	Real ship: Cruiser-size	5-6	7 s
Zhao <i>et al.</i>	MCA	Sim ship: 8362 t, 154 m	3	20 s
Mok	MCA	Real ship: Specs unknown	4	5 s

Table 2.1 - Ship motion prediction algorithm summary

2.3.2 LANDING CRITERIA ANALYSIS

Landing criteria analysis involves comparing ship and helicopter states of motion with certain criteria in order to identify safe landing opportunities, where the ship and helicopter states of motion are also dependent on various environmental effects.

If the relevant environmental effects are out of bounds, the ship and helicopter motion criteria are unlikely to be met. Limits on environmental effects can therefore be seen as preliminary criteria which must be met before landings can be considered. The speed and direction of the wind relative to the ship, as well as the aerodynamic wake of the ship's superstructure, must be within the disturbance rejection capabilities of the helicopter's controllers [12]. The sea state must also be calm enough (for the given ship) to ensure that ship motion will be within bounds, if only for a short period of time [12, 29]. The effect of sea state on ship pitch and roll amplitudes is illustrated in Figure 2.6 for a sample ship.

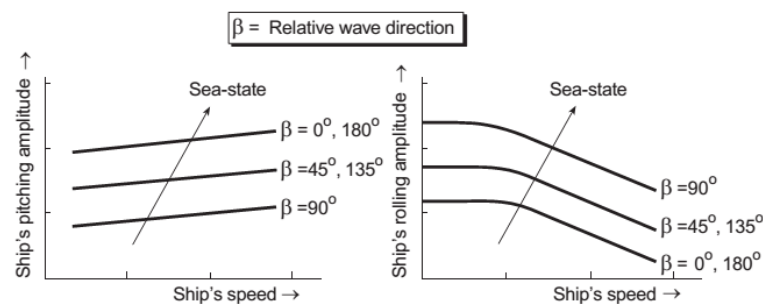


Figure 2.6 - Example ship pitch and roll amplitudes vs. ship speed and heading [12]

In addition to being a function of sea state, ship motion is a function of wave direction (and therefore ship heading) and ship speed [29]. During helicopter operations, ships are typically operated at constant heading and speed [30]. A heading chosen so that the waves come from approximately the bow or stern of the ship (i.e. not from the side) typically provides the

largest landing envelope, as illustrated in Figure 2.7 [31]. The effect of ship speed and heading on ship pitch and roll amplitudes is illustrated in Figure 2.6 for a sample ship.

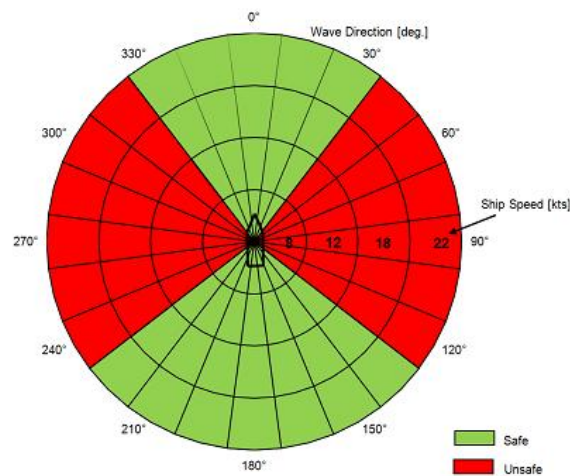


Figure 2.7 - Safe and unsafe wave directions and corresponding ship speeds for an unrestrained UAV [31]

The ship flight deck's absolute heave acceleration is of critical importance at landing time [30]. At heave velocity peaks and troughs, heave acceleration is approximately equal to zero, but at heave velocity peaks (in the inertial north-east-down (NED) frame) the descending flight deck may lead to soft touchdowns. A soft touchdown may result in multiple contacts which could damage the helicopter [32]. During an upward heave motion of the flight deck, the helicopter can simply maintain its position and positive contact will occur. At heave velocity troughs (NED), upward heave motion and zero heave acceleration are experienced simultaneously. Therefore, heave velocity troughs (NED) should be targeted for landing.

The relative velocity between the helicopter and the ship's flight deck is also important at landing time [30]. Thus minimum relative velocity between the helicopter and the ship flight deck should be targeted for landing.

At a hover throttle setting, a helicopter cannot maintain commanded roll and pitch angles without accelerating laterally or longitudinally. Therefore, minimum absolute ship roll and pitch angles should be targeted for landing. Bounds on ship roll and pitch angles should take into account the angle at which dynamic rollover can occur [12] and the angles at which tail strikes or main rotor strikes can occur.

Under ideal conditions, the helicopter's lateral and longitudinal position should be fixed at landing time. Additionally, the heave velocity of the flight deck should be a minimum (NED trough) and the relative velocity between the helicopter and the ship should be 0 m/s. Finally, helicopter roll and pitch angles should be 0° while ship roll and pitch angles should also be

0°. Meeting these criteria simultaneously on a real ship/helicopter system is highly unlikely. In practice, various bounds are set for the motion states where successful landings are known to be possible. Ship-Helicopter Operating Limits (SHOLs) or an Energy Index (EI) define such bounds.

2.3.2.1 SHIP-HELICOPTER OPERATIONAL LIMITS

SHOLs are traditionally used to define landing envelopes for ship-helicopter combinations. The landing envelopes depend on the approach, wind speed, wind direction, ship roll and ship pitch [12]. Example SHOLs for a port-side fore/aft approach (as described in Section 2.2.1) are provided in Figure 2.8 for two helicopters with different masses (black vs. red lines). The polar plot represents the deck relative wind speed and direction envelope.

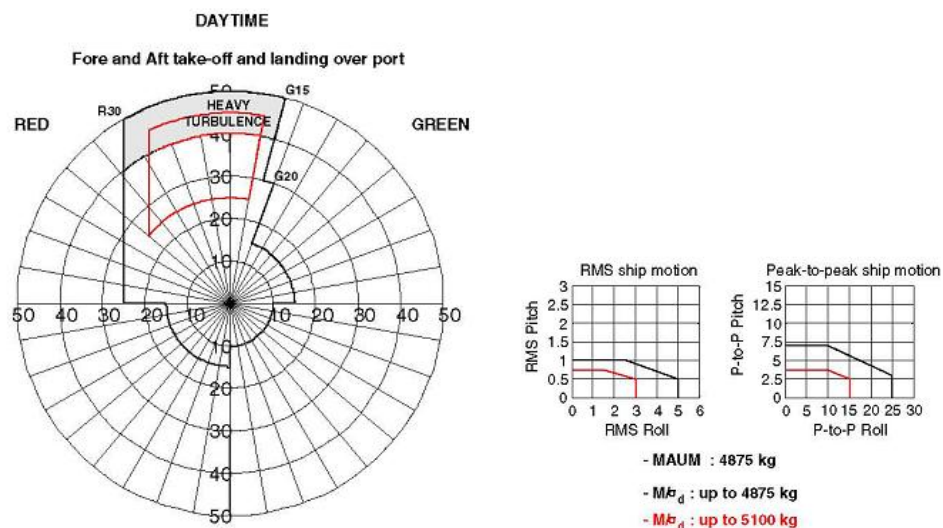


Figure 2.8 - Example SHOLs [29]

SHOLs do not provide a way to identify calm or quiescent periods of ship motion. During manned helicopter operations using SHOLs a Landing Safety Officer (LSO) or Flight Deck Officer (FDO) is given that task [13].

SHOLs for a specific ship-helicopter combination are traditionally determined by experimental testing at sea [29]. A more conservative version of the helicopter's on-shore flight envelope is used as the initial landing envelope. The purpose of testing is to expand this initial landing envelope. In order to save time and money, some testing can be performed through simulations. Landings are judged by the size of the impact forces experienced at touchdown. SHOLs are typically 20° to 25° for the ship's roll angle and 4° to 6° for the ship's pitch angle [30]. Static limits like SHOLs are quite conservative and therefore produce restrictive landing envelopes [13].

2.3.2.2 ENERGY INDEX

The EI and its limits offer another way to define landing envelopes for ship-helicopter combinations. The EI characterises the kinetic and potential energy state of the ship and is therefore dependent on ship motion states [33]. The limits are dependent on the effect of ship motions on the structural integrity of the helicopter when landing. Ferrier *et al.* [34] proposed the following equation to calculate the EI,

$$EI = a_1\dot{y}^2 + a_2\ddot{y}^2 + a_3\dot{z}^2 + a_4\ddot{z}^2 + a_5\dot{\phi}^2 + a_6\ddot{\phi}^2 + a_7\dot{\theta}^2 + a_8\ddot{\theta}^2 \quad (2.1),$$

where a_1 to a_8 are weighted dynamic coefficients, \dot{y} and \ddot{y} are the lateral velocity and acceleration at the landing point, \dot{z} and \ddot{z} are the heave velocity and acceleration at the landing point, ϕ and $\dot{\phi}$ are the roll angle and rate of the ship, and θ and $\dot{\theta}$ are the pitch angle and rate of the ship. The weighted dynamic coefficients are calculated in real time and depend on the ship's velocity, the relative wave angle, the significant wave height, the modal period, the coupling between the various degrees-of-freedom and aircraft limitations [33].

The EI does not only provide information about the instantaneous energy state of the ship. In order for a ship to transition from a low to a high energy state, a certain quantity of energy must be transferred to it from the sea. The minimum amount of time required to transition from a low energy state to the beginning of a high energy state is fairly consistent for a given ship-helicopter combination and is called the rise time as indicated in Figure 2.9 [33]. When performing operations with a Lynx helicopter the rise time is 4.8 s for a Type 23 class frigate (4900 tons) and 4.9 s for a Type 22 class frigate (5300 tons) [35]. Therefore, while the EI does not produce ship motion predictions per se, once the EI has identified a low energy state, the duration of the calm or quiescent period of ship motion has an element of predictability. Landings can be attempted during the quiescent periods.

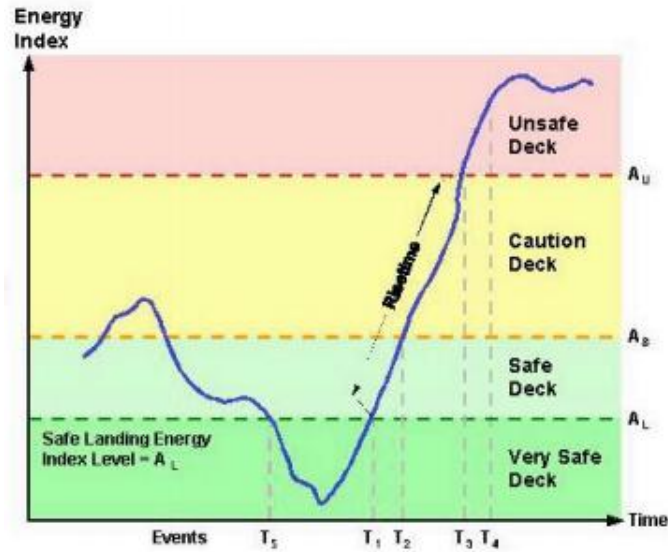


Figure 2.9 - Deck availability and rise time determined by EI [33]

The EI limits are determined analytically or experimentally [33]. Due to the scalar nature of the EI, it is difficult to define initial EI limits without having prior ship deck landing data available to test the limits. A combination of experimental tests at sea and simulations are used to expand the landing envelope. Dynamic limits such as those provided by the EI provide wider operational envelopes than static limits while maintaining similar safety margins [13].

2.4 DESCENT

After a landing opportunity has been identified, a descent must be initiated in order to make timeous use of the landing opportunity. The descent should be initiated from the hover position reached at the end of the approach.

Due to ground effect, lift will increase gradually as the descent to the ship's deck proceeds from an altitude of two main rotor blade lengths above the flight deck to touchdown as discussed in Section 2.2.

As suggested in Section 2.3, a minimum relative heave velocity between the helicopter and the ship should be targeted for landing.

The helicopter's maximum allowable absolute descent velocity is the velocity just before it enters the vortex ring state (VRS), also known as settling with power (SWP). The VRS occurs when the helicopter descends faster than the velocity of the induced airflow over the inner part of the main rotor, reversing the direction of the flow in this area [10, 36]. The opposing directions of the induced air flows over the main rotor result in the development of vortices as

illustrated in Figure 2.10. The resulting turbulent flow over the main rotor severely reduces lift.

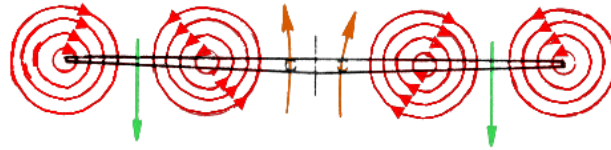


Figure 2.10 - Flow over main rotor during VRS [37]

With the above mentioned descent factors in mind, two descent strategies are considered: (1) absolute velocity descent and (2) deck heave motion tracking descent.

2.4.1 ABSOLUTE VELOCITY DESCENT

A descent strategy which is commonly used has the helicopter proceed from a high hover to a low hover when a calm or quiescent period of ship motion appears to be approaching, followed by a final descent if all landing criteria have been met [29, 38, 39, 40, 41]. For the purposes of this thesis, this strategy is referred to as the *absolute velocity descent* as the ship flight deck's heave velocity is not tracked.

There is a possibility that there will be insufficient vertical separation between the helicopter and deck at some point during the descent before the landing point is reached. It is therefore necessary to constantly monitor ship motion during the descent and, if there is a possibility of premature deck contact, adjust the descent appropriately or abort the descent.

Absolute heave velocity is controlled by the helicopter's heave controller. In order to ensure that landing occurs at the predicted suitable landing time, the ship motion prediction algorithm must make accurate predictions of both the phase and the amplitude of the heave position of the flight deck. This is because the required final descent velocity is calculated by taking the vertical separation between the helicopter and the *predicted* flight deck heave position over the time to landing. As relative heave velocity is not controlled with this descent strategy a minimum relative heave velocity cannot be controlled directly. Care should be taken to not exceed the absolute descent velocity at which the helicopter enters the VRS.

As commanded descent velocities are almost constant, the absolute velocity descent strategy demands little of the helicopter's heave controller.

2.4.2 DECK HEAVE MOTION TRACKING DESCENT

A descent strategy where the helicopter has to track the heave motion of the ship's flight deck throughout the entire descent is also used [42, 43, 44, 45]. For the purposes of this thesis, this

strategy is referred to as the *deck heave motion tracking descent*. Such a descent strategy is only suitable for helicopters that are capable of following typical ship motions.

Premature deck contact is avoided as the relative heave position between the helicopter and the deck is constantly controlled by the helicopter's heave controller.

Relative heave velocity is also controlled by the helicopter's heave controller. This allows for better control over the future landing time as, to land at a desired time, a relative velocity is commanded which equals the *current* relative heave position over the time to landing. As a result, lower demands are made on the accuracy of the amplitude of the heave position predictions made by the ship motion prediction algorithm. Control over the relative heave velocity also allows the helicopter to minimise the relative velocity between itself and the ship at landing time. The absolute descent velocity should also be monitored to ensure that the helicopter does not enter the VRS.

As the helicopter tracks the heave motion of the flight deck throughout the entire descent, the deck heave motion tracking descent places relatively high demands on the helicopter's heave controller.

2.5 TOUCHDOWN

Upon completion of the descent, touchdown occurs on the ship's flight deck. At touchdown, minimum relative motion between the helicopter and the ship should be targeted.

In order to reduce the relative motion, the friction between the helicopter and the flight deck should be increased. Friction is increased by maximizing the force which the helicopter exerts on the ship by lowering the collective to the full down position and centring the cyclic [32]. In addition, the gyroscopic rigidity of the helicopter should be minimised to avoid rolling or pitching relative to the ship due to a rolling or pitching ship motion. This is achieved by throttling down the engine to spin down the main rotor.

Absolute minimum relative motion between the helicopter and the ship can be achieved with a suitable arrestor system which physically fastens the helicopter to the ship at touchdown. The landing envelope for unrestrained landings of a certain ship-helicopter combination is provided in Figure 2.7. This landing envelope is increased greatly with a landing arrestor system [12, 31]. The landing envelope for restrained landings of the same ship-helicopter combination of Figure 2.7 is provided in Figure 2.11. The weight and complexity which a landing arrestor system adds to a helicopter must be weighed up against the advantages of such a system.

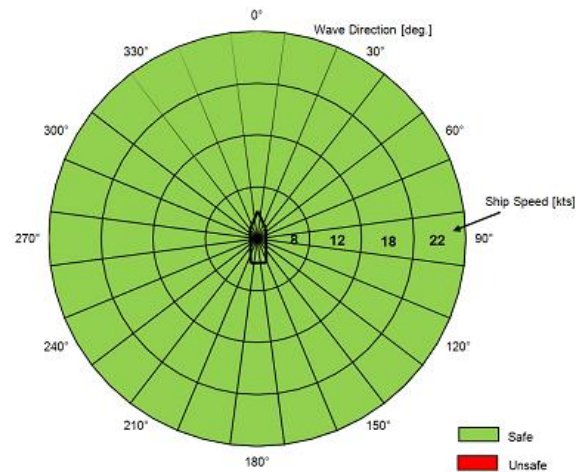


Figure 2.11 - Safe and unsafe wave directions and corresponding ship speeds for a restrained UAV [31]

An example of an arrestor system is the Light Harpoon Landing Restraint System used by Northrop Grumman's MQ-8B Fire Scout [46]. It fastens the helicopter to the ship's deck at touchdown by shooting a metal harpoon-like device into a metal grid.

2.6 3-DOF PLATFORM LANDING ALGORITHM

Based on the above considerations of the various aspects of a ship deck landing algorithm, an algorithm was designed in this study for landing an unmanned helicopter on a 3-DOF platform while it is simulating ship flight deck motion.

The approaches discussed in Section 2.2 take into account ground effect, the wind relative to the flight deck and the aerodynamic wake turbulence behind the superstructure of the ship. To avoid ground effect, the approach should be executed at an altitude of at least two main rotor blade lengths above the platform. As a ship superstructure is not present during 3-DOF platform landings, aerodynamic wake turbulence need not be taken into account. The relative wind (RW) approach, discussed in Section 2.2.2, deals with wind the best and was therefore chosen.

The existing literature on the topic of ship motion prediction as presented in Section 2.3.1 suggests that NN predictors have superior performance to the other predictors considered when processing real ship motion data. NN predictors have the disadvantage that they converge to an unknown mathematical structure. The mathematical structure of MCA predictors, which offer the next best performance, is known. As this is preferred for the current study, MCA predictors were chosen.

The preliminary landing criteria mentioned in Section 2.3.2 place limits on the type of ship motion data simulated by a 3-DOF platform during helicopter landing tests. Suitable ship motion data is data which is recorded by a ship at constant heading and speed at sea in a state

which is sufficiently calm for helicopter operations. While the aerodynamic wake of a ship's superstructure is not experienced during platform landing operations, the speed and direction of the wind relative to the platform must be within the disturbance rejection capabilities of the helicopter's controllers. As 3-DOF platforms typically offer a smaller landing area than a ship's flight deck, stricter lateral and longitudinal position error limits must be enforced during platform landings. Simultaneously, helicopter roll and pitch angles must be kept to a minimum. Furthermore, minimum absolute platform heave acceleration, an upward platform heave motion and minimum relative heave velocity between the helicopter and the platform must be targeted for landing. Of the methods of defining landing criteria limits discussed in sections 2.3.2.1 and 2.3.2.2, the EI is preferred as it provides automatic calm or quiescent period identification and a wider landing envelope than SHOLs. Due to the difficulties associated with determining initial EI limits, the EI was only chosen for established platform-helicopter combinations and SHOLs were chosen for new platform-helicopter combinations.

Of the descent strategies considered in Section 2.4, the *deck heave motion tracking descent* strategy is preferred due to its ability to directly control and minimise the relative velocity between the helicopter and the ship at touchdown, critical for the structural integrity of the helicopter's landing gear. As the *deck heave motion tracking descent* is only suitable for helicopters which are capable of following typical ship motions, it was chosen for such helicopters. For other helicopters the *absolute velocity descent* strategy was chosen.

As discussed in Section 2.5, at touchdown, in addition to lowering the collective to the full down position, centring the cyclic and throttling down the engine, an arrestor system must be used in order to provide the widest possible landing envelope.

The complete algorithm designed for 3-DOF platform landings is presented in the flowchart provided in Figure 2.12.

2.7 SUMMARY

Various aspects of ship deck landing algorithms for helicopters were considered. Based on these considerations, an algorithm was designed for landing on a 3-DOF platform while it is simulating ship flight deck motion. The development of the systems which are required to implement the proposed landing algorithm for landing of the ESL's X-Cell helicopter test bed on the ESL's 3-DOF platform is the topic of the following chapters.

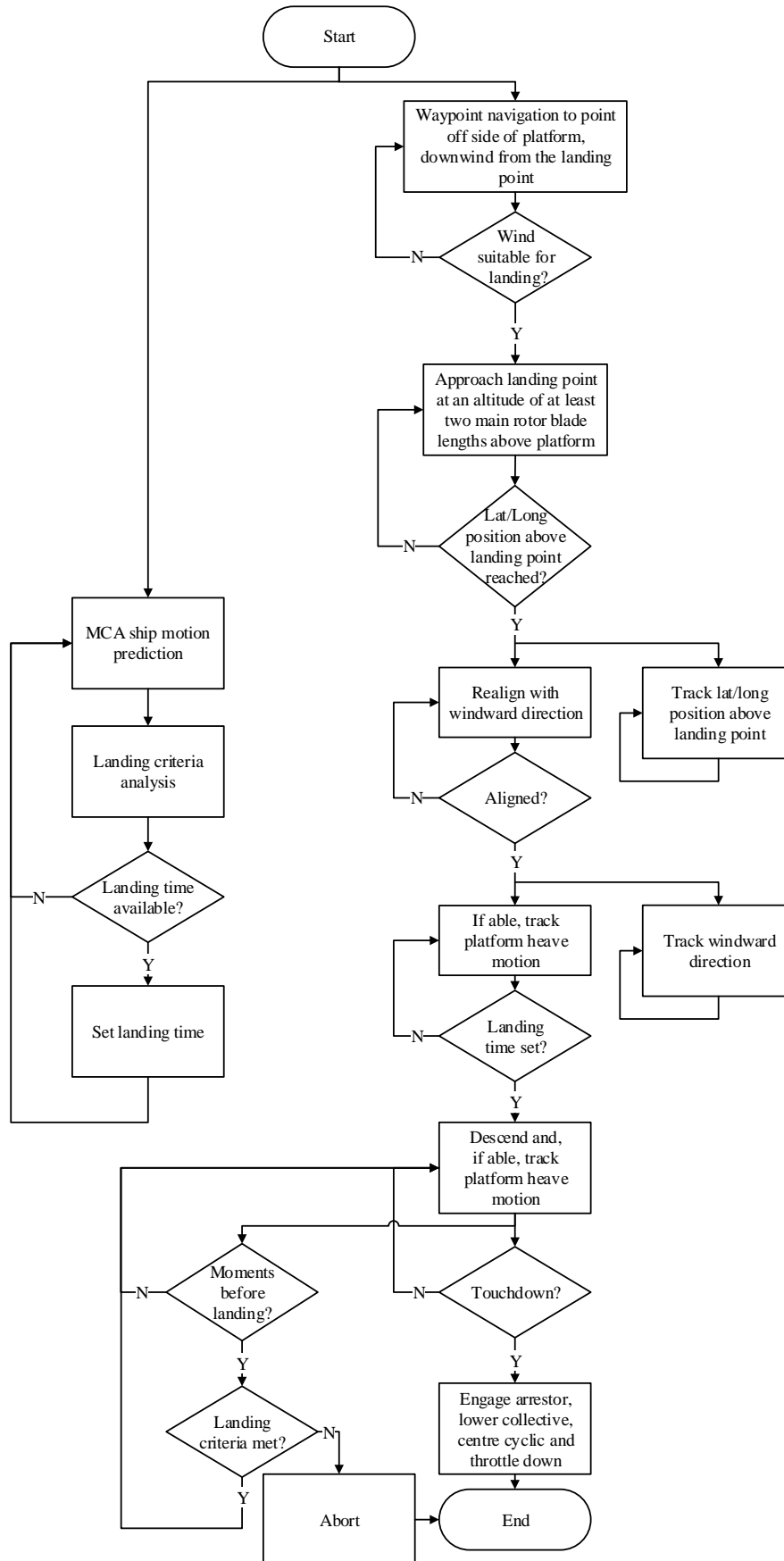


Figure 2.12 - Flowchart of the designed 3-DOF platform landing algorithm

3. SHIP MOTION PREDICTION

3.1 INTRODUCTION

The ship motion prediction algorithm chosen in Section 2.6 is MCA-based. Requirements set out for the algorithm are:

- Produce the greatest possible prediction horizon. The greater the prediction horizon provided by the prediction algorithm, the lower the helicopter's descent rate relative to the ship's deck can be. For the planned *deck heave motion tracking descent*, the accuracy of the phase of the predictions is the most important while the accuracy of the amplitude of the predictions is of secondary importance.
- Use a C implementation to allow easy porting to a microprocessor in future.
- Run in real-time on the available laptop computer based on an Intel Core i5-2415M processor clocked at 2.3 GHz.

In this chapter the theory, implementation and testing of the MCA-based prediction algorithm used for this project is described.

3.2 MINOR COMPONENT ANALYSIS

MCA or minor subspace analysis (MSA) is a technique used for the extraction of the minor components of a dataset. The minor components form an orthogonal basis for the minor or noise subspace which contains the components of the dataset with the smallest variance. As a result, if a dataset is captured in a matrix $\mathbf{X} \in \mathbb{R}^{P \times L}$ containing P samples of an L -dimensional time series and M minor components of \mathbf{X} are captured in the columns of the matrix $\mathbf{C} \in \mathbb{R}^{L \times M}$, the following approximate equation holds [16], which can eventually be used for ship motion prediction as explained in the following sections:

$$\mathbf{XC} \approx \mathbf{0} \quad (3.1).$$

MCA is mathematically similar to the popular principal component analysis (PCA) which is used for the extraction of the principal components of a dataset. The principal components form an orthogonal basis for the principal or signal subspace which contains the components of the dataset with the greatest variance. PCA finds the principal components by taking the eigenvectors corresponding to the largest eigenvalues of the dataset's covariance matrix. MCA also involves the eigenvalue decomposition of the dataset's covariance matrix except that the minor components are the eigenvectors corresponding to the smallest eigenvalues.

3.2.1 INPUT DATA

Ship data is sampled at a rate of at least twice the highest frequency of significant ship motion in order to avoid aliasing [47]. The resolution of the predictions is also determined by the sampling rate.

In order to obtain the correct input data formatting, sampled ship motion data $x[k]$ is placed into a number of row vectors $\mathbf{x}_n \in R_{1 \times L}$ of length L :

$$\mathbf{x}_n = \{ x[n] \quad x[1+n] \quad \dots \quad x[L-1+n] \} \quad (3.2).$$

L is chosen so that each vector contains a number of full motion cycles in order to capture the behaviour of the axis of motion in question. P vectors are then placed into the matrix $\mathbf{X}_O \in R_{P \times L}$ as follows:

$$\mathbf{X}_O = \begin{bmatrix} \mathbf{x}_1 \\ \mathbf{x}_2 \\ \vdots \\ \mathbf{x}_P \end{bmatrix} \quad (3.3).$$

For clarity, matrix \mathbf{X}_O is expanded:

$$\mathbf{X}_O = \begin{bmatrix} x[1] & x[2] & \dots & x[L] \\ x[2] & x[3] & \dots & x[L+1] \\ \vdots & \vdots & \ddots & \vdots \\ x[P] & x[1+P] & \dots & x[L-1+P] \end{bmatrix} \quad (3.4).$$

3.2.2 MINOR AND PRINCIPAL COMPONENT EXTRACTION

The minor and principal components can be extracted by finding the eigenvalue decomposition of the uniformly weighted autocovariance matrix [16, 28]. In order to increase the effect of recent measurements and decrease the effect of old measurements, an exponentially weighted autocovariance matrix is also considered.

3.2.2.1 UNIFORMLY WEIGHTED AUTOCOVARANCE MATRIX

In order to obtain the uniformly weighted autocovariance matrix, matrix \mathbf{X}_O must first be column centred. The vector of column means $\bar{\mathbf{x}} \in R_{1 \times L}$ is calculated by summing all the rows of \mathbf{X}_O (the row vectors \mathbf{x}_n) and dividing by the number of rows:

$$\bar{\mathbf{x}} = \frac{1}{P} \sum_{n=1}^P \mathbf{x}_n \quad (3.5).$$

Next, the vector of column means ($\bar{\mathbf{x}}$) is copied P times into the rows of matrix $\bar{\mathbf{X}} \in R_{P \times L}$:

$$\bar{\mathbf{X}} = \begin{bmatrix} \bar{x} \\ \bar{x} \\ \vdots \\ \bar{x} \end{bmatrix} \quad (3.6).$$

Now the column centred matrix $\mathbf{X} \in R_{P \times L}$ is calculated by subtracting the matrix of column means $\bar{\mathbf{X}}$ from matrix \mathbf{X}_0 :

$$\mathbf{X} = \mathbf{X}_0 - \bar{\mathbf{X}} \quad (3.7).$$

The uniformly weighted autocovariance matrix $\mathbf{R} \in R_{L \times L}$ of $x[k]$ is now calculated as follows:

$$\mathbf{R} = \mathbf{X}^T \mathbf{X} \quad (3.8).$$

Strictly speaking the right hand side of equation (3.8) should be multiplied by $\frac{1}{P-1}$ to get the unbiased sample autocovariance matrix, but this simply results in a scaling of the eigenvalues of \mathbf{R} and does not affect the eigenvectors.

3.2.2.2 EXPONENTIALLY WEIGHTED AUTOCOVARANCE MATRIX

In order to obtain the exponentially weighted autocovariance matrix, a set of exponential weights must first be calculated. The following equations are used to determine a suitable set of exponential weights $w[k]$,

$$w_0[k] = e^{\alpha(k-P)} \quad (3.9),$$

$$w[k] = \frac{w_0[k]}{\sum_{m=1}^P w_0[m]} \quad (3.10),$$

where α is the exponential decay factor. As α tends to 0, the weights tend to uniformity. The larger α becomes, the less the oldest measurements and the more the newest measurements affect the autocovariance estimate.

Matrix \mathbf{X}_0 must now be column centred. The vector of weighted column means $\bar{\mathbf{x}} \in R_{1 \times L}$ is calculated by summing the weighted rows of \mathbf{X}_0 [48]:

$$\bar{x} = \sum_{n=1}^P w[n] x_n \quad (3.11).$$

Next, the vector of column means \bar{x} is copied P times into the rows of matrix $\bar{\mathbf{X}} \in R_{P \times L}$:

$$\bar{\mathbf{X}} = \begin{bmatrix} \bar{x} \\ \bar{x} \\ \vdots \\ \bar{x} \end{bmatrix} \quad (3.12).$$

Now the column centred matrix $\mathbf{X}_I \in R_{P \times L}$ is calculated by subtracting the matrix of weighted column means $\bar{\mathbf{X}}$ from matrix \mathbf{X}_O :

$$\mathbf{X}_I = \mathbf{X}_O - \bar{\mathbf{X}} \quad (3.13).$$

Each element $R_{i,j}$ of the exponentially weighted autocovariance matrix $\mathbf{R} \in R_{L \times L}$ of $x[k]$ is calculated by the following formula [48]:

$$R_{i,j} = \sum_{k=1}^P w[k] (X_{I_{k,i}}) (X_{I_{k,j}}) \quad (3.14).$$

For implementation purposes a matrix calculation like the one represented in equation (3.8) is preferred and therefore $\mathbf{X}^T \mathbf{X}$ is desired in the final calculation. From equation (3.14) it is apparent that each row of \mathbf{X}_I can simply be weighted by the square root of each weighting factor in order to find a suitable matrix \mathbf{X} . For better clarity, \mathbf{X}_I is first expanded slightly:

$$\mathbf{X}_I = \begin{bmatrix} (x_1 - \bar{x}) \\ (x_2 - \bar{x}) \\ \vdots \\ (x_P - \bar{x}) \end{bmatrix} \quad (3.15).$$

Now \mathbf{X} , the exponentially weighted version of \mathbf{X}_I , is found as follows:

$$\mathbf{X} = \begin{bmatrix} (x_1 - \bar{x})\sqrt{w[1]} \\ (x_2 - \bar{x})\sqrt{w[2]} \\ \vdots \\ (x_P - \bar{x})\sqrt{w[P]} \end{bmatrix} \quad (3.16).$$

Finally, the exponentially weighted autocovariance matrix $\mathbf{R} \in R_{L \times L}$ of $x[k]$ is calculated as follows:

$$\mathbf{R} = \mathbf{X}^T \mathbf{X} \quad (3.17).$$

Strictly speaking the right hand side of equation (3.17) should be multiplied by a factor to get the unbiased sample autocovariance matrix, but this simply results in a scaling of the eigenvalues of \mathbf{R} and does not affect the eigenvectors.

3.2.2.3 EIGENVALUE DECOMPOSITION

The singular value decomposition (SVD) of \mathbf{X} can be used to calculate the eigenvalues and corresponding eigenvectors of \mathbf{R} [28]. The advantage of using the SVD is that it is numerically robust, automatically sorts the eigenvalues and corresponding eigenvectors from largest to smallest eigenvalue and is available in many mathematical programming libraries. If \mathbf{X} only contains real elements, its SVD gives

$$\mathbf{X} = \mathbf{U}\mathbf{\Sigma}\mathbf{V}^T \quad (3.18),$$

where the diagonal of $\mathbf{\Sigma} \in \mathbb{R}^{P \times L}$ contains the square roots of the eigenvalues of \mathbf{R} in descending order and the columns of $\mathbf{V} \in \mathbb{R}^{L \times L}$ contain the corresponding eigenvectors of \mathbf{R} which are the minor and principal components. The eigenvalues \mathbf{E} of \mathbf{R} can be found by squaring $\mathbf{\Sigma}$:

$$\mathbf{E} = \mathbf{\Sigma}^2 \quad (3.19).$$

3.2.3 MINOR COMPONENT SELECTION

The eigenvectors corresponding with the smallest eigenvalues of \mathbf{R} are the minor components. Minor components can be selected based on the percentage of the total energy of the input data which they contain [16]. The percentage of the total energy of the input data contained in the n th component can be calculated by taking the eigenvalue corresponding with the n th eigenvector (element n, n of \mathbf{E}) and dividing it by the sum of all the eigenvalues (the trace of \mathbf{E}):

$$\%E_n = \frac{E_{n,n}}{\text{trace}(\mathbf{E})} \quad (3.20).$$

The total energy contained in the M components (eigenvectors) corresponding with the M smallest eigenvalues is

$$\%E = \sum_{n=L}^{L-M+1} \frac{E_{n,n}}{\text{trace}(\mathbf{E})} \quad (3.21).$$

The sum spans from L to $L - M + 1$ as the eigenvalues on the diagonal of \mathbf{E} appear in descending order. If $\%E$ is smaller than 1.5%, the M eigenvectors corresponding with the M eigenvalues can be considered to be the minor components of \mathbf{X} [16]. The minor components are placed in the columns of matrix $\mathbf{C} \in \mathbb{R}^{L \times M}$.

3.2.4 PREDICTION

Having found the minor components $\mathbf{C} \in R_{L \times M}$ of $\mathbf{X} \in R_{P \times L}$, equation (3.1) holds. Therefore, for any row $(\mathbf{x}_n - \bar{\mathbf{x}}) \in R_{1 \times L}$ of \mathbf{X} the following approximate equality holds:

$$(\mathbf{x}_n - \bar{\mathbf{x}})\mathbf{C} \approx \mathbf{0} \quad (3.22).$$

The matrix \mathbf{C} can be divided into two submatrices such that $\mathbf{C} = [\mathbf{C}_1 \quad \mathbf{C}_2]^T$ where $\mathbf{C}_1 \in R_{d \times M}$ and $\mathbf{C}_2 \in R_{L-d \times M}$ with d chosen to be larger than $\frac{2}{3}L$ [16]. Similarly, the vector \mathbf{x}_n can be divided into two subvectors such that $\mathbf{x}_n = \{\mathbf{x}_{n1} \quad \mathbf{x}_{n2}\}$ where $\mathbf{x}_{n1} \in R_{1 \times d}$ and $\mathbf{x}_{n2} \in R_{1 \times L-d}$. Additionally, the vector $\bar{\mathbf{x}}$ can be divided into two subvectors such that $\bar{\mathbf{x}} = \{\bar{\mathbf{x}}_1 \quad \bar{\mathbf{x}}_2\}$ where $\bar{\mathbf{x}}_1 \in R_{1 \times d}$ and $\bar{\mathbf{x}}_2 \in R_{1 \times L-d}$. Therefore equation (3.22) can be rewritten as follows:

$$(\mathbf{x}_{n1} - \bar{\mathbf{x}}_1)\mathbf{C}_1 + (\mathbf{x}_{n2} - \bar{\mathbf{x}}_2)\mathbf{C}_2 \approx \mathbf{0} \quad (3.23).$$

After rearranging, the following equation for \mathbf{x}_{n2} is found:

$$\mathbf{x}_{n2} \approx -(\mathbf{C}_2\mathbf{C}_2^T)^{-1}\mathbf{C}_2\mathbf{C}_1^T(\mathbf{x}_{n1} - \bar{\mathbf{x}}_1)^T + \bar{\mathbf{x}}_2 \quad (3.24).$$

With \mathbf{C}_1 , \mathbf{C}_2 , $\bar{\mathbf{x}}_1$ and $\bar{\mathbf{x}}_2$ known and recent motion data placed into vector \mathbf{x}_{n1} , vector \mathbf{x}_{n2} attempts to predict future motion data, d steps into the future.

Due to the stochastic nature of sea surface waves the model identified by the prediction algorithm can change regularly [28]. The prediction rate should be chosen high enough to account for these changes before they lead to significant errors.

3.3 IMPLEMENTATION

For the real-time, ground station-based execution of ship motion prediction algorithms a Qt-based C++ application was written. The functions used in the application are all platform independent to allow the application to be deployed on any platform supported by Qt [49]. Testing was performed with the application compiled for Windows. The main program functions perform ship motion data sampling, prediction and performance analysis. The sampling and prediction functions are executed in independent threads in order to allow those processes to run independently.

TCP and data file interfaces were implemented for the ship motion data sampling function. The TCP client interface allows the application to be interfaced with a ship's onboard computer or a motion simulation platform's onboard computer. The data file interface allows the application to be tested on various pre-recorded ship motion datasets.

The MCA prediction algorithm was implemented in the C programming language and wrapped appropriately in the C++ prediction function of the above mentioned Qt application. C was chosen due to its speed and portability – it can be compiled to run on a variety of platforms including PIC microprocessors and Windows computers. A numerical library was used to simplify matrix operations and for the calculation of SVDs. Of the numerous numerical libraries available, OpenCV was chosen because of its popularity, also amongst undergraduate students, in the hope of decreasing the steepness of the learning curve for students who will work on this project in future. Testing was performed with OpenCV 2.2 which uses the LAPACK library to calculate SVDs [50]. Due to a change in the implementation of OpenCV, subsequent OpenCV versions have inferior SVD performance [51].

Real-time prediction algorithm performance analysis was implemented by implementing the performance indicator calculations described in Section 3.4 in C++, placing them in the performance analysis function and writing appropriate functions to display them and compare them with set bounds. Prediction algorithm output parameters were also made available for monitoring. If the bounds for the parameters or indicators are set and exceeded, the prediction is deemed to be invalid. For real-time visual performance analysis, prediction output plots were implemented using the QWT extension [52] for Qt. Figure 3.1 is a screenshot of the application taken during a simulation showing the real-time plots.

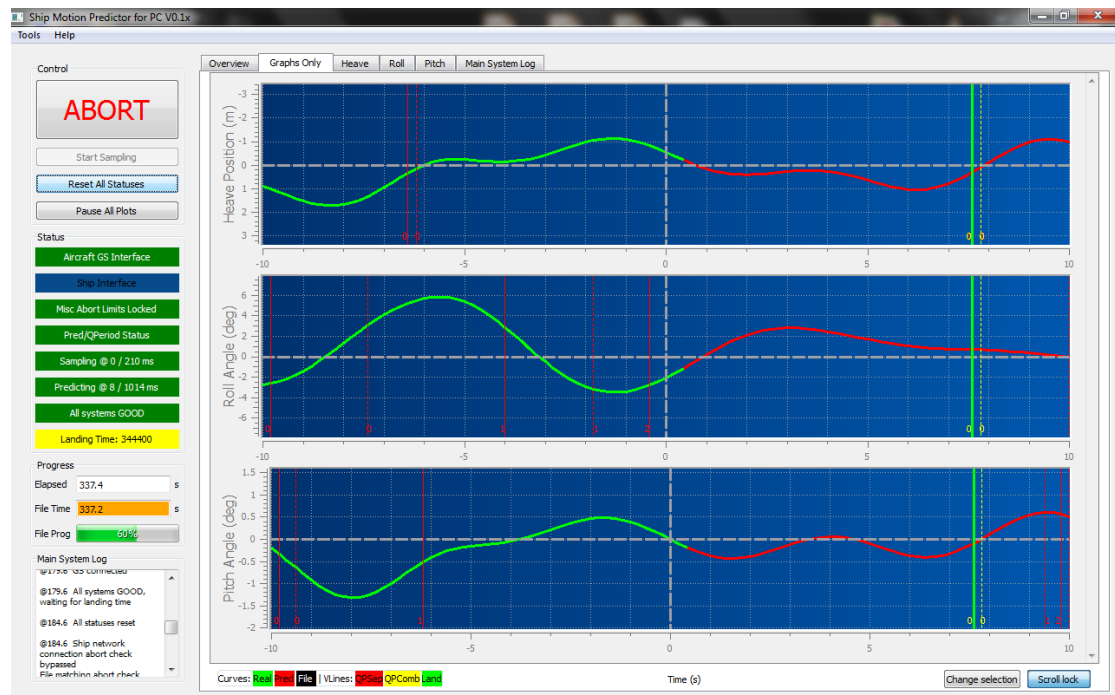


Figure 3.1 - SMPLCA application during simulation

3.4 TESTING

The MCA prediction algorithm was tested on real ship motion data recorded on a 3500 ton, 121 metre long [53] Valour class frigate at sea state 4. The heave position and rate at the flight deck was determined by the transformations given in equations (A.6) and (A.7) respectively.

In the datasets available to the ESL the highest frequency of significant ship motion is 0.22 Hz [7]. The sampling rate should therefore be at least 0.44 Hz. Accordingly, a sampling rate of 1 Hz was chosen which provides a prediction resolution of 1 s. The vector length, L from equation (3.2), of 200 samples (or 200 s with the 1 Hz sampling rate) was chosen. Good performance was observed with the number of vectors, P from equation (3.3), chosen as 50 samples (or 50 s with the 1 Hz sampling rate). A prediction rate of 1 Hz was chosen to obtain the best possible prediction accuracy.

The performance of 1 s, 5 s and 10 s predictors using both uniformly and exponentially weighted autocovariance matrices was tested. Prediction performance was judged based on a number of performance indicators. An indication of how closely the phases of the predictions matched the true phase was required. The correlation between two datasets is a measure of how strongly linearly related the datasets are. As a result, it gives an indication of how closely the phases of the datasets match. The correlation between true and predicted data can be obtained from the correlation coefficient,

$$CC = \frac{\sum_{i=1}^n (y_i - \bar{y})(\hat{y}_i - \bar{\hat{y}})}{(n-1)\sigma_y\sigma_{\hat{y}}} \quad (3.25),$$

where n is the sample size, y_i is a true ship motion state, \hat{y}_i is a predicted ship motion state, $\bar{*}$ are sample means and σ_* are sample standard deviations. An indication of the magnitude of the prediction errors was desired. The RMS error of the predictions,

$$RMSE = \sqrt{\frac{1}{n} \sum_{i=1}^n e_i^2} \quad (3.26),$$

gives such an indication, where the prediction error e_i is the difference between y_i and \hat{y}_i . An indication of the range of prediction errors can be obtained from the 95% error prediction interval:

$$EPI = \bar{e} \pm 1.96\sigma_e \quad (3.27).$$

As prediction errors depend on the amplitude of true motions [28] the significance of the magnitude error indicators can be appreciated better with an idea of the ratio between the true motion and the error. The signal-to-noise ratio, where the true motion is considered to be the signal and prediction error is considered to be the noise, provides such a ratio:

$$SNR = \frac{\sigma_y^2}{\sigma_e^2} \quad (3.28).$$

In equations (3.25) to (3.28) the sample means are

$$\bar{*} = \frac{1}{n} \sum_{i=1}^n *_{i} \quad (3.29)$$

and sample standard deviations are

$$\sigma_* = \sqrt{\frac{1}{n-1} \sum_{i=1}^n (*_{i} - \bar{*})^2} \quad (3.30).$$

3.4.1 ROLL ANGLE

A comparison between the true roll motion and the 5 s and 10 s roll motion predictions is provided in Figure 3.2. The predictors used exponentially weighted autocovariance matrices with an exponential decay factor (α) of 0.1. As the 1 s predictions were almost exactly the same as the true motion, they are not shown in order to improve the clarity with which the other predictions are shown.

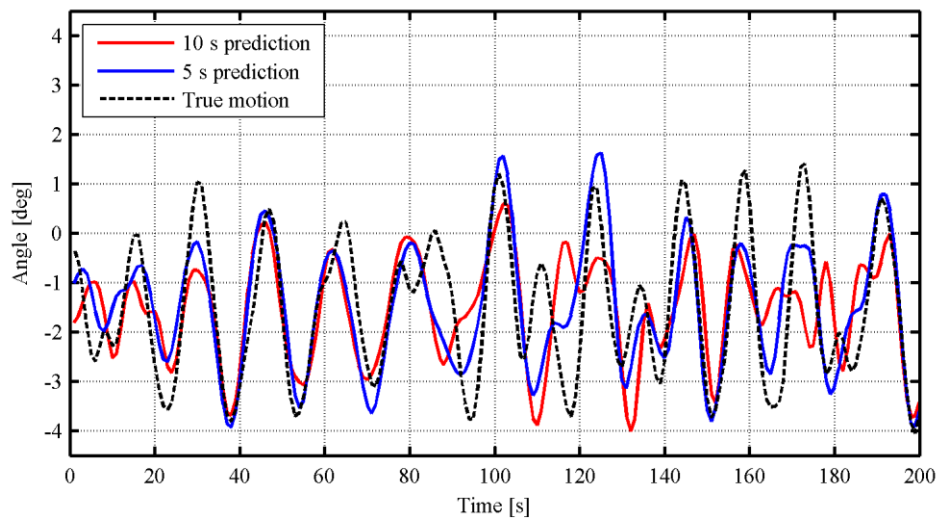


Figure 3.2 - Roll angle predictions with $\alpha=0.1$

By visual inspection it is apparent that, while the 5 s predictor made a number of magnitude errors, the predictions were approximately in phase with the true motion for most of the test duration. The 10 s predictor offered poor magnitude and phase predictions. The large deviations, for example at approximately 120 s and 170 s, were likely due to stochastic sea surface waves which caused deviations from the current prediction model.

The predictors were also tested when using uniformly weighted autocovariance matrices. The prediction performance of the various predictor configurations is detailed in Table 3.1.

α	1 s prediction				5 s prediction				10 s prediction			
	<i>CC</i>	<i>RMSE</i> (deg)	<i>EPI</i> (deg)	<i>SNR</i>	<i>CC</i>	<i>RMSE</i> (deg)	<i>EPI</i> (deg)	<i>SNR</i>	<i>CC</i>	<i>RMSE</i> (deg)	<i>EPI</i> (deg)	<i>SNR</i>
0.0	0.94	0.50	0±0.98	8.01	0.77	0.92	0±1.81	2.35	0.48	1.31	0±2.57	1.16
0.1	0.97	0.32	0±0.64	19.00	0.79	0.88	0±1.73	2.56	0.53	1.24	0±2.43	1.31

Table 3.1 - Roll angle prediction performance

The predictors which used exponentially weighted autocovariance matrices performed better than those which used uniformly weighted autocovariance matrices. The performance of the 1 s predictor improved the most: its *SNR* increased by more than a factor of two.

The 1 s predictions were very strongly correlated with the true motion and 95% of the prediction errors fell within a $0\pm 0.64^\circ$ interval. This interval is small when compared with the true motion amplitude, as confirmed by the *SNR* of 19.00. This suggests that the 1 s roll angle predictor provides good phase and magnitude predictions.

The 5 s predictor output predictions were well correlated with the true motion, but to a lesser extent than the 1 s predictor. The 95% error prediction interval of 0 ± 1.73 m was still smaller than the true motion amplitude as verified by the *SNR* of 2.56. As a result the predictions output by the 5 s roll angle predictor are considered reasonable. This agrees with the conclusions made above from visual inspection.

The output of the 10 s predictor was less correlated with the true motion than the outputs of the 1 s and 5 s predictors and the 95% error prediction interval was approximately equal to the true motion amplitude as confirmed by the *SNR* of 1.31. When the prediction error is greater than the true motion signal the predictions are of little value. This scenario presents itself when the *SNR* is smaller than 1. As the *SNR* of the output of the predictor was close to this

value, the output of the 10 s roll angle predictor is deemed to be of little value. This is in agreement with the visual inspection of Figure 3.2.

It is interesting to note that the 95% error prediction interval increased approximately logarithmically with an increase in prediction time.

3.4.2 PITCH ANGLE

Similarly to the roll angle predictions shown in Figure 3.2, Figure 3.3 shows the output of 5 and 10 s predictors when predicting pitch angle. The predictors used exponentially weighted autocovariance matrices with an exponential decay factor (α) of 0.1. The output of the 1 s predictor is once again not shown as it is very similar to the true motion and to improve the clarity with which the other predictions are shown.

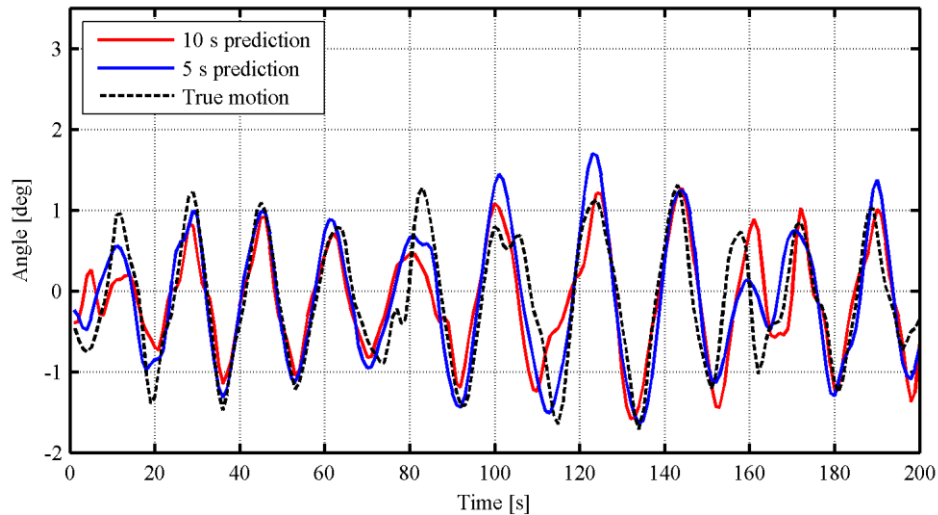


Figure 3.3 - Pitch angle predictions with $\alpha=0.1$

By visual inspection it appears that both 5 s and 10 s predictors produced predictions which are relatively accurate in both magnitude and phase. The larger errors observed were likely due to prediction model deviations caused by stochastic sea surface waves.

The predictors were also tested when using uniformly weighted autocovariance matrices. The prediction performance details of the various predictor configurations which were tested are provided in Table 3.2.

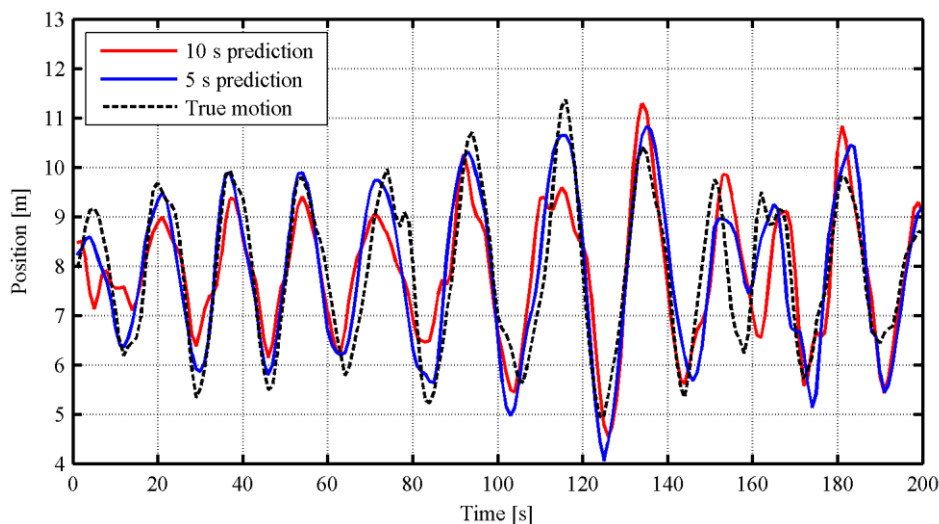
α	1 s prediction				5 s prediction				10 s prediction			
	<i>CC</i>	<i>RMSE</i> (deg)	<i>EPI</i> (deg)	<i>SNR</i>	<i>CC</i>	<i>RMSE</i> (deg)	<i>EPI</i> (deg)	<i>SNR</i>	<i>CC</i>	<i>RMSE</i> (deg)	<i>EPI</i> (deg)	<i>SNR</i>
0.0	0.95	0.25	0±0.49	9.19	0.88	0.38	0±0.75	3.95	0.71	0.56	0±1.11	1.82
0.1	0.98	0.17	0±0.34	19.79	0.88	0.39	0±0.77	3.75	0.77	0.50	0±0.97	2.34

Table 3.2 - Pitch angle prediction performance

The observations made from the performance details of the various pitch angle predictors are similar to those which were made from the performance details of the roll angle predictors. The main difference is that the predictions output by the 10 s predictor using exponentially weighted autocovariance matrices were well correlated with the true motion and had an *SNR* of greater than two suggesting that the output of the 10 s pitch angle predictor is useful. This corresponds with the visual inspection of Figure 3.3.

3.4.3 HEAVE POSITION

As for the above cases, the heave position outputs of the 5 s and 10 s predictors when using exponentially weighted autocovariance matrices with an exponential decay factor of 0.1 are provided in Figure 3.4. The output of the 1 s predictor is not shown for the same reason as the above cases.

Figure 3.4 - Heave position predictions with $\alpha=0.1$

From a visual inspection it appears that the 5 s predictor produced predictions with good magnitude and phase accuracy. The 10 s predictor also produced predictions with good phase accuracy, but with poorer magnitude accuracy than the 5 s predictor. The larger errors

observed (for example at approximately 160 s) were likely due to deviations from the prediction model caused by stochastic sea surface waves.

Similarly to the above sections, prediction performance indicators with various prediction configurations are provided in Table 3.3.

α	1 s prediction				5 s prediction				10 s prediction			
	CC	RMSE (m)	EPI (m)	SNR	CC	RMSE (m)	EPI (m)	SNR	CC	RMSE (m)	EPI (m)	SNR
0.0	0.96	0.42	0±0.83	12.88	0.89	0.73	0±1.44	4.27	0.73	1.08	0±2.12	1.96
0.1	0.98	0.31	0±0.62	23.13	0.89	0.73	0±1.44	4.24	0.79	0.95	0±1.86	2.56

Table 3.3 – Heave position prediction performance

The observations made from the prediction performance indicators are similar to those for the roll and pitch angle predictors. As the outputs of the predictors using exponentially weighted autocovariance matrices were all well correlated with the true motion and all had SNRs greater than 2, the outputs of the predictors are all deemed to be useful. This corresponds with the visual inspection of Figure 3.4.

3.4.4 HEAVE RATE

As with to the predictions considered above, the outputs of the 5 s and 10 s heave rate predictors using exponentially weighted autocovariance matrices are compared with the true heave rate in Figure 3.5. The output of the highly accurate 1 s predictor is not shown.

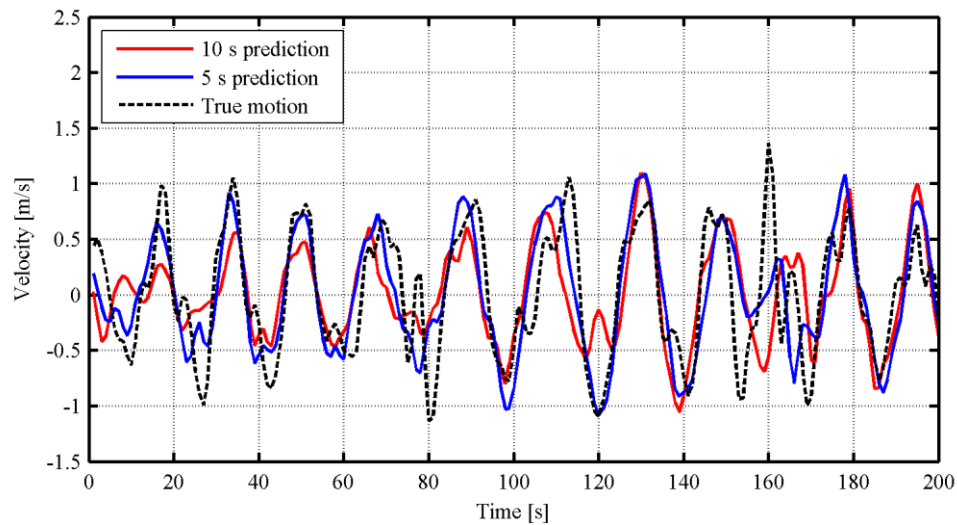


Figure 3.5 - Heave rate predictions with $\alpha=0.1$

From a visual inspection the 5 s predictor appears to have produced predictions with good magnitude and phase accuracy. While the 10 s predictor followed the general trend of the true motion, it made frequent, large magnitude errors. The occasional large prediction errors were likely due to stochastic sea surface waves which caused prediction model deviations.

The performance indicators of various heave rate predictor configurations are provided in Table 3.4.

α	1 s prediction				5 s prediction				10 s prediction			
	<i>CC</i>	<i>RMSE</i> (m/s)	<i>EPI</i> (m/s)	<i>SNR</i>	<i>CC</i>	<i>RMSE</i> (m/s)	<i>EPI</i> (m/s)	<i>SNR</i>	<i>CC</i>	<i>RMSE</i> (m/s)	<i>EPI</i> (m/s)	<i>SNR</i>
0.0	0.88	0.27	0±0.53	4.30	0.73	0.40	0±0.79	1.97	0.50	0.52	0±1.03	1.16
0.1	0.94	0.19	0±0.37	9.01	0.75	0.39	0±0.76	2.13	0.57	0.48	0±0.94	1.39

Table 3.4 – Heave rate prediction performance

The observations made from the heave rate prediction performance indicators are similar to the observations made from the prediction performance indicators provided above for the other axes of motion. As the output of the 10 s predictor was relatively poorly correlated with the true motion and had an *SNR* of smaller than 2, it is deemed to be of little value. This corresponds with the visual inspection of Figure 3.5.

3.5 SUMMARY

The theory of an MCA-based prediction algorithm was detailed. The algorithm was implemented in C in a larger C++ application on the given laptop computer. Testing showed that real-time execution of the algorithm was possible on the given laptop. Useful roll angle predictions of up to 5 s, pitch angle predictions of up to 10 s, heave position predictions of up to 10 s and heave rate predictions of up to 5 s are possible with the prediction algorithm.

4. LANDING CRITERIA ANALYSIS

4.1 INTRODUCTION

Landing criteria analysis has to be performed to identify safe landing opportunities. It must meet the following requirements:

- Identify as many valid safe landing opportunities as possible.
- Lead to a minimum number of aborted landing attempts.

Landing criteria for a generic platform-helicopter combination and methods to define landing criteria bounds were chosen in Section 2.6. As the platform-helicopter combination given for this project is new, SHOLs should be used to define landing criteria bounds. Therefore, SHOLs and relevant landing criteria bounds not covered by SHOLs are required. Additionally, appropriate methods of landing criteria analysis and safe landing opportunity identification are required. The theory, implementation and testing of these components are detailed in this chapter.

4.2 ENVIRONMENTAL CRITERIA ANALYSIS

The sea state must be within limits at landing time. As the ship motion prediction algorithm was tested on ship motion data recorded at sea state 4 (as presented in Section 3.4), its performance is only known for sea state 4 and lower. As a result, the ship motion data simulated by the platform must be limited to data recorded at sea state 4 or lower.

The wind conditions during landing operations must be within acceptable bounds. The maximum constant wind speed allowed during flight tests of previous projects with the given helicopter was 3 m/s. The same wind speed limit is used for this project. The wind speed limit is enforced manually by monitoring the wind speed before and during flight tests. No restrictions are placed on the wind direction as the helicopter points into the wind when using the chosen RW approach as described in Section 2.2.2.

4.3 PLATFORM MOTION CRITERIA ANALYSIS

4.3.1 THEORY

The simulated ship's heading and speed must be constant from the start of the approach until touchdown. Accordingly, the ship motion data simulated by the platform must be limited to data which was recorded when the ship had a constant heading and speed.

Minimum absolute platform heave acceleration and upward heave motion is desired at landing time. Such a motion state exists when the inertial down platform velocity reaches a trough. Velocity troughs can also be identified by local minima of negative gradients of inertial down platform position. Ship motion prediction algorithms can be used to predict the motion of the platform when simulating ship motion. Such predictions can be compared to platform motion criteria to determine possible landing opportunities.

Platform roll and pitch angles must be within bounds at landing time. As numerous stationary platform landings with the helicopter have been performed at a roll angle of 6° , a conservative initial roll angle limit of 3° is defined for the platform at landing time. As noted in Section 2.3.2.1, the ratio between roll and pitch limits is typically 5:1. As a result, an initial pitch angle limit of 0.6° is defined for the platform at landing time. When these limits are applied to ship motion predictions, they should be increased by the upper bound of the 95% error prediction interval applicable to each prediction as given in equation (3.27) to ensure that 95% of potential landing opportunities are identified. Ideally the 95% error prediction interval of the current predictions should be added to the platform motion criteria limits but, as the true motion is not available at the time when the current predictions are made, the 95% error prediction interval of the current predictions cannot be calculated. The 95% error prediction interval of recent past predictions where the true motion is already known can be used instead. To avoid falsely positively identified landing opportunities from resulting in actual landings, 1 s from landing the limits should once again be applied more conservatively without the 95% error prediction interval.

When a desired predicted heave motion aligns with predicted pitch and roll motions which are within bounds, a potential landing opportunity is identified. A potential landing opportunity, which is first identified in the predictions with the largest available prediction horizon, is tracked at each prediction update. As the time to the tracked potential landing opportunity is reduced at each prediction update, the required prediction horizon is reduced and therefore prediction accuracy is improved. The improved predictions are used to fine-tune the time of the potential landing opportunity by up to 1 s (or one prediction update period, whichever is shorter). If the landing criteria are not met within 1 s (or one prediction update period) of the tracked landing opportunity, the landing opportunity is invalidated. The tracked landing opportunity is fine-tuned from the largest available prediction horizon until 1 s from the tracked landing opportunity. In order to avoid any sudden changes in the descent in the last second before landing, the helicopter's high-level controllers commit to landing at the tracked landing opportunity if the 1 s predictions meet the landing criteria as discussed in Section 7.3.3.2. This is further justified by the fact that the 1 s predictions are highly accurate as seen in Section 3.4. When a landing opportunity expires or when a landing opportunity is

prematurely invalidated the system waits for a period of time equivalent to the largest available prediction horizon before searching for new landing opportunities.

4.3.2 IMPLEMENTATION

As platform landing criteria depend on platform motion predictions the preferred application for the execution of platform landing criteria analysis is the same application used for platform motion prediction as described in Section 3.3 where data can be shared freely between parts of the application. Additionally, as platform landing criteria analysis may be implemented on a microprocessor in future, a C implementation is preferred. Thus, platform landing criteria analysis as described above was implemented in C and wrapped in an appropriate C++ function in the platform motion prediction application. The application was therefore named the SMPLCA or Ship Motion Prediction Landing Criteria Analysis application. Periods of platform motion which meet the landing criteria and landing opportunities are displayed on the real-time plots produced by the application.

4.3.3 TESTING

The performance of the proposed methods of platform landing criteria analysis was tested. Tests were performed on the real ship motion predictions presented in Section 3.4. As the heave position predictions are better than the heave rate predictions, heave motion criteria were applied to heave position predictions. As useful predictions of all axes are possible for a prediction horizon of up to 5 s, testing focussed on 5 s predictions, but tests were also performed on 10 s predictions for comparison. Dynamic criteria bounds and static criteria bounds were also compared where dynamic criteria bounds were adjusted by the 95% error prediction interval and static criteria bounds remained constant.

As the requirements of the landing criteria analysis are dependent on the number of valid safe landing opportunities identified and the number of aborted landing attempts, a success rate performance indicator was used to compare the performance of the various landing criteria analysis configurations. The success rate (SR) is the number of valid safe landing opportunities identified (V) over the total number of landing attempts, where the total number of landing attempts is also equal to the sum of the number of valid safe landing opportunities identified and the number of aborted landing attempts (A):

$$SR = \frac{V}{V + A} \quad (4.1)$$

Testing was started with static criteria bounds, not adjusted by the 95% error prediction interval. The results of the test are well illustrated on the 5 s and 1 s roll angle prediction plots of Figure 4.1 and Figure 4.2 respectively.

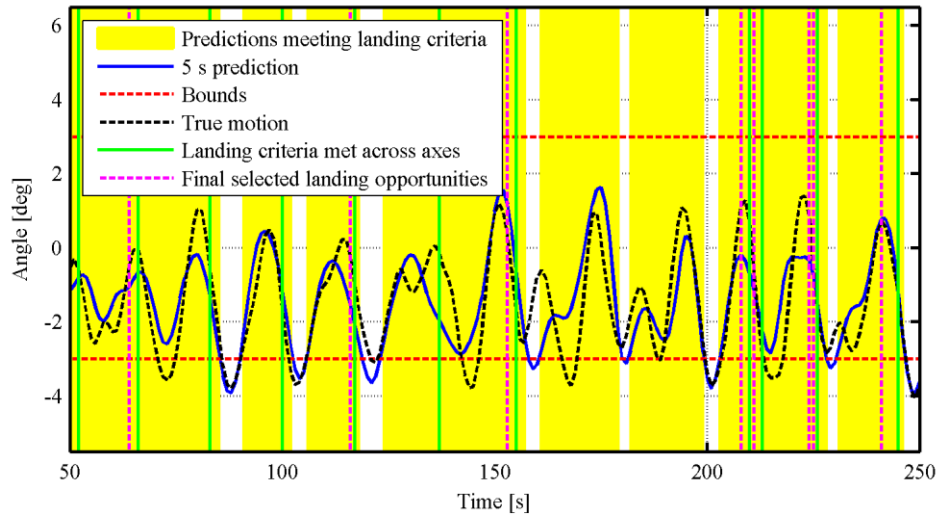


Figure 4.1 – Results of landing criteria analysis with static bounds on 5 s roll angle predictions

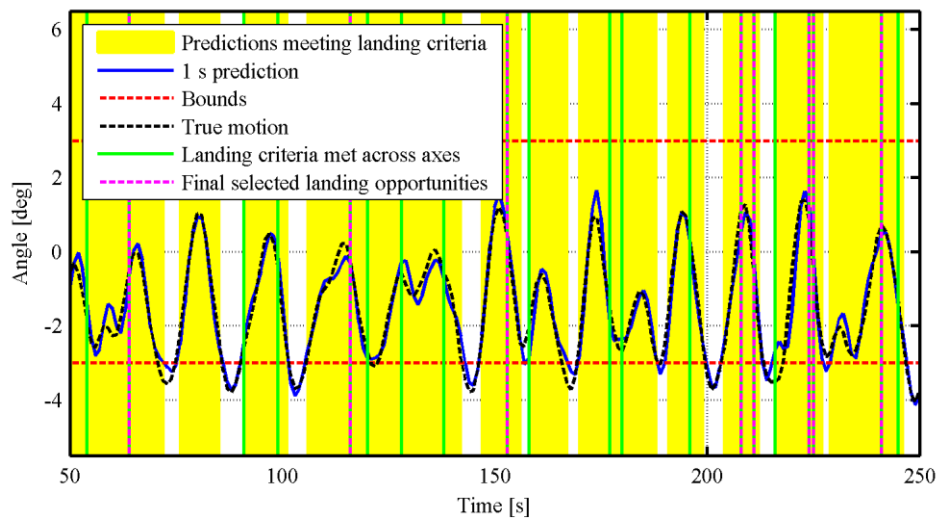


Figure 4.2 – Results of landing criteria analysis with static bounds on 1 s roll angle predictions

The yellow bands represent predictions which meet the landing criteria of the current axis. While some of the yellow bands between the 5 s and 1 s prediction plots correspond well and narrow as expected, anomalies are noted where yellow bands of the 1 s predictions are wider than and offset from those of the 5 s predictions. This suggests that potential landing opportunities may have been missed.

The green lines indicate when landing criteria were met across all axes at a certain time instant and the dotted pink lines indicate which landing opportunities remained valid from the

5 s predictions to the 1 s predictions. Due to the high accuracy of the 1 s predictions the green lines and pink lines in Figure 4.2 provide a good indication of all the landing opportunities which were actually available, 20 in total. Of this total number, the eight represented by the pink lines were correctly identified 5 s from landing and remained valid until 1 s from landing. The number of missed landing opportunities was therefore 12. The green lines which do not have a pink line nearby in Figure 4.1 indicate falsely identified or prematurely invalidated landing opportunities of which there were 4 in total. This gives an *SR* of 67%.

Testing continued with dynamic bounds obtained by adding the 95% error prediction interval to the static bounds. The results of the test are illustrated well in Figure 4.3 and Figure 4.4.

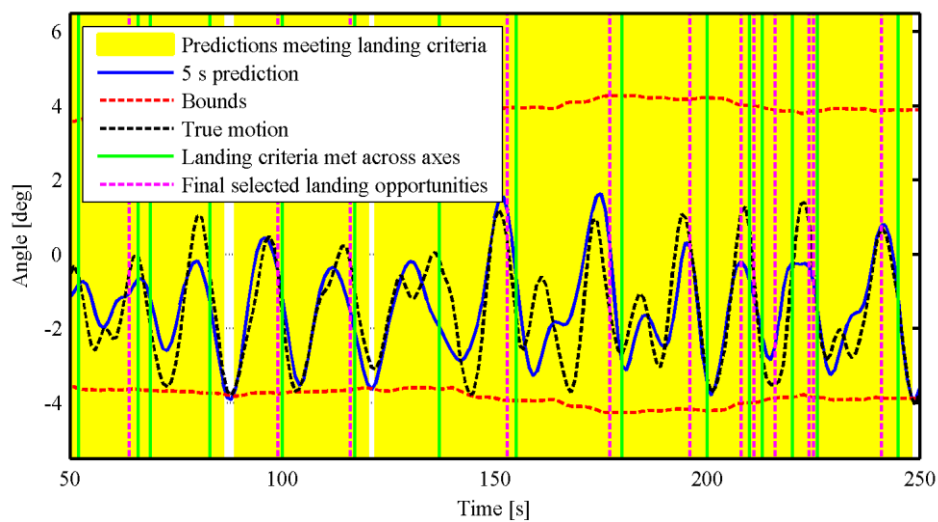


Figure 4.3 - Results of landing criteria analysis with dynamic bounds on 5 s roll angle predictions

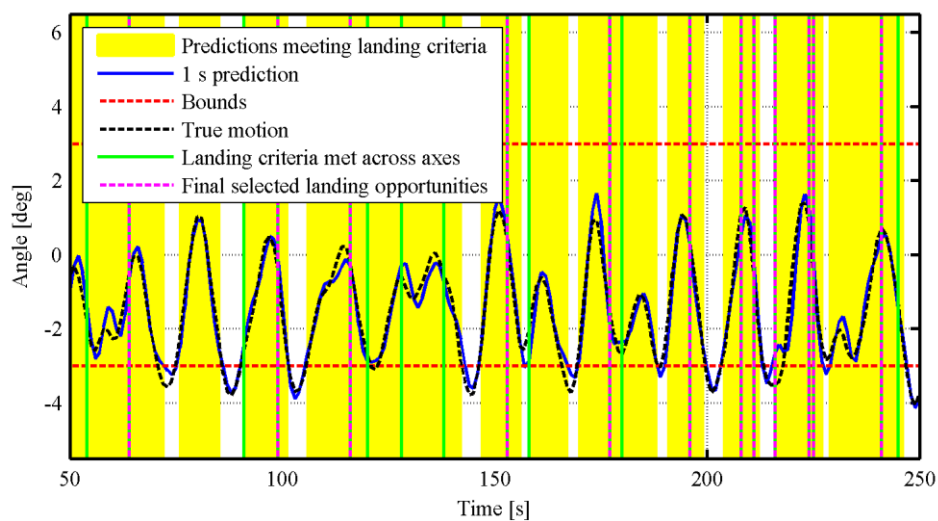


Figure 4.4 - Results of landing criteria analysis with dynamic bounds on 1 s roll angle predictions

The yellow bands which indicate predictions which meet the landing criteria of the current axis are much wider for the 5 s predictions than for the 1 s predictions. This suggests that false positives may be identified in the 5 s predictions, but it also suggests that actual landing opportunities are unlikely to be missed. As expected, all yellow bands narrow from the 5 s to the 1 s predictions.

As the same dataset is used as for the case with static bounds, the number of landing opportunities which were actually available is also 20. As seen from the pink lines in Figure 4.4 the number of landing opportunities which were successfully tracked from the 5 s predictions to the 1 s predictions is 12. The number of aborted attempts, which can be identified by the green lines without a nearby pink line in the 5 s predictions of Figure 4.3, is 4. As a result the success rate (*SR*) is 75%.

While the number of aborts remained the same whether dynamic or static bounds were used, more valid safe landing opportunities were tracked and therefore a higher *SR* was obtained with dynamic bounds.

The results of landing criteria analysis with dynamic bounds on the other axes are also shown below.

Figure 4.5 and Figure 4.6 show the results of landing criteria analysis with dynamic bounds on pitch angle predictions. As was the case for the roll angle analysis, the yellow bands narrow nominally from the 5 s predictions to the 1 s predictions.

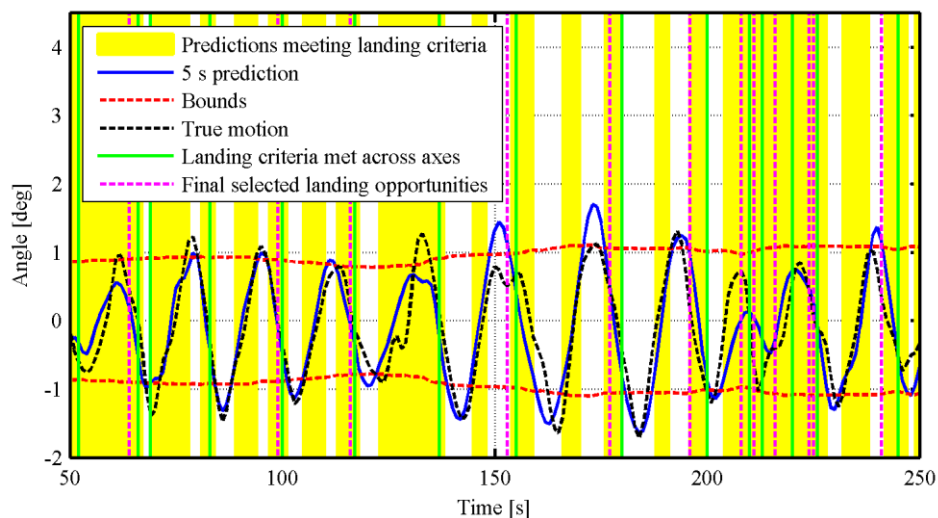


Figure 4.5 - Results of landing criteria analysis with dynamic bounds on 5 s pitch angle predictions

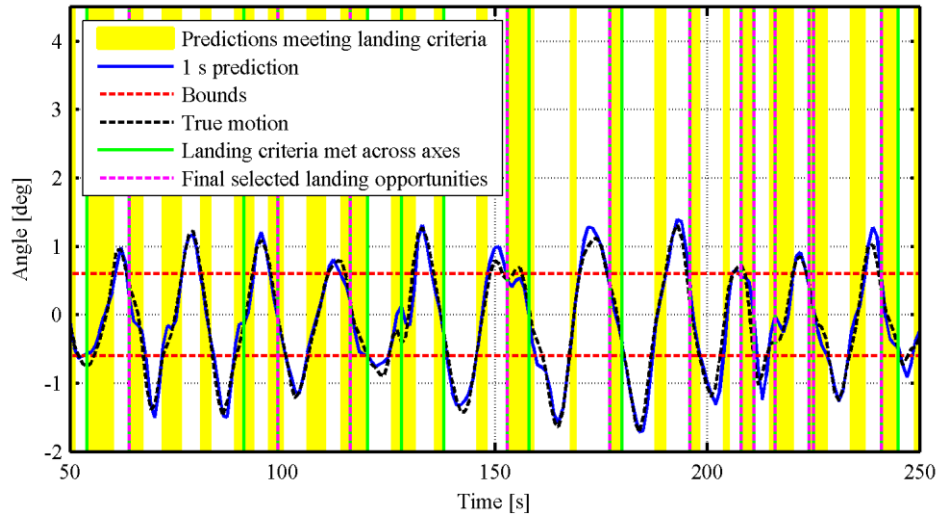


Figure 4.6 - Results of landing criteria analysis with dynamic bounds on 1 s pitch angle predictions

Figure 4.7 and Figure 4.8 show the results of landing criteria analysis with dynamic bounds on heave position predictions. As local minima of negative gradients of inertial down platform position are desired at landing time no bounds are set. There is no difference between the landing criteria analysis of heave motion using static and dynamic bounds.

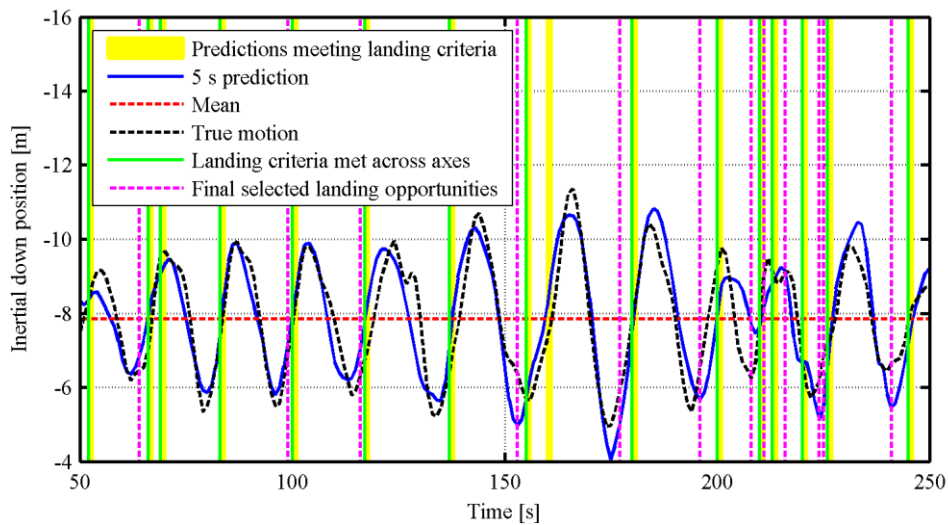


Figure 4.7 - Results of landing criteria analysis with dynamic bounds on 5 s heave position predictions

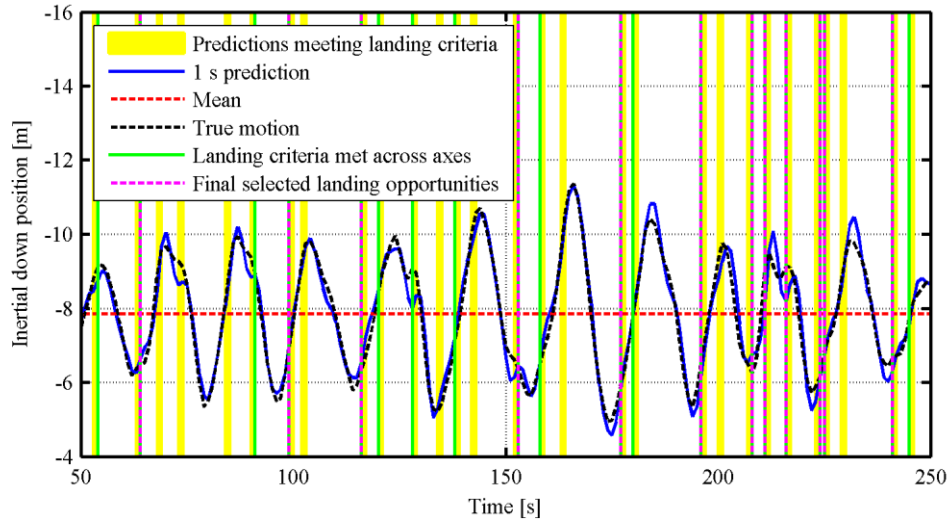


Figure 4.8 - Results of landing criteria analysis with dynamic bounds on 1 s heave position predictions

The performance of landing criteria analysis performed on 10 s predictions was also tested for static and dynamic criteria bounds. The results of the tests are summarised and compared with the performance of landing criteria analysis performed on 5 s predictions in Table 4.1.

	Landing opportunities identified (V)	Aborted landing attempts (A)	Success rate (SR)
5 s / dynamic	12	4	75%
5 s / static	8	4	67%
10 s / dynamic	8	14	36%
10 s / static	1	12	8%

Table 4.1 - Landing criteria analysis performance comparison

From Table 4.1 it is clear that landing criteria analysis with dynamic criteria bounds results in better landing criteria analysis performance. The success rate of landing criteria analysis on 10 s predictions is too low to be useful. This is as expected as 10 s roll angle predictions discussed in Section 3.4.1 were poor, likely leading to numerous false positives or missed landing opportunities. Landing criteria analysis with dynamic criteria bounds on 5 s predictions offers a high success rate of 75% and is therefore the preferred means of platform motion criteria analysis.

4.4 HELICOPTER MOTION CRITERIA ANALYSIS

A minimum relative velocity between the helicopter and the platform is desired at landing time. In previous projects with the helicopter, nominal stationary platform landings were all performed at a descent velocity of 0.5 m/s. An off-nominal stationary platform landing was performed during a previous project at at least 1.5 m/s without damaging the helicopter [6]. This suggests that safe landings can occur at relative velocities which are greater than the nominal 0.5 m/s chosen for previous projects. Accordingly, a relative velocity limit of 0.8 m/s was chosen. This limit is applied to the relative velocity references by the high-level controllers as described in Section 7.2.

The north and east position error between the helicopter and the platform must be within acceptable bounds at landing time to ensure that the landing occurs on the given landing platform. Acceptable bounds are based on the dimensions of the helicopter landing platform as provided in Section A.3.1.1 as 2.5 x 2.5 m. As a result, the minimum distance between the centre and the edge of the platform is 1.25 m. The offset between the helicopter's GPS antenna and the furthest point on the landing gear is 0.5 m. Accordingly, the maximum allowable distance between the helicopter and the centre of the platform as measured by the helicopter is 0.75 m. In order to allow some margin for error, the radius of the chosen acceptable circle of north and east position error between the helicopter was chosen as 0.6 m. This limit is enforced by the high-level controllers as described in Section 7.3.2.3.

Finally, helicopter roll and pitch angles should be a minimum at landing time. During level flight roll and pitch angles are small.

4.5 SUMMARY

Landing criteria were found for environmental factors, platform motion and helicopter motion. The sea state, ship speed and ship heading prerequisites must be met by choosing a ship motion dataset recorded during appropriate conditions. Methods of analysing the landing criteria and subsequently choosing landing points were also discussed. Platform landing criteria analysis with dynamic bounds applied to 5 s predictions produced very good performance and is therefore the preferred means of platform motion criteria analysis.

5. KINEMATIC ESTIMATOR

5.1 INTRODUCTION

The helicopter's kinematic estimator must meet the following requirements in order for the helicopter to execute the landing algorithm chosen in Section 2.6:

- Estimate the helicopter's heave motion states accurately, especially when tracking the heave motion of a platform which is simulating ship flight deck motion.
- Estimate the heave motion states of the part of the platform directly under the helicopter.
- Estimate the helicopter's position, velocity, attitude and rate states required for near-hover flight.

The original estimator of the helicopter system is assumed to be capable of estimating helicopter motion states well enough for near-hover flight. An overview of the original estimator, problems affecting its performance, solutions to those problems, the design of a new platform motion estimator and the implementation of all of these components are described in this chapter.

5.2 HELICOPTER POSITION AND VELOCITY ESTIMATION

In the original helicopter system, latitude and longitude data from the GPS are used to determine the helicopter's inertial north and east positions. The lateral and longitudinal velocity vector obtained from the GPS is transformed into lateral and longitudinal components in the helicopter's body reference frame to obtain lateral and longitudinal velocities. A complementary filter is used to combine GPS and accelerometer measurements for inertial down position and velocity estimation.

5.2.1 COMPLEMENTARY FILTER

A complementary filter extracts low frequency data from measurements with high frequency noise and high frequency data from measurements with low frequency noise and combines the data to obtain an estimate with higher accuracy (in phase and magnitude) than either independent measurement [54]. It does this by low-pass filtering measurements with high frequency noise, high-pass filtering measurements with low frequency noise and summing the filter outputs. The filters are designed with equal cut-off frequencies so that the complementary filter has a unity gain across the frequency spectrum as illustrated in the combined Bode magnitude plot in Figure 5.1.

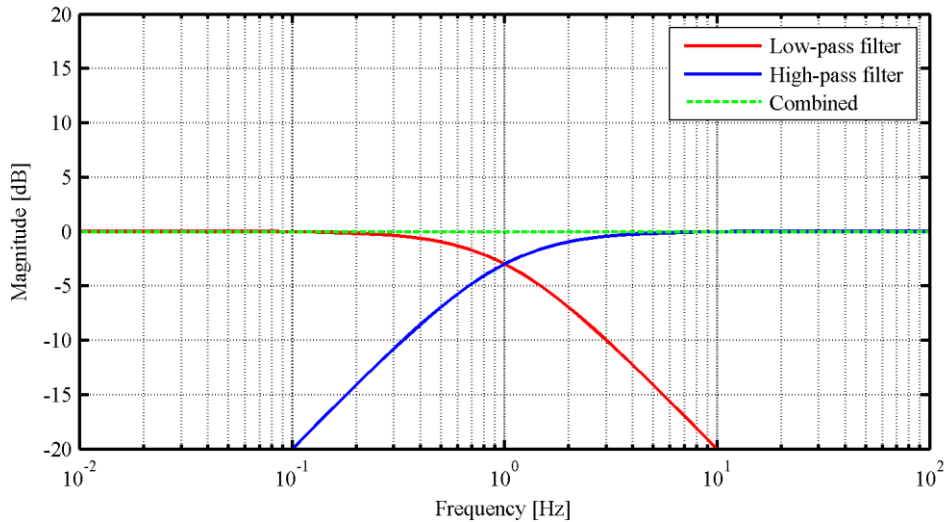


Figure 5.1 - Bode magnitude plot of low- and high-pass filter pair

In the complementary filter of the original estimator of the helicopter system, GPS measurements are combined with accelerometer measurements. The GPS measurements used are in the inertial frame. Accordingly, accelerometer measurements are transformed to the inertial frame before being used. The accelerometer measurements are passed through a high-pass filter with a cut-off frequency of 0.1 rad/s to remove any bias on the measurements. The filtered measurements are integrated to obtain the velocity. The velocity is passed through a high-pass filter with a cut-off frequency of 1 rad/s. The GPS's inertial down velocity measurements are passed through a low-pass filter with the same cut-off frequency as the high-pass filter. The final velocity estimate is the sum of the high-pass filtered velocity originating from integrated accelerometer measurements and the low-pass filtered GPS velocity measurements. A similar process is followed for position estimation except that high frequency measurements are obtained from high-pass filtered, integrated velocity estimates and low frequency measurements are obtained from low-pass filtered GPS position measurements. A block diagram of the complementary filter is shown in Figure 5.2.

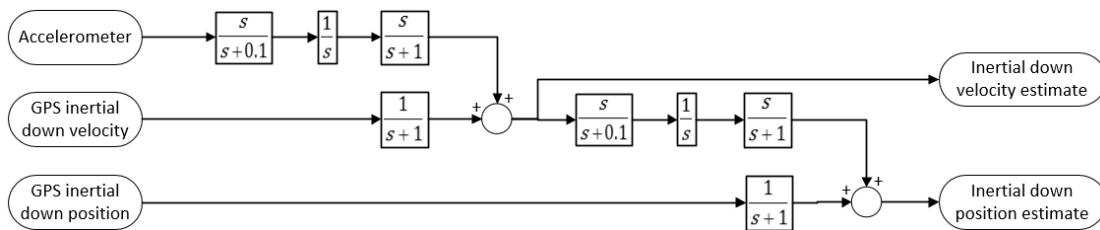


Figure 5.2 - Block diagram of complementary filter

The accuracy of the complementary filter outputs depend on the accuracy of the input measurements.

5.2.2 GPS MEASUREMENT ERRORS

A NovAtel OEMV GPS rover unit is used on the helicopter. The accuracy of the position and velocity estimates depend on a number of factors including the magnitude and phase errors introduced by the GPS.

The GPS rover unit uses differential corrections from a DGPS base station together with the real-time kinematic (RTK) technique to improve its position solution accuracy [55]. When using the RTK technique the velocity solution is determined by taking the difference between subsequent position solutions over the sample time. As a result the accuracy of the velocity solution improves as the accuracy of the position solution improves. The accuracy of the solutions is mostly dependant on the distance between the rover and base station, the accuracy of the known location of the base station and the quality of the base station's satellite observations [56]. When providing its most accurate solution type (Integer L1 ambiguity), the GPS rover unit provides measurements with a lateral and longitudinal standard deviation of ± 1 cm and an altitude standard deviation of ± 2 cm [55].

GPS measurements have an inherent latency associated with them as a result of processing delays [57]. Additional delays are added when measurement data is sent from the GPS unit to the computer where the measurements are used [58]. The GPS unit provides an estimate of the latency between position and velocity measurements. When the RTK velocity solution is requested from the unit at 10 Hz, this latency is 50 ms [55]. The data transmission delays which contribute to the absolute latency of GPS measurements can be calculated quite accurately when taking into account the amount of data which needs to be transferred and the speed of the data connection [58]. Processing delays are not that easy to determine. As a result, the absolute latency of GPS measurements is typically determined experimentally.

The transfer function of a time delay is

$$G(s) = e^{-s\tau} \quad (5.1),$$

where τ is the delay in seconds [47]. As a result, for measurements within the bandwidth of the GPS's internal filters, the following relationships exist between the real inertial down position (D) and the GPS's inertial down position (D_{GPS}) and velocity (\dot{D}_{GPS}) measurements,

$$D_{GPS} = D e^{-s(\tau a)} \quad (5.2),$$

$$\dot{D}_{GPS} = D s e^{-s(\tau a + \tau b)} \quad (5.3),$$

where τ_a is the absolute latency of GPS position measurements and τ_b is the relative latency between GPS position and velocity measurements. A block diagram of the complementary filter described in Section 5.2.1 including GPS latency is shown in Figure 5.3.

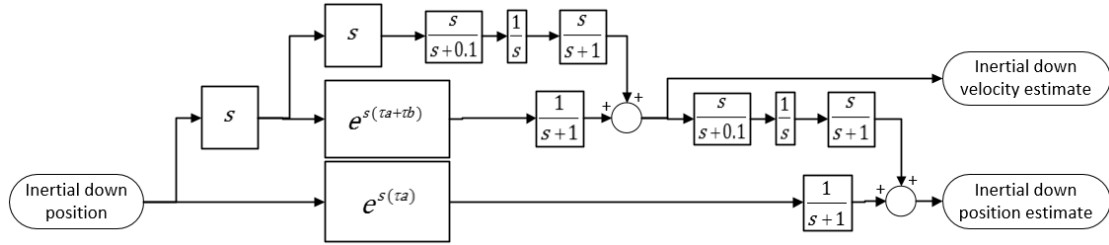


Figure 5.3 - Block diagram of complementary filter with GPS measurement latency

The transfer function from the inertial down position (D) to the inertial down position estimate (\hat{D}) is

$$\frac{\hat{D}}{D} = \frac{e^{-s(\tau_a)}}{s+1} + \left(\frac{e^{-s(\tau_a+\tau_b)}}{s+1} + \frac{s^3}{s(s+0.1)(s+1)} \right) \left(\frac{s^2}{(s+0.1)(s+1)} \right) \quad (5.4).$$

The time delay elements of the transfer function can be replaced by rational transfer functions such as second order Padé-approximations [47]:

$$e^{-s\tau} \approx \frac{1 - k_1s + k_2s^2}{1 + k_1s + k_2s^2} \quad (5.5),$$

$$k_1 = \frac{\tau}{2} \quad (5.6),$$

$$k_2 = \frac{\tau^2}{12} \quad (5.7).$$

After replacing the time delay elements with Padé-approximations, the transfer function from the inertial down position (D) to the inertial down position estimate (\hat{D}) becomes:

$$\begin{aligned} \frac{\hat{D}}{D} = & \frac{1 - \frac{(\tau_a)}{2}s + \frac{(\tau_a)^2}{12}s^2}{(s+1) \left(1 + \frac{(\tau_a)}{2}s + \frac{(\tau_a)^2}{12}s^2 \right)} \quad (5.8) \\ & + \left(\frac{1 - \frac{(\tau_a + \tau_b)}{2}s + \frac{(\tau_a + \tau_b)^2}{12}s^2}{(s+1) \left(1 + \frac{(\tau_a + \tau_b)}{2}s + \frac{(\tau_a + \tau_b)^2}{12}s^2 \right)} \right. \\ & \left. + \frac{s^3}{s(s+0.1)(s+1)} \right) \left(\frac{s^2}{(s+0.1)(s+1)} \right) \end{aligned}$$

Figure 5.4 is a Bode plot of this transfer function with an absolute latency of GPS position measurements (τ_a) of 200 ms and a relative latency between GPS position and velocity measurements (τ_b) of 50 ms.

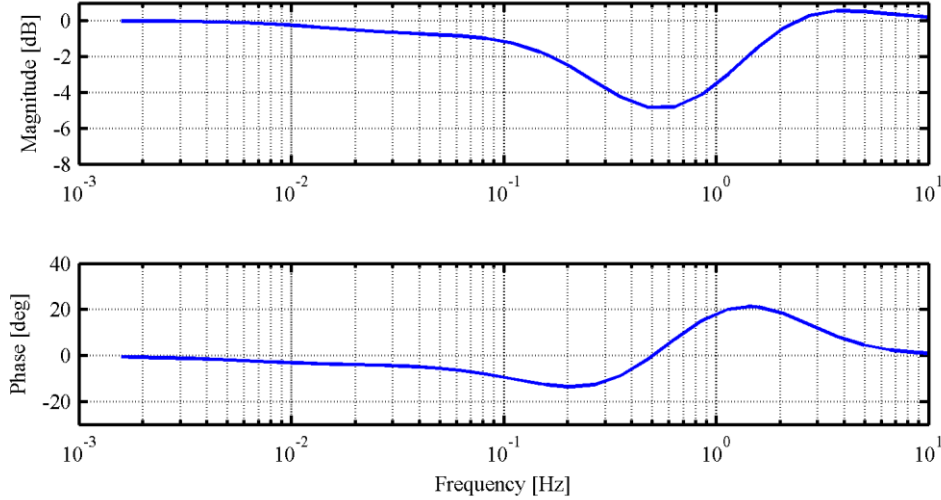


Figure 5.4 - Bode plot of complementary filter transfer function with GPS measurement latency

From the magnitude plot it is apparent that signals with frequencies of between approximately 0.2 Hz and 1 Hz are attenuated significantly (-3 dB gain or less) by the complementary filter when GPS measurement latency is present. The highest frequency of significant heave motion data is 0.22 Hz in the ship motion data sample sets available to the ESL [7]. Compensation for GPS measurement latency is therefore required.

5.2.3 GPS MEASUREMENT LATENCY COMPENSATION

The method of filter replay can compensate for GPS measurement latency [58, 59]. The method first synchronises all measurements. A history of accelerometer measurements and filter states is stored for the duration of the absolute GPS measurement delay. Once GPS measurements are received, the oldest accelerometer measurement and filter states are taken from the history and put into the complementary filter together with the GPS measurements. By delaying the measurements equally they become synchronised. This results in the following transfer function

$$\frac{\hat{D}}{D} = e^{-s(\tau_a + \tau_b)} \left(\frac{1}{s+1} + \left(\frac{1}{s+1} + \frac{s^3}{s(s+0.01)(s+1)} \right) \left(\frac{s^2}{(s+0.01)(s+1)} \right) \right) \quad (5.9),$$

where the total measurement delay ($\tau_a + \tau_b$) is 250 ms. It is important to note that the cut-off frequency of the 0.1 rad/s high pass filters was changed to 0.01 rad/s to reduce their effect on

the expected measurement band of 0 Hz to 0.22 Hz [7]. A Bode plot of the transfer function is given in Figure 5.5.

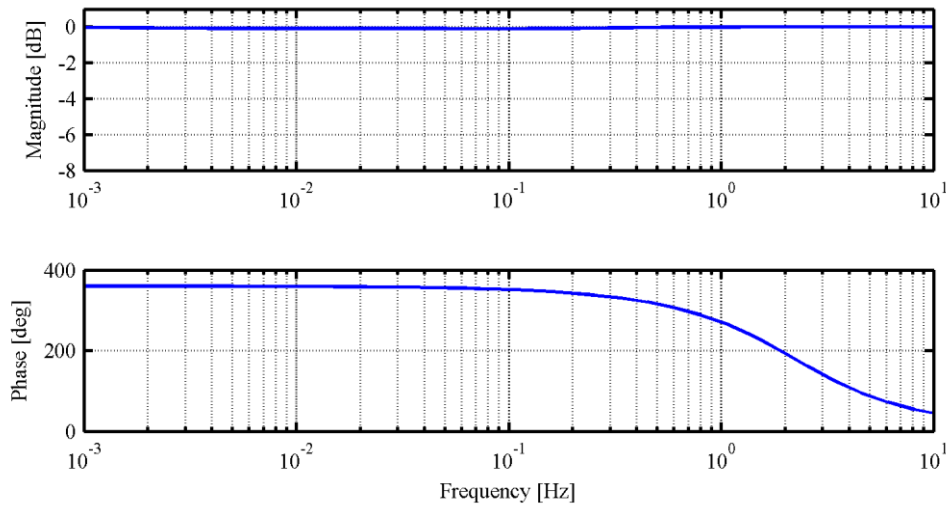


Figure 5.5 - Bode plot of complementary filter transfer function with GPS measurement latency compensation

From the magnitude plot it is apparent that measurement synchronisation addresses the problem of signal attenuation, but from the phase plot it is apparent that this is at the expense of a significant phase delay. The second step of filter replay addresses the phase delay problem: after measurements are synchronised the complementary filter is rerun until the accelerometer measurement history is exhausted. This process is repeated every time a new GPS measurement is received.

5.3 HELICOPTER ATTITUDE ESTIMATION

In the original helicopter system, attitude measurements and gyro measurements are combined in a Kalman filter to obtain attitude estimates. Between GPS updates, roll, pitch and yaw estimates are propagated by Euler rates in the inertial frame. These rates are obtained from transformed rate gyro measurements. At each GPS update, magnetometer, accelerometer and GPS measurements are combined in an algorithm to determine attitude measurements. The tilt-compensated magnetometer heading measurement is considered.

5.3.1 TILT-COMPENSATED MAGNETOMETER HEADING MEASUREMENT

A magnetometer measures the local magnetic field vector relative to itself and the vehicle to which it is attached. If the magnetic field vector is only dependent on the Earth's magnetic field, it can be used to determine the vehicle's heading. When the vehicle is perfectly level, its heading measurement relative to magnetic north ($\psi_{level,mag}$) can be calculated by the following equation,

$$\psi_{level,mag} = \arctan \frac{B_y}{B_x} \quad (5.10),$$

where B_x and B_y are measurements obtained from the x-axis and y-axis magnetometers respectively [60].

Equation (5.10) is extended to the case where the vehicle is tilted. First, estimates of the current Euler roll and pitch angles are required. In the original helicopter system's implementation the estimates provided by the Kalman filter are used, but in some implementations the current gravity vector in the body frame is used to determine the current roll and pitch angles [61]. The gravity vector (\mathbf{g}) is found by finding the difference between the inertial acceleration obtained from GPS measurements (transformed to the body axis) and the accelerometer measurements. The roll (ϕ) and pitch (θ) measurements are then

$$\phi = \arctan \frac{g_y}{g_z} \quad (5.11),$$

$$\theta = \arctan \frac{g_x}{\sqrt{g_y^2 + g_z^2}} \quad (5.12),$$

where g_* are the components of the gravity vector in the body frame. While Kalman filter estimates of roll and pitch angle are used at this point in the original helicopter system's implementation, roll and pitch measurements as calculated in equations (5.11) and (5.12) are fed into the Kalman filter after the heading measurement has been calculated as described below.

The current Euler angle estimates are used to transform the body x-, y- and z-axis magnetometer measurements to measurements in the horizontal plane [61],

$$B_{xh} = B_x \cos \theta + B_y \sin \phi \sin \theta + B_z \cos \phi \sin \theta \quad (5.13),$$

$$B_{yh} = B_y \cos \phi - B_z \sin \phi \quad (5.14),$$

where B_z is the z-axis magnetometer measurement, B_{*h} are the magnetometer measurements transformed to the horizontal plane and the other symbols retain their definitions from above. The transformed measurements are substituted into equation (5.10) in the place of B_x and B_y to determine the current heading measurement relative to magnetic north:

$$\psi_{mag} = \arctan \frac{B_{yh}}{B_{xh}} \quad (5.15).$$

In order to convert ψ_{mag} to a heading relative to geographic north, the declination angle,

$$\psi_{declination} = \arctan \frac{B_{yref}}{B_{xref}} \quad (5.16),$$

is added, where B_{xref} and B_{yref} are magnetic reference values for the current location on Earth [60]. The current heading measurement is therefore:

$$\psi = \psi_{mag} + \psi_{declination} \quad (5.17).$$

It is important to note that the above equations which are dependent on magnetometer measurements only apply to interference-free measurements.

5.3.2 MAGNETIC INTERFERENCE

A magnetometer which is free of any magnetic interference measures the Earth's local magnetic field vector free of any distortion regardless of orientation. As a result, the magnitude of the magnetic field vector is the same regardless of orientation. This can be represented in equation form,

$$B_x^2 + B_y^2 + B_z^2 = B^2 \quad (5.18),$$

where B_x , B_y and B_z are the measurements obtained from the x-axis, y-axis and z-axis magnetometers respectively and B is the magnitude of the total magnetic field [60]. As a result, the locus of interference free magnetometer measurements is a sphere around the origin with the radius B as illustrated in blue in Figure 5.6 [62].

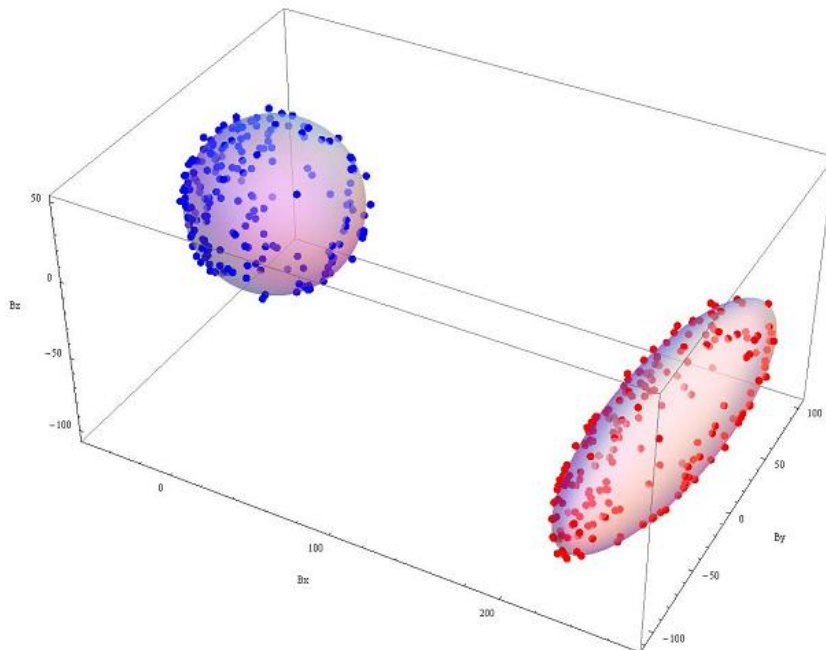


Figure 5.6 - Magnetometer measurements without interference (blue) and magnetometer measurements with interference (red) (axes represent x-, y- and z-axis magnetometer measurements in μT) [63]

Unlike the locus of interference free magnetometer measurements, the locus of measurements taken by a magnetometer which is attached to a typical vehicle is an ellipsoid which is offset from the origin as illustrated in red in Figure 5.6. The distorted locus of magnetometer measurements is a result of magnetic field vector distortion due to magnetic interference. Interference sources can be separated into two categories: hard and soft iron interference.

5.3.2.1 HARD IRON INTERFERENCE

Hard iron interference is caused by permanent magnets and other objects which generate a magnetic field (such as conductors with current flowing through them). The generated magnetic field distorts surrounding magnetic fields such as the Earth's magnetic field as illustrated by the magnetic field model in Figure 5.7 [62].

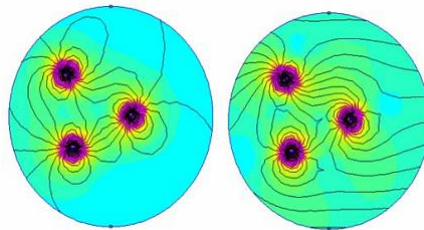


Figure 5.7 – Model of the magnetic field of three permanent magnets in the absence of an external magnetic field (left) and within a uniform magnetic field (right) [62]

A magnetometer located near a source of hard iron interference measures the sum of the magnetic field generated by the source and the Earth's magnetic field. If the position of the hard iron interference source is fixed with respect to the magnetometer the result is a constant magnetometer measurement offset and the locus of magnetometer moves away from the origin as illustrated in red in Figure 5.6. Variable hard iron interference occurs when the magnetic field generated by a source of hard iron interference varies with respect to the magnetometer. This can occur when a permanent magnet moves with respect to the magnetometer or when the current in a conductor varies.

5.3.2.2 SOFT IRON INTERFERENCE

Soft iron interference is caused by temporary magnetic fields induced in ferrous materials by external magnetic fields. The induced magnetic field distorts surrounding magnetic fields such as the Earth's magnetic field as illustrated by the magnetic field model in Figure 5.8 [62].

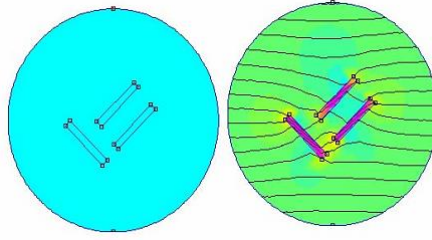


Figure 5.8 - Model of the magnetic field of three unmagnetised ferromagnetic bars in the absence of an external magnetic field (left) and within a uniform magnetic field (right) [62]

As induced magnetic fields vary with orientation relative to external magnetic fields (e.g. the Earth's magnetic field), soft iron interference varies with vehicle orientation. As a result, the locus of magnetometer measurements is skewed resulting in an ellipsoid as illustrated in red in Figure 5.6. Additional variable soft iron interference occurs when ferrous materials move relative to the magnetometer.

5.3.3 MAGNETOMETER CALIBRATION

In order to reduce the effects of magnetic interference, magnetometers should be mounted as far as possible from interference sources. At the very least magnetometers should be mounted far enough from interference sources to ensure that they are not saturated as saturation makes it impossible to measure the variation of the magnetic field relative to the magnetometer with changes in attitude [62]. The effect of the remaining constant sources of interference can be reduced by calibration. Calibration effectively involves the determination of suitable scaling factors and offsets to change the locus of magnetometer measurements from an offset ellipsoid to a correctly scaled sphere at the origin. An equation for such a transformation is

$$\begin{bmatrix} B_{xcal} \\ B_{yca} \\ B_{zca} \end{bmatrix} = \begin{bmatrix} f_{1,1} & f_{1,2} & f_{1,3} \\ f_{2,1} & f_{2,2} & f_{2,3} \\ f_{3,1} & f_{3,2} & f_{3,3} \end{bmatrix} \begin{bmatrix} B_{xraw} \\ B_{yraw} \\ B_{zraw} \end{bmatrix} + \begin{bmatrix} B_{xoff} \\ B_{yoff} \\ B_{zoff} \end{bmatrix} \quad (5.19),$$

where B_{*raw} are raw magnetometer measurements, $f_{*,*}$ are suitable scaling factors, B_{*off} are suitable offsets and B_{*cal} are calibrated magnetometer measurements [64]. As calibrated measurements approximate interference free measurements, equation (5.18) applies:

$$B^2 = B_{xcal}^2 + B_{yca}^2 + B_{zca}^2 \quad (5.20).$$

This equation can be expanded by substituting the B_{*cal} terms with equivalents in terms of B_{*raw} , $f_{*,*}$ and B_{*off} taken from equation (5.19):

$$\begin{aligned}
B^2 = & (f_{1,1}B_{xraw} + f_{1,2}B_{yraw} + f_{1,3}B_{zraw} + B_{xoff})^2 \\
& + (f_{2,1}B_{xraw} + f_{2,2}B_{yraw} + f_{2,3}B_{zraw} + B_{yoff})^2 \\
& + (f_{3,1}B_{xraw} + f_{3,2}B_{yraw} + f_{3,3}B_{zraw} + B_{zoff})^2
\end{aligned} \tag{5.21}$$

If the local strength of the Earth's magnetic field is known and a number of suitable raw magnetometer measurements are available, the unknowns $f_{*,*}$ and B_{*off} in equation (5.21) can be solved in the least squares sense by minimising the sum of the squared errors between the known Earth's magnetic field (B_{ref}) and the measured magnetic field (B):

$$\text{error} = \sum (B_{ref} - B)^2 \tag{5.22}.$$

As the method of least squares is used, it is important when recording raw magnetometer measurements for calibration purposes that the magnetometer is rotated equally (the same amount and speed) through all angles of rotation so that all of its axes cut the magnetic field equally [64].

Once suitable values for $f_{*,*}$ and B_{*off} are found, calibrated measurements (B_{*cal}) can be found from raw measurements (B_{*raw}) using equation (5.19). B_{*cal} can then be substituted into equations (5.13) and (5.14) to facilitate heading measurement.

As mentioned above, calibration only reduces the effect of constant sources of interference. Variable sources of interference still affect magnetometer measurements after calibration, for example the varying magnetic field around a conductor carrying a varying current.

5.4 PLATFORM HEAVE ESTIMATION

Platform motion measurements are made available on the helicopter's OBC via its RF link as described in Section 8.3. Between measurements, platform heave estimates are required. A platform heave estimator is proposed.

5.4.1 TARGET LANDING POINT

The platform motion measurements sent to the helicopter via its RF link are of the target landing point on the platform. Measurements are propagated between samples. Position (D) is propagated by velocity (\dot{D}), velocity is propagated by acceleration (\ddot{D}) and acceleration is propagated by jerk (\dddot{D}):

$$D_T(k) = D_T(k-1) + \dot{D}_T(k-1)T \tag{5.23},$$

$$\dot{D}_T(k) = \dot{D}_T(k-1) + \ddot{D}_T(k-1)T \quad (5.24),$$

$$\ddot{D}_T(k) = \ddot{D}_T(k-1) + \dddot{D}_T(k-1)T \quad (5.25).$$

When a jerk (\ddot{D}) measurement is not available directly the latest acceleration gradient is used to propagate the acceleration measurement:

$$\ddot{D}_T(k) = \ddot{D}_T(k-1) + \left(\frac{\ddot{D}_T(k-1) - \ddot{D}_T(k-2)}{10T} \right) T \quad (5.26).$$

T in equations (5.23) to (5.26) is the period between estimator updates. $10T$ is used in the denominator as the rate at which measurements are received via the RF link is 10 times slower (5 Hz) than the rate at which the estimator is updated (50 Hz).

5.4.2 PLATFORM POINT UNDER HELICOPTER

The heave motion states of the point on the platform directly underneath the helicopter are required for platform heave tracking purposes. The platform motion states received via the helicopter's RF link are of the target landing point on the platform. Due to the rolling and pitching motion of the platform, any lateral or longitudinal misalignment with the target landing point results in a deviation of the heave motion states of the point on the platform directly underneath the helicopter from the heave motion states of the target landing point. A suitable transformation from the target landing point heave motion states to the heave motion states of the point on the platform directly underneath the helicopter is required.

5.4.2.1 POSITION

The inertial down position of the point on the platform directly under the helicopter is the sum of the inertial down position of the target landing point and the inertial down component of a vector between the target landing point and the point on the platform under the helicopter. Such an offset vector is represented by the green arrow in Figure 5.9 with the rotated platform represented by the grey plane, the helicopter represented by the red circle, the corresponding point on the platform under the helicopter represented by the yellow circle and the target landing point represented by the blue circle.

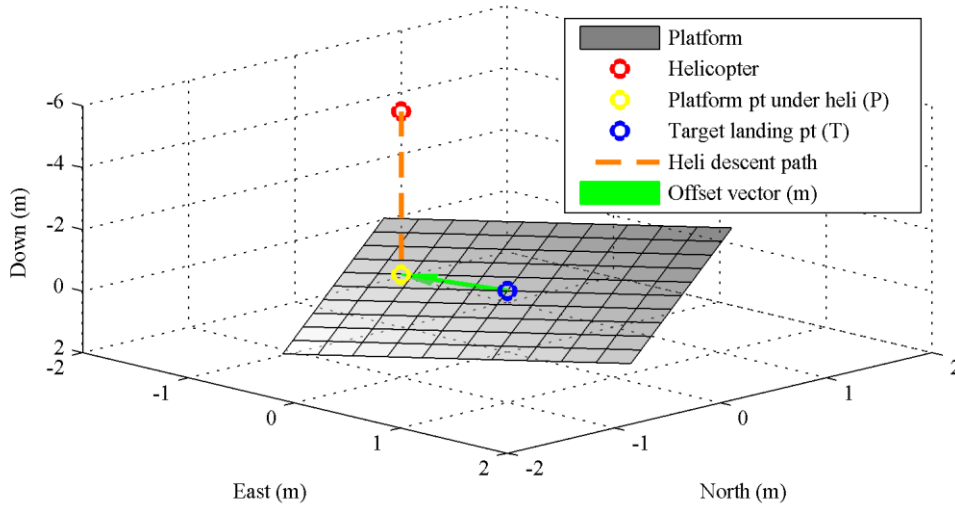


Figure 5.9 - Platform and helicopter system

In the body frame of the platform, the offset vector (with its origin at the target landing point) is defined as follows,

$$\mathbf{m} = [x_P \quad y_P \quad z_P]^T \quad (5.27),$$

where x_P , y_P and z_P describe the position of point P in the platform's the body frame. The inertial down component of the offset vector is required. Therefore the vector must be transformed to the inertial NED frame. The following direction cosine matrix (*DCM*) is suitable for transformations from the inertial NED frame to the platform's body frame using the axis definitions given in Figure A.4 and the Euler 3-2-1 angle sequence:

$$DCM(-\phi, \theta, -\psi) = \begin{bmatrix} \cos \theta \cos(-\psi) & \cos \theta \sin(-\psi) & -\sin \theta \\ \sin(-\phi) \sin \theta \cos(-\psi) - \cos(-\phi) \sin(-\psi) & \sin(-\phi) \sin \theta \sin(-\psi) - \cos(-\phi) \cos(-\psi) & \sin(-\phi) \cos \theta \\ \cos(-\phi) \sin \theta \cos(-\psi) - \sin(-\phi) \sin(-\psi) & \cos(-\phi) \sin \theta \sin(-\psi) - \sin(-\phi) \cos(-\psi) & \cos(-\phi) \cos \theta \end{bmatrix} \quad (5.28).$$

ϕ , θ and ψ are the roll, pitch and heading angles respectively. The inverse *DCM* must be used for the transformation from the platform's body frame to the inertial NED frame:

$$\begin{bmatrix} N_P \\ E_P \\ D_P \end{bmatrix} = [DCM]^{-1} \begin{bmatrix} x_P \\ y_P \\ z_P \end{bmatrix} + \begin{bmatrix} N_T \\ E_T \\ D_T \end{bmatrix} \quad (5.29).$$

N_P , E_P and D_P are the inertial north, east and down positions respectively of the point on the platform under the helicopter. D_P is required. As point P is directly under the helicopter, its north and east positions are the same as the helicopter's north and east positions. Therefore N_P and E_P are known. As the platform's roll, pitch and heading angles are known, the elements of the *DCM* can be calculated. As x_P and y_P change as the helicopter's lateral and

longitudinal position changes, they are not directly available. z_P is constant and equal to 0 for the current system. The inertial position states of the target landing point, N_T , E_T and D_T , are known. To aid with the removal of the unknowns, equation (5.29) is rearranged:

$$\begin{bmatrix} x_P \\ y_P \\ z_P \end{bmatrix} = [DCM] \begin{bmatrix} N_P - N_T \\ E_P - E_T \\ D_P - D_T \end{bmatrix} \quad (5.30).$$

The last row of equation (5.30) is expanded:

$$z_P = DCM_{3,1}[N_P - N_T] + DCM_{3,2}[E_P - E_T] + DCM_{3,3}[D_P - D_T] \quad (5.31).$$

D_P is found by rearranging equation (5.31):

$$D_P = \frac{z_P - DCM_{3,1}[N_P - N_T] - DCM_{3,2}[E_P - E_T]}{DCM_{3,3}} + D_T \quad (5.32).$$

Expanding the DCM elements leads to the following equation:

$$D_P = D_T + \frac{z_P - [\cos(-\phi) \sin \theta \cos(-\psi) - \sin(-\phi) \sin(-\psi)][N_P - N_T] - [\cos(-\phi) \sin \theta \sin(-\psi) - \sin(-\phi) \cos(-\psi)][E_P - E_T]}{\cos(-\phi) \cos \theta} \quad (5.33).$$

Consideration of the signs of the angles leads to the following inertial down position function:

$$D_P = D_T + \frac{z_P - [\cos \phi \sin \theta \cos \psi - \sin \phi \sin \psi][N_P - N_T] - [-\cos \phi \sin \theta \sin \psi + \sin \phi \cos \psi][E_P - E_T]}{\cos \phi \cos \theta} \quad (5.34).$$

5.4.2.2 VELOCITY

The inertial down velocity of the point on the platform directly under the helicopter (\dot{D}_P) is the total derivative of the inertial down position function given in equation (5.34):

$$\begin{aligned} \frac{dD_P}{dt} = & \frac{\partial D_P}{\partial D_T} \frac{dD_T}{dt} + \frac{\partial D_P}{\partial \phi} \frac{d\phi}{dt} + \frac{\partial D_P}{\partial \theta} \frac{d\theta}{dt} + \frac{\partial D_P}{\partial \psi} \frac{d\psi}{dt} + \frac{\partial D_P}{\partial N_P} \frac{dN_P}{dt} + \frac{\partial D_P}{\partial N_T} \frac{dN_T}{dt} \\ & + \frac{\partial D_P}{\partial E_P} \frac{dE_P}{dt} + \frac{\partial D_P}{\partial E_T} \frac{dE_T}{dt} \end{aligned} \quad (5.35).$$

The 3-DOF platform used in this project maintains a fixed heading angle, longitudinal position and lateral position. Therefore equation (5.35) reduces to:

$$\dot{D}_P = \frac{\partial D_P}{\partial D_T} \dot{D}_T + \frac{\partial D_P}{\partial \phi} \dot{\phi} + \frac{\partial D_P}{\partial \theta} \dot{\theta} + \frac{\partial D_P}{\partial N_P} \dot{N}_P + \frac{\partial D_P}{\partial E_P} \dot{E}_P \quad (5.36).$$

\dot{D}_T is the inertial down velocity of the target landing point, $\dot{\phi}$ is the roll rate of the platform, $\dot{\theta}$ is the pitch rate of the platform and \dot{N}_P and \dot{E}_P are the inertial north and east velocities of the point on the platform directly underneath the helicopter, equal to the inertial north and east velocities of the helicopter. The partial derivatives must be solved. Equation (5.34) can be expanded to

$$D_P = D_T + \frac{z_P}{\cos \phi \cos \theta} - \frac{\cos \phi \sin \theta \cos \psi N_P}{\cos \phi \cos \theta} + \frac{\cos \phi \sin \theta \cos \psi N_T}{\cos \phi \cos \theta} \quad (5.37),$$

$$+ \frac{\sin \phi \sin \psi N_P}{\cos \phi \cos \theta} - \frac{\sin \phi \sin \psi N_T}{\cos \phi \cos \theta} + \frac{\cos \phi \sin \theta \sin \psi E_P}{\cos \phi \cos \theta}$$

$$- \frac{\cos \phi \sin \theta \sin \psi E_T}{\cos \phi \cos \theta} - \frac{\sin \phi \cos \psi E_P}{\cos \phi \cos \theta} + \frac{\sin \phi \cos \psi E_T}{\cos \phi \cos \theta}$$

and then simplified to

$$D_P = D_T + \frac{z_P}{\cos \phi \cos \theta} - \tan \theta \cos \psi N_P + \tan \theta \cos \psi N_T + \frac{\tan \phi \sin \psi N_P}{\cos \theta} \quad (5.38).$$

$$- \frac{\tan \phi \sin \psi N_T}{\cos \theta} + \tan \theta \sin \psi E_P - \tan \theta \sin \psi E_T$$

$$- \frac{\tan \phi \cos \psi E_P}{\cos \theta} + \frac{\tan \phi \cos \psi E_T}{\cos \theta}$$

Now each of the partial derivatives of equation (5.36) can be solved:

$$\frac{\partial D_P}{\partial D_T} = 1 \quad (5.39)$$

$$\frac{\partial D_P}{\partial \phi} = \frac{z_P \tan \phi}{\cos \theta \cos \phi} + \frac{(\sec \phi)^2 \sin \psi (N_P - N_T)}{\cos \theta} - \frac{(\sec \phi)^2 \cos \psi (E_P - E_T)}{\cos \theta} \quad (5.40)$$

$$\frac{\partial D_P}{\partial \theta} = \frac{z_P \tan \theta}{\cos \phi \cos \theta} + (\sec \theta)^2 \cos \psi (N_T - N_P) + \frac{\tan \phi \sin \psi \tan \theta (N_P - N_T)}{\cos \theta} \quad (5.41)$$

$$+ (\sec \theta)^2 \sin \psi (E_P - E_T) + \frac{\tan \phi \cos \psi \tan \theta (E_T - E_P)}{\cos \theta}$$

$$\frac{\partial D_P}{\partial N_P} = -\tan \theta \cos \psi + \frac{\tan \phi \sin \psi}{\cos \theta} \quad (5.42)$$

$$\frac{\partial D_P}{\partial E_P} = \tan \theta \sin \psi - \frac{\tan \phi \cos \psi}{\cos \theta} \quad (5.43)$$

Finally, \dot{D}_P , the inertial down velocity of the point directly under the helicopter as a function of \dot{D}_T , $\dot{\phi}$, $\dot{\theta}$, \dot{N}_P and \dot{E}_P as well as z_P , ϕ , θ , ψ , N_P , N_T , E_P and E_T , can be found by substituting equations (5.39) to (5.43) into equation (5.36). The large number of trigonometric

functions used in the calculation makes it computationally demanding for the helicopter's onboard computer if repeated at 50 Hz. Additionally, the difference between \dot{D}_P and \dot{D}_T is small if the helicopter's lateral and longitudinal position error with respect to the target landing point is small. As described in Section 7.3.2.3, a large lateral and longitudinal position error results in an aborted landing attempt. These factors suggest that the demanding calculation of \dot{D}_P is not justifiable if \dot{D}_T is available. The small difference can be compensated for by the helicopter's heave controller.

5.4.2.3 ACCELERATION

The heave acceleration of the point on the platform directly under the helicopter (\ddot{D}_P) is the total derivative of equation (5.36). Such a calculation is not justifiable for similar reasons to those mentioned for the velocity calculation in Section 5.4.2.2. Additionally, the lack of direct access to the platform's angular accelerations required for the calculation is problematic. The inertial down acceleration of the target landing point can be used instead and the difference can be compensated for by the helicopter's heave controller.

5.5 IMPLEMENTATION

The helicopter's OBC is based on a Microchip dsPIC 6014A microprocessor which runs its main loop at 50 Hz. The MPLAB X IDE allows the microprocessor to be programmed in C.

The original system's C implementation of the complementary filter, where the low- and high-pass filters are discretised, was used. GPS latency compensation by filter replay was implemented in C for the complementary filter. While accelerometer measurements are received at the frequency of the main loop, GPS measurements are received at 10 Hz. At every GPS update the complementary filters are rewound by the number of time steps which represent the GPS latency (where each time step for a 50 Hz main loop is 0.02 s in length) and replayed for GPS latency compensation. As the stored filter states and measurements use a significant amount of the microprocessor's stack, a maximum measurement and filter history of 0.4 s or 20 time steps is stored.

The original system's C implementation of the Kalman filter attitude estimator was used.

The proposed platform heave estimator is discrete by design and was therefore implemented directly in C. Platform motion measurements are received via the helicopter's RF link at 5 Hz as described in Section 8.3.

5.6 SUMMARY

In addition to the original system's helicopter position and velocity estimator, GPS latency compensation by filter replay was added to the inertial down position and velocity complementary filter to improve its bandwidth. The original system's helicopter Kalman filter attitude estimator was not changed, but magnetometer interference and calibration was discussed. Platform target landing point motion states were estimated by propagating measurements between samples. Target landing point data was transformed to the point on the platform directly underneath the helicopter. The estimator was implemented in C and run on a microprocessor at 50 Hz. Practical tuning and testing of the estimator and magnetometer calibration is described in Chapter 9.

6. LOW-LEVEL CONTROLLERS

6.1 INTRODUCTION

The helicopter's low-level (longitudinal, lateral, heave and heading) controllers have to meet the following requirements in order to execute the landing algorithm chosen in Section 2.6 for landing on the ESL's 3-DOF platform:

- Track the heave motion of a platform which is simulating ship flight deck motion.
- Maintain longitudinal and lateral position within 1.25 m and heading within 4° while pointing into the wind.

The original low-level controllers of the helicopter are assumed to be appropriate for near-hover flight. While a theoretical controller design is outside the scope of this project, the original controllers can be tuned via practical tests as they were designed by a successive loop closure (SLC) approach [65]. This is because controllers designed by an SLC approach allow control loops to be closed successively. The innermost loop can be closed first and tuned until the fastest dynamics are under control. If successive loops are sufficiently timescale separated (bandwidths at least five times apart), tuned loops can be approximated as a unity gain plant – a system which follows its reference input exactly. The next loop can then be closed around this plant and tuned. The process is complete once the outermost loop has been closed and tuned until the slowest dynamics are under control.

In this chapter an overview of the structure of the original controllers is provided. Ways of further improving the performance of the heave controller are also discussed.

6.2 INERTIAL POSITION CONTROL

The original inertial position controllers are proportional (P) controllers. The inertial position controllers' output commands are transformed to the body frame. A block diagram of the original inertial position control architecture is shown in Figure 6.1.

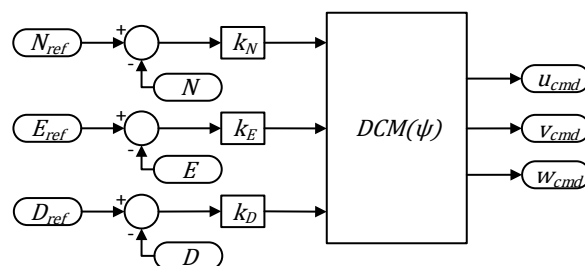


Figure 6.1 - Block diagram of inertial position controller

In the block diagram, N , E and D are the inertial positions in metres; u , v and w are the body velocities in metres per second; $DCM(\psi)$ is a transformation from the inertial frame to the body frame; $*_{ref}$ are control reference inputs; k_* are proportional control gains; and $*_{cmd}$ are control output commands.

6.2.1 TRANSFORMATION

As the output of the inertial position controllers becomes the reference input to body velocity controllers (described in sections 6.3, 6.4 and 6.5), the output is transformed from the inertial frame to the body frame. During near-hover flight the helicopter is approximately level. During approximately level flight the helicopter's roll and pitch angles are small. As a result, a transformation only due to the heading angle (ψ) is sufficient. A suitable transformation matrix is

$$DCM(\psi) = \begin{bmatrix} \cos \psi & \sin \psi & 0 \\ -\sin \psi & \cos \psi & 0 \\ 0 & 0 & 1 \end{bmatrix} \quad (6.1).$$

From the third row of the transformation matrix it is apparent that the third element of an inertial vector maps directly to the third element of a body vector when using this transformation matrix. As a result, the output command of the inertial down position controller is effectively used directly as the reference input to the heave velocity controller.

6.2.2 COMMAND LIMITS

Before the output commands from the position controllers become the reference input to the velocity controllers, the commands are limited to prevent excessive movement or actuator saturation. The longitudinal and lateral velocity commands are limited to 3 m/s and the heave velocity command is limited to 1.5 m/s.

6.3 LONGITUDINAL CONTROL

The original longitudinal velocity controller is a proportional integral (PI) controller. Its output command becomes the reference input to the pitch angle controller, a P controller. The pitch angle controller's output becomes the input to the pitch rate controller: a P controller combined with an 8 rad/s low-pass filter and an integrator. The pitch rate controller's output becomes the longitudinal cyclic command. A block diagram of the original longitudinal control architecture is shown in Figure 6.2.

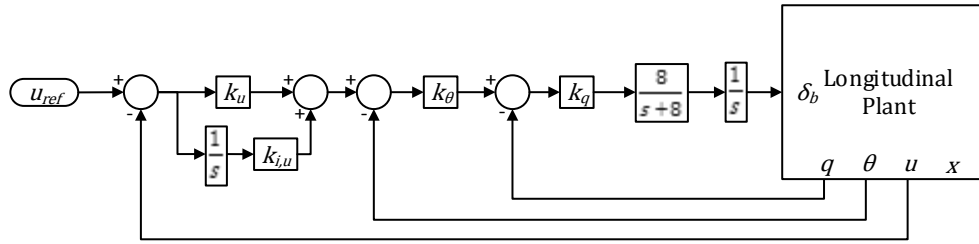


Figure 6.2 - Block diagram of longitudinal controller

In the block diagram, u is the longitudinal velocity in metres per second, θ is the pitch angle in radians, q is the pitch rate in radians per second, u_{ref} is the longitudinal velocity reference in metres per second, k_* are the proportional control gains (except $k_{i,u}$ which is the integral longitudinal velocity control gain) and δ_b is the longitudinal cyclic command in radians.

The linearised, decoupled model of the longitudinal plant as derived by Rossouw [3] is provided in equation (6.2). The model was linearised around hover trim conditions.

$$\frac{q}{\delta_b} = \frac{7108.5}{s^2 + 8.3s + 203.1} \quad (6.2)$$

According to this model the open-loop dynamics of the longitudinal plant in near-hover conditions can be approximated by a complex pole pair with a natural frequency of 14.25 rad/s and a damping ratio of 0.30.

6.3.1 PITCH RATE LOOP

The open-loop poles of the pitch rate model are lightly damped. In order to increase the damping of the closed-loop poles, the pitch rate controller consists of a low-pass filter and an integrator. The cut-off frequency of the filter was chosen so that the dominant closed-loop poles originate at the known pole positions of the filter and integrator. As a result an 8 rad/s (1.27 Hz) cut-off frequency is set for the filter. Within the ESL this filter is known as a *pilot filter*.

6.3.2 LONGITUDINAL VELOCITY CONTROL INTEGRATOR

The velocity control integrator is designed to reject constant disturbances such as a constant wind. To avoid excessive integrator wind-up, an integration limit is implemented. The limit is equal to the longitudinal velocity control output limit of 0.28 rad (16°) as discussed next.

6.3.3 COMMAND LIMITS

The output commands of each of the successive controllers which provide longitudinal control are limited to prevent excessive movement or actuator saturation. The output

command of the longitudinal velocity controller is limited to 0.28 rad (16°) before it becomes the reference input of the pitch angle controller. The output command of the pitch angle controller is limited to 0.70 rad/s (40°/s) before it becomes the reference input of the pitch rate controller. The output command of the pitch rate controller is limited to 0.05 rad (3°) before it is fed to the cyclic.

6.4 LATERAL CONTROL

The longitudinal and lateral control loops are identical in structure but, as the innermost control gains and models differ, lateral control is presented in this separate section. A block diagram of the original lateral control architecture is shown in Figure 6.3.

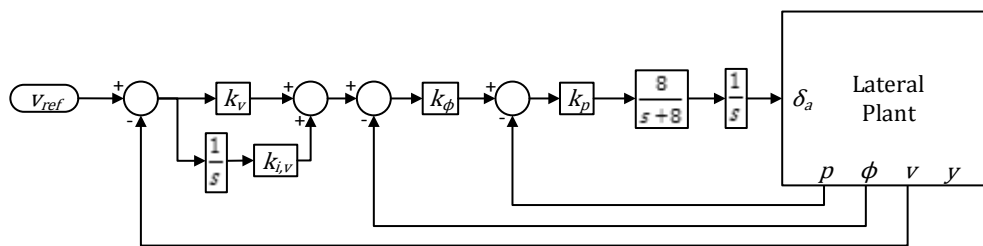


Figure 6.3 - Block diagram of lateral controller

In the block diagram, v is the lateral velocity in metres per second, ϕ is the roll angle in radians, p is the roll rate in radians per second, v_{ref} is the lateral velocity reference in metres per second, k_* are the proportional control gains (except $k_{i,v}$ which is the integral lateral velocity control gain) and δ_a is the lateral cyclic command in radians.

The linearised, decoupled model of the lateral plant as derived by Rossouw [3] is provided in equation (6.3). The model was linearised around hover trim conditions.

$$\frac{p}{\delta_a} = \frac{13426}{s^2 + 8.3s + 383.6} \quad (6.3)$$

According to this model the open-loop dynamics of the lateral plant in near-hover conditions can be approximated by a complex pole pair with a natural frequency of 19.59 rad/s and a damping ratio of 0.21.

6.4.1 ROLL RATE LOOP

The same low-pass filter and integrator discussed in Section 6.3.1 are implemented in the original roll rate controller.

6.4.2 LATERAL VELOCITY CONTROL INTEGRATOR

As for the longitudinal velocity controller, the lateral velocity controller has an integrator to reject constant disturbances. To avoid excessive integrator wind-up, an integration limit is implemented. The limit is equal to the lateral velocity control output limit of 0.28 rad (16°) as discussed next.

6.4.3 COMMAND LIMITS

The limits imposed on the output commands of the longitudinal controllers are mirrored to the lateral controllers: the lateral velocity control output limit is 0.28 rad (16°), the roll angle control output limit is 0.70 rad/s (40°/s) and the roll rate control output limit is 0.05 rad (3°).

6.5 HEAVE CONTROL

The original heave velocity controller is a PI controller. The output command of the heave velocity controller becomes the collective command. A block diagram of the original heave control architecture is shown in Figure 6.4.

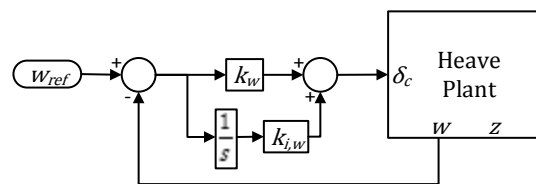


Figure 6.4 - Block diagram of original heave controller

In the block diagram, w is the heave velocity in metres per second, w_{ref} is the heave velocity reference in metres per second, k_w and $k_{i,w}$ are the proportional and integral heave velocity control gains respectively and δ_c is the collective command in radians.

The linearised, decoupled model of the heave plant as derived by Rossouw [3] is provided in equation (6.4). The model was linearised around hover trim conditions.

$$\frac{w}{\delta_c} = -\frac{164.5}{s + 1.11} \quad (6.4)$$

According to this model the open-loop dynamics of the heave plant in near-hover conditions can be approximated by a real pole with a natural frequency of 1.11 rad/s.

6.5.1 ORIGINAL SYSTEM

As mentioned in Section 6.2.1, the output of the inertial down position controller is effectively used directly as the reference input to the heave velocity controller during

approximately level flight. A block diagram of the original combined heave control architecture during approximately level flight is shown in Figure 6.5.

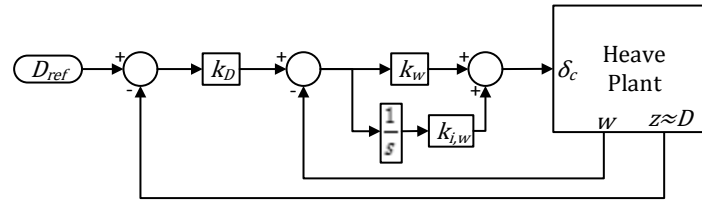


Figure 6.5 - Block diagram of original combined heave controller during approximately level flight

In the block diagram, D is the inertial down position in metres. When using the transformation matrix for approximately level flight from Section 6.2.1, D maps directly to z , the position in the body z -axis. The other symbols retain their definitions from Figure 6.1 and Figure 6.4.

When the original combined heave controller is used to control the heave model of equation (6.4) during approximately level flight, the following transfer function can be found from the inertial down position reference (D_{ref}) to the inertial down position (D):

$$\frac{D}{D_{ref}} = \frac{-164.5k_D(k_{i,w} + k_w s)}{s^3 + (1.11 - 164.5k_w)s^2 - 164.5(k_{i,w} + k_w k_D)s - 164.5k_{i,w}k_D} \quad (6.5).$$

6.5.1.1 STEADY STATE ERROR

The steady state error of a system in response to a certain input can be determined by the final-value theorem formulated in the following equation [47]:

$$e_{ss} = \lim_{s \rightarrow 0} sE(s) \quad (6.6),$$

where $E(s)$ is the error signal in the s -domain or

$$E(s) = D_{ref} - D \quad (6.7).$$

By rearranging, the function in terms of the transfer function $\left(\frac{D}{D_{ref}}\right)$ and the input signal (D_{ref}) is found:

$$E(s) = \left(1 - \frac{D}{D_{ref}}\right) D_{ref} \quad (6.8).$$

By substituting equation (6.5) into equation (6.8) and substituting the result into equation (6.6), the following equation is found:

$$e_{ss} = \lim_{s \rightarrow 0} s \left(\frac{s[s^2 + (1.11 - 164.5k_w)s - 164.5k_{i,w}]}{s^3 + (1.11 - 164.5k_w)s^2 - 164.5(k_{i,w} + k_w k_D)s - 164.5k_{i,w}k_D} \right) D_{ref} \quad (6.9).$$

From this equation it is apparent that the original system has one free integrator. It is therefore a type-1 system. Type-1 systems have zero steady-state error for a unit-step input ($D_{ref} = \frac{1}{s}$), constant steady-state error for a unit ramp input ($D_{ref} = \frac{1}{s^2}$) and infinite steady-state error for a unit parabolic input ($D_{ref} = \frac{1}{s^3}$) [47]. It is not possible to find the steady-state error of a sinusoidal input by using the final-value theorem because it has poles on the imaginary axis ($D_{ref} = \frac{a^2}{s^2 + a^2}$).

6.5.1.2 BANDWIDTH

In order to determine if the controller is capable of tracking the heave motion of a platform which is simulating ship flight deck motion, its bandwidth must be analysed. The bandwidth of a controller is easily determined with a Bode plot. In order to find a Bode plot for the heave controller, its transfer function must be available only in terms of s . This is found by substituting appropriate controller gains into equation (6.5). The original controller gains are given in Table 6.1.

k_D	k_w	$k_{i,w}$
0.5	-0.02	-0.0080

Table 6.1 - Original heave controller gains (G1)

The transfer function is therefore:

$$\frac{D}{D_{ref}} = \frac{1.645s + 0.658}{s^3 + 4.4s^2 + 2.961s + 0.658} \quad (6.10).$$

A Bode plot for the transfer function is given in Figure 6.6.

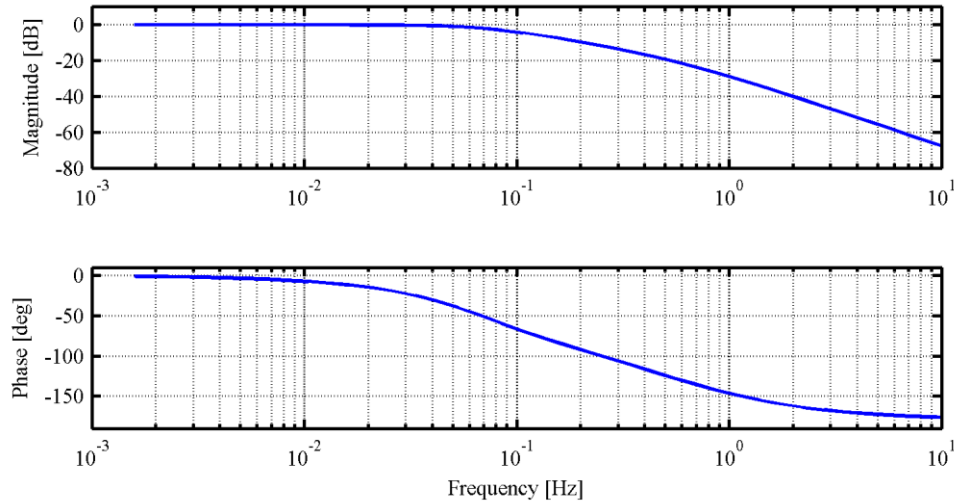


Figure 6.6 - Bode plot of heave controller with original gains

The -3 dB point on the magnitude Bode plot and therefore the bandwidth of the heave controller with the original controller gains is approximately 0.08 Hz. The highest frequency of significant heave motion data is 0.22 Hz in the ship motion data sample sets available to the ESL [7]. Therefore the bandwidth of the heave controller with the original controller gains is too low to track the heave motion of a platform which is simulating ship flight deck motion.

The bandwidth of the controller can be increased by increasing the controller gains. Modified controller gains are given in Table 6.2.

k_D	k_w	$k_{I,w}$
0.8	-0.036	-0.0144

Table 6.2 - Modified heave controller gains (G2/G3/G4/G5)

The transfer function of the heave controller with the modified control gains is found by substituting the gains into equation (6.5):

$$\frac{D}{D_{ref}} = \frac{4.738s + 1.895}{s^3 + 7.032s^2 + 7.106s + 1.895} \quad (6.11).$$

A Bode plot for the transfer function is given in Figure 6.7.

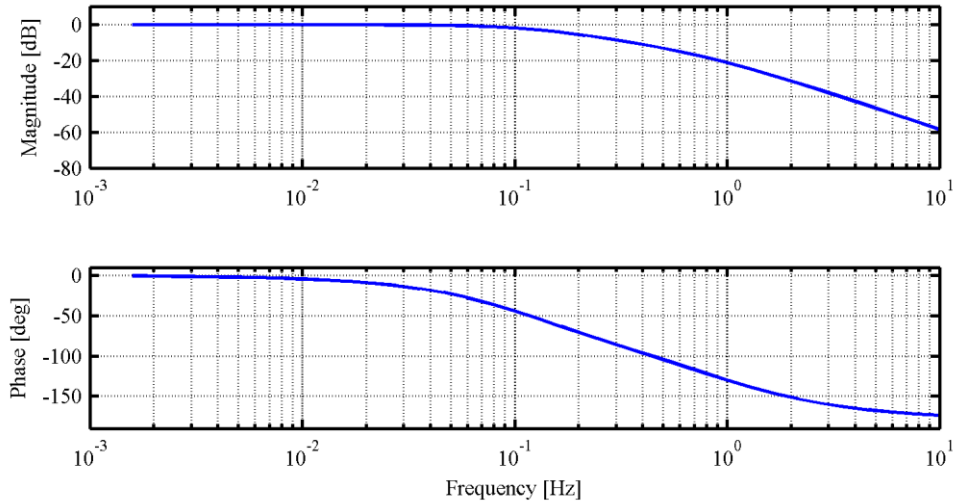


Figure 6.7 - Bode plot of heave controller with modified gains

The increases in controller gains increase the bandwidth of the controller to approximately 0.13 Hz. This is still insufficient for tracking the heave motion of a platform which is simulating ship flight deck motion.

6.5.2 VELOCITY AND ACCELERATION FEED FORWARD

The heave controller needs as many free integrators as possible in order to allow it to track as many types of reference signals as possible. To this end, a controller is proposed with velocity and acceleration feed forward terms. As the heave velocity controller is a body frame controller, inertial down velocities and accelerations are transformed to the helicopter’s body frame before being fed forward. As mentioned in Section 6.2.1, the inertial down axis maps directly to the body z-axis during approximately level flight. As a result, inertial down velocities and accelerations are effectively fed forward directly during approximately level flight. A block diagram of the proposed controller during approximately level flight is shown in Figure 6.8.

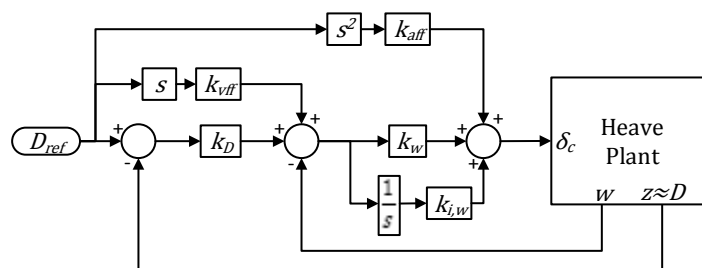


Figure 6.8 - Block diagram of proposed combined heave controller during approximately level flight

In the block diagram, k_{vff} and k_{aff} are the velocity and acceleration feed forward gains respectively. The other symbols retain their previous definitions.

When the proposed controller is used to control the heave model of equation (6.4) during approximately level flight, the following transfer function can be found from inertial down position reference (D_{ref}) to inertial down position (D):

$$\frac{D}{D_{ref}} = \frac{-164.5[k_{aff}s^3 + k_{vff}k_w s^2 + (k_{vff}k_{i,w} + k_w k_D)s + k_{i,w}k_D]}{s^3 + (1.11 - 164.5k_w)s^2 - 164.5(k_{i,w} + k_w k_D)s - 164.5k_{i,w}k_D} \quad (6.12).$$

6.5.2.1 STEADY STATE ERROR

$E(s)$ for the proposed controller is found by substituting equation (6.12) into equation (6.8) and rearranging:

$$E(s) = \left(\frac{s[(1 + 164.5k_{aff})s^2 + (1.11 - 164.5k_w + 164.5k_{vff}k_w)s + 164.5(-k_{i,w} + k_{vff}k_{i,w})]}{s^3 + (1.11 - 164.5k_w)s^2 - 164.5(k_{i,w} + k_w k_D)s - 164.5k_{i,w}k_D} \right) D_{ref} \quad (6.13).$$

From equation (6.13) it is apparent that the system has at least one free integrator. By choosing an appropriate value for the velocity feed forward gain k_{vff} , another free integrator can be gained. By substituting $k_{vff} = 1$ into equation (6.13) and substituting the result into equation (6.6), the steady-state error for any reference input (with stable poles only) becomes:

$$e_{ss} = \lim_{s \rightarrow 0} s \left(\frac{s^2[(1 + 164.5k_{aff})s + 1.11]}{s^3 + (1.11 - 164.5k_w)s^2 - 164.5(k_{i,w} + k_w k_D)s - 164.5k_{i,w}k_D} \right) D_{ref} \quad (6.14).$$

The system now has two free integrators and is therefore a type-2 system. Type-2 systems have zero steady-state error for a unit-step input ($D_{ref} = \frac{1}{s}$), zero steady-state error for a unit ramp input ($D_{ref} = \frac{1}{s^2}$) and constant steady-state error for a unit parabolic input ($D_{ref} = \frac{1}{s^3}$) [47].

From equation (6.14) it is apparent that the steady-state error can be minimised if an appropriate value for k_{aff} is selected. If $k_{aff} = -\frac{1}{164.5}$, the steady state error reduces to:

$$e_{ss} = \lim_{s \rightarrow 0} s \left(\frac{1.11s^2}{s^3 + (1.11 - 164.5k_w)s^2 - 164.5(k_{i,w} + k_w k_D)s - 164.5k_{i,w}k_D} \right) D_{ref} \quad (6.15).$$

The accuracy of the theoretical value of k_{aff} selected in this section depends on the accuracy of the heave model.

6.5.2.2 BANDWIDTH

The transfer function of the proposed controller is found by substituting the modified gains from Table 6.2 and the feed forward gains from Section 6.5.2.1 into equation (6.12):

$$\frac{D}{D_{ref}} = \frac{s^3 + 5.922s^2 + 7.106s + 1.895}{s^3 + 7.032s^2 + 7.106s + 1.895} \quad (6.16).$$

A Bode plot for the transfer function is provided in Figure 6.9.

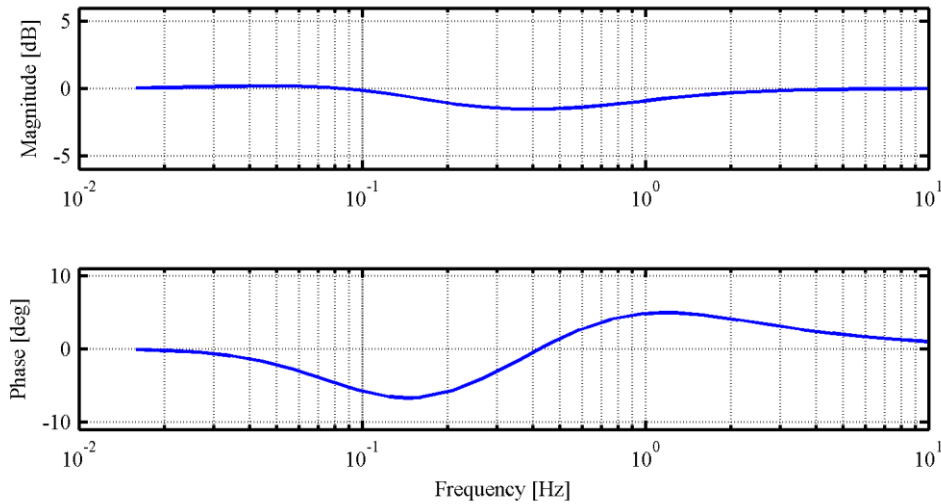


Figure 6.9 - Bode plot of heave controller with modified gains and velocity and acceleration feed forward

The Bode plot of the transfer function suggests that the bandwidth of the proposed controller is much higher than the original controller. Heave motion tracking of a platform which is simulating ship flight deck motion should be possible with the proposed controller.

6.5.3 COMMAND LIMITS

The output commands of the various controllers which make up the heave control architecture are limited to prevent excessive movement or actuator saturation. As mentioned in Section 6.2.2, the output command of the inertial down position controller is limited to 1.5 m/s. The velocity feed forward term is limited separately to 1.5 m/s. The acceleration feed forward term is limited to 0.04 rad (2.3°). The output command of the heave velocity controller is combined with the acceleration feed forward term and limited to 0.17 rad (10°) before it is fed to the collective.

6.6 HEADING CONTROL

The original heading angle controller is a P controller. Its output command becomes the reference input to the yaw rate controller, a PI controller. The output command of the yaw rate controller becomes the tail rotor command. A block diagram of the original heading control architecture is shown in Figure 6.10:

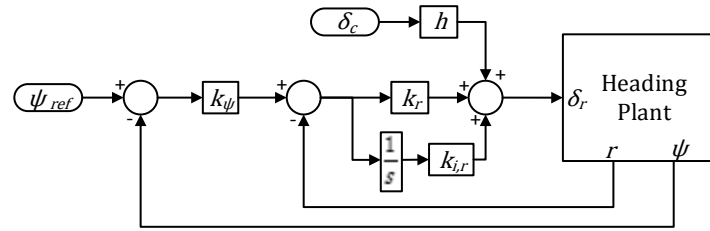


Figure 6.10 - Block diagram of heading controller

In the block diagram, ψ is the heading angle in radians, r is the yaw rate in radians per second, ψ_{ref} is the heading angle reference in radians, k_* are the proportional control gains (except $k_{i,r}$ which is the integral yaw rate control gain), h is the collective to tail rotor pitch mixing function, δ_c is the collective command in radians and δ_r is the tail rotor command in radians.

6.6.1 MODEL DERIVATION

The Master’s projects of Rossouw and Van Schalkwyk made use of the RC gyro installed on the helicopter to provide active yaw rate damping for the heading controller [4, 3]. In *heading hold* mode the gyro implements PI control. In *normal* mode the gyro provides rate feedback with a gain of $-\frac{1}{6.6}$ [3]. The previously undocumented original system bypasses the RC gyro when using the heading controller. The RC gyro is replaced by a yaw rate controller. An open loop transfer function from yaw rate to input cyclic should be found to gain insight about the dynamics of the heading loop.

Rossouw uses the gyro in *normal* mode and therefore includes the effect of the gyro in the derivation of the linearised, decoupled open loop transfer function from heading angle to input cyclic shown in equation (6.17) [3]. The model was linearised around hover trim conditions.

$$\frac{\psi}{\delta_r} = \frac{147.3}{s(s + 23.37)} \tag{6.17}$$

A block diagram of the model provided by Rossouw is shown in Figure 6.11.

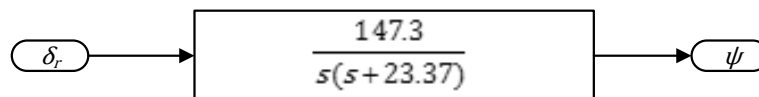


Figure 6.11 - Block diagram of existing heading model

A block diagram of the same model is shown in Figure 6.12, revealing the effect of the RC gyro.

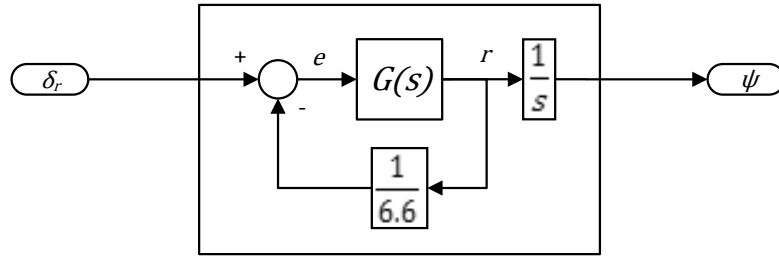


Figure 6.12 - Block diagram of the existing heading model revealing effect of gyro

In the block diagram, $G(s)$ is the transfer function from yaw rate to input cyclic which is required.

Equations for the unknown symbols in Figure 6.12 are:

$$G(s) = \frac{r}{e} \quad (6.18),$$

$$e = \delta_r - \frac{r}{6.6} \quad (6.19),$$

$$r = s\psi \quad (6.20).$$

After rearranging, equations (6.17), (6.18) and (6.20) can be substituted into equation (6.19):

$$\frac{s\psi}{G(s)} = \frac{s(s + 23.37)\psi}{147.3} - \frac{s\psi}{6.6} \quad (6.21).$$

By rearranging, $G(s)$, the transfer function from yaw rate to input cyclic, is solved:

$$G(s) = \frac{147.3}{s + 1.05} \quad (6.22).$$

According to this model the open-loop dynamics of the heading plant in near-hover conditions can be approximated by a real pole with a natural frequency of 1.05 rad/s.

6.6.2 COLLECTIVE TO TAIL ROTOR PITCH MIXING

One of the major functions of the helicopter's tail rotor is to counteract the torque effect of the main rotor. This torque is dependent on the amount of main rotor collective which is commanded. The relationship between the main rotor collective command and the tail rotor pitch command required to counteract the resulting torque effect can be described by a suitable mixing function. If fed with main rotor collective commands, the mixing function outputs the required tail rotor pitch commands to counteract the torque effect of the main rotor. The use of such a mixing function is referred to as *revo mixing* or *revolution mixing* in radio-control hobby circles [66].

The tail rotor pitch command of the original heading controller is the sum of the outputs of the yaw rate controller and a main rotor collective mixing function. The mixing function is labelled h in Figure 6.10. The original heading controller approximates a linear mixing function with a unity gain. The heading angle and yaw rate controllers are expected to counteract any residual main rotor torque effects.

During hover flight the added tail rotor command reduces the demand on the heading controller's rate integrator, improving the controller's disturbance rejection capabilities. It also reduces the demand on the heading controller when the vehicle performs heave manoeuvres.

6.6.3 COMMAND LIMITS

In order to prevent excessive movement or actuator saturation, controller output commands are limited. The output command of the heading angle controller is limited to 0.70 rad/s ($40^\circ/\text{s}$) and the output command of the yaw rate controller is limited to 0.17 rad (10°).

6.7 IMPLEMENTATION

The helicopter's OBC is based on a Microchip dsPIC 6014A microprocessor which runs its main loop at 50 Hz. The MPLAB X IDE allows the microprocessor to be programmed in C.

The original system's C implementation of the controllers was used where low-pass filters are discretised, integrators are implemented by the Euler integration method and the rest of the controllers are implemented using emulation. The proposed heave controller was also implemented in C.

6.8 SUMMARY

The structures of the original inertial position, longitudinal, lateral, heave and heading controllers were discussed. The addition of velocity and acceleration feed forward terms to the heave controller was proposed to increase the bandwidth of the controller. The original controllers are implemented in C. The proposed heave controller was also implemented in C. The controllers are run on a microprocessor at 50 Hz. Practical tuning of the heave controller is detailed in Chapter 9. As the original low-level controllers of the helicopter are assumed to be appropriate for near-hover flight the lateral, longitudinal and heading controllers should meet the requirements set without tuning. For the benefit of future projects lateral, longitudinal and heading controller tuning data is provided in Appendix C.

7. HIGH-LEVEL CONTROLLERS

7.1 INTRODUCTION

The high-level controllers of the helicopter have to provide the following in order to execute the landing algorithm chosen in Section 2.6:

- Waypoint navigation controller for approach purposes
- Timed deck landing descent controller in order to make use of landing opportunities specified by time
- Landing state machine (LSM) to ensure that the correct sequence is followed under safe conditions

The original high-level controllers include a waypoint navigation controller and an LSM suitable for stationary platform landings. A timed deck landing descent controller is proposed and the extension of the original LSM for the execution of the required landing algorithm is discussed in this chapter.

7.2 TIMED DECK LANDING DESCENT CONTROLLER

A timed deck landing descent controller is required to control the helicopter's descent to the platform so that landing occurs at a landing opportunity specified by a time in the future. For the chosen landing algorithm, landing descent occurs while tracking platform heave motions. It is therefore the task of the controller to control a relative descent to the platform. Such a descent is illustrated in Figure 7.1 in the platform relative frame and in an inertial frame for a landing opportunity which is tracked from 5 s in the future from an initial relative vertical separation between the helicopter and platform of 3 m.

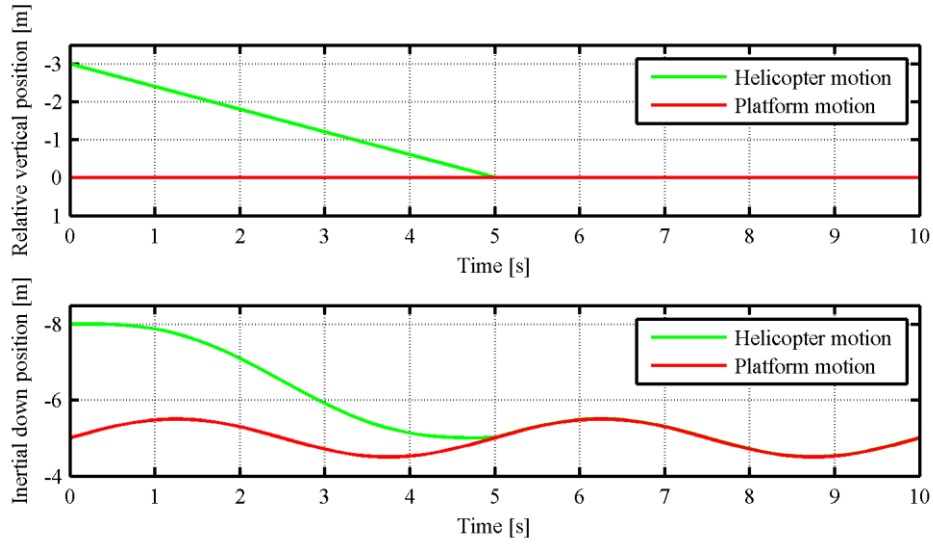


Figure 7.1 - Landing descent in platform relative frame (top) and inertial frame (bottom)

In order to achieve a relative descent to the platform, the helicopter's heave controller's inertial down position reference and velocity feed forward must be adjusted appropriately.

The required inertial down position reference (D_{ref}) is the difference between the platform's inertial down position (D_p) and the adjusted relative vertical position. The adjusted relative vertical position is the difference between the current relative vertical position ($D_p - D$) and the required change in relative vertical position per time step (ΔD_{PH}). Therefore, the formula for D_{ref} is

$$D_{ref} = D_p - [(D_p - D) - \Delta D_{PH}] \quad (7.1),$$

which can be simplified to

$$D_{ref} = D + \Delta D_{PH} \quad (7.2).$$

It is apparent that the required altitude reference (D_{ref}) is simply the sum of the helicopter's current inertial down position (D) and the required change in relative vertical position per time step (ΔD_{PH}).

The required velocity feed forward (\dot{D}_{ff}) is simply the sum of the platform's current inertial down velocity (\dot{D}_p) and the required relative descent velocity (\dot{D}_{PH}), or

$$\dot{D}_{ff} = \dot{D}_p + \dot{D}_{PH} \quad (7.3).$$

The proposed timed deck landing descent controller starts by calculating the unknowns in equations (7.2) and (7.3). The required relative descent velocity (\dot{D}_{PH}) is calculated first. This is done by dividing the current relative vertical position between the helicopter and the

platform by the amount of time left before landing. The current relative vertical position is calculated by finding the difference between the current inertial down positions of the platform (D_p) and the helicopter (D). The amount of time left before landing is the difference between the tracked landing opportunity time (t_l) and the current time (t). The resulting formula for \dot{D}_{PH} is:

$$\dot{D}_{PH} = \frac{D_p - D}{t_l - t} \quad (7.4).$$

If the magnitude of the required relative descent velocity (\dot{D}_{PH}) is found to be greater than the *relative velocity limit*, it is limited before being used further to ensure that the controller does not command excessively high relative descent rates. The *relative velocity limit* was chosen as 0.8 m/s in Section 4.4.

The proposed controller also calculates the required change in relative heave position per time step (ΔD_{PH}). This is done by multiplying the required relative descent velocity (\dot{D}_{PH}) by the system sample period (T) (0.02 s for the current system):

$$\Delta D_{PH} = \dot{D}_{PH} T \quad (7.5).$$

Having solved all the unknowns in equations (7.2) and (7.3), the controller sets the helicopter's heave controller's inertial down position reference and velocity feed forward to achieve a relative descent to the platform.

7.3 LANDING STATE MACHINE

A landing state machine (LSM) is required to execute the landing algorithm chosen in Section 2.6 in the correct sequence and to perform various landing criteria checks to ensure that landings can only be performed if conditions are safe. A proposed extension of the original system's LSM is described in this section. An overview of the proposed LSM is provided in Figure 7.2. Each state is detailed in this section. While a discrete *landing opportunity identification state* as defined in Section 2.6 is not defined in the proposed LSM, the landing criteria checks and the SMPLCA application evaluate possible landing opportunities on an ongoing basis.

7.3.1 START

The proposed LSM starts by commanding the waypoint navigation controller to navigate the helicopter to a position off the side of the platform, directly downwind from the landing point. An example of a position which meets these requirements is the starting position shown in Figure 7.3. This position is set manually by the ground station operator.

The current wind conditions are checked to ensure that they are suitable for landing. This check is performed manually by the ground station operator. As described in Section 4.2, the maximum allowable constant wind speed is 3 m/s. The direction of the wind blowing over the platform is uploaded to the helicopter's OBC by the ground station operator.

Upon completion of these tasks, the ground station operator gives the landing command to allow the LSM to proceed autonomously.

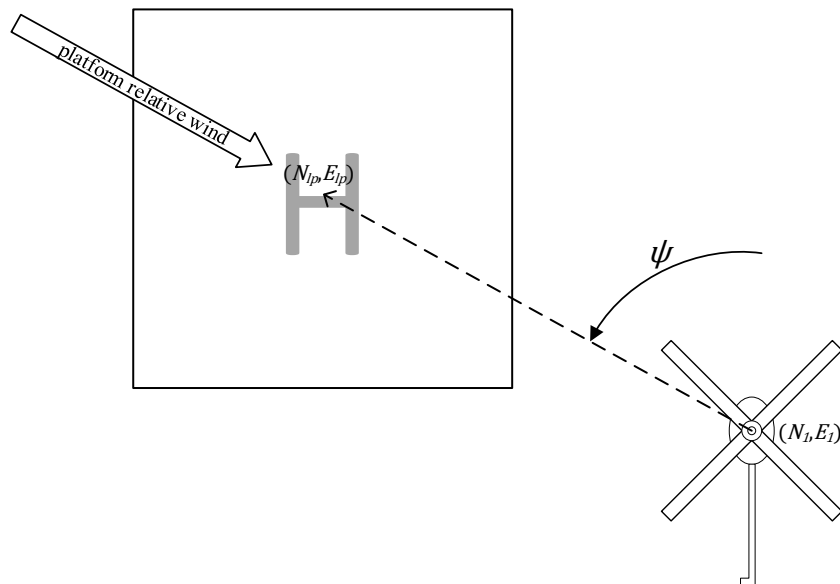


Figure 7.3 - Top view of platform and helicopter during *rotate* state

7.3.2 APPROACH

The approach is the route which must be followed from the starting waypoint to a stable hover position over the platform. The original system's LSM defines various states designed to execute an approach to a stationary landing point. The states are adapted for an approach to a moving platform.

7.3.2.1 ROTATE

The helicopter must rotate to a heading where it points in the direction of the landing point (which is also the windward direction) as shown in Figure 7.3. Given the inertial north and east positions of the starting point (N_1, E_1) and the landing point (N_{lp}, E_{lp}) , the original

system's LSM's *rotate* state is capable of performing the required manoeuvre. The workings of the state are discussed briefly.

First the required heading,

$$\psi = \tan^{-1} \frac{E_{lp} - E_1}{N_{lp} - N_1} \quad (7.6),$$

is calculated, where ψ is the required heading angle. All other symbols retain their previous definition.

In order to ensure that the shortest rotation is executed, the required rotation direction is determined. If the required heading angle is greater than the current heading estimate, the rotation must be in a clockwise direction. If the opposite is true, the rotation must be in an anti-clockwise direction.

The heading reference of the lower-level heading controller is ramped up to the required heading angle in the appropriate direction. The default absolute ramp rate is 7.5° per second.

In order to transition to the next state, the heading estimate must be within 4° of the final heading reference.

7.3.2.2 HEAVE

The helicopter must heave to its approach altitude. The platform's heave motion is observed throughout the previous states and its maximum inertial down position is recorded. The helicopter's approach altitude should be this maximum position plus an offset of at least two main rotor blade lengths. This offset is defined by the *initial ship deck heave offset* parameter. As this parameter defines the distance which must be covered by the helicopter upon descent in the time allowed before the tracked landing opportunity presents itself, it also defines the relative velocity for descent. For the 5 s prediction horizon provided by the prediction algorithm and the 0.8 m/s *relative velocity limit* the maximum allowable *initial ship deck heave offset* is 4 m. In order to allow some room for fine tuning of tracked landing opportunities, an *initial ship deck heave offset* of 3 m was chosen. Given the inertial down positions of the starting point and the approach altitude, the original system's LSM's *heave* state is capable of performing the required manoeuvre. The workings of the state are discussed briefly.

The first part of the heave manoeuvre is performed under heave velocity control. If the required approach altitude is below the current altitude, the heave velocity reference is ramped up to 0.5 m/s. On the other hand, if the required approach altitude is above the current

altitude, the heave velocity reference is ramped down to -0.5 m/s. The default absolute ramp rate is 0.25 m/s per second.

As soon as the altitude is reached where the heave position controller would command a velocity with a magnitude within ± 0.5 m/s, heave position control is enabled. The position reference provided to the controller is the required approach altitude.

In order to transition to the next state, the inertial down estimate of the helicopter must be within 0.2 m of the required approached altitude.

7.3.2.3 MOVE

The helicopter must move to the lateral and longitudinal position above the landing point as shown in Figure 7.4. Given the inertial north and east positions of the starting point (N_1, E_1) and the landing point (N_{lp}, E_{lp}) , the original system's LSM's *move* state is capable of performing the required manoeuvre. The workings of the state are briefly discussed.

The first part of the move manoeuvre is done under longitudinal velocity control. The longitudinal velocity reference is ramped up to 1 m/s. The default absolute ramp rate is 0.25 m/s per second. While under longitudinal velocity control, the cross-track error is regulated by the lateral controller.

As soon as the longitudinal position is reached where the inertial position controllers would command a velocity with a magnitude smaller than or equal to 0.25 m/s, inertial position control is enabled. The inertial north and east position references are then the inertial north and east positions of the landing point (N_{lp}, E_{lp}) .

In order to transition to the next state, the inertial north and east estimates must be within 0.5 m of the inertial north and east positions of the landing point (N_{lp}, E_{lp}) . The final inertial north and east position references remain set and the inertial north and east position are controlled for the rest of the landing procedure. If the position error magnitude exceeds the set maximum of 0.6 m detailed in Section 4.4, the LSM transitions to the *abort attempt* state described in Section 7.3.5.1.

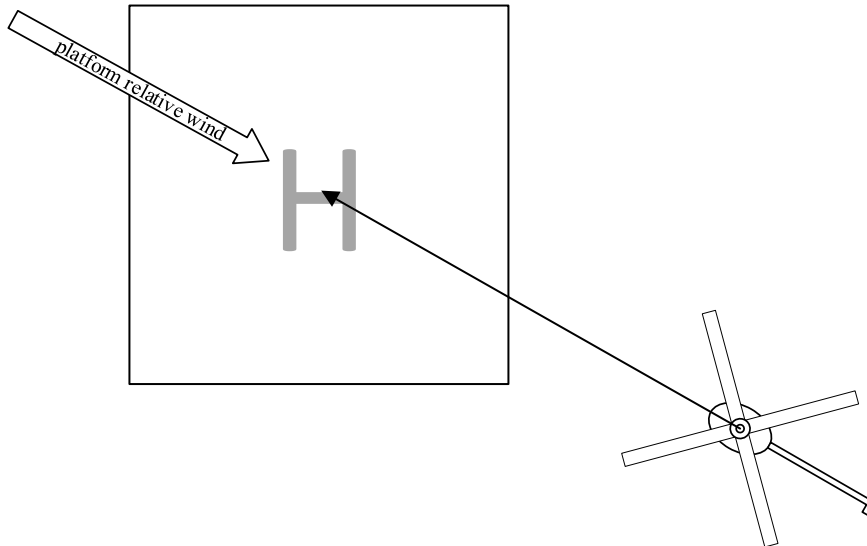


Figure 7.4 - Top view of platform and helicopter during *move* state

7.3.2.4 ALIGN

The helicopter must fine tune its windward heading. The wind direction is set as described in Section 7.3.1. This becomes the required heading angle. Given the required heading angle, the original system's LSM's *rotate* state is capable of performing the required manoeuvre as described in Section 7.3.2.1.

In order to transition to the next state, the heading estimate must be within 4° of the wind direction. The final heading reference remains set and the heading is controlled for the rest of the landing procedure.

7.3.2.5 WAIT

Upon completion of the approach stage, the helicopter waits for 5 s for its motion to settle. At the end of the *wait* state the position and heading shown in Figure 7.5 is desired.

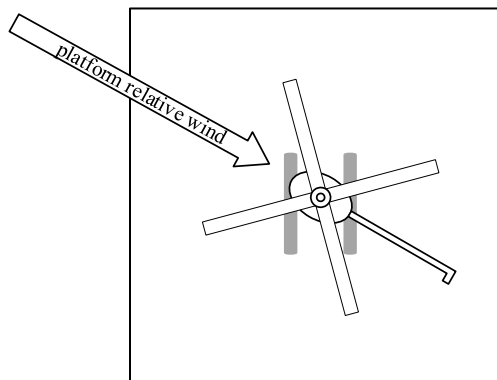


Figure 7.5 - Top view of platform and helicopter upon completion of the approach

7.3.3 DESCENT

The original system's LSM's *descent* state for landing on a stationary platform is left completely intact. Two new descent states are defined for descent to a platform.

7.3.3.1 TRACK DECK

The helicopter must track the heave motion of the ship with an offset. This offset is defined by the *initial ship deck heave offset* parameter which was chosen as 3 m in Section 7.3.2.2.

The heave controller with velocity and acceleration feed forward terms as proposed in Section 6.5.2 is used. In order to avoid sudden changes in motion, the inertial down position reference is gradually ramped up for 10 s from the hover altitude to the moving platform's inertial down position. Simultaneously, the velocity and acceleration feed forward values are ramped up from zero.

In order to transition to the next state the *track deck* state must have run for at least 30 s and, in order to prevent a sudden descent, a valid landing time must be set which is at least 3.5 s in the future. The 30 s period allows for platform tracking performance to be analysed before landing.

7.3.3.2 TRACK DECK DESCENT

The *track deck* state tracks the heave motion of the ship with a *fixed* offset. The *track deck descent* state uses the timed deck landing descent controller described in Section 7.2 to gradually reduce the offset between the helicopter and the ship to finally land at the targeted landing opportunity time.

As for the *track deck* state, the proposed heave controller with velocity and acceleration feed forward terms is used. The starting inertial down position reference is the platform's inertial down position plus the *initial ship deck heave offset*. The starting velocity and acceleration feed forward values are the platform's inertial down velocity and acceleration. At each time step the inertial down position reference and velocity feed forward required for a relative descent are updated by the timed deck landing descent controller. The acceleration feed forward remains equivalent to the platform's acceleration throughout.

The amount of time before the targeted landing opportunity is reached is constantly monitored throughout the descent. Depending on the amount of time before landing, different actions are performed:

- If there is more than 1 s to landing, a check is done to see if a landing time is still set. If a landing time is no longer set, the LSM transitions to the *abort attempt* state described in Section 7.3.5.1. If a landing time is set, it is compared to the previously set landing time. If the two landing times differ by more than 1 s (and therefore a completely different landing point is being targeted), the LSM transitions to the *abort attempt* state. Otherwise, the descent proceeds as before.
- If there is exactly 1 s to landing and the most recently received landing time is valid, all landing criteria are considered to be met and the system commits to the currently set landing time. Otherwise, the LSM transitions to the *abort attempt* state.
- If the landing time has passed but is less than 1 s in the past, heave position control as well as the velocity and acceleration feed forwards are turned off. This causes the helicopter to enter a coasting state where it continues moving in the direction which it last moved until it reaches a 0 m/s heave velocity.
- If a landing time is more than 1 s in the past the LSM transitions to the *abort attempt* state.

The relative vertical distance between the helicopter and the ship is also monitored constantly throughout the descent. Depending on the magnitude of the distance, various actions are performed:

- If the relative distance is smaller than 1 m, touchdown detection is enabled. This means that accelerometer measurements are monitored for spikes which could indicate that touchdown has occurred. Touchdown detection is disabled at higher altitudes to prevent false touchdown detections.
- If the relative distance is smaller than 0.6 m, lateral and longitudinal position control is disabled to prevent the helicopter from making sudden roll or pitch movements when close to the landing surface.

In order to transition to the *touchdown* state, a touchdown must be detected. A motion is considered a touchdown when a spike of magnitude 12.5 m/s^2 is observed on the z-axis accelerometer measurement.

7.3.4 TOUCHDOWN

During the *touchdown* state the various actuator commands are ramped to the required touchdown commands within 1 s. The touchdown commands are:

- Negative collective
- Zero lateral and longitudinal cyclic
- Zero tail collective
- Zero throttle

Thereafter the landing state machine ends.

7.3.5 ABORTS

For practical landing purposes where many landing attempts may be required, two abort types are defined: *abort attempt* which simply goes to a safe, previous state and *full abort* which ends the state machine.

7.3.5.1 ABORT ATTEMPT

During the *abort attempt* state, the heave velocity and acceleration feed forwards are disabled and the helicopter heaves to the approach altitude: the sum of the platform's maximum observed inertial down position and the *initial ship deck heave offset* parameter. Thereafter, the landing state machine returns to the *wait* state described in Section 7.3.2.5.

7.3.5.2 FULL ABORT

During the *full abort* state the heave velocity and acceleration feed forwards are disabled and the helicopter heaves to a safe inertial down position of -10 m while maintaining its current inertial north and east positions. Thereafter, the landing state machine ends. If the *abort mode* parameter is set to *navigation abort*, the waypoint navigation state machine is started. Currently this state can only be entered by commanding an abort from the ground station.

7.3.6 VIRTUAL LANDING MODE

The virtual landing mode of the landing state machine is a mode in which most of the functionality of the landing state machine can be tested without performing physical touchdown. This is achieved by offsetting the platform's heave position state by a constant value and defining a new way of detecting a completed landing. The constant offset is defined by the *descent altitude* parameter, chosen as 7 m in order to allow a large margin for error for initial tests. Virtual landings are considered complete when the landing time is more than 1 s in the past. Therefore, in virtual landing mode the *abort attempt* state is not entered when the

landing time is more than 1 s in the past. Instead a new *virtual landing* state is entered where the helicopter hovers until further commands are received from the ground.

7.4 IMPLEMENTATION

The proposed timed deck landing descent controller and the LSM extensions were implemented in C for the helicopter's dsPIC-based OBC and added to the original high-level controllers.

7.5 SUMMARY

A timed deck landing descent controller was proposed for relative landing descents. Extensions to the original system's LSM were also proposed for moving platform landings. The proposed LSM commands the waypoint navigation controller to perform the approach and, when all criteria have been met and a landing opportunity has presented itself it, commands the timed deck landing descent controller to descend. Finally, it commands suitable post touchdown actions. The high-level controllers were implemented in C for execution on the helicopter's dsPIC-based OBC. Practical testing of the high-level controllers is discussed in Chapter 10.

8. SYSTEM INTEGRATION

8.1 INTRODUCTION

The systems required to implement the landing algorithm designed in Section 2.6 were developed in chapters 3 to 7. Integration of the systems is required in order for them to achieve their combined goal.

The following systems are required to be integrated:

- 3-DOF platform ground station software controlling the 3-DOF platform system
- SMPLCA application implementing the systems described in chapters 3 and 4
- Helicopter's onboard computer running the software implementing the estimator and controllers described in chapters 5, 6 and 7

The following outcomes are required from the integration process:

- A common time reference must be available to all systems for system synchronisation purposes.
- The platform motion states must be available to the SMPLCA application and the helicopter's onboard computer.
- The landing opportunity times output by the SMPLCA application must be available to the helicopter's onboard computer.
- Basic status information about the 3-DOF platform and the SMPLCA application must be made available to the helicopter's ground station to allow it to determine if the combined system is in a nominal state and, if not, command the helicopter to enter a safe state.

An overview of the integrated system is provided in Figure 8.1. The integration of two sets of systems is detailed in this chapter:

- 3-DOF platform ground station software with the SMPLCA application
- 3-DOF platform ground station software and SMPLCA application with the helicopter's onboard computer

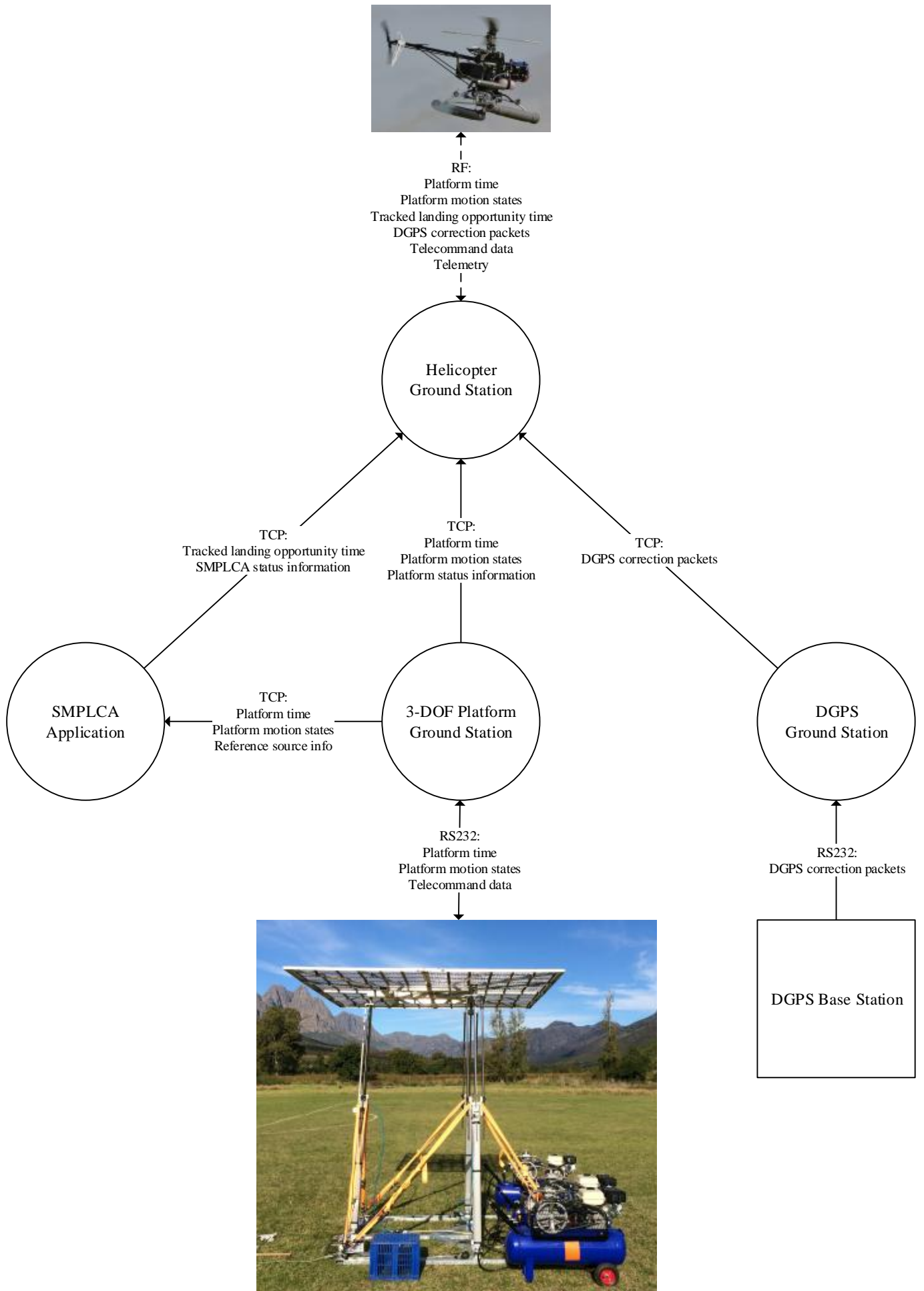


Figure 8.1 - Integrated system

8.2 3-DOF PLATFORM - SMPLCA

The SMPLCA application requires the platform's time, roll angle, roll rate, pitch angle, pitch rate, inertial down position and heave velocity. On the 3-DOF platform ground station these variables are each 32 bits in size. Therefore, one sample set is 224 bits in size. In order to obtain an accurate representation of the platform's motion the SMPLCA application needs to receive this data at a frequency which meets the Nyquist sampling criterion. In other words, the sampling frequency must be at least twice the maximum frequency contained in the signal [47]. In the ship motion dataset available to the ESL the highest frequency of ship motion is 0.22 Hz. Therefore, an interface with a data transfer rate of at least 99 bits per second is required.

8.2.1 INTERFACING

The 3-DOF platform ground station software is equipped with a TCP server and UDP interface. The SMPLCA application is equipped with a TCP client which is capable of connecting to the 3-DOF platform ground station's TCP server. TCP interfaces are typically connected on a local computer or via an Ethernet network, many times faster than the required data transfer rate. TCP's built-in error checking is advantageous for the current application, but the protocol may be inappropriate due to the delays which it introduces [67]. The interaction between Nagle's algorithm and delayed packet receipt acknowledgements is one source of such delays.

8.2.1.1 NAGLE'S ALGORITHM AND DELAYED ACKNOWLEDGEMENT INTERACTION PROBLEM

Nagle's algorithm reduces the amount of data sent via TCP interfaces by buffering data which needs to be sent and sending it in larger batches (the lower the number of data batches, the lower the number of headers which need to be sent) [68]. The data is sent when the buffer is filled with a certain amount of data or when an acknowledgement (ACK) is received of the previously sent data.

Packet receipt ACKs form part of TCP. The receiver of data must send an ACK of receipt of the data to the sender. Instead of acknowledging the receipt of every piece of data immediately, ACKs are sent upon receipt of every second packet, when the delayed ACK timer expires or when the receiver has to send data [69].

The interaction between Nagle's algorithm and delayed ACKs can cause delays, in particular if one node is sending small data packets to another node at a high frequency without

expecting a response. The sender sends its first packet and waits for an ACK before sending another packet. The receiver receives the packet but does not send an ACK until it receives another packet. A deadlock is therefore reached which must be resolved by the delayed ACK timer. This introduces delays, typically 200 ms in Windows [69]. This is unacceptable for applications where data must be sent with a minimum delay and where data is sent at a rate of higher than approximately 4 Hz (the network round trip time adds additional delays making 5 Hz problematic).

8.2.1.2 NAGLE/DELAYED ACK WORKAROUND

One way in which the problem of the interaction between Nagle's algorithm and delayed ACKs can be worked around is by manually responding to every received packet. The manual response then includes the ACK for the received packet. The above mentioned case where one node is sending small data packets to another node at a high frequency is reconsidered with the workaround in place: The sender sends its first packet and waits for an ACK before sending another packet. The receiver receives the packet and manually sends a response, thereby triggering ACK sending. No deadlock problem occurs with this configuration.

The largest delays introduced into the current system were due to the interaction between Nagle's algorithm and delayed packet receipt ACKs. With the proposed workaround in place, TCP provides satisfactory performance for communications between the 3-DOF ground station software and the SMPLCA application.

8.2.2 DATA EXCHANGE

The 3-DOF platform ground station software makes platform status, reference source information, current time and all motion states available at 5 Hz via its TCP server. Instead of the SMPLCA application's TCP client simply extracting the platform's current time and motion states from the data received, it also extracts the reference source information. With this information the SMPLCA application can determine which data file the 3-DOF platform is currently using and which sample is currently being read from the file. Platform motion data can therefore be extracted by the SMPLCA application from a local copy of the data file. From the data file, future motion data can be compared with prediction algorithm outputs to check the accuracy of prediction algorithms under test circumstances. Additionally, the future data can be used by the SMPLCA application to bypass the prediction algorithm outputs with the future states for testing purposes. While this is more data and a higher sampling rate than the minimum requirement stated above, the required data transfer rate is far below the maximum transfer rate of the chosen interface. Data exchange was therefore implemented as described.

8.2.3 FAIL SAFE

The SMPLCA application is equipped with a high performance timer which measures the platform data sampling period. For the platform data sampling frequency of 5 Hz, a sampling period of 200 ms is expected. Due to timing inaccuracies inherent to Windows [70] and possible network delays the sampling period measured by the SMPLCA can vary slightly from 200 ms under nominal conditions. Large variations in the sampling period indicate off-nominal conditions of either the 3-DOF platform or the 3-DOF – SMPLCA interface. Accordingly, a platform data sampling period check was implemented on the SMPLCA application. If the sampling period is more than 50 ms more or less than the nominal sampling period of 200 ms, the SMPLCA application invalidates its currently tracked landing opportunity.

8.3 3-DOF PLATFORM & SMPLCA – HELICOPTER OBC

The helicopter's OBC requires the platform's time, inertial north, east and down positions, heave velocity, heave acceleration, heave jerk, roll angle, pitch angle and heading angle from the 3-DOF platform. As the 3-DOF platform does not translate or yaw, the inertial north and east positions and heading angle can be set once off. The helicopter's OBC requires a stream of the platform's time, inertial down position, heave velocity, heave acceleration, heave jerk, roll angle and pitch angle. On the 3-DOF platform ground station these variables are each 32 bits in size. Therefore each sample of the data which must be streamed is 224 bits in size. At the proposed sampling rate of 5 Hz, an interface with a data transfer rate of at least 1120 bits per second is required.

The helicopter's OBC requires the tracked landing opportunity time from the SMPLCA application as soon as it is available. This requires a 5 Hz stream. On the SMPLCA application the landing opportunity time variable is 32 bits in size. An interface with a data transfer rate of 160 bits per second is therefore required for the stream.

8.3.1 INTERFACING

The 3-DOF platform ground station software is equipped with a TCP server and a UDP interface. The SMPLCA application is equipped with a TCP server. The helicopter's ground station software is equipped with TCP clients which are capable of connecting with the TCP servers provided by the 3-DOF platform ground station software and the SMPLCA application. The helicopter's ground station software is connected to the helicopter's OBC via an RF link. Therefore, if the TCP and RF interfaces are fast enough, the 3-DOF platform ground station software and SMPLCA application could be interfaced with the helicopter's OBC via its ground station software.

TCP interfaces can operate over high-speed connections on a local computer or across an Ethernet network, sufficiently meeting the data transfer demands. With the workaround mentioned in Section 8.2.1.2, the most significant delays experienced with TCP on the current systems are accounted for. The original RF link is a half-duplex, 9600 bits per second link built up by two MaxStream 2.4 GHz OEM RF modules. Previous projects with the helicopter system noted that the original RF link was already almost saturated with telemetry and command data [4]. The situation worsened with the introduction of the helicopter's DGPS system because of the requirement to send DGPS correction packets to the helicopter's GPS module via the RF link. It is unrealistic to try to send an additional 1280 bps over the original RF link without reducing the amount of other data sent over it and without changing its configuration.

8.3.1.1 RF LINK DATA TRANSFER DEMAND REDUCTION

A great reduction in the data transfer demand was achieved at the cost of some loss of platform motion data accuracy. The 32 bit platform motion states are converted to and sent as 16 bit representations. As centimetre accuracy is maintained, the loss of accuracy is deemed acceptable for the required application. As timing accuracy must be maintained, time packets remain 32 bits in size.

Telemetry transmission from the helicopter to the ground was optimised. Instead of constantly sending all telemetry values, a means of requesting only the telemetry required for the current ground station view was implemented. The OBC is notified which ground station tab is currently selected (2 bytes) and only sends the telemetry required for that tab as well as critical status data which must be monitored at all times. Additionally, the rate at which high priority telemetry is sent to the ground station was reduced from 3.3 Hz to 2 Hz.

8.3.1.2 RF LINK CONFIGURATION MODIFICATION

The original RF link configuration provides a best-effort connection between the helicopter's OBC and ground station: data which is sent is not guaranteed to be delivered; data which is delivered is not delivered in a fixed amount of time. This is mainly because transmitting and receiving across the half-duplex link is not timed. Instead, data is transmitted at random and collision detection and resolution is dealt with by the RF module's firmware. With the original configuration, when data is successfully received by a module it transmits an acknowledge packet. If the source module does not receive the acknowledge packet, it assumes that a collision has occurred and waits 0 ms, 38 ms or 76 ms before trying to transmit the data again [71]. This repeats up to 4 times for repeated collisions. Additionally, each time an RF module changes from receive mode to transmit mode the RF channel must be

reinitialised, a process which takes 35 ms [71]. As the number of changes between receive and transmit modes is not directly controlled, many changes can occur. The result is a very inefficient RF link.

The decision was made to take control of transmission and receipt timing to reduce the required number of changes from receive mode to transmit mode and to reduce the number of collisions which occur. The reduction in collisions reduced the need for the RF module's collision detection and resolution. Deactivating this disabled the transmission of data receipt acknowledge packets, further reducing the required number of changes from receive mode to transmit mode. The above mentioned random delays and resends were also disabled. The efficiency of the link was therefore improved. Data integrity checking is still performed by the ground station software and OBC. Finally, to better accommodate the higher demands on the RF link, the speed of the RF link was changed from 9600 bps to 19200 bps.

As the timely transmission of platform motion data packets is of utmost importance, the decision was made to synchronise RF transmission and receipt with the receipt of platform motion data from the 3-DOF platform. Therefore, as the helicopter's ground station software receives platform motion data from the 3-DOF platform at 5 Hz, RF transmission from the ground occurs at 5 Hz. After the start of an RF transmission from the ground, all RF communications must be completed before the next start of a ground RF transmission. Effectively, 200 ms RF communications slots were defined.

It is necessary to determine the transmission limits of the 200 ms RF communications slots. MaxStream provides equation (8.1) for the calculation of transmission latency (T_{lat} in milliseconds) for data packets of size B (in bytes) [71]. Transmission latency is the time it takes from the start of data transmission on one RF module until the start of data receipt on another RF module (including channel initialisation time):

$$T_{lat} = \begin{cases} 41.6 + 0.4B, & B < 64 \\ 66.8, & B \geq 64 \end{cases} \quad (8.1).$$

The following equation can be used to calculate the transmission time (T_{trans} in milliseconds) of a packet of a given size (B in bytes) across a 19200 bps data link:

$$T_{trans} = \frac{1000B}{\left(\frac{19200}{8}\right)} \quad (8.2).$$

The total time required from the start of data transmission on one module until the end of data receipt on another module is the sum of T_{lat} and T_{trans} .

If only one module transmits for the entire 200 ms communication slot, the maximum amount of data it can transmit (so that receipt on the other module ends at the end of the 200 ms communications slot) can be determined by equations (8.1) and (8.2). After subtracting the 66.8 ms of transmission latency, 133.2 ms remain to transfer data. Substituting into equation (8.2) and rearranging we find that the maximum amount of data which can be sent in one RF slot is 319.6 bytes or 2557 bits.

If one module transmits for half of the communications slot and the other module transmits for the other half of the slot, the amount of data which can be transferred by each module is not simply halved because two periods of transmission latency are experienced. If each module is given 100 ms of the communications slot, equations (8.1) and (8.2) can solve for the maximum data which can be transferred. After subtracting the 66.8 ms of transmission latency, 33.2 ms remain to transfer data. Substituting into equation (8.2) and rearranging we find that the maximum amount of data which can be sent by each RF module is 79.6 bytes or 637 bits.

8.3.2 DATA EXCHANGE

The amount of data which must be exchanged was modified to lower the demand on the limiting communications interface, the RF link as described in Section 8.3.1.1. Two additional pieces of data must be sent across the RF link as described next.

It is clear from equations (8.1) and (8.2) that the 16 bytes of platform data (+6 byte header) are delayed by between 50.4 ms and 59.6 ms. The effect of this delay is assumed to be negligible but, to allow for compensation for the delay if it is later desired, an approximation of the delay is sent up in an 8 bit (1 byte) representation together with the platform data. The delay is measured by measuring and halving the *ping* or round-trip time of the current RF link.

For the GPS module on the helicopter to work in its most accurate differential GPS mode it requires that two sets of correction packets be sent to it from the GPS base station, defined by the manufacturer (NovAtel) as RTCAOBS2 and RTCAREF [55]. RTCAOBS2 is dependent on the number of satellites currently visible by the GPS base station, but has an absolute maximum size of 255 bytes. RTCAREF has a constant size of 24 bytes. Each of these messages also has a 28 bytes header and 4 bytes footer (CRC data). RTCAOBS2 must be sent at between 0.5 Hz and 1 Hz. RTCAREF must be sent at between 0.1 Hz and 1 Hz. In the worst case both RTCAOBS2 and RTCAREF have to be sent at the same time. The sum of the size of the headers, messages and footers to be sent is 343 bytes.

In summary, the total data which needs to be sent across the RF link is:

- Up to 343 bytes of DGPS correction packets at 1 Hz
- 16 bytes of platform motion data + 1 byte of RF delay data at 5 Hz
- 4 bytes of landing opportunity data at 5 Hz
- 2 bytes of ground station tab selection info as a telemetry request at 2 Hz
- High priority telemetry at 2 Hz (up to 81 bytes split across three packets)
- Lower priority telemetry at 1 Hz (up to 13 bytes)
- Settings and confirmations (asynchronous)

Every data packet includes a header, CRC data and packet length data adding 6 bytes of data.

The lowest frequency at which data must be sent is 1 Hz. Therefore, a 1 Hz RF transmissions cycle was defined during which all required communications occur each second. Accordingly, each RF transmissions cycle comprises of five RF transmission slots. RF transmissions are split across the five slots to meet the data transmission requirements while keeping within the 200 ms limit imposed by the RF slots.

The decision was made to split the DGPS correction packets into three parts and send the parts together with platform motion data in three RF slots per second in which only the ground station transmits data. The two remaining RF slots per second are used by the ground station to send platform motion data to the helicopter and by the helicopter to send telemetry data to the ground station. Using equations (8.1) and (8.2) and the worst case scenario transmission data sizes, the timing diagram of a transmission cycle is drawn up as shown in Figure 8.2.

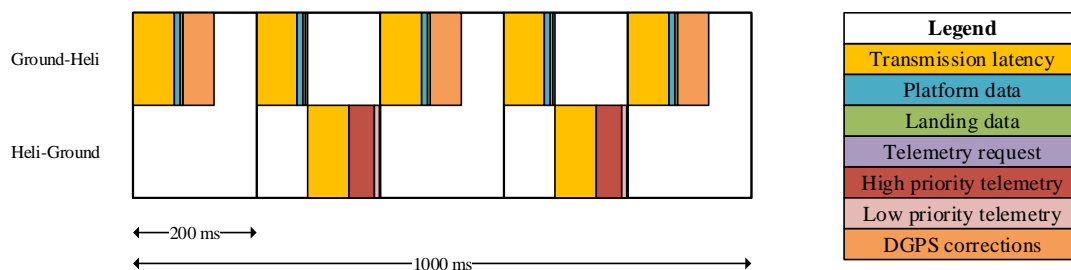


Figure 8.2 – RF transmission cycle

A magnified view of the individual RF transmission slots which mainly contain DGPS correction data and telemetry data are shown in Figure 8.3 and Figure 8.4 respectively.

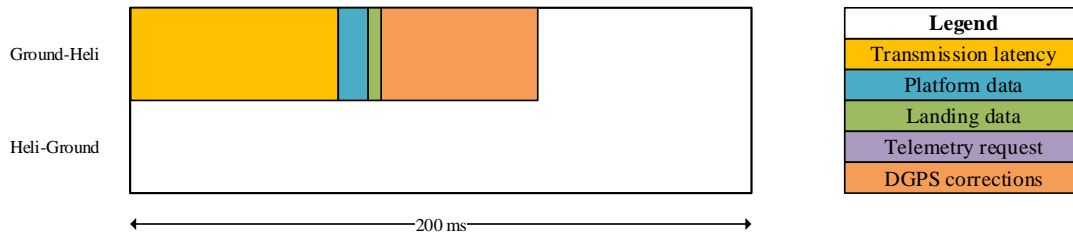


Figure 8.3 - RF transmission slot mainly containing DGPS correction data

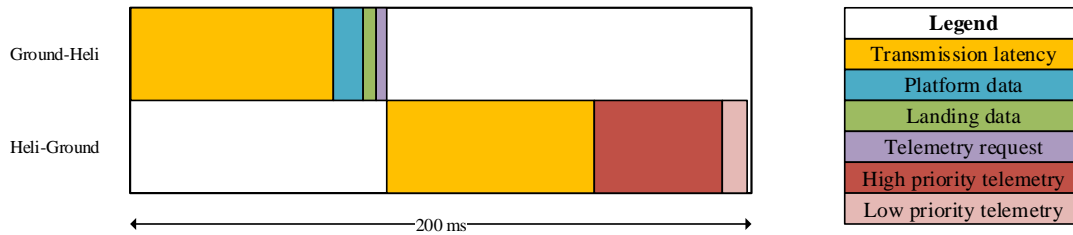


Figure 8.4 – RF transmission slot mainly containing telemetry data

Data which can be sent asynchronously is queued and sent in the time left over in each slot.

From the timing diagrams it is clear that none of the communications slots are saturated and therefore, in theory, the communications setup should work.

8.3.3 FAIL SAFE

The platform motion data and landing opportunity time data update periods are measured on the helicopter’s OBC. Large variations in the update periods indicate off-nominal conditions in some of the upstream systems (SMPLCA application, 3-DOF platform, TCP interface, helicopter ground station or RF link). Accordingly, if an update period is measured to be greater than its set limit while executing the landing state machine described in Section 7.3, an appropriate abort is commanded.

As platform motion states are estimated between received platform motion data updates, the system is more robust to platform data update losses. Conservatively, an abort limit for the platform motion data update period of 500 ms was chosen. In other words, an abort is executed if any more than one platform motion data update is lost. As the landing state machine described in Section 7.3 cannot function without platform motion data, a *full abort*, described in Section 7.3.5.2, is commanded if the platform motion data update period limit is exceeded.

As landing opportunity time data updates remain valid for about 1 s, a more relaxed abort limit for the landing time data update period of 900 ms was chosen. As most of the landing state machine described in Section 7.3 can function without landing time data, an *abort*

attempt, described in Section 7.3.5.1, is commanded if the landing opportunity time data update period limit is exceeded.

As RF communications are synchronised with the receipt of platform motion data from the 3-DOF platform, RF communications come to a halt if the 3-DOF platform is disconnected from the helicopter's ground station software or if it is not sending platform motion data. This is unacceptable as commands and DGPS correction packets can then no longer be sent to the helicopter and helicopter telemetry can no longer be received. A backup RF communications timer was implemented to take over control of RF communications timing if platform motion data is no longer received. A high performance timer was implemented on the helicopter's ground station software to monitor the platform data sampling period and to detect when it is appropriate to use the backup RF communications timer. The sampling period limit of 1 s was chosen as this guarantees that no false detections can occur.

8.4 SUMMARY

In order to execute their ultimate goal, the various systems developed in the previous chapters had to be integrated. The various systems were integrated by TCP and a modified RF link. Figure 8.1 provides a good overview of the resulting combined system. Practical testing of the modified RF link is presented in Section 9.3. Overall system integration is tested through the tests described in Chapter 10.

9. PRACTICAL TESTING: LOW-LEVEL SYSTEMS

9.1 INTRODUCTION

The practical estimator tests referred to in Chapter 5 and practical low-level controller tests referred to in Chapter 6 are detailed in this chapter. For all tests take-offs and landings were performed manually by a safety pilot.

9.2 INITIAL HEAVE CONTROLLER TUNING

The heave controller was tuned in an attempt to meet the requirement specified in Section 6.1:

- Track the heave motion of a platform which is simulating ship flight deck motion.

For the initial controller tuning flight tests the following system configuration was used:

- Ground station and OBC software used by De Jager and Basson (see Section 1.1) with minor changes for maximum stability
- Single point GPS instead of differential GPS to reduce the demand on the helicopter's RF link

The controller gains used by De Jager and Basson were used as a starting point. Position step manoeuvres were performed and responses were analysed visually in order to determine appropriate gain adjustments. Due to the sensitive nature of practical gain adjustments the project supervisor, Prof. Thomas Jones, made gain adjustment calls for this initial tuning test. Gain adjustments started at the innermost loops and proceeded to the outer loops. Gain adjustments continued until any of the following occurred:

- Undesired behaviour was observed (e.g. instabilities)
- Control limits were hit
- Gain adjustments were 100% more than their original values

The responses were analysed in detail post flight.

9.2.1 FLIGHT 1 (2013-02-22)

9.2.1.1 AIM

The purpose of tuning the heave controller was to improve its bandwidth for platform tracking purposes.

9.2.1.2 SYSTEM

The original helicopter system's heave controller was used for this flight test as described in Section 6.5.1. For convenience, the block diagram of the original combined heave controller during approximately level flight is presented again in Figure 9.1.

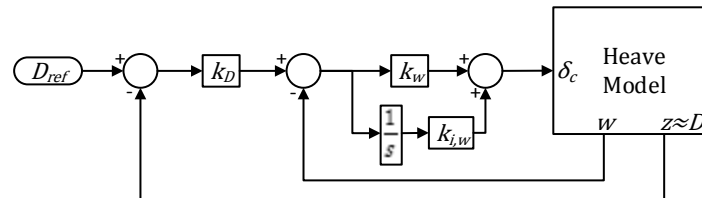


Figure 9.1 - Block diagram of original combined heave controller

9.2.1.3 PROCEDURE

Heave controller tuning started with the original control gains referred to as $G1$ in Table 9.1. From hover flight, position step commands were given: -2 m and $+2$ m in the inertial down direction. The response was observed from the ground. As none of the gain adjustment continuation criteria were violated, gain adjustments were made.

The heave velocity loop is the innermost loop and was therefore tuned first. The velocity control gains were increased by 20% ($G1A$ in Table 9.1). The same position step commands were given without violating the gain adjustment continuation criteria. This process was repeated for velocity control gains at 40% ($G1B$) and 60% ($G1C$) greater than their original values.

As the controller was designed by a successive loop closure approach (discussed in Section 6.1), the outer loop control gains could be increased by a smaller or equal percentage as the inner loop control gains while maintaining sufficient timescale separation. Accordingly, the control gain of the inertial down position loop was increased by 60%. In addition, the control gains of the heave velocity loop were increased to values 80% greater than their original values. The new set of gains is referred to as $G2$. When step commands were given with these gains a control limit was reached. The gain adjustment continuation criteria were therefore violated and further control gain adjustments were halted.

	k_D	k_w	$k_{i,w}$
G1	0.5	-0.020	-0.0080
G1A		-0.024	-0.0096
G1B		-0.028	-0.0112
G1C		-0.032	-0.0128
G2	0.8	-0.036	-0.0144

Table 9.1 - Heave control gains for tuning flight

9.2.1.4 RESULTS

The collective command responses to the positive position steps performed with the $G1$, $G1C$ and $G2$ gains are provided in Figure 9.2. The dotted red line at 0.17 rad is the command limit. None of the commands exceeded the limit and no undesired oscillatory commands were given.

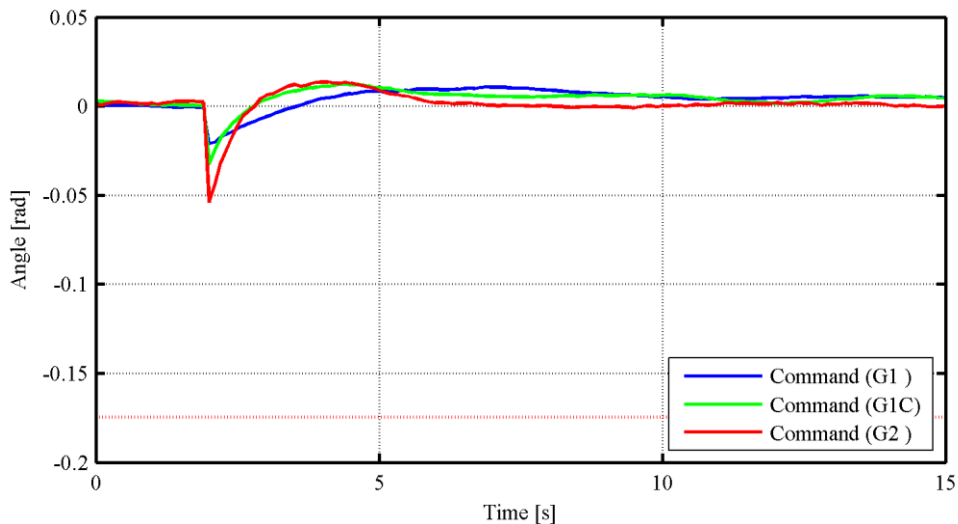


Figure 9.2 - Collective command responses

The heave velocity responses to the positive position steps performed with the $G1$, $G1C$ and $G2$ gains are provided in Figure 9.3. The velocity response of the step performed with $G1C$ gains was faster than the response with $G1$ gains. When compared with the response with $G1C$ gains, the slightly higher velocity control gains of $G2$ did not manifest in a much faster velocity response, but the response is acceptable as no undesired oscillations were present. The dotted red line at -1.5 m/s is the velocity reference limit. The velocity reference limit was

enforced very briefly during the step performed with $G2$ gains. This explains the gain adjustment criteria violation.

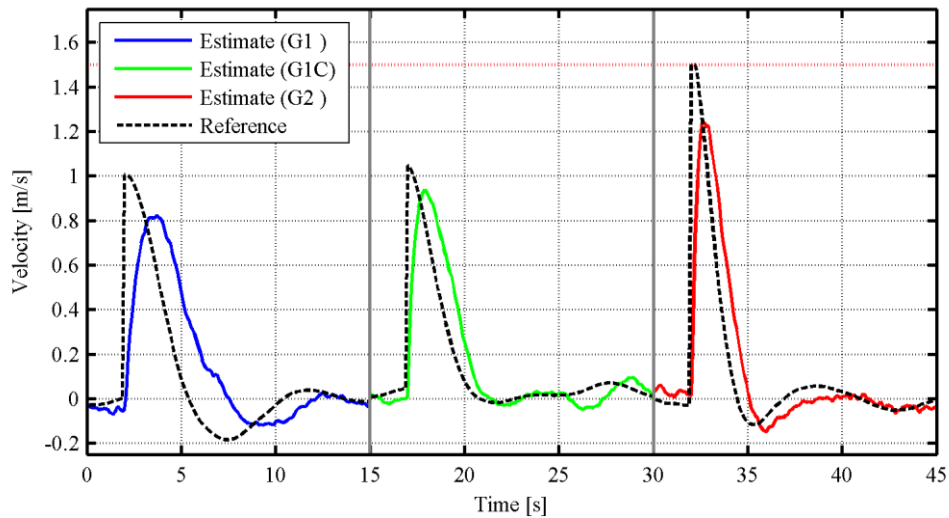


Figure 9.3 - Heave velocity responses

The inertial down position responses to the positive position steps performed with the $G1$, $G1C$ and $G2$ gains are provided in Figure 9.4. An improvement in response speed and lower overshoot was observed with the $G1C$ gains when compared with the $G1$ gains. The response with the $G2$ gains showed a marked improvement in response speed. No undesired motion such as oscillations was present.

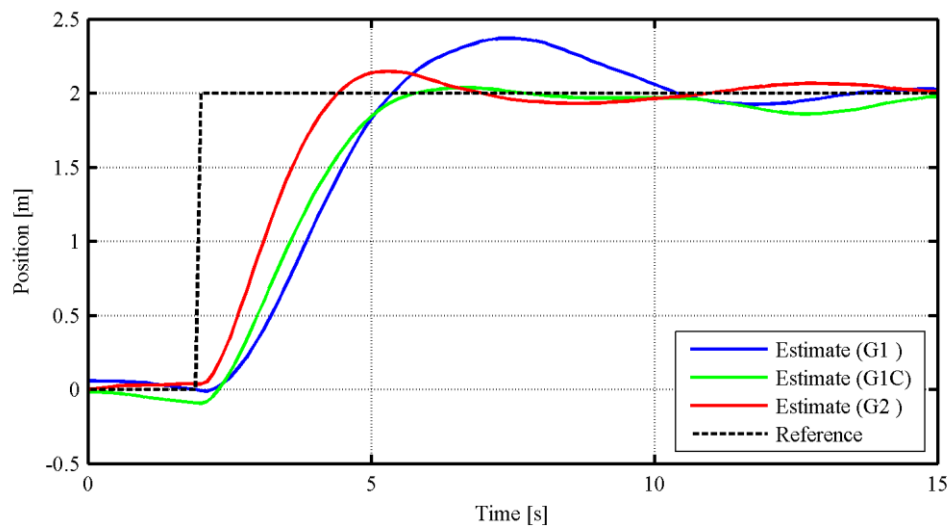


Figure 9.4 – Inertial down position responses

The collective command responses, heave velocity responses and inertial down position responses to the negative position steps performed are provided in Appendix D.1.1.

In order to approximate the bandwidth of the inertial down controller in practice its step response can be approximated as the response of a second order system. The bandwidth (ω_b) in radians per second of a second order system is

$$\omega_b = \omega_n \sqrt{[(1 - 2\zeta^2) + \sqrt{4\zeta^4 - 4\zeta^2 + 2}]} \quad (9.1),$$

where ω_n is the natural frequency in radians per second and ζ is the damping ratio [47]. The damping ratio (ζ) and natural frequency (ω_n) can be found from a step response using the following equations [47]:

$$\zeta = \frac{\sqrt{[\ln(M_p)]^2}}{\sqrt{[\ln(M_p)]^2 + \pi^2}} \quad (9.2),$$

$$\omega_n = \frac{\pi}{t_p \sqrt{1 - \zeta^2}} \quad (9.3).$$

In equation (9.2) M_p is the peak overshoot and in equation (9.3) t_p is the peak time. The values of M_p and t_p can be read from the step responses in Figure 9.4.

For the system with $G1$ gains M_p is 0.185 and t_p is 5.4 s. Substituting M_p into equation (9.2) gives ζ of 0.47. Substituting ζ and t_p into equation (9.3) gives ω_n of 0.66 rad/s. Substituting ζ and ω_n into equation (9.1) gives ω_b , the bandwidth of the system, of 0.86 rad/s or 0.14 Hz. The value is 0.06 Hz higher than the bandwidth of the theoretical system calculated in Section 6.5.1.2. This discrepancy is likely due to errors in both the heave model and the approximation that the system is second order.

For the system with $G2$ gains M_p is 0.073 and t_p is 3.3 s. Following the same procedure as above, the bandwidth of the system is determined to be 1.36 rad/s or 0.22 Hz. This is 0.09 Hz higher than the theoretical system calculated in Section 6.5.1.2. This discrepancy is also likely due to heave model and second order system approximation errors.

9.2.1.5 CONCLUSION

While the bandwidth of the heave controller with $G2$ gains is approximately 0.22 Hz, the highest frequency of ship motion data which is required to be followed, this implies that heave motion tracking at 0.22 Hz will be attenuated by -3 dB. For a 1 m peak-to-peak heave motion this implies a tracking error of 0.293 m which is quite large for the task at hand. The bandwidth of the controller with $G2$ gains is therefore still not sufficient for platform tracking purposes. The proposed controller described in Section 6.5.2 was implemented, tuned and

tested as described in sections 9.6 and 9.7 in order to attempt to meet the controller bandwidth requirement.

9.3 BASIC SYSTEM VERIFICATION

After the initial controller tuning tests described in Section 9.2, a number of changes were made to the helicopter system in order to achieve the goals set out for this project. The changes implemented include:

- SMPLCA application integration
- New RF link configuration
- Platform heave motion estimator described in Section 5.4
- Feed forward heave controller described in Section 6.5.2
- Differential GPS functionality (reactivated)

While much care was taken to ensure that the helicopter's original systems were not affected detrimentally while implementing the various changes, the ultimate test to determine if original functionality was retained is a practical test. The primary goal of the practical tests described in this section was to test if the system's original functionality was retained. Simultaneously the performance of the new RF link configuration, basic SMPLCA application integration and platform heave estimator was tested.

9.3.1 HIL SIMULATION

9.3.1.1 AIM

The purpose of this simulation was to test basic automatic control of the helicopter system under HIL simulation conditions.

9.3.1.2 SYSTEM

The new helicopter system as described in the introduction to this section was used with the $G2$ gains from Section 9.2.

9.3.1.3 PROCEDURE

A number of lateral, longitudinal and heave position steps and heading angle steps were performed and the responses were analysed.

9.3.1.4 RESULTS

The various step manoeuvres were performed with no undesired motion. An aerial view of a longitudinal position step is given in Figure 9.5 for comparison with subsequent sections.

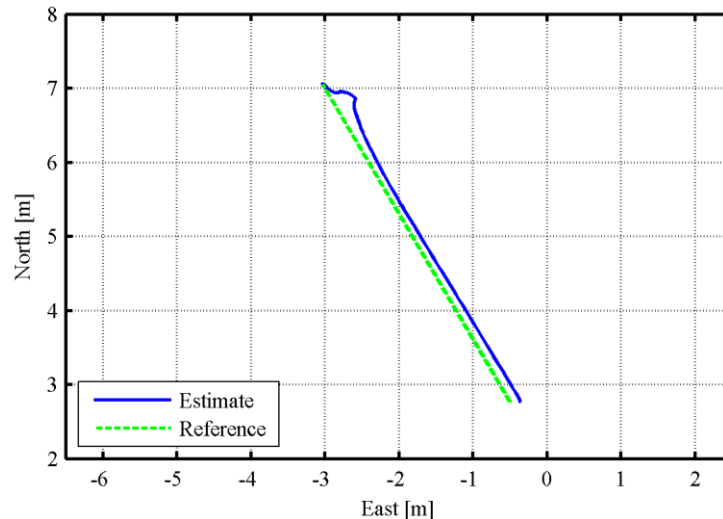


Figure 9.5 - Aerial plan (initial HIL simulation)

9.3.1.5 CONCLUSION

In a HIL simulation the new helicopter system can control itself automatically under near-hover flight conditions.

9.3.2 FLIGHT 1 (2013-10-03)

9.3.2.1 AIM

The purpose of the first basic system verification flight was to test the new RF link configuration, basic SMPLCA application integration, platform heave estimation and basic automatic control under real flight conditions.

9.3.2.2 SYSTEM

The new helicopter system, as described in the introduction to this section, was used with the G2 controller gains from Section 9.2. The SMPLCA application was connected to the helicopter's ground station via its TCP interface. The helicopter's ground station was connected to the helicopter via the newly configured RF link.

9.3.2.3 PROCEDURE

Sinusoidal platform motion data with a frequency of 0.20 Hz was sent from the SMPLCA application to the helicopter's ground station which sent it further to the helicopter's platform estimator via the RF link.

The latency associated with RF transmissions was measured by sending a *ping* from the ground station to the helicopter with every transmission. Half the time required to receive a response is approximately the latency associated with RF transmissions.

In order to detect packet losses, the time elapsed between the receipt of valid platform motion data packets was measured. As platform motion data was sent from the ground station to the helicopter at 5 Hz, the nominal platform data sample period is 200 ms. A sample period greater than or equal to approximately twice the nominal sample period indicates packet losses.

Finally, various position and angle step manoeuvres were performed and the responses analysed to test the helicopter's basic automatic control.

9.3.2.4 RESULTS

A graph of RF transmission latency estimates for a 50 s portion of the flight test is shown in Figure 9.6. The dotted red line is the mean of 89 ms.

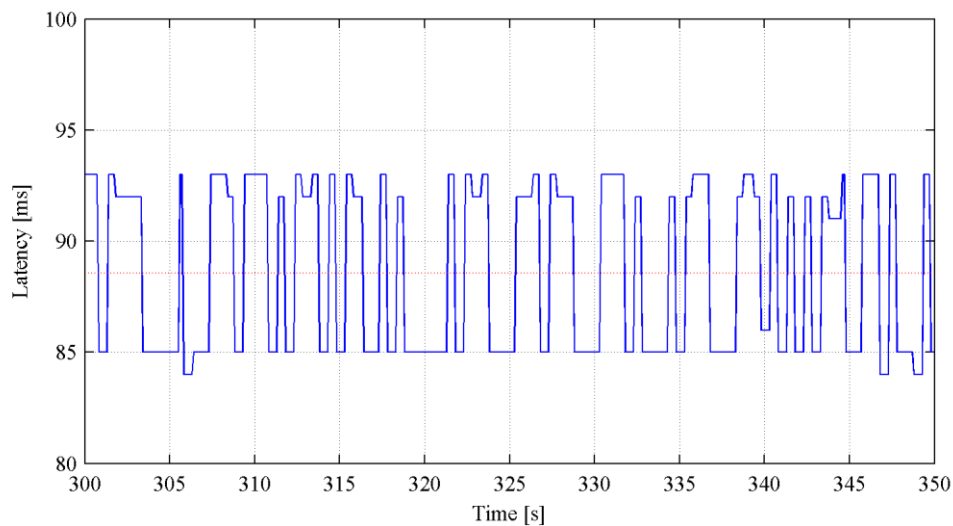


Figure 9.6 - RF transmission latency estimates

A graph of platform data sample periods for a 50 s portion of the flight test is shown in Figure 9.7. Two packet losses were experienced during the portion of the flight as indicated by the 400 ms peaks. From the figure it is also apparent that the sample rate varied regularly by ± 15 ms.

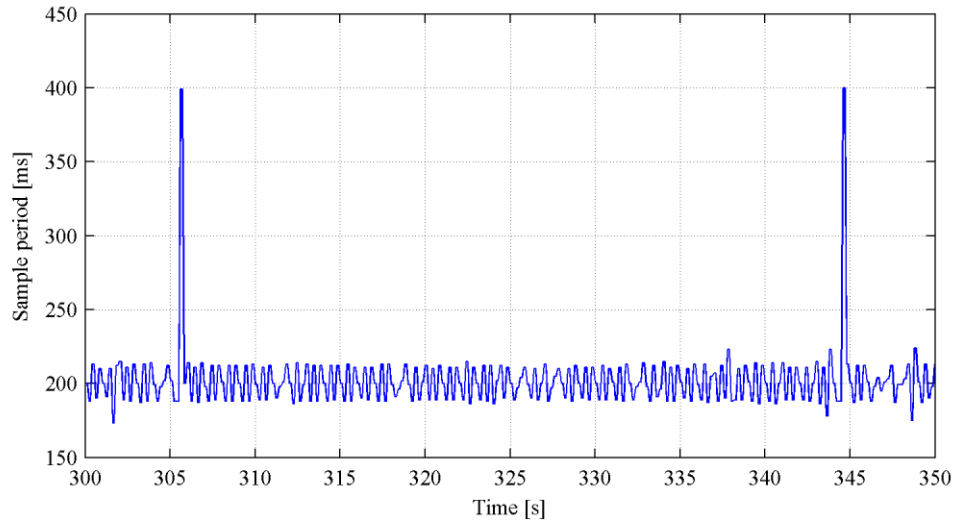


Figure 9.7 - RF platform data sample period

Raw platform jerk motion as received by the helicopter from the SMPLCA application via the RF link and TCP interface is shown in Figure 9.8 for a 20 s portion of the flight test. The true platform motion data shown, led the raw RF data approximately by the mean RF transmission latency mentioned above. The 0.55 m/s^3 error observed coincided with the packet lost at 344.5 s. The effect of multiple packet losses is not shown as the system would then abort as described in Section 8.2.3.

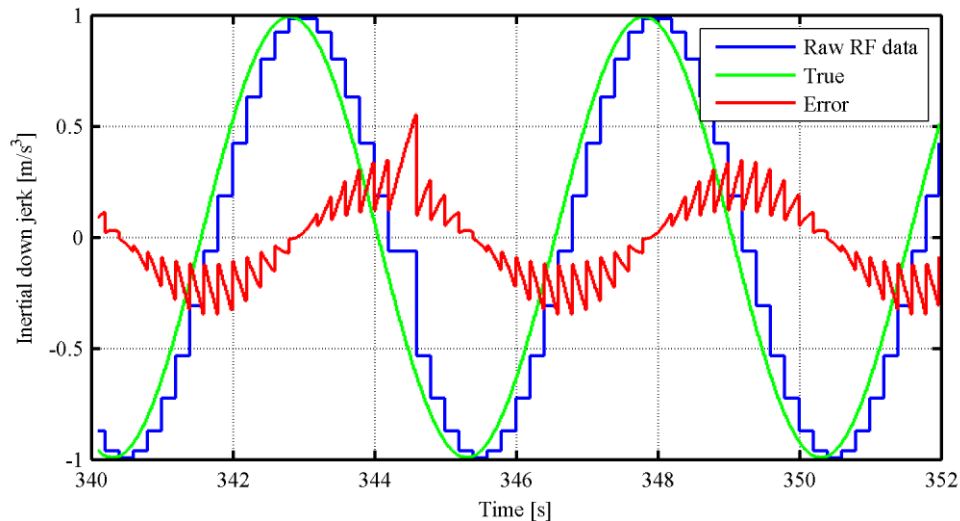


Figure 9.8 - True vs. raw RF platform jerk

The platform acceleration as output by the helicopter's platform heave motion estimator is compared with the true platform motion as shown in Figure 9.9. The maximum jerk error at 344.5 s propagated into a momentary 0.097 m/s^2 error. The RMS error of the estimates was 0.035 m/s^2 .

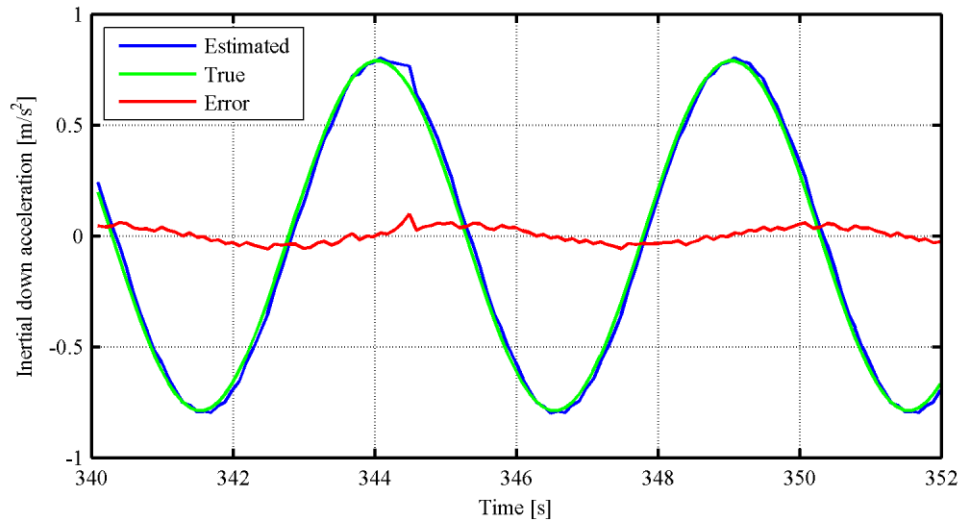


Figure 9.9 - True vs. estimated platform acceleration

The velocity estimates output by the platform heave motion estimator are shown in Figure 9.10. For the time period shown the estimates had a maximum error of 0.046 m/s and an RMS error of 0.026 m/s.

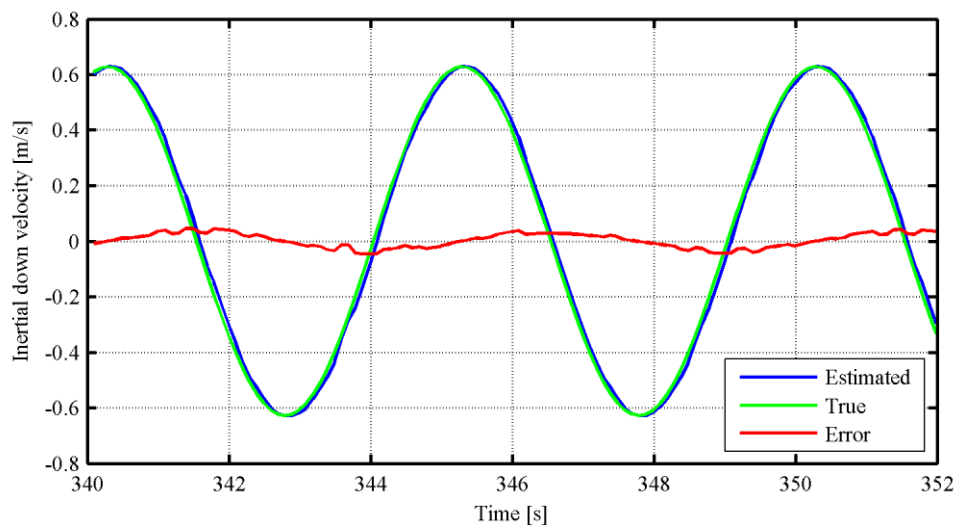


Figure 9.10 - True vs. estimated platform velocity

The estimates of platform position as output by the platform heave motion estimator are shown in Figure 9.11. The estimates had a maximum error of 0.046 m and an RMS error of 0.022 m.

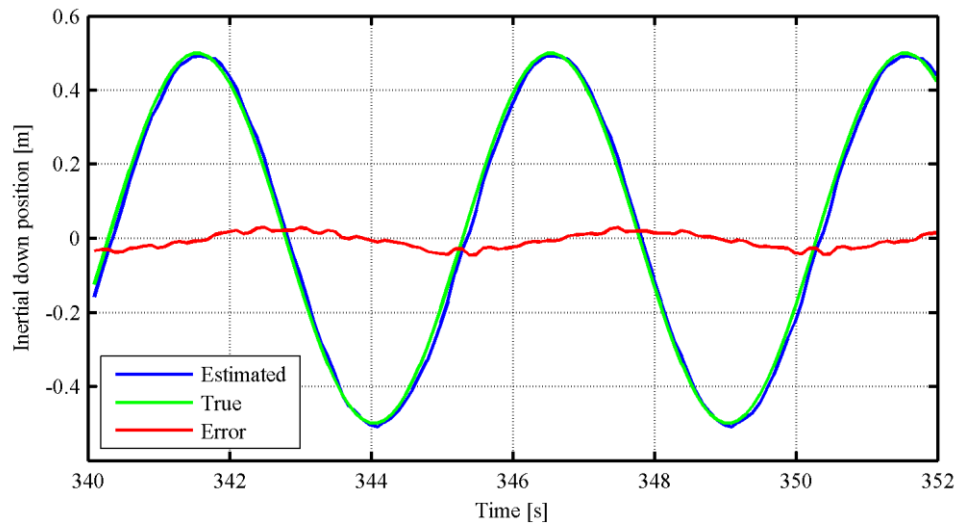


Figure 9.11 - True vs. estimated platform position

During longitudinal (and lateral) position step manoeuvres a spiral motion instead of a straight motion was observed as illustrated in the aerial view of Figure 9.12.

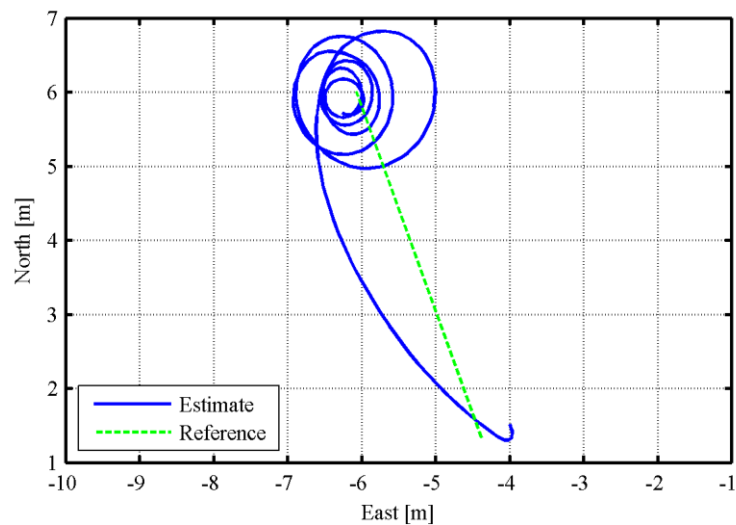


Figure 9.12 - Aerial plan (flight; problematic spiral motion)

9.3.2.5 CONCLUSION

The new RF link configuration can send and receive all data required with a minimum of packet losses.

The SMPLCA application data sent to the helicopter is received successfully, verifying successful basic integration.

As the jerk motion state is not used as an input to any controllers, jerk errors are acceptable if their effects do not propagate too seriously to the other platform motion states via the

platform motion estimator. Despite RF transmission delays and small platform motion sampling variations, the platform heave motion estimates which will be used as an input to the helicopter's heave controller (acceleration, velocity and position) are centimetre accurate, comparable with the accuracy of the GPS unit used on the helicopter [55]. The performance of the estimator is therefore deemed acceptable.

The spiral motion observed during lateral and longitudinal position steps was not seen in previous flight tests and was therefore suspected to be due to the changes made to the helicopter system since the previous flight test.

9.3.3 MAGNETOMETER CALIBRATION (2013-11-04)

All the changes which were made to the helicopter system between the flights described in sections 9.2 and 9.3.2 were checked in order to find an explanation for the spiral lateral and longitudinal motion observed during the previous flight test. No problems were found and nominal flight could still be achieved during HIL simulations. The rest of the helicopter system was checked and the magnetometer was found to give heading measurements with errors of up to 30°. The magnetometer therefore needed to be calibrated.

9.3.3.1 AIM

The purpose of this practical exercise was to improve the accuracy of the magnetometer heading measurements by calibrating the magnetometer.

9.3.3.2 SYSTEM

The system was put into a state suitable for magnetometer calibration. All previously used calibration factors were zeroed in order to obtain raw, uncalibrated magnetometer measurements. As the rotor blades cause magnetometer interference, they were fixed in a position which aligned them with the longitudinal axis of the helicopter to prevent the interference from varying during the calibration process.

9.3.3.3 PROCEDURE

A way of performing magnetometer calibration is detailed in Section 5.3.3. Suitable raw uncalibrated magnetometer measurements were obtained by rotating the magnetometer equally (the same amount and speed) through all angles of rotation as illustrated in Figure 9.13.

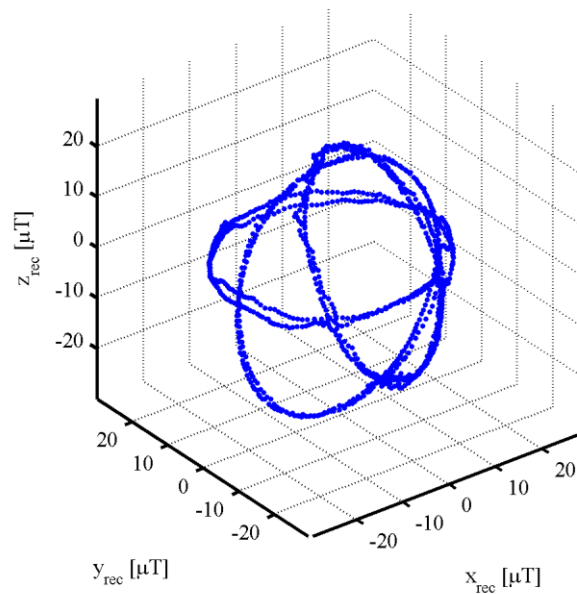


Figure 9.13 - 3D locus of uncalibrated magnetometer measurements as recorded during calibration

The magnetic field strength in Stellenbosch (the calibration location) is $26 \mu\text{T}$ [64]. As a result a perfectly calibrated magnetometer is expected to produce a perfectly spherical locus of measurements with a radius of $26 \mu\text{T}$. The distortions in the helicopter's magnetometer measurements are best observed in the 2D plots provided in Figure 9.14.

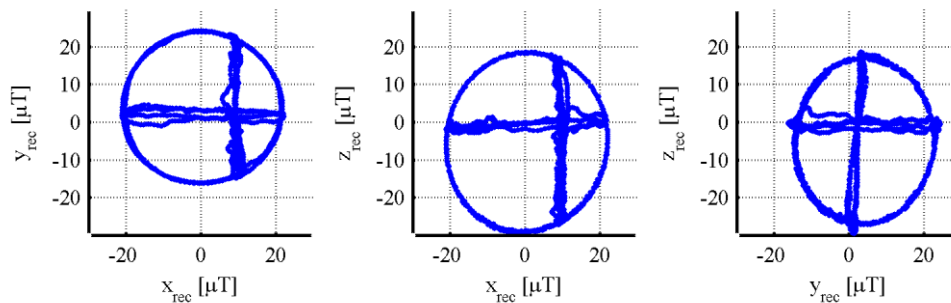


Figure 9.14 – 2D loci of uncalibrated magnetometer measurements as recorded during calibration

The method of least squares was used to determine appropriate calibration factors for the correction of the magnetometer measurement distortions as described in Section 5.3.3.

9.3.3.4 RESULTS

The calibration factors determined for the helicopter's magnetometer are provided in the following equation for the conversion of the helicopter's raw magnetometer measurements into calibrated magnetometer measurements,

$$\begin{bmatrix} B_{xcal} \\ B_{ycal} \\ B_{zcal} \end{bmatrix} = \begin{bmatrix} 1.19 & -0.05 & 0.01 \\ 0.04 & 1.25 & 0.00 \\ -0.06 & 0.00 & 1.07 \end{bmatrix} \begin{bmatrix} B_{xraw} \\ B_{yraw} \\ B_{zraw} \end{bmatrix} + \begin{bmatrix} -0.17 \\ -4.85 \\ 5.87 \end{bmatrix} \quad (9.4),$$

where B_{*raw} are raw magnetometer measurements in μT and B_{*cal} are calibrated magnetometer measurements in μT . The raw magnetometer measurements presented in Figure 9.14 were converted into calibrated measurements by equation (9.4) and loci of the calibrated measurements are presented in Figure 9.15. The x-y and x-z loci are almost perfect circles with a radius of $26 \mu\text{T}$, centred at the origin as desired. The y-z locus is almost perfectly centred at the origin, but still somewhat elliptically shaped and reaches only $22 - 24 \mu\text{T}$ at the extremes of its rotation. This is acceptable for near-level flight as the effect of the z-axis magnetometer measurements is small at small roll and pitch angles as suggested by equations (5.13) and (5.14).

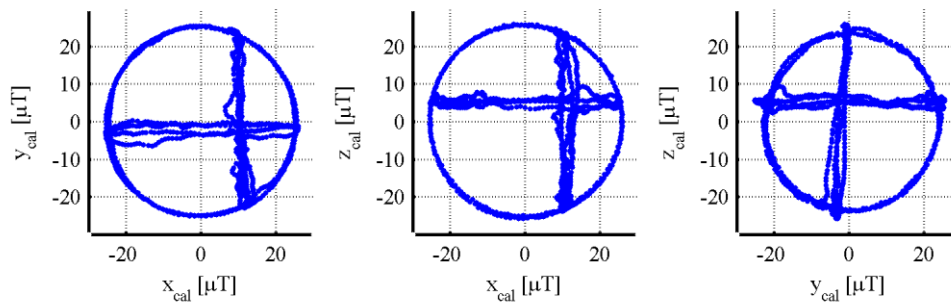


Figure 9.15 - 2D loci of calibrated magnetometer measurements

The newly calibrated magnetometer produces heading measurements which are accurate to within 10° , an improvement from the original 30° error noted earlier. The rotation of the rotor blades introduces a variable source of interference which results in the 10° variation in measurements. Variable sources of interference cannot be accounted for through calibration.

9.3.3.5 CONCLUSION

The newly calibrated magnetometer produces more accurate heading measurements than with the old calibration. The variation introduced by the variable interference from the rotor blades justifies relocating the magnetometer to a position where it is less susceptible to rotor blade interference in a future project.

9.3.4 HILS: EFFECT OF MAGNETOMETER CALIBRATION ERROR

9.3.4.1 AIM

The purpose of this simulation was to determine the effect on basic automatic flight of a magnetometer calibrated as poorly as the helicopter system's original magnetometer.

9.3.4.2 SYSTEM

The HILS system was configured with similar magnetometer errors as those experienced with the original magnetometer calibration. The original calibration factors are provided in equation (9.5):

$$\begin{bmatrix} B_{xcal} \\ B_{yca} \\ B_{zca} \end{bmatrix} = \begin{bmatrix} 1.16 & 0.0 & 0.0 \\ 0.0 & 1.20 & 0.0 \\ 0.0 & 0.0 & 1.05 \end{bmatrix} \begin{bmatrix} B_{xraw} \\ B_{yraw} \\ B_{zraw} \end{bmatrix} + \begin{bmatrix} 3.89 \\ -7.84 \\ 0.38 \end{bmatrix} \quad (9.5).$$

The main difference between the original calibration factors and the new calibration factors presented in equation (9.4) is the difference in offset factors. Accordingly, calibrated magnetometer measurements were offset by the offset difference for the purposes of the simulation. The x-axis measurements were offset by 4.06 μT , the y-axis measurements were offset by -2.99 μT and the z-axis measurements were offset by -5.49 μT .

The $G2$ controller gains were used for this simulation.

9.3.4.3 PROCEDURE

Lateral and longitudinal position step manoeuvres were performed while maintaining a similar heading to the heading maintained during flight.

9.3.4.4 RESULTS

Figure 9.16 is an aerial view of a longitudinal position step manoeuvre. A spiral lateral and longitudinal motion is observed, similar to the motion seen during flight.

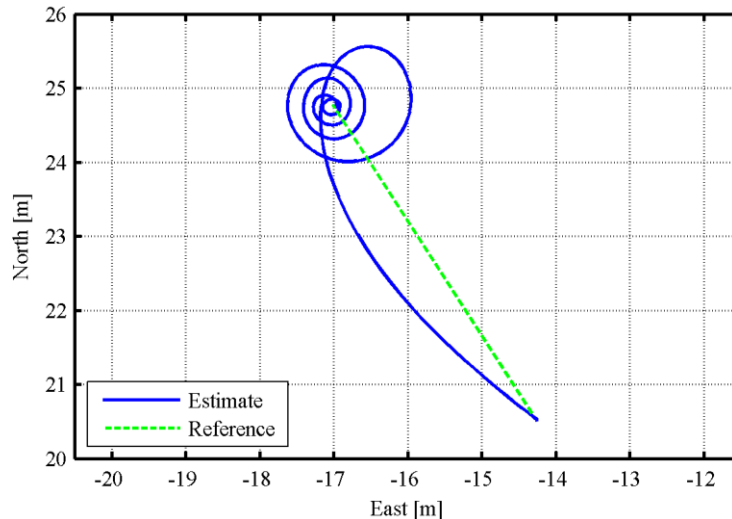


Figure 9.16 - Aerial plan (HIL simulation; uncalibrated magnetometer)

9.3.4.5 CONCLUSION

The poorly calibrated magnetometer of the original helicopter system was responsible for the spiral lateral and longitudinal motion observed during the flight test detailed in sections 9.3.2. This makes sense because, for example for the longitudinal position step case, the new north and east position references are worked out based on the starting position, the magnitude of the desired longitudinal position step and the current heading angle as measured by the magnetometer. Due to the discrepancy between the true and measured heading, the new north and east position references were off the longitudinal axis of the helicopter. The position step manoeuvre therefore started in the longitudinal direction but, as soon as the control system realised that the helicopter was not headed directly for the new reference position, it corrected with a lateral control input. This process repeated itself until the helicopter finally settled on the desired position reference.

This problem most likely did not occur in the last number of flight tests performed with the original helicopter system as presented in Section 9.2 and in previous projects [6] as those tests were all performed with a near-north heading, a heading angle where heading estimates were quite accurate with the original helicopter system.

9.3.5 FLIGHT 3 (2013-11-05)

9.3.5.1 AIM

The purpose of this flight test was to prove that the problem which resulted in the spiral lateral and longitudinal had been solved and that basic automatic control was possible with the new helicopter system.

9.3.5.2 SYSTEM

The newly calibrated magnetometer was used during this flight test.

9.3.5.3 PROCEDURE

Lateral and longitudinal position step manoeuvres were performed and the responses were analysed.

9.3.5.4 RESULTS

An aerial view of the helicopter's motion in response to a longitudinal position step is provided in Figure 9.17. While the reference path was not followed perfectly, the spiral motion observed during previous flight tests was not present.

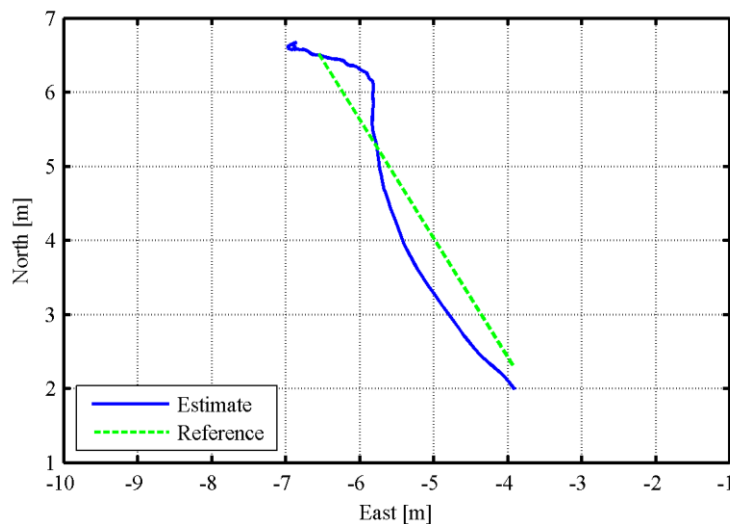


Figure 9.17 - Aerial plan (flight; calibrated magnetometer)

9.3.5.5 CONCLUSION

The problem which resulted in the spiral lateral and longitudinal motion observed in previous practical flight tests was solved. Basic automatic control is possible with the new helicopter system.

9.4 GPS LATENCY COMPENSATION

As discussed in Section 5.2.2, the latency associated with GPS measurements can degrade estimator performance. The method of filter replay for GPS latency compensation described in Section 5.2.3 was implemented for the helicopter system. The tuning and testing of the GPS latency compensator was performed during practical flight tests and HIL simulations.

9.4.1 FLIGHTS: INITIAL LATENCY DETERMINATION (2013-11-05; 2014-01-29)

9.4.1.1 AIM

The purpose of these flight tests was to obtain a rough estimate of the GPS latency experienced by the helicopter.

9.4.1.2 SYSTEM

The GPS was configured to provide GPS measurements at 10 Hz, the nominal flight configuration. Due to limitations with the original helicopter system, flight data was logged at 10 Hz.

9.4.1.3 PROCEDURE

Heave position step manoeuvres were performed. The difference in time between the accelerometer spikes and corresponding changes in GPS measurements were analysed post flight to obtain an idea of the GPS latency. Due to the logging and measurement rate limitations the resolution of the latency measurements was limited to 0.1 s. A number of heave position steps were executed in order to obtain a larger sample set and therefore better latency estimates.

9.4.1.4 RESULTS

Accelerometer, GPS velocity and GPS position data recorded immediately after the heave position step manoeuvres were performed are presented in Figure 9.18.

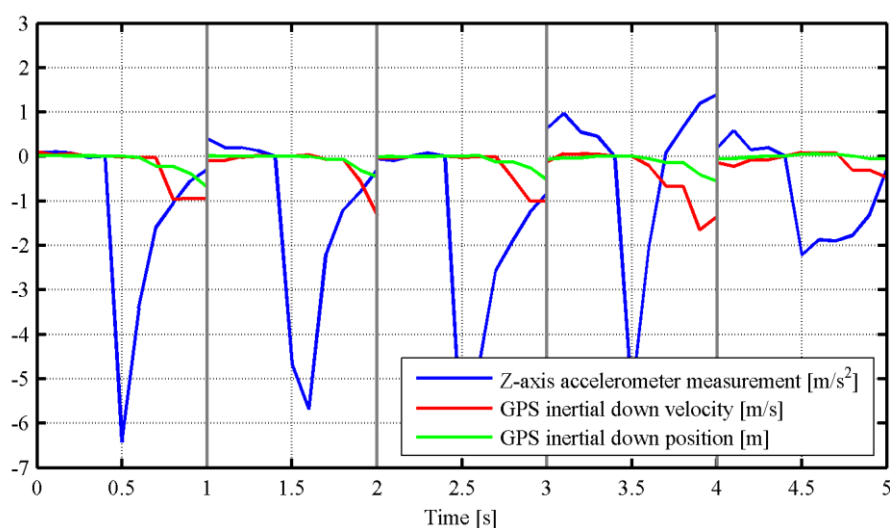


Figure 9.18 - GPS vs. accelerometer response instants

The latency figures obtained from each position step are provided in Table 9.2.

	GPS position to accelerometer	GPS velocity to GPS position
Step 1	0.2 s	0.1 s
Step 2	0.2 s	0.0 s
Step 3	0.2 s	0.1 s
Step 4	0.1 s	0.0 s
Step 5	0.3 s	0.0 s

Table 9.2 - GPS latency figures from test data

The GPS position measurements lagged the corresponding accelerometer measurements by an average of 0.2 s. The GPS velocity measurements lagged the corresponding GPS position measurements by an average of 0.04 s. This estimate is close to the 0.05 s latency specified by the GPS's manufacturer for 10 Hz velocity measurements [55].

9.4.1.5 CONCLUSION

The latency of the helicopter system's GPS position measurements is approximately 0.2 s. The latency between GPS position and velocity measurements is 0.05 s as specified by the GPS's manufacturer.

9.4.2 HILS: LATENCY EFFECT AND COMPENSATION TUNING

9.4.2.1 AIM

The purpose of this simulation was to determine the effect of GPS latency on uncompensated heave estimates of 0.2 Hz heave motions, to gain experience with tuning out the effect via GPS latency compensation in the safety of the HILS environment and to find optimal GPS latency compensation times for HIL simulations.

9.4.2.2 SYSTEM

The GPS latency compensator described in Section 5.2.3 and the feed forward heave controller described in Section 6.5.2 were implemented on the helicopter system. Preliminary feed forward gains were set for this test, as feed forward gains tuning is the topic of another flight test described in Section 9.6. This was acceptable as heave tracking accuracy was not important for this test. The logging rate problems experienced during previous flight tests were addressed sufficiently to allow 25 Hz logging during less computationally demanding tests such as this one.

9.4.2.3 PROCEDURE

The helicopter was commanded to track a 0.2 Hz sinusoidal heave motion.

First no GPS latency compensation was used and the heave motion estimation error was noted.

As the GPS velocity to GPS position latency experienced during HIL simulations is not necessarily the same as the latency specified by the GPS's manufacturer, this value was found through a number of tuning simulations to be 0.08 s. This process is not detailed here as this value is known for practical flight applications. Testing continued with GPS velocity to GPS position latency compensation time fixed at 0.08 s.

GPS position to accelerometer latency compensation time started at 0.20 s and the heave motion estimation error was noted. Further tests continued with slightly lower and slightly higher compensation times until those times which gave minimum estimation errors were found.

9.4.2.4 RESULTS

GPS heave motion measurements and estimated heave motion states are compared for the estimator without GPS latency compensation in Figure 9.19 and Figure 9.20. The GPS measurements are shifted by the amount of time which they are delayed. As the measurements obtained from the helicopter's GPS unit are centimetre accurate [55], appropriately time shifted GPS measurements give a good idea of the true motion states. The velocity estimates had a maximum error of 0.26 m/s and an RMS error of 0.13 m/s. The position estimates had a maximum error of 0.26 m and an RMS error of 0.15 m.

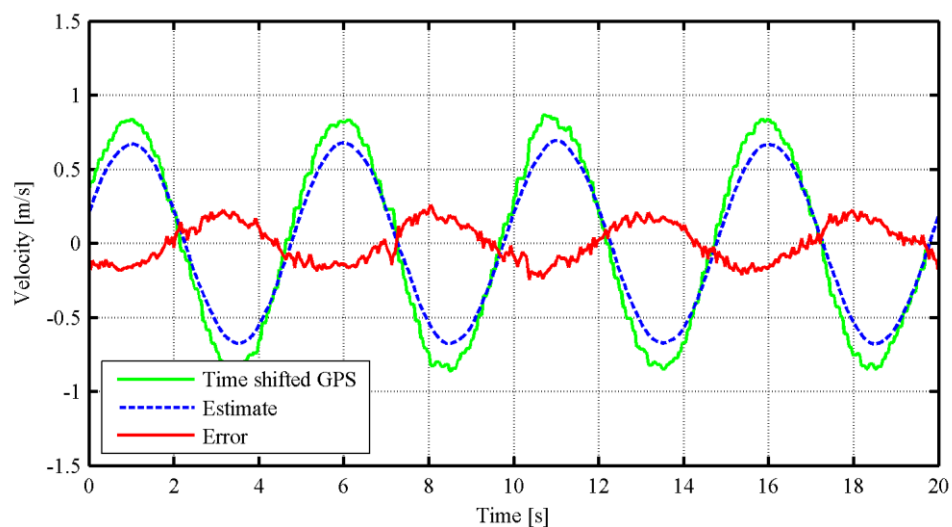


Figure 9.19 - GPS latency effect on heave velocity estimates (HILS)

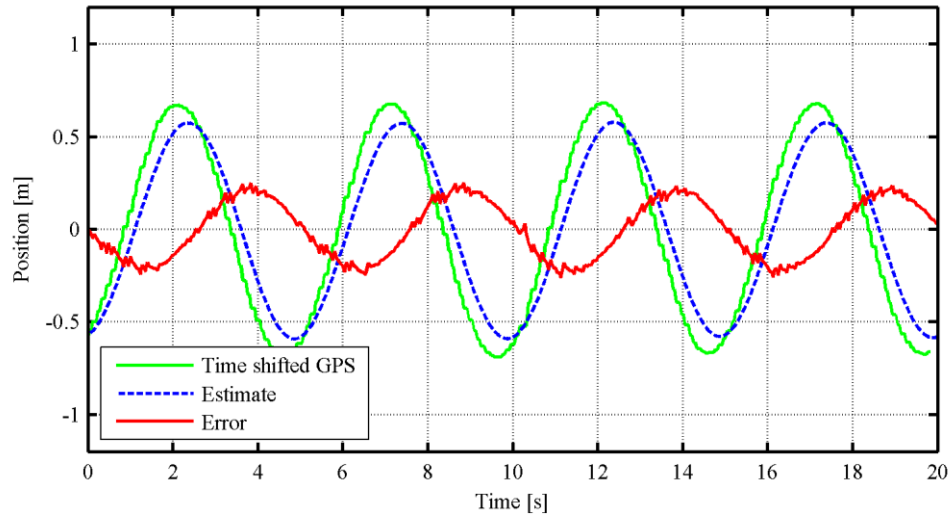


Figure 9.20 - GPS latency effect on heave position estimates (HILS)

GPS latency compensated heave motion estimates are compared with appropriately time shifted GPS measurements in Figure 9.21 and Figure 9.22. A GPS position to accelerometer latency compensation time of 0.20 s and GPS velocity to GPS position latency compensation time of 0.08 s was used. The velocity estimates had a maximum error of 0.07 m/s and an RMS error of 0.02 m/s. The position estimates had a maximum error of 0.06 m and an RMS error of 0.02 m.

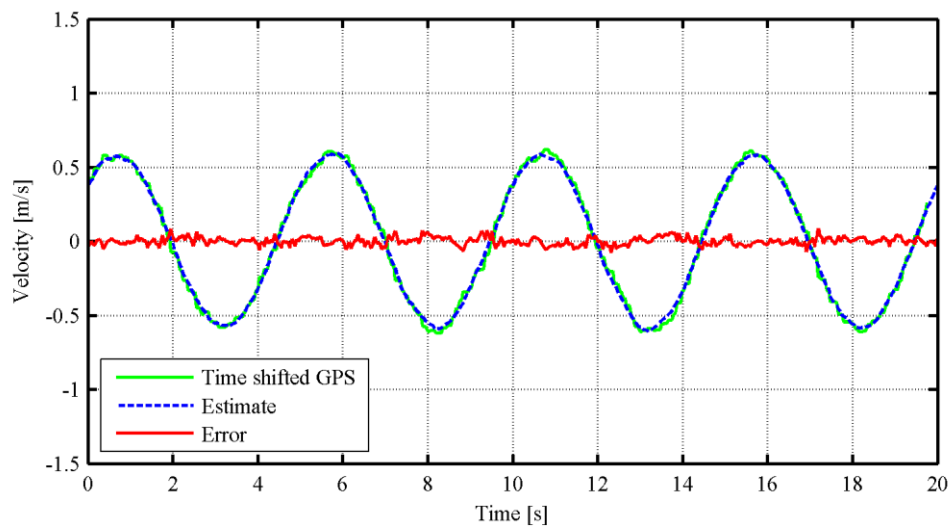


Figure 9.21 - GPS latency compensated heave velocity estimates (HILS)

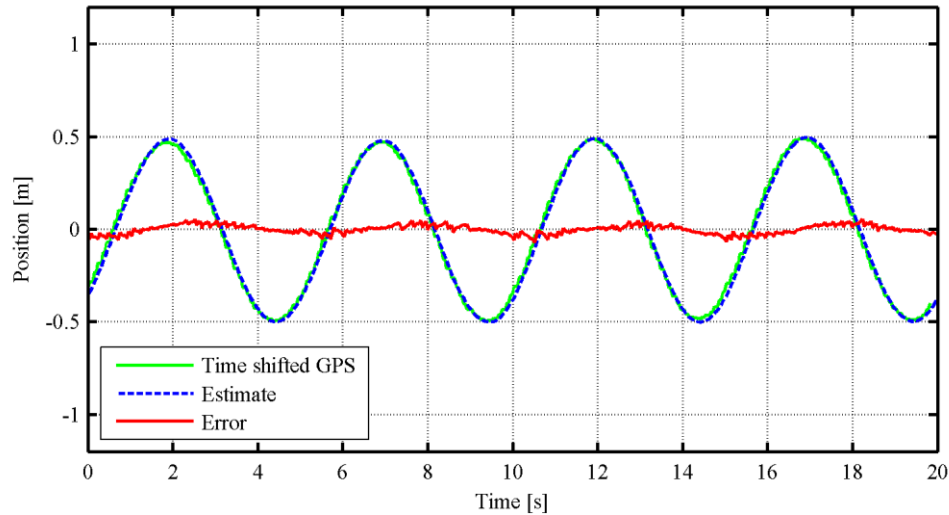


Figure 9.22 - GPS latency compensated heave position estimates (HILS)

The estimation errors noted with the various levels of GPS latency compensation used are detailed in Table 9.3. The lowest estimation error was observed with a GPS position to accelerometer latency compensation time of 0.20 s and a GPS velocity to GPS position latency compensation time of 0.08 s.

	Velocity (m/s)		Position (m)	
	Max error	RMSE	Max error	RMSE
0.00 s	0.26	0.13	0.26	0.15
0.18 s	0.09	0.03	0.06	0.02
0.20 s	0.07	0.02	0.06	0.02
0.22 s	0.07	0.03	0.07	0.03

Table 9.3 - GPS latency compensation time vs. heave motion estimation errors (HIL)

9.4.2.5 CONCLUSION

If GPS latency is not compensated for, it causes significant heave estimation errors when estimating a 0.2 Hz heave motion. The optimal amount of GPS latency compensation can be found by tuning the amount of compensation until an estimation error minimum is found. For the HIL environment the optimal GPS position to accelerometer latency compensation time is 0.20 s and the optimal GPS velocity to GPS position latency compensation time is 0.08 s.

9.4.3 FLIGHT: COMPENSATION TUNING (2014-04-17)

The various timing resolution restrictions of the type of latency determination experiment performed in Section 9.4.1 justified fine tuning of the latency compensation times.

9.4.3.1 AIM

The purpose of this flight test was to find the optimal GPS latency compensation times for real flight conditions via a tuning process.

9.4.3.2 SYSTEM

The system used during the previous HIL simulation was used for this flight test.

9.4.3.3 PROCEDURE

GPS position to accelerometer latency compensation time started at 0.20 s and GPS velocity to GPS position latency compensation time was fixed at 0.04 s. The manufacturer specified 0.05 s would have been preferred but the helicopter's OBC runs at 50 Hz and therefore has a timing resolution of 0.02 s. A 0.2 Hz heave motion was tracked and the heave motion estimation error analysed. The test was repeated for GPS position to accelerometer latency compensation times of 0.18 s and the heave motion estimation error analysed. The lower amount of compensation resulted in less heave motion estimation error. As a result the amount of GPS latency compensation time was reduced to 0.16 s. The heave motion estimation error increased as a result.

9.4.3.4 RESULTS

The heave motion estimates for the test with a GPS latency compensation time of 0.18 s are compared with time-shifted GPS measurements in Figure 9.23 and Figure 9.24. The GPS measurements are used for comparison as they are considered to be centimetre accurate [55], but delayed measurements. The GPS measurements are time shifted by the same amount as the GPS latency compensation times. The maximum velocity estimation error was 0.17 m/s and the RMS error was 0.06 m/s. The maximum position estimation error was 0.09 m and the RMS error was 0.03 m.

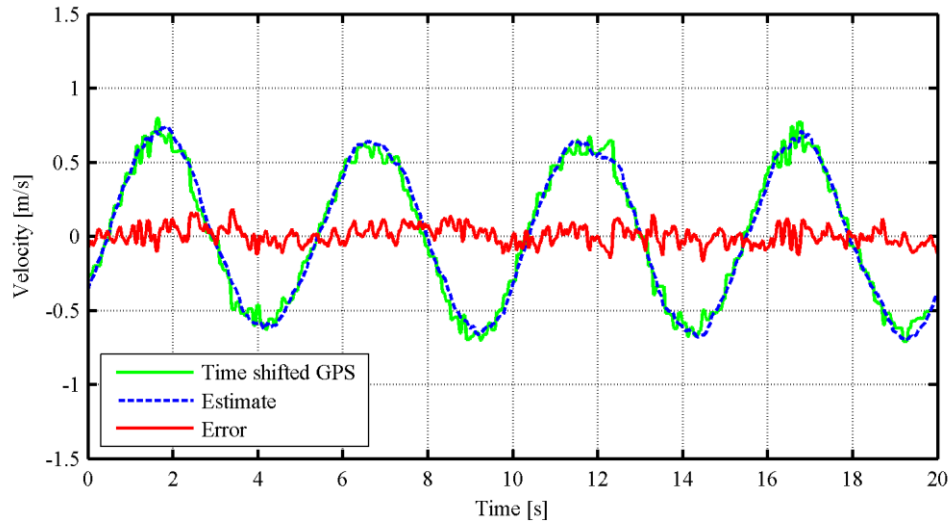


Figure 9.23 - GPS latency compensated heave velocity estimates (flight)

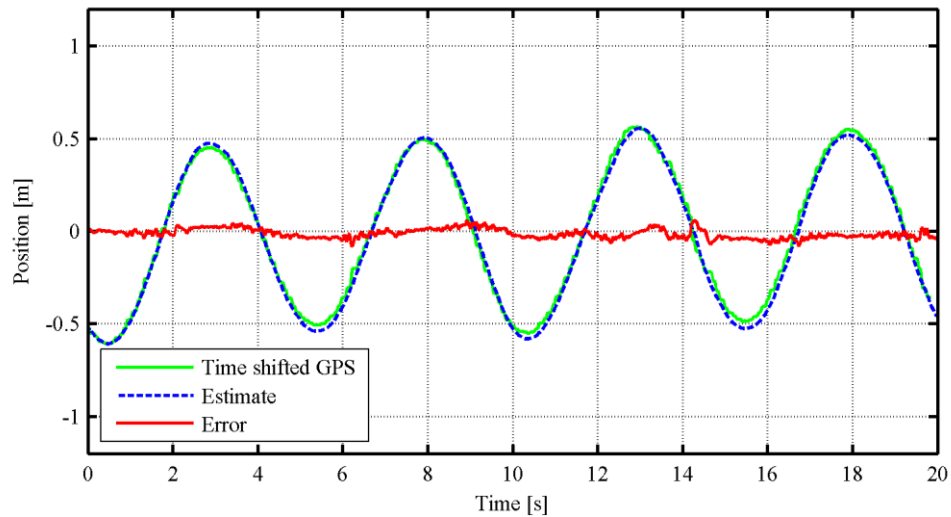


Figure 9.24 - GPS latency compensated heave position estimates (flight)

The heave motion estimation errors resulting from various amounts of GPS latency compensation are detailed in Table 9.4. The lowest heave motion estimation errors occur with a GPS position to accelerometer latency compensation time of 0.18 s and a GPS velocity to GPS position latency compensation time of 0.04 s.

	Velocity (m/s)		Position (m)	
	Max error	RMSE	Max error	RMSE
0.16 s	0.22	0.07	0.12	0.05
0.18 s	0.18	0.06	0.09	0.03
0.20 s	0.23	0.07	0.15	0.06

Table 9.4 - GPS latency compensation time vs. heave motion estimation errors (flight)

9.4.3.5 CONCLUSION

The optimal GPS position to accelerometer latency compensation time is 0.18 s and the optimal GPS velocity to GPS position latency compensation time is 0.04 s for the helicopter system in real flight conditions.

9.5 HEAVE CONTROLLER TUNING VERIFICATION

While the heave controller gains remained unchanged since the initial controller tuning test described in Section 9.2, the change in heave motion estimation justified a heave controller gain tuning verification flight. Additionally, the performance of the heave controller was compared in real flight and HIL simulation conditions to determine how accurate the HIL simulation is for heave motions.

9.5.1 FLIGHT (2014-04-17)

9.5.1.1 AIM

The purpose of this flight test was to determine the performance of the heave controller after GPS latency compensation was added to the heave motion estimator.

9.5.1.2 SYSTEM

The helicopter system was used with the new GPS latency compensated heave motion estimator. The optimal latency compensation times determined in Section 9.4.3 for real flight were used. G_2 heave controller gains were used.

9.5.1.3 PROCEDURE

Negative and positive 2 m heave position step manoeuvres were performed and the responses were compared to the responses recorded in the initial controller tuning test described in Section 9.2.1.

9.5.1.4 RESULTS

The collective command response to the positive heave position step is compared with the collective command response recorded during the initial controller tuning test in Figure 9.25. The data recorded during the current flight test is labelled as “including GPS latency compensation” and the data recorded during the initial controller tuning test is labelled as “excluding GPS latency compensation”. Collective commands remained within limits (indicated by the dotted red line) and showed no undesired motion such as oscillations.

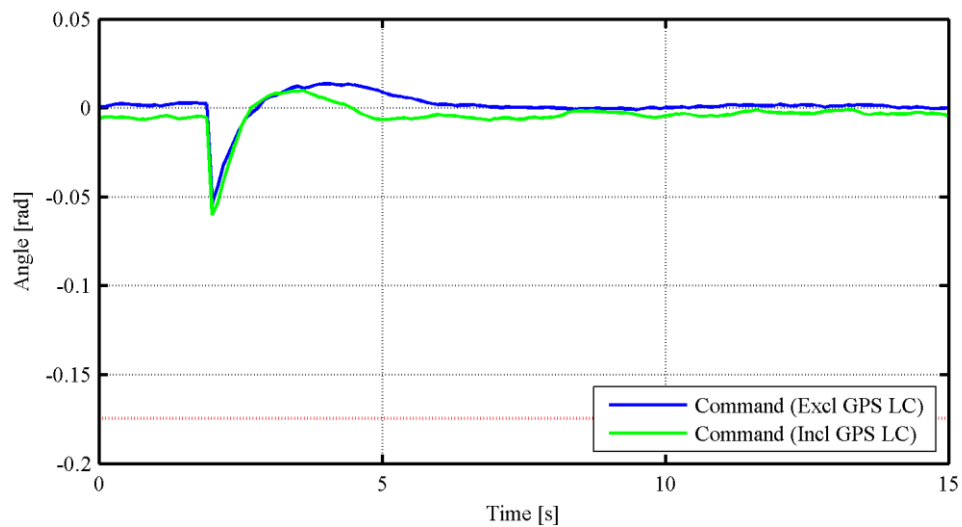


Figure 9.25 - Collective command responses

The heave velocity response to the positive heave position step is compared with the heave velocity response recorded during the initial controller tuning test in Figure 9.26. The response of the system with the GPS latency compensated estimator was faster than the system without GPS latency compensation.

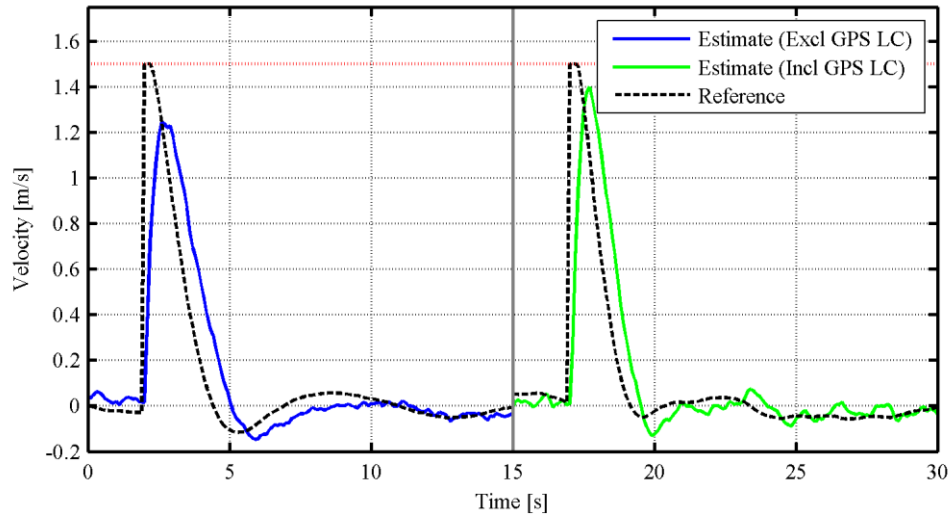


Figure 9.26 - Heave velocity responses

The heave position response to the positive heave position step is compared with the heave position response recorded during the initial controller tuning test in Figure 9.27. The GPS latency compensated system was faster and better damped than the system without GPS latency compensation.

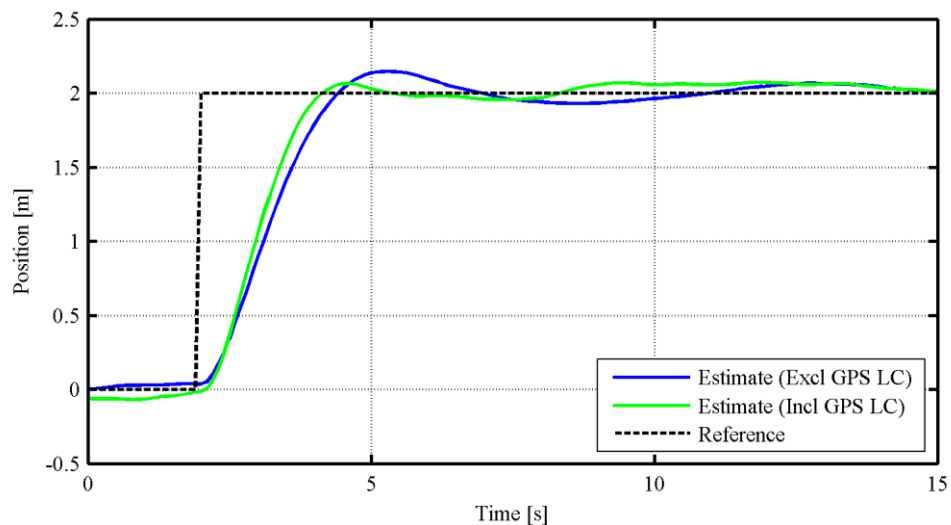


Figure 9.27 - Inertial down position responses

The collective command responses, heave velocity responses and inertial down position responses to the negative position steps performed are provided in Appendix D.1.2.

The bandwidth of the system including GPS latency compensation can be approximated by assuming that the system is second order and solving equation (9.1). From the position step response M_p is 0.032 and t_p is 2.6 s. Substituting M_p into equation (9.2) gives ζ of 0.74. Substituting ζ and t_p into equation (9.3) gives ω_n of 1.79 rad/s. Substituting ζ and ω_n into

equation (9.1) gives ω_b , the bandwidth of the system, of 1.71 rad/s or 0.27 Hz. This is 0.05 Hz higher than the bandwidth of the system excluding GPS latency compensation as calculated in Section 9.2.1.4.

9.5.1.5 CONCLUSION

With the GPS compensated heave motion estimator, the heave controller performs better than without the GPS compensated heave motion estimator. The bandwidth of the controller is estimated to increase by 0.05 Hz.

9.5.2 HIL SIMULATION

9.5.2.1 AIM

The purpose of this simulation was to compare the performance of the heave controller in real flight conditions to the performance of the heave controller in HIL simulation conditions.

9.5.2.2 SYSTEM

The helicopter system was used with the new GPS latency compensated heave motion estimator. The optimal latency compensation times determined in Section 9.4.2 for HIL simulations were used. *G2* heave controller gains were used.

9.5.2.3 PROCEDURE

Negative and positive 2 m heave position step manoeuvres were performed and the responses were compared with the responses determined for real flight in Section 9.5.1.

9.5.2.4 RESULTS

In Figure 9.28 the collective command response to the positive heave position step is compared with the collective command response recorded during flight. The command offset was due to a difference in the pilot commands captured when autopilot handover was performed. Other than the offset, the commands were similar.

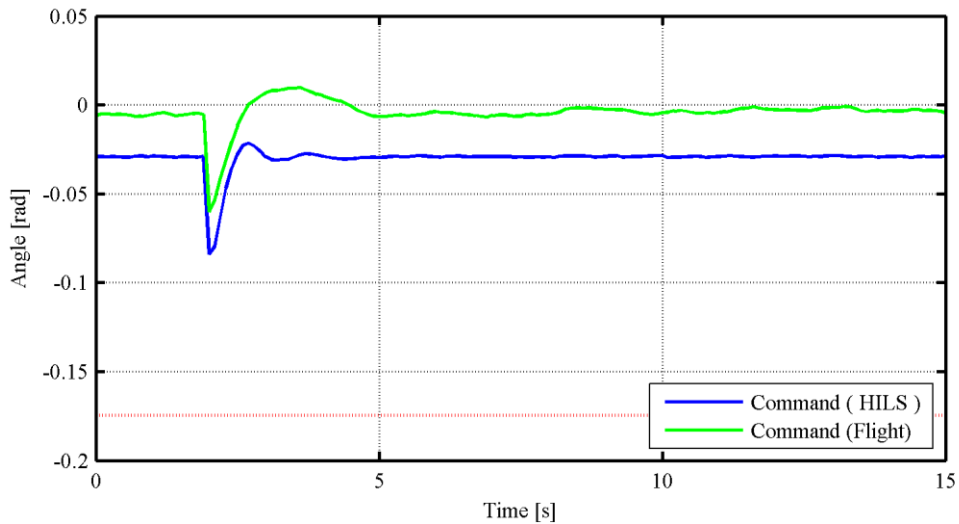


Figure 9.28 - Collective command responses

In Figure 9.29 the heave velocity response to the positive heave position step is compared with the heave velocity response recorded during flight. The speed of the responses was fairly similar but the velocity reference differed in the latter portion of the manoeuvre.

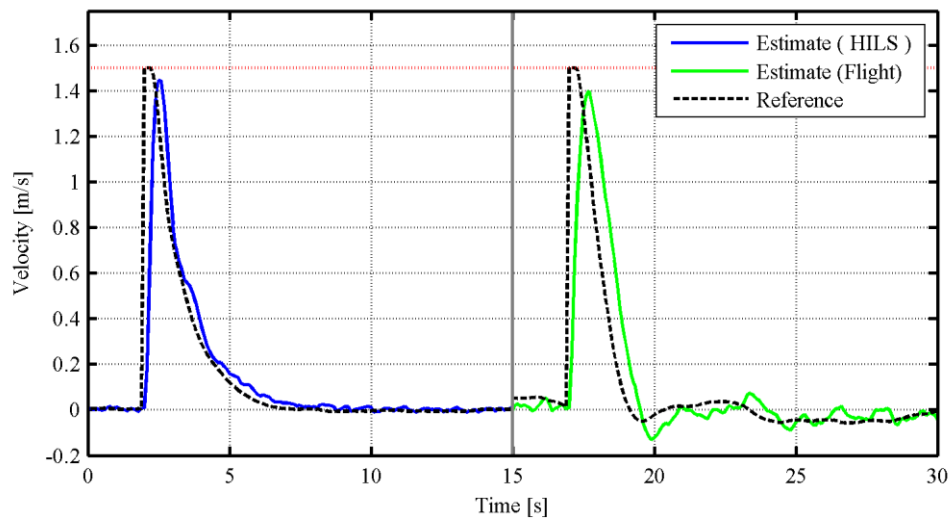


Figure 9.29 - Heave velocity responses

In Figure 9.30 the heave position response to the positive position step is compared with the heave position response recorded during flight. The flight response is about twice as fast as the HILS response.

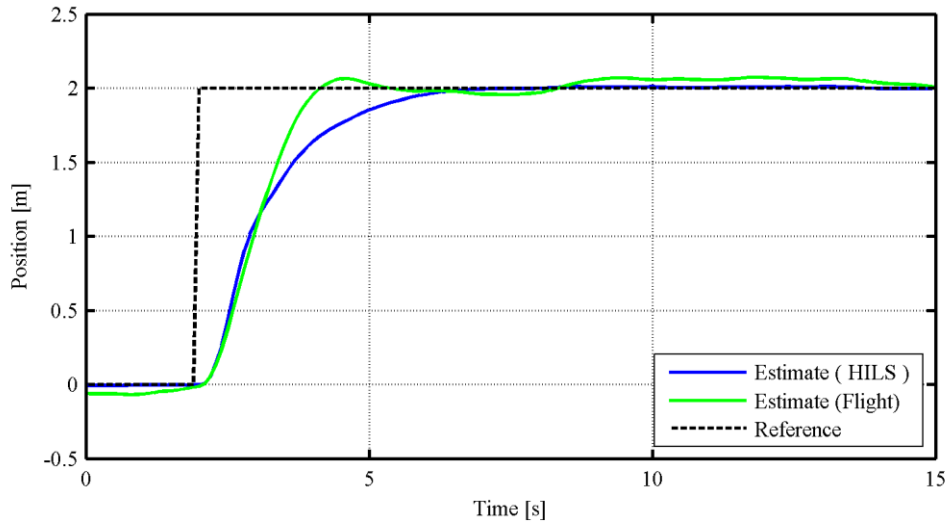


Figure 9.30 - Inertial down position responses

The collective command responses, heave velocity responses and inertial down position responses to the negative position steps performed are provided in Appendix D.1.3.

9.5.2.5 CONCLUSION

The heave position controller is much slower in HILS than in flight. The various problems associated with the HILS setup for the helicopter should be addressed in a future project.

9.6 PROPOSED HEAVE CONTROLLER

The heave controller proposed in Section 6.5.2 had to be tuned and tested. The block diagram of the controller is repeated in Figure 9.31. Optimal values for k_{vff} , the velocity feed forward gain and k_{aff} , the acceleration feed forward gain, had to be determined. The tuning process was tested in a HIL simulation and thereafter executed in a practical flight test.

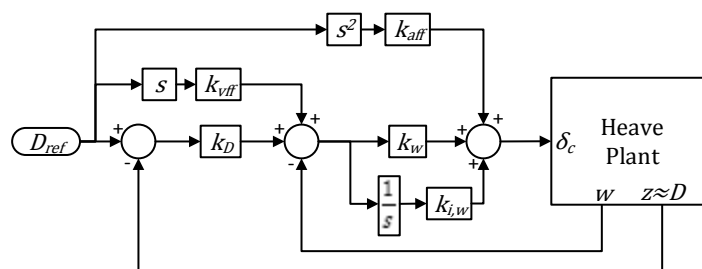


Figure 9.31 - Block diagram of proposed combined heave controller during approximately level flight

9.6.1 HILS: ORIGINAL CONTROLLER & FEED FORWARD TUNING

9.6.1.1 AIM

The purpose of this simulation was to test the heave motion tracking performance of the original heave controller and to find optimal feed forward gains for the proposed heave controller in HIL simulation conditions. The simulation also provided experience with feed forward gain tuning in the safety of a HIL simulation environment.

9.6.1.2 SYSTEM

The helicopter system with the proposed heave controller was used for this test with the GPS latency compensated estimator configured for HIL simulations.

9.6.1.3 PROCEDURE

The heave controller was first configured with its feed forward gains zeroed, effectively resulting in the original heave controller. The helicopter was commanded to track a 0.2 Hz, 1 m peak-to-peak sinusoidal heave motion and the response was analysed. The controller was then configured with a k_{vff} of 1 as suggested in Section 6.5.2.1 and the test was repeated. Then the test was repeated with the controller configured with the theoretical optimal k_{aff} determined in Section 6.5.2.1 of $-\frac{1}{164.5}$ or -0.006. As noted in Section 6.5.2.1, only k_{aff} is sensitive to modelling errors and could therefore differ from the theoretical value. The theoretical value for k_{vff} should apply to any condition and therefore only k_{aff} was changed in subsequent tests. The test was repeated for k_{aff} values of -0.005 and -0.004.

9.6.1.4 RESULTS

The velocity and position tracking responses for the original heave controller are shown in Figure 9.32 and Figure 9.33 respectively. The maximum velocity error was 0.16 m/s and the RMS error was 0.09 m/s. The maximum position tracking error was 0.49 m and the RMS error was 0.33 m.

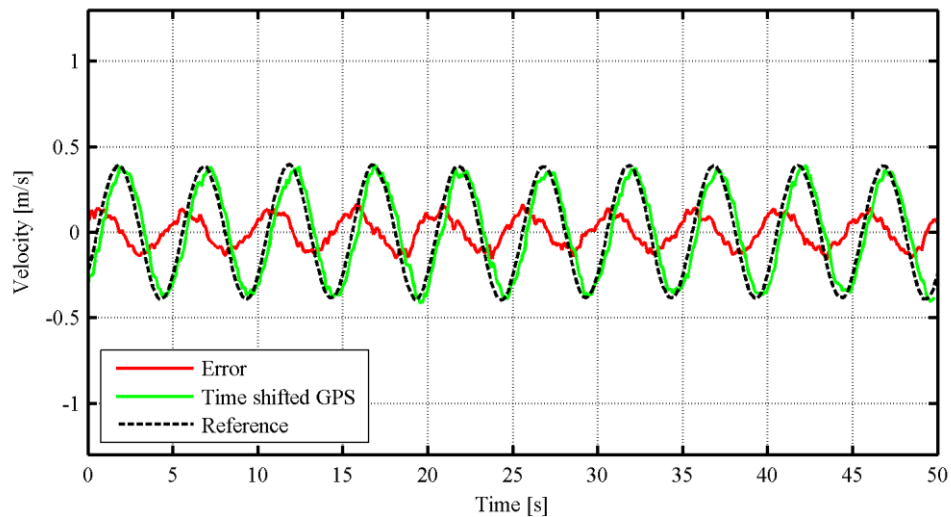


Figure 9.32 - Velocity response (HILS; no feed forwards)

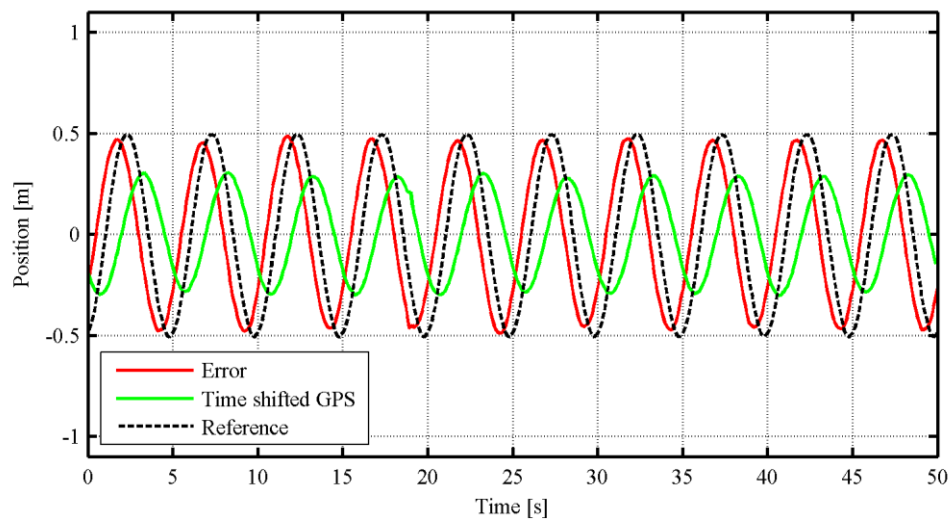


Figure 9.33 - Position tracking response (HILS; no feed forwards)

The velocity and position tracking responses for the proposed heave controller with a k_{aff} value of -0.005 and a k_{vff} value of 1 are shown in Figure 9.34 and Figure 9.35 respectively. The maximum velocity tracking error was 0.19 m/s and the RMS error was 0.08 m/s. The maximum position tracking error was 0.05 m and the RMS error was 0.02 m.

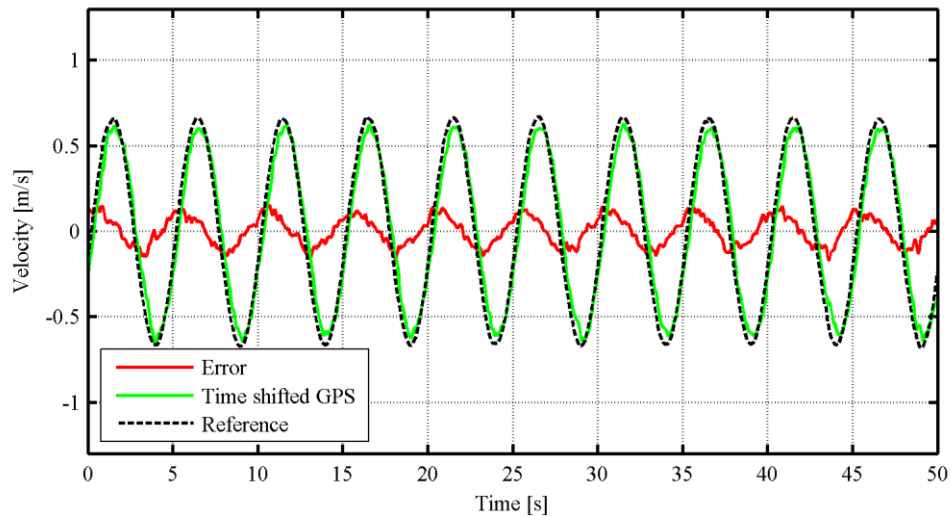


Figure 9.34 - Velocity response (HILS; optimal feed forward gains)

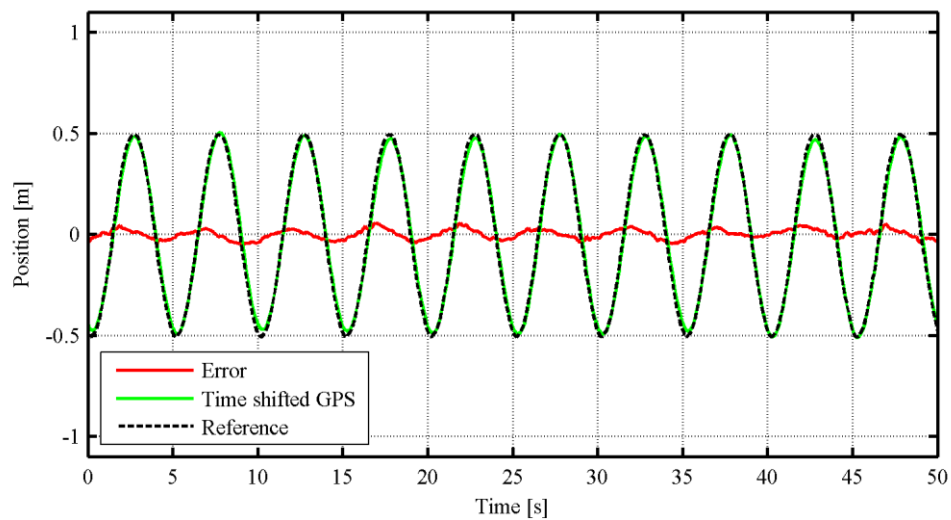


Figure 9.35 - Position tracking response (HILS; optimal feed forward gains)

The heave tracking errors which were measured during the test are detailed in Table 9.5. Minimum tracking errors were observed with a k_{aff} value of -0.005 and a k_{vff} value of 1.

Test	Gain		Velocity (m/s)		Position (m)	
	k_{vff}	k_{aff}	Max error	RMSE	Max error	RMSE
1	0	0	0.16	0.09	0.49	0.33
2	1	0	0.25	0.14	0.16	0.06
3	1	-0.004	0.25	0.08	0.09	0.03
4	1	-0.005	0.19	0.08	0.05	0.02
5	1	-0.006	0.17	0.07	0.08	0.03

Table 9.5 – Velocity and acceleration feed forward gains vs. heave tracking errors (HIL)

9.6.1.5 CONCLUSION

The heave motion tracking performance of the original heave controller is not sufficient to track heave motions with a frequency of 0.2 Hz, within the frequency band of expected platform motion frequencies. The proposed feed forward heave controller performs much better than the original controller for heave tracking purposes. The optimal feed forward gains for the controller in HIL conditions are a k_{aff} value of -0.005 and a k_{vff} value of 1. Optimal values can be found in real flight tests by comparing the heave tracking errors measured when performing the same manoeuvres with different gains.

9.6.2 FLIGHT: FEED FORWARD TUNING (2014-04-17)

9.6.2.1 AIM

The purpose of this flight test was to determine optimal feed forward gains for the heave controller.

9.6.2.2 SYSTEM

The helicopter system was equipped with the heave controller proposed in Section 6.5.2 and with the GPS compensated heave estimator configured for real flight.

9.6.2.3 PROCEDURE

The optimal feed forward gains for HIL conditions determined in Section 9.6.1 were used as a starting point:

$$k_{vff} = 1 \quad (9.6),$$

$$k_{aff} = -0.005 \quad (9.7).$$

The helicopter was provided with 0.2 Hz heave motion reference and the response was analysed. Tests were also performed with acceleration feed forward gains k_{aff} of -0.006 and -0.007.

9.6.2.4 RESULTS

The velocity tracking response with a k_{aff} value of -0.006 and a k_{vff} value of 1 is provided in Figure 9.36. The maximum velocity tracking error was 0.33 m/s and the RMS error was 0.15 m/s.

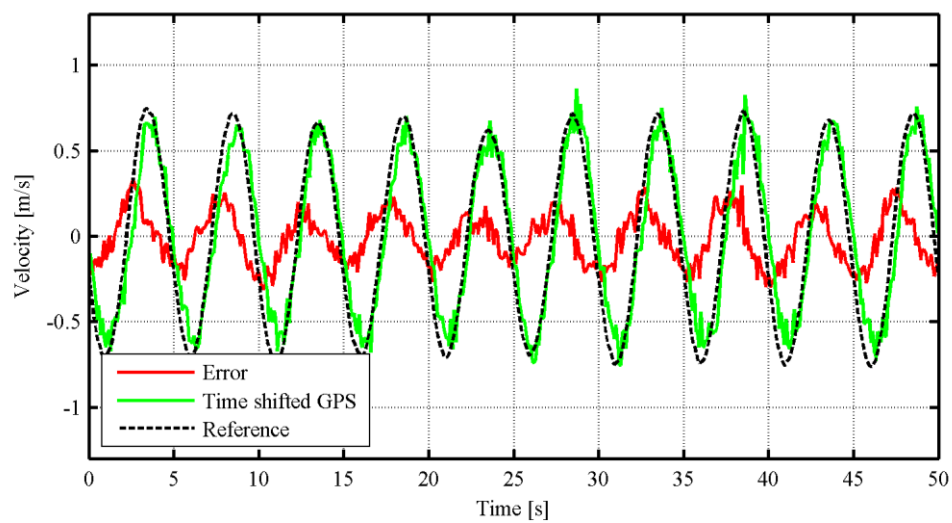


Figure 9.36 - Velocity response (flight; 0.20 Hz reference; optimal feed forward gains)

The position tracking response with the same gains is provided in Figure 9.37. The maximum position tracking error was 0.20 m and the RMS error was 0.08 m.

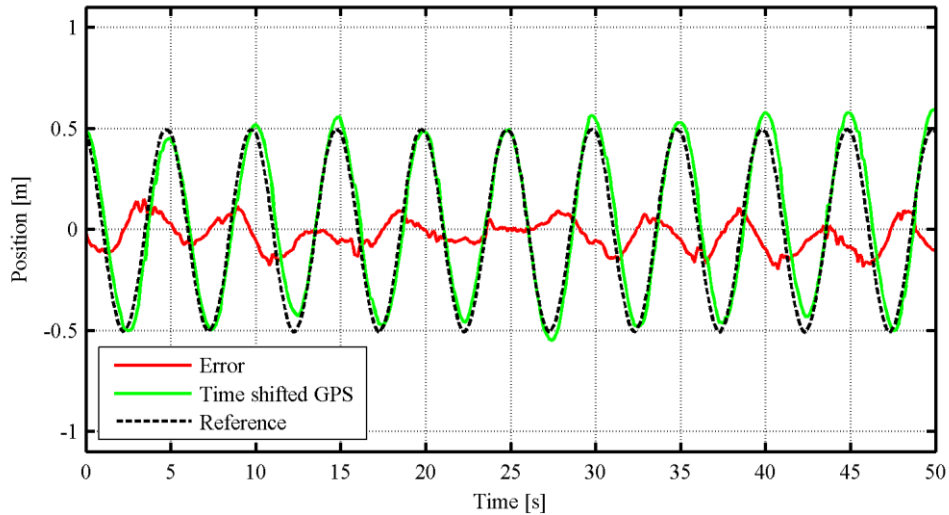


Figure 9.37 - Position tracking response (flight; 0.20 Hz reference; optimal feed forward gains)

The tracking errors measured during the various heave motion tracking tests are detailed in Table 9.6. The tracking error was a minimum with a k_{aff} value of -0.006 and a k_{vff} value of 1, the same as the theoretically determined values of Section 6.5.2.1.

Gain	Velocity (m/s)		Position (m)	
	Max error	RMSE	Max error	RMSE
-0.005	0.38	0.17	0.29	0.09
-0.006	0.33	0.15	0.20	0.08
-0.007	0.35	0.15	0.21	0.09

Table 9.6 - Acceleration feed forward gains vs. heave tracking errors (flight)

9.6.2.5 CONCLUSION

The optimal feed forward gains for the heave controller during real flight tests are a k_{aff} value of -0.006 and a k_{vff} value of 1.

9.7 SINE TRACKING

After tuning the proposed heave controller's feed forward gains, its bandwidth had to be analysed. This was done by commanding the helicopter to track sinusoidal heave motions with different frequencies and noting the tracking error. Frequencies from 0.1 Hz to 0.4 Hz were tested in HILS. Due to the very limited flight testing time available towards the end of this project only two frequencies were tested in practice: 0.1 Hz and 0.2 Hz. The 0.2 Hz

tracking data from the tuning test of Section 9.6.2 was used and 0.1 Hz tracking data was obtained via a separate flight test.

9.7.1 HIL SIMULATION

9.7.1.1 AIM

The purpose of this simulation was to determine the bandwidth of the proposed heave controller in the HILS environment.

9.7.1.2 SYSTEM

The helicopter system was equipped with the proposed heave controller and the optimal feed forward gains from the HILS tuning test described in Section 9.6.1: a k_{aff} value of -0.005 and a k_{vff} value of 1. The GPS latency compensated heave motion estimator was also configured for HILS as described in Section 9.4.2.

9.7.1.3 PROCEDURE

The helicopter was commanded to track various heave motion signals and the tracking error was analysed. The heave motion signals were sinusoidal and the position motion was 1 m peak-to-peak. Frequencies between 0.1 Hz and 0.4 Hz were tested in 0.05 Hz increments.

9.7.1.4 RESULTS

The velocity response when tracking a 0.3 Hz sinusoidal reference signal is shown in Figure 9.38. The maximum velocity error was 0.29 m/s and the RMS error was 0.09 m/s.

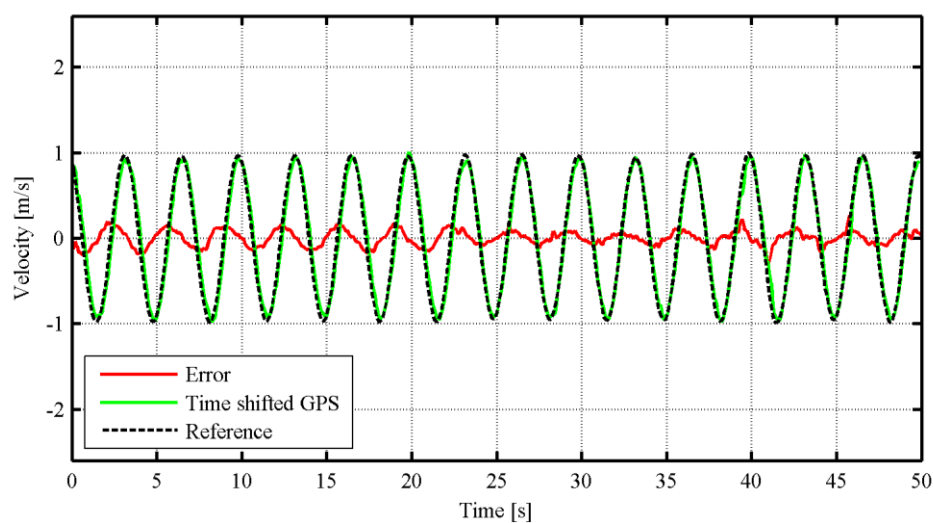


Figure 9.38 - Velocity response (HILS; 0.30 Hz reference)

The position tracking response to the same 0.30 Hz heave motion signal is provided in Figure 9.39. The maximum tracking error was 0.10 m and the RMS error was 0.03 m.

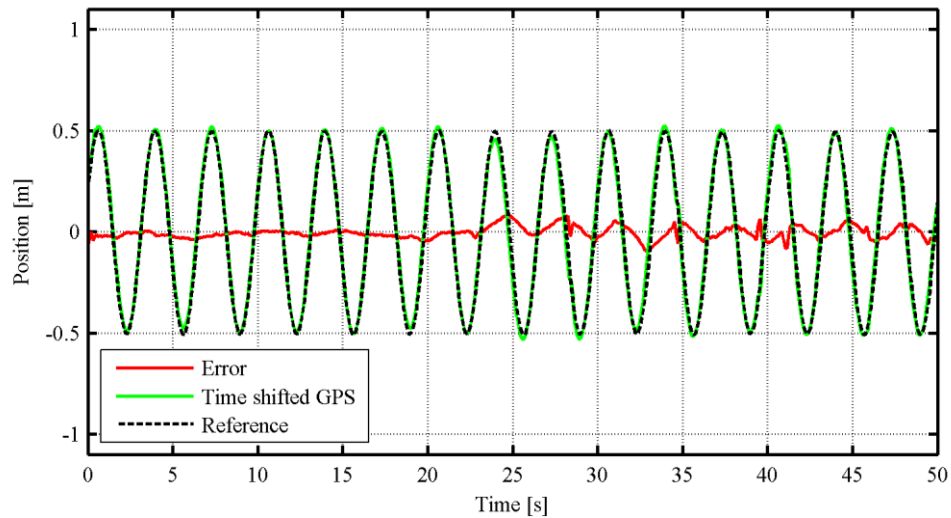


Figure 9.39 - Position tracking response (HILS; 0.30 Hz reference)

The tracking errors observed in response to a number of heave motion signals are detailed in Table 9.7. While the position signals are all 1 m peak-to-peak, the velocities all scale by the frequency in radians. Thus, to better compare the velocity errors observed at the various frequencies, the RMS errors are normalised (NRMSE) by the peak-to-peak magnitude of the reference signals. The normalised tracking errors observed do not change appreciably across the range of frequencies which were tested.

	Velocity (m/s)			Position (m)	
	Max E	RMSE	NRMSE	Max E	RMSE
0.10 Hz	0.09	0.04	0.06	0.06	0.02
0.15 Hz	0.12	0.05	0.06	0.06	0.03
0.20 Hz	0.14	0.07	0.06	0.07	0.03
0.25 Hz	0.20	0.07	0.04	0.11	0.04
0.30 Hz	0.30	0.09	0.05	0.10	0.03
0.35 Hz	0.41	0.12	0.05	0.15	0.05
0.40 Hz	0.64	0.21	0.08	0.15	0.05

Table 9.7 - Reference frequencies vs. heave tracking errors (HILS)

9.7.1.5 CONCLUSION

The proposed heave controller has a bandwidth of at least 0.40 Hz in HILS, twice the bandwidth of the 3-DOF platform.

9.7.2 FLIGHTS (2014-04-17)

9.7.2.1 AIM

The purpose of this flight test was to determine the bandwidth of the proposed heave controller in practical flight test conditions.

9.7.2.2 SYSTEM

For this test the helicopter system used the proposed heave controller tuned with the optimal feed forward gains for practical flight conditions from Section 9.6.2: a k_{aff} value of -0.006 and a k_{vff} value of 1. The heave motion estimator with GPS latency compensation for practical flight conditions (as described in Section 9.4.3) was used.

9.7.2.3 PROCEDURE

Due to time constraints towards the end of this project, the heave tracking performance of the proposed heave controller could not be tested with a wide range of frequencies. Instead, only one additional frequency, 0.1 Hz, was tested and the data from the feed forward tuning test of Section 9.6.2 was used for comparison. The 0.1 Hz signal was sinusoidal with a position magnitude of 1 m peak-to-peak.

9.7.2.4 RESULTS

The velocity tracking response to the 0.1 Hz heave motion signal is provided in Figure 9.40. The maximum velocity error was 0.28 m/s and the RMS error was 0.08 m/s.

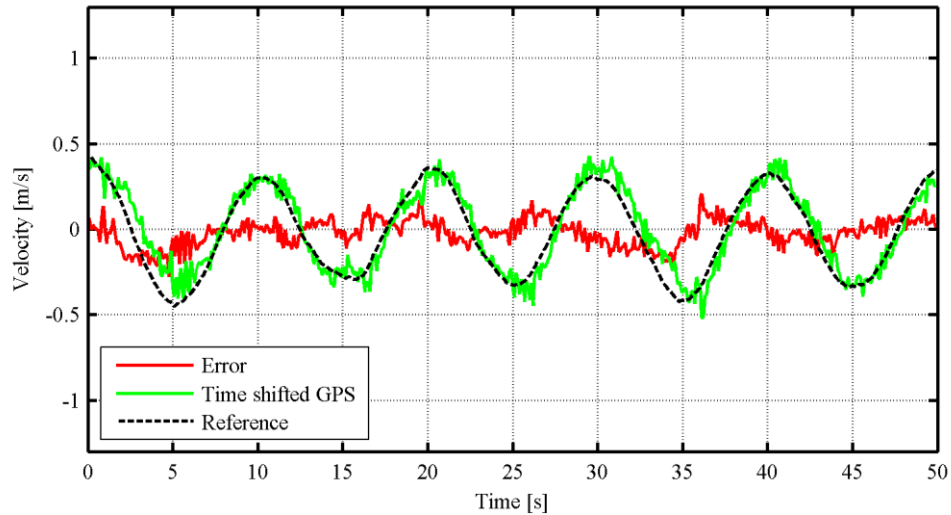


Figure 9.40 - Velocity response (flight; 0.10 Hz reference)

The position tracking response to the 0.1 Hz heave motion signal is provided in Figure 9.41. The maximum tracking error observed was 0.22 m and the RMS error was 0.07 m.

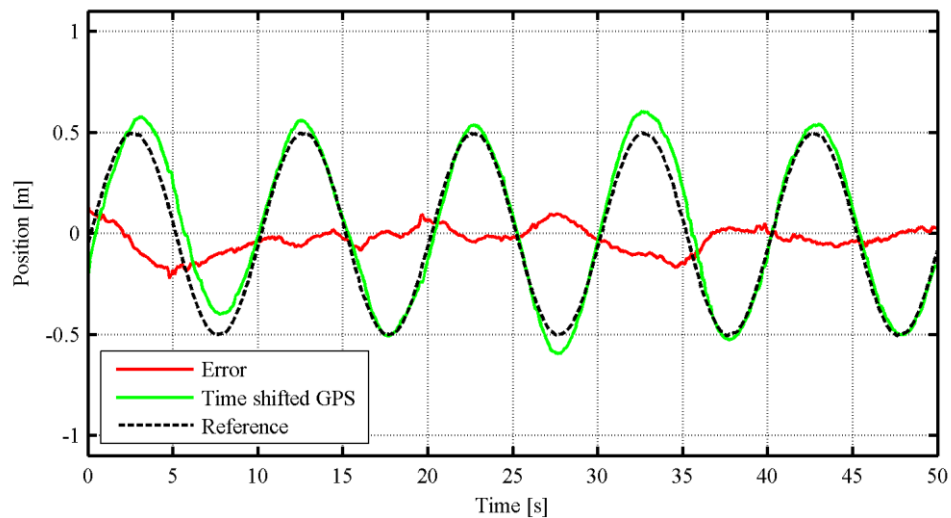


Figure 9.41 - Position tracking response (flight; 0.10 Hz reference)

The tracking errors in response to both practically tested signals, 0.1 Hz and 0.2 Hz, are provided in Table 9.8. As in Table 9.7, the velocity RMS errors are normalised by the peak-to-peak reference signal magnitude. The velocity and position errors for the two frequencies were similar.

	Velocity (m/s)			Position (m)	
	Max E	RMSE	NRMSE	Max E	RMSE
0.1 Hz	0.28	0.08	0.13	0.22	0.07
0.2 Hz	0.33	0.15	0.12	0.20	0.08

Table 9.8 - Reference frequencies vs. heave tracking errors (flight)

9.7.2.5 CONCLUSION

The bandwidth of the proposed heave controller is at least 0.2 Hz in practical flight conditions. As this is the bandwidth of the 3-DOF platform it is acceptable for the current project. Further tests should be performed during future projects to determine the limits of the proposed heave controller.

9.8 SUMMARY

Practical estimator tests and practical low-level controller tests were detailed in this chapter. After a number of modifications the new helicopter system developed to meet the requirements for this project achieved stable near-hover automated flight. In order to address the effects of GPS latency on heave motion estimates the GPS latency magnitude was determined and was compensated for by filter replay. The proposed heave controller's feed forward gains were optimised and the heave motion tracking performance of the controller was found to be sufficient for tracking the heave motion of the 3-DOF platform when simulating ship motions.

10. PRACTICAL TESTING: HIGH-LEVEL CONTROL

10.1 INTRODUCTION

The practical high-level controller tests referred to in Chapter 7 are detailed in this chapter. Take-offs and landings were performed manually by a safety pilot for all tests. As the approach is simply an application of the helicopter's original waypoint navigation controller, this chapter focuses on the performance of the descent and touchdown states of the landing state machine. Through these tests the success of the system integration is also tested.

In order to introduce a moving platform into HIL simulations a MATLAB Simulink block was developed to interface with either the SMPLCA application or the platform's ground station software via UDP. The block feeds platform motion data to the existing ground model in order to simulate a moving platform. A 3D model of a ship is used to represent the platform in OpenGL.

10.2 VIRTUAL LANDING - SINUSOIDAL SHIP DATA

10.2.1 FLIGHTS (2014-04-17)

10.2.1.1 AIM

The purpose of the virtual landing test was to test the basic functionality of the landing state machine and to test the performance of the timed deck landing descent controller.

10.2.1.2 SYSTEM

The helicopter's estimators and low-level controllers were configured as they were for the flight sinusoidal reference tracking flight of Section 9.7.2. The high-level controllers were implemented as described in Chapter 7 except that, in order to provide a slower descent during initial high-level controller tests the prediction algorithm was configured to provide a prediction horizon of 10 s. The *descent altitude* parameter of the virtual landing mode was set to 7 m.

10.2.1.3 PROCEDURE

The SMPLCA application was configured to provide a 0.1 Hz, 1 m peak-to-peak heave motion reference to simulate platform measurements. The landing state machine was used to transition from general waypoint navigation flight to a platform heave tracking state directly above the platform. After performing platform heave tracking for 60 s, predicted landing opportunities were monitored. When a landing opportunity became available the landing state

machine transitioned to the track deck descent state. Once the landing time expired the helicopter entered a heave coasting state and a second later it entered a position hold state to complete the landing on the virtual platform. This process was repeated twice.

10.2.1.4 RESULTS

The inertial down position data recorded during of one of the descents is illustrated in Figure 10.1 with a virtual touchdown occurring at 20 s. The measurements are all shifted down by 7 m so that the error can be plotted on the same system of axes without requiring a very large y-axis. As in Chapter 9, the helicopter is represented by time shifted GPS measurements.

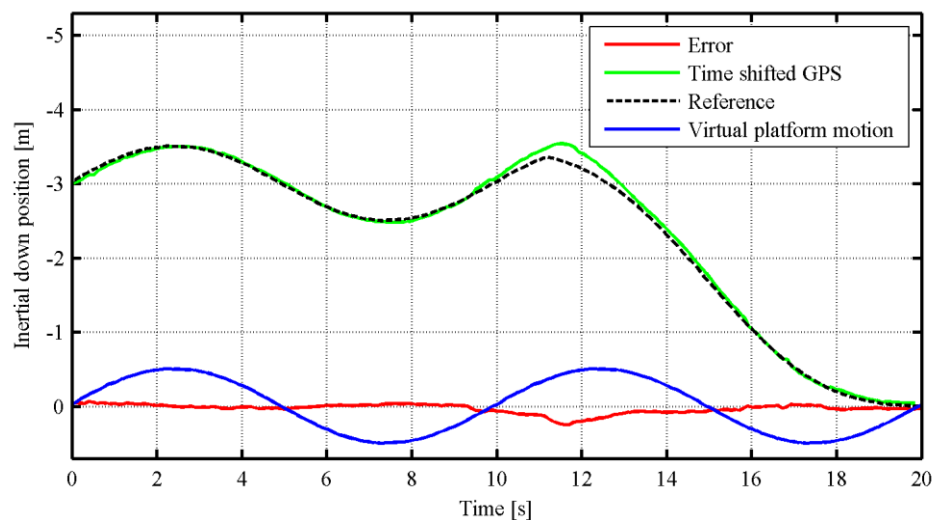


Figure 10.1 - Position response during landing (flight; 0.10 Hz platform reference)

After the initial descent transient the helicopter follows, both descents which were executed followed the desired descent trajectory to within 0.1 m. Virtual touchdowns were observed to within 0.2 s of the tracked landing opportunity. As a result the relevant landing criteria were close to perfect at touchdown: for both descents the relative heave velocity between the helicopter and the platform was within -0.44 m/s, under the -0.80 m/s limit, and virtual platform acceleration was within 0.02 m/s², about 10% of the virtual platform acceleration peaks.

10.2.1.5 CONCLUSION

Through the use of the timed deck landing descent controller, the landing state machine achieves accurate and timeous platform landing descents. The conditions observed at virtual touchdowns suggest that the landing state machine can also achieve safe touchdowns.

10.3 ACTUAL LANDING - STATIONARY SHIP DATA

10.3.1 FLIGHTS (2014-05-01)

10.3.1.1 AIM

The purpose of this flight test was to perform an initial test of the full landing state machine (ending in touchdown), to determine the performance of the helicopter near and on the platform and to test the fully integrated system.

10.3.1.2 SYSTEM

The system was configured similarly to how it was configured for the previous flight test, except that the helicopter was configured to perform an actual landing instead of a virtual landing and the physical platform and its software was used instead of a virtual platform.

10.3.1.3 PROCEDURE

The platform's was configured to remain stationary throughout the flight test. The helicopter used the landing state machine to navigate to a position above the platform and, as soon as a valid landing time was received from the SMPLCA application, to perform a descent to the platform. At touchdown the landing arrestor system captured the helicopter securely on the platform and the touchdown state of the landing state machine was executed.

10.3.1.4 RESULTS

The inertial down position data recorded during the descent is illustrated in Figure 10.2. Touchdown is observed at 20 s. The data is offset by the stationary platform position to facilitate comparisons with the error signal which is plotted on the same system of axes. The helicopter is represented by the time shifted GPS measurements.

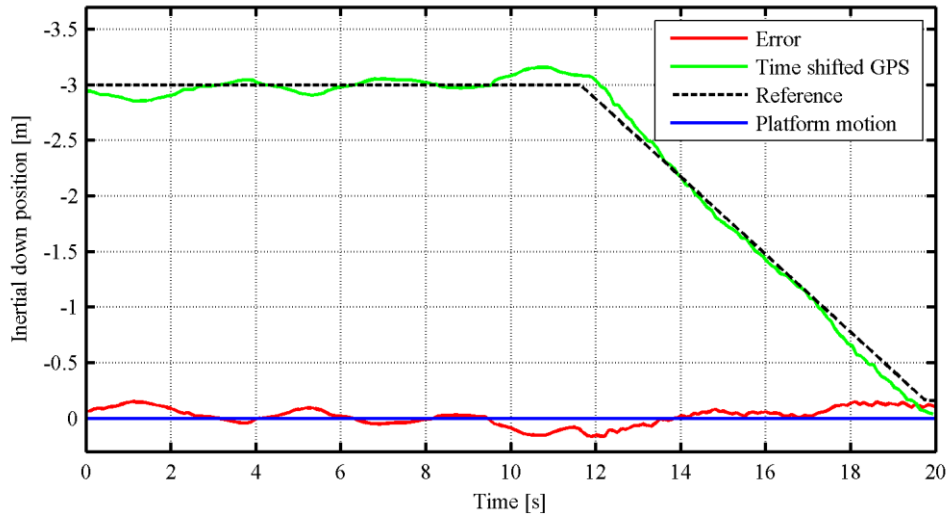


Figure 10.2 - Position response during landing (flight; stationary platform)

Touchdown occurred approximately 0.5 s early, hence the 0.16 m error. Of concern was the lateral and longitudinal position throughout the deck tracking and descent states. While deck tracking during this flight simply entailed holding a fixed position above the platform, it did not hold its position well as illustrated in Figure 10.3. Landing took place approximately a metre away from the desired position, on the edge of the platform. The landing arrestor system held the helicopter firmly in place where it landed.

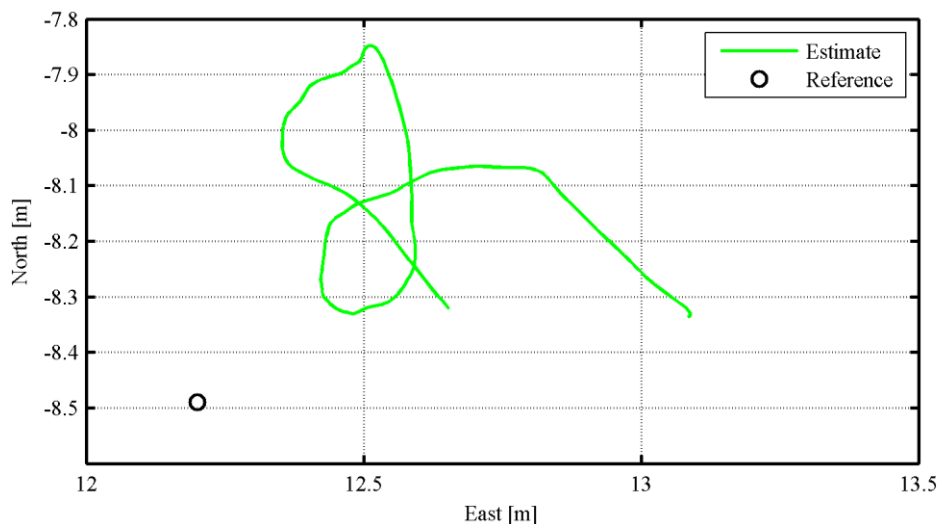


Figure 10.3 - Aerial plan during landing (flight; stationary platform)

10.3.1.5 CONCLUSION

While a successful landing was performed, landing was performed on the edge of the available platform. The helicopter's lateral and longitudinal controllers therefore perform too poorly for platform landing operations and require rework in future projects. The acceptable

lateral and longitudinal position bounds were narrowed to an error magnitude of 0.6 m to prevent such landings from occurring too close to the edge of the platform in future.

10.4 ACTUAL LANDING - SINUSOIDAL SHIP DATA

10.4.1 HIL SIMULATION

10.4.1.1 AIM

The purpose of this simulation was to demonstrate that the system is capable of performing platform landings in the HIL environment.

10.4.1.2 SYSTEM

The SMPLCA application was configured to provide a prediction horizon of 5 s. The landing state machine was configured for actual landings.

10.4.1.3 PROCEDURE

The platform was configured to follow a 0.20 Hz, 1 m peak-to-peak sinusoidal heave signal. The landing state machine guided the helicopter to a lateral and longitudinal position above the platform. Thereafter deck tracking took place and, when the SMPLCA application identified a suitable landing opportunity, descent took and touchdown took place.

10.4.1.4 RESULTS

The inertial down position data recorded during the landing procedure is provided in Figure 10.4. The data was offset by the mean platform motion to facilitate comparisons with the error signal which is plotted on the same system of axes. The time shifted GPS measurements represent the helicopter. Touchdown took place at 20 s.

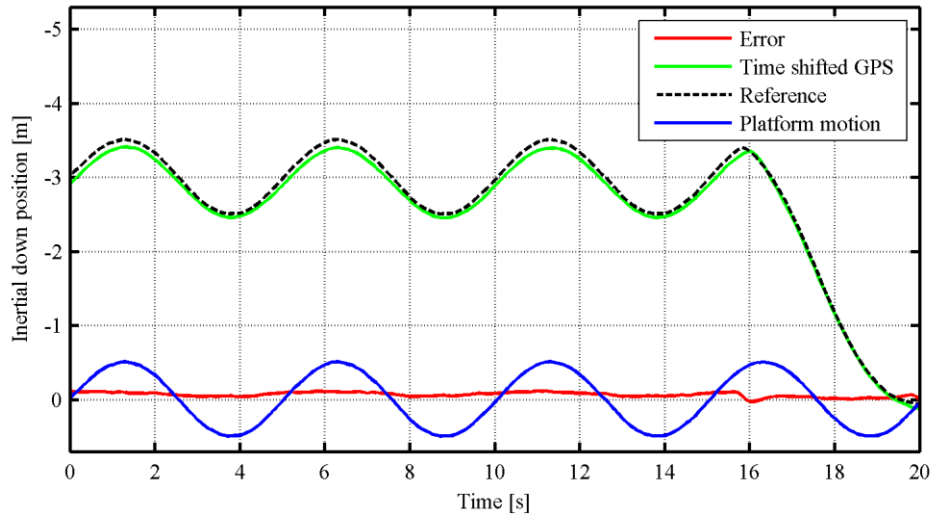


Figure 10.4 - Position response during landing (HILS; 0.20 Hz platform motion)

Landing took place 0.1 s early. As a result the target heave motion was missed by 0.1 m. This resulted in a platform acceleration of -0.16 m/s^2 at touchdown, 20% of the peak value. The relative velocity between the helicopter and the platform was -0.67 m/s at touchdown, within the -0.80 m/s limit. Unlike the practical flight test of Section 10.3, the lateral and longitudinal position of the helicopter remained well within acceptable bounds throughout the landing procedure as illustrated in Figure 10.5.

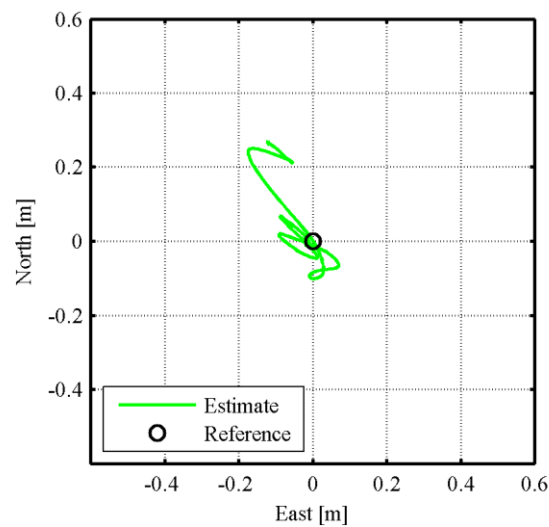


Figure 10.5 - Aerial plan during landing (HILS; 0.20 Hz platform motion)

10.4.1.5 CONCLUSION

The ideal landing opportunity was missed by a small margin which still resulted in acceptable landing conditions. Therefore the system is capable of performing helicopter landings on the

platform while it is performing heave motions with a 0.20 Hz, 1 m peak-to-peak sinusoidal motion.

10.5 ACTUAL LANDING - REAL SHIP DATA

10.5.1 HIL SIMULATION

10.5.1.1 AIM

The purpose of this simulation was to demonstrate the ability of the helicopter to land on a platform which is simulating the motion of a real ship.

10.5.1.2 SYSTEM

The system was configured identically to the previous simulation. As the ship motion dataset available did not include heave acceleration data the acceleration feed forward component of the helicopter's heave controller was effectively disabled.

10.5.1.3 PROCEDURE

The platform was configured to follow references of a real ship motion dataset recorded at sea state 4. The helicopter's landing state machine guided the helicopter from general waypoint navigation to the deck tracking state. Upon receiving information about a suitable future landing opportunity from the SMPLCA application the helicopter descended and touched down on the platform.

10.5.1.4 RESULTS

The inertial down position data recorded during the simulation is provided in Figure 10.6. The data is offset by the desired heave position at landing in order to facilitate comparisons with the error signal. The helicopter is represented by the time shifted GPS measurements.

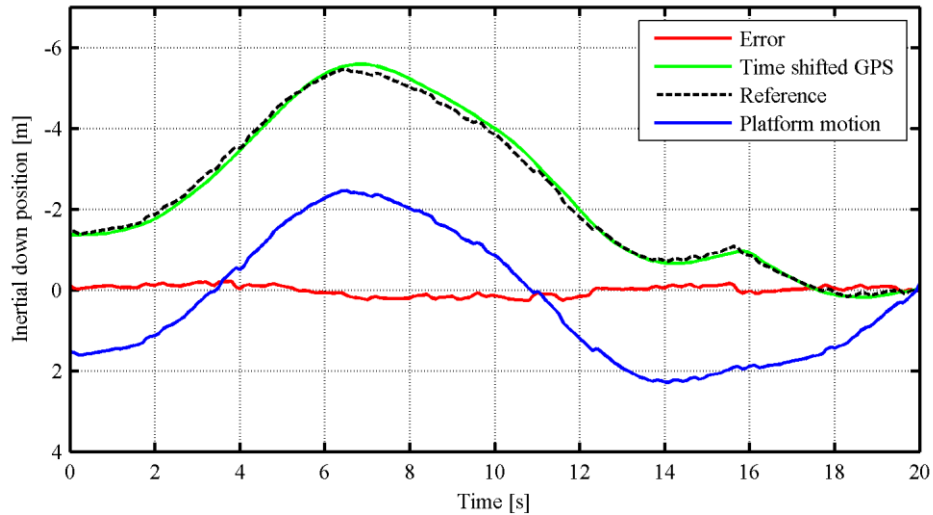


Figure 10.6 - Position response during landing (HILS; real ship platform landing)

Landing took place within 0.02 s of the desired landing opportunity, with a heave position error of approximately 0.01 m. The relative velocity between the helicopter and the platform at touchdown was -0.73 m/s, within the -0.80 m/s limit. As platform acceleration data was not available to the helicopter during this simulation platform acceleration information is not available for this touchdown. Platform roll and pitch states were within $\pm 3^\circ$ and $\pm 0.5^\circ$ respectively. Lateral and longitudinal position control remained well within the acceptable error bounds of 0.6 m.

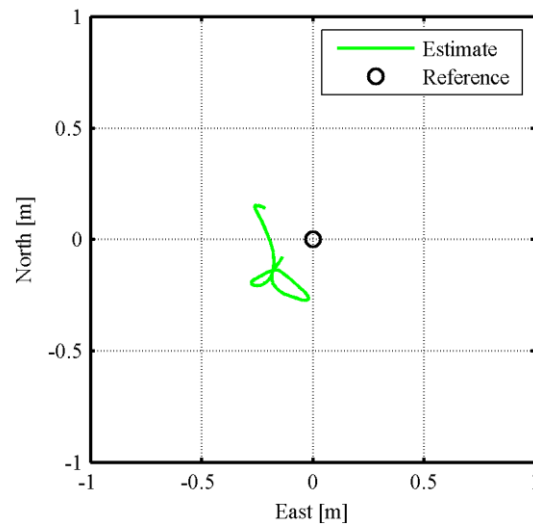


Figure 10.7 - Aerial plan during landing (HILS; real ship platform landing)

10.5.1.5 CONCLUSION

The system is capable of performing landings on a platform which is simulating real ship motion at sea state 4.

10.6 SUMMARY

The timed deck landing controller and landing state machine achieved accurate and timeous platform landing descents and safe touchdowns. Practically, landings were performed on a virtual platform with a 0.2 Hz, 1 m peak-to-peak sinusoidal heave motion and on the real platform in a stationary configuration. Due to poor lateral and longitudinal position control the remaining tests were performed during hardware-in-the-loop simulations where landings on a platform with a 0.2 Hz, 1 m peak-to-peak sinusoidal heave motion and on a real ship at sea state 4 were demonstrated.

11. CONCLUSIONS & RECOMMENDATIONS

11.1 CONCLUSIONS

A moving platform landing algorithm for an unmanned autonomous helicopter was successfully designed based on existing ship deck landing algorithms and a number of systems were developed in order to implement the landing algorithm.

An MCA-based ship motion prediction algorithm was implemented and software was developed for the real-time execution thereof. Platform motion criteria, helicopter motion criteria and environmental criteria were developed. These criteria were analysed in real-time in order to determine suitable landing opportunities. The result was a system which can identify valid landing opportunities in real ship motion data recorded at sea state 4 for up to 5 s into the future with a 75% success rate. Considering the stochastic nature of sea surface waves and the resulting prediction difficulty, this is viewed to be a significant result.

In order to allow the helicopter to track the heave motion of a platform which is simulating the motion of a ship, its estimators and heave controller were modified. The bandwidth of the heave estimator was increased using GPS latency compensation. A basic platform motion estimator was implemented. The bandwidth of the heave controller was increased with the addition of velocity and acceleration feed forward terms. The result was a system with a heave control bandwidth of at least 0.20 Hz, as verified during practical flight tests. This is very close to the highest significant frequency of 0.22 Hz observed in ship motion data available to the ESL and therefore indicates that the helicopter can track the heave motion well of a platform which is simulating the motion of a ship at sea state 4 and lower.

In order to guide the helicopter to land at a specific landing opportunity a relative descent controller and a suitable landing state machine were developed. After integrating the various systems, practical testing of the system was conducted. A stationary platform landing was demonstrated successfully during flight tests, verifying the functionality of the high-level controllers and the integration of the system. Landings on a platform simulating the motion of a ship at sea state 4 were demonstrated successfully in hardware-in-the-loop simulations.

It was not possible to perform moving platform landings during flight tests due to the poor inertial north and east position control of the helicopter. As the tuning of the lateral and longitudinal controllers was outside the scope of this project, this problem was not addressed. The accuracy with which virtual landings were performed during flight tests and the accuracy with which moving platform landings were performed during simulations suggest that, had

the inertial north and east position control been better, moving platform landings would have been possible during flight tests.

Overall, a suitable moving platform landing algorithm was designed and implemented successfully, while testing was a partial success as moving platform landings were completed in simulations but not during practical flight tests.

11.2 RECOMMENDATIONS

11.2.1 PREDICTION

OpenCV 2.2 and lower uses the LAPACK library to calculate SVDs [50]. The inferior performance in subsequent versions where a different implementation is used [51] motivates migration of the prediction algorithm from an OpenCV implementation to a direct LAPACK implementation.

The batch processing nature of the MCA-based prediction algorithm is computationally demanding. Adaptive MCA should be considered to lower the computational demand.

11.2.2 LANDING CRITERIA

Landing criteria analysis via EI could not be used in this project as no past platform landing data were available to test the EI limits. After gathering much platform landing data, EI limits should be determined and EI should be used for landing criteria analysis as it provides wider landing envelopes.

11.2.3 ESTIMATOR

Poor inertial north and east position estimates as well as lateral and longitudinal velocity estimates are possibly partially to blame for the inertial north and east position control problem. An improved estimator is needed for these states of motion.

11.2.4 MAGNETOMETER

The large amount of magnetic interference experienced by the magnetometer used on the helicopter suggests that it should be relocated to a position which is less susceptible to magnetic interference.

11.2.5 CONTROLLERS

Due to the limited time available for flight testing towards the end of this project, the performance limits of the heave controller proposed in this project were not established during practical flight tests. Further tests should be performed to determine these limits.

A detailed theoretical design of the inertial north and east position controllers as well as the lateral and longitudinal controllers should be completed and the design should be tested and fine-tuned during practical flight tests. The addition of integrators on the position loops may improve position holding capabilities.

11.2.6 RF LINK

While the RF link currently used functions very well, in future one may want to increase the demands on the RF link (for example to send more platform motion states to the helicopter).

The current definition of RF communication slots states that a communication slot is defined from the start of the first transmission until the end of the last transmission. While this definition is necessary for a slot where both modules send and receive data, during a slot where only one module transmits and where the following slot will also be started by transmission from that module, the definition of a communications slot can be changed slightly. In such cases a communications slot needs to only be defined from the beginning of transmission until the end of transmission. This has a few advantages. Firstly, more time is available for data transmission. Additionally, the subsequent slot could be started without the need for channel initialisation, saving further time. With such a configuration it may be possible to send DGPS correction packets during two (or even just one) slot. This would open another one (or two slots) for telemetry receipt. Either more telemetry could be received during this (these) slot (s) or the original telemetry could be divided among the three or four telemetry slots. This would further allow for a greater platform motion data stream.

Currently 35 ms is spent at the start of each transmission on channel initialisation. After the first channel initialisation it should not be necessary to reinitialise the channel if the channel session is maintained. The SY parameter (time before initialisation) on the MaxStream RF module defines a channel expiration time [71]. If no data is sent or received within the defined time, the channel expires and a reinitialisation is required with the next transmission. MaxStream recommends setting this parameter to 100 ms longer than the delay between transmissions. A value of 100 ms or 200 ms should therefore be set quite safely. MaxStream does warn that this setting reduces the robustness of the link, especially in a noisy environment. With the 2.4 GHz transmitter used by the safety pilot during flight tests, noise levels can be quite high at times. Preliminary tests showed that with SY set to 200 ms, packet loss increased and the decision was made to revert to the default setting of 0 where channel initialisations occur during every transmission. This should be reinvestigated with another antenna configuration as discussed next.

While the 3 dBi antenna currently used by the ground station's RF module is suitable for the current application, a directional antenna would provide greater signal gain in the direction where it is actually used, improving link robustness. A highly directional antenna with an active helicopter tracking mechanism could be built, but less complicated alternatives exist. The positional boundaries of nominal flight could be defined and an antenna with suitable horizontal and vertical beam widths could be selected.

A dual-radio setup can also be considered. One radio can be dedicated to data transmission and another radio can be dedicated to data receipt.

If data rate requirements are still not met, another radio system should be considered. The ESL's SLADe project has had limited success with a Wi-Fly system.

11.2.7 HILS

Numerous problems were experienced with the ESL's hardware-in-the-loop simulation setup. Communications between the Simulink environment and the OBC are often plagued with delays. These delays could be addressed with a real-time HIL implementation.

A. 3-DOF PLATFORM

A.1 INTRODUCTION

The three degrees of freedom (3-DOF) platform required for the task at hand must:

- be able to simulate the roll, pitch and heave motion typically experienced on a ship's flight deck accurately and safely
- provide a landing surface suitable for helicopter landings
- include a landing arrestor system

The ESL's original 3-DOF platform system, the modifications made to it to meet the above requirements and testing of the modified system are described in this appendix.

A.2 ORIGINAL SYSTEM

The system has a 2350 x 1776 mm steel base. Attached to the base are three pneumatic pistons with a stroke of 1200 mm. The pistons' air inlets are attached to proportional directional control valves which are fed by the central departmental air supply available at the ESL. Attached to the pistons is a 1400 x 1200 mm aluminium platform. A drawing of the main mechanical system of the platform is shown in Figure A.1. An orthographic drawing of the base-piston-valve-platform assembly is shown in Figure A.2.

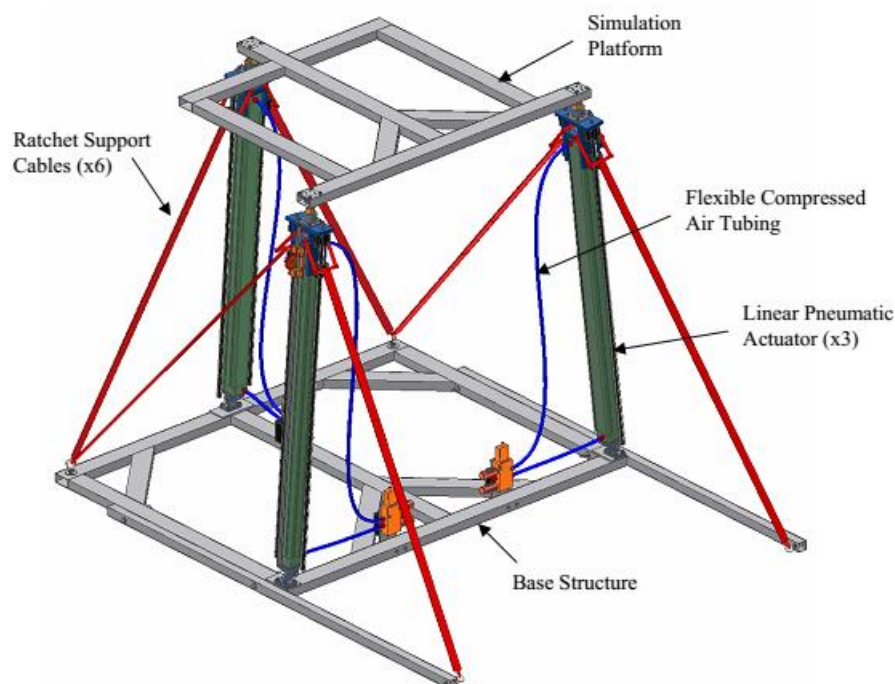


Figure A.1 - Main mechanical system of the original 3-DOF platform [7]

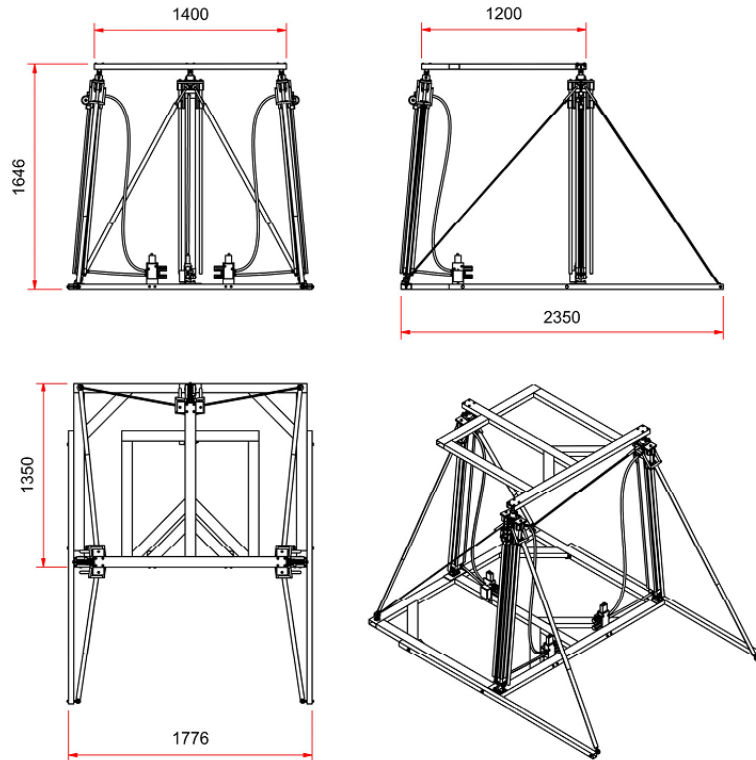


Figure A.2 - Orthographic drawing of base-piston-valve-platform assembly [7]

The piston extensions are controlled via the proportional directional control valves by PIC microcontrollers (one per valve) running sliding mode control systems. All three piston extension position references are sent from a PC (running Borland C++ ground station software) to one of the microcontrollers via an RS232 interface. The receiving (master) microcontroller uses the reference applicable to the piston which it controls and sends the other two references to the other (slave) microcontrollers via a CAN interface. Piston extension position feedback is provided to the microcontrollers by quadrature encoders mounted on the pistons. A detailed description of the system is presented by Smit [7].

In order for the system to achieve its goal of simulating ship roll, pitch and heave motions, Smit derived functions for the conversion of ship motion to piston motion and vice-versa [7]. The ship states used in the conversion functions are defined in the axis system of the target ship as shown in Figure A.3. The ship's attitude is defined in the Euler 3-2-1 angle sequence.



Figure A.3 - Target ship

Figure A.4 shows the platform system aligned with the target ship's axis system. The piston numbers shown correspond to the numbers used in the actual assembled system. The red dot is the point around which all the motions occur and is referred to as the platform's *zero point*.

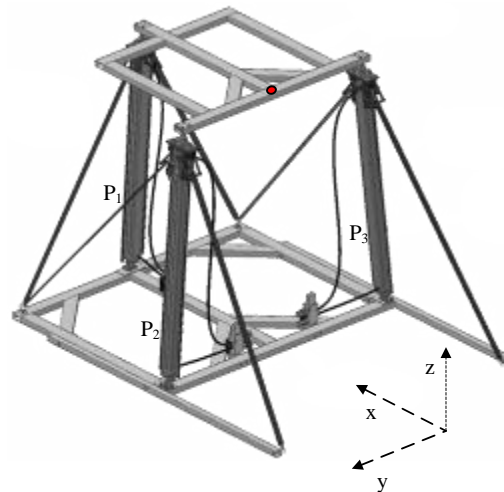


Figure A.4 - Platform system aligned with target ship axis system [7]

While the full performance specifications of the system were not explicitly stated by Smit, the performance of the system in response to a number of reference inputs was presented [7]. One of the sets of reference inputs is a set of sinusoidal heave, pitch and roll inputs. The results are summarised in Table A.1.

	Frequency (Hz)	Amplitude (peak to peak)	RMS error	Maximum error (+/-)
Heave	0.2	600 mm	4.31 mm	8 mm
Pitch	0.2	20°	0.12°	0.3°
Roll	0.2	20°	0.14°	0.4°

Table A.1 - Platform performance indicators

It is important to note that the errors are relative to a version of the references which was synchronised with the phase of the measurements as Smit considered phase errors to be of little significance for the task of the platform.

A.3 MODIFICATIONS

The original system is not suitable for helicopter landings. The shortcomings of the original system and the implemented modifications are discussed next. These modifications were made by the author and various ESL lab engineers. In order to document the system thoroughly, all modifications are described and reference is made to relevant ESL engineers where credit is due.

A.3.1 MECHANICAL

A.3.1.1 LANDING SURFACE

The original simulation platform is not suitable for helicopter landings due to its small, discontinuous surface. A larger, continuous surface is required to allow the helicopter some margin for lateral and longitudinal position error.

A suitable helicopter landing platform was designed and built [Runhaar]. In order to keep actuator demands as low as possible and to facilitate transportation, a light weight material was required. Aluminium was chosen due to its high strength to weight ratio [72]. To allow the helicopter some margin for lateral and longitudinal position error during landing operations, the platform's dimensions of 2.5 m by 2.5 m were chosen. To facilitate transportation, a design which allows the platform to be split into four 1.25 m by 1.25 m squares was chosen. To lower wind resistance and therefore reduce platform actuator and control demands, mesh panels were chosen for the squares. Aluminium frames were chosen to provide additional structural rigidity to the panels. The panels were welded to the frames to make up the squares and four squares were bolted to the simulation platform and fastened by heavy-duty cable ties.

It is important to note that the mesh reduces the ground effect (briefly discussed in Section 2.2) experienced by helicopters when flying close to the platform. While this is not representative of the ground effect experienced when flying close to a real ship's deck, it allows the problem at hand to be simplified slightly which is perfect for the incremental system design process in use.

A.3.1.2 LANDING ARRESTOR SYSTEM

In order to prevent the helicopter from making undesired motions after touching down on the platform the helicopter must be fastened to it with a suitable landing arrestor system at touchdown. A landing arrestor system is therefore required.

A landing arrestor system was designed and built. In order to keep the complexity of the system to a minimum heavy duty Velcro was employed to provide the fastening mechanism of the system. It has the additional advantage that it adds only a small amount of additional mass to the helicopter.

The loop side of 50 mm Velcro strips was attached to the foam on the helicopter's skids. The loop side was placed on the helicopter as it is less likely to pick up dirt if not landing on the platform.

The hook side of 25 mm Velcro strips was attached to the platform via a wooden frame. In order to use the least amount of Velcro while still providing sufficient arresting force, the frame was made up of a number of 0.2 x 0.2 m squares, smaller than half the length of the landing gear. Thereby, in the worst case, four Velcro strips would arrest the helicopter. This is illustrated well in Figure A.5. From the figure it is clear that if the helicopter was repositioned further longitudinally forwards or backwards it would still be attached by at least four strips of Velcro – there exists no possible orientation where the helicopter would be attached by only two Velcro strips.

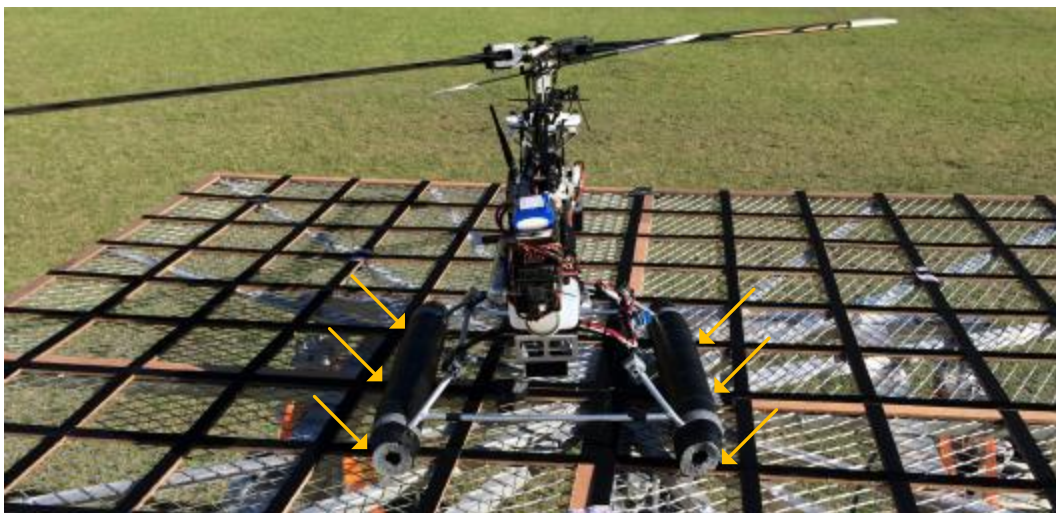


Figure A.5 - Landing arrestor near worst case (attachment points indicated by yellow arrows)

In order to test the arresting force experienced in the worst case, aluminium rods similar to the helicopter's landing gear were equipped with foam like the padding on the helicopter and 50 mm wide Velcro was attached to the foam. A wooden structure like the frame used on the

platform built and 25 mm wide Velcro was attached to it. A number of tensile strength tests were performed by attaching the items to each other in such a way that only four Velcro strips are in contact with each other and pulling the items apart slowly. The force which had to be exerted to pull the items apart was measured with a fish scale. The result of 15 tensile strength tests was that the arrestor system can provide a mean holding force of 157 N with a standard deviation of 17 N. The helicopter was removed from its landing gear and replaced with a dummy weight for initial arrestor system tests. Testing ceased out of concerns for the structural integrity of the landing gear when the landing arrestor successfully arrested the test item with an impact velocity of 3 m/s.

The main disadvantage of the arrestor system is that it is difficult to disengage. After touchdown on the platform it is necessary to remove the platform with the helicopter attached to it in order to carefully remove the helicopter from it.

A.3.1.3 AIR SUPPLY

The central departmental air supply originally used for the platform is not portable and can therefore not be used for flight tests. Additionally, the air supply is of too low pressure and can provide too little flow rate to operate the system reliably. The lack of pressure regulation is also problematic. Finally, the lack of air supply filtering exposes the pistons and valves to impurities which may shorten their operational lives.

Three Mac-Afric GAS 3065 petrol engine powered air compressors equipped with 70 litre reservoirs and delivering 360 l/min at up to 8 bar [73] were acquired to meet the platform system's pneumatic demands and to make the platform portable [Alberts, Basson, Beeton, Runhaar]. In an attempt to stabilise the pressure in the system, a filter-regulator was acquired for the system [De Jager]. As its name suggests, the filter-regulator also filters the air supply: water is separated and solid particles are filtered out.

The modified mechanical system is shown on its own in Figure A.6 and the platform and the helicopter are shown in Figure A.7.



Figure A.6 - Modified mechanical system



Figure A.7 – Helicopter and platform

A.3.2 SAFETY

The original system offers very limited safety features. It aborts when ground station to microprocessor or master microprocessor to slave microprocessor communication failures occur. It also provides a software emergency stop function.

A.3.2.1 EMERGENCY STOP

As the emergency stop function is only implemented in software, the only way to immediately shut down the original system upon software failure is by turning off its power

supply, situated very close to the platform. Shutting down the system could therefore pose a dangerous situation.

A system was built which allows the ground station operator to disconnect power to the system via a remotely operated relay [Beeton]. While this system relies on the relay working at the very least, it is more robust than the software abort previously implemented.

A.3.2.2 ABORT LIMITS

The original system provides no minimum or maximum extension protection or maximum roll and pitch angle protection.

The motion limits detailed in Table A.2 were implemented. With the new limits in place the system shuts down if it is close to minimum or maximum stroke on any of the pistons or if the measured roll or pitch angles are close to the mechanical limits of the platform. The limits are adjustable from the ground station software.

	Min extension (m)	Max extension (m)	Max pitch (deg)	Max roll (deg)
Manual control	0.000	1.016	27	27
Auto control	0.179	1.016	10	10

Table A.2 - Platform motion limits

The reference limits detailed in Table A.3 were also implemented. The references which are commanded are monitored and, if they exceed any of the limits, the system shuts down. A full system shut down is preferred to reference clamping as clamped references may lead to undesirable motions.

	Min extension (m)	Max extension (m)	Max pitch (deg)	Max roll (deg)
Manual control	0.000	1.111	30	30
Auto control	0.084	1.111	13	13

Table A.3 - Platform reference limits

A.3.3 CONTROL

A.3.3.1 SHIP RECORDING POINT TRANSFORMATION

The functions for the conversion of ship heave motion states at the ship's INS recording point to the ship's flight deck provided by Smit [7] require revision. The heave position at the ship's flight deck (H_{FD}) is the sum of the heave position at the ship's INS recording point (H_{RP}) and the inertial down component of the vector between the ship's INS recording point and the ship's flight deck (\mathbf{o}). As illustrated in Figure A.8, vector \mathbf{o} is defined as follows in the ship's body frame:

$$\mathbf{o} = [x_o \quad y_o \quad z_o]^T \quad (\text{A.1}).$$

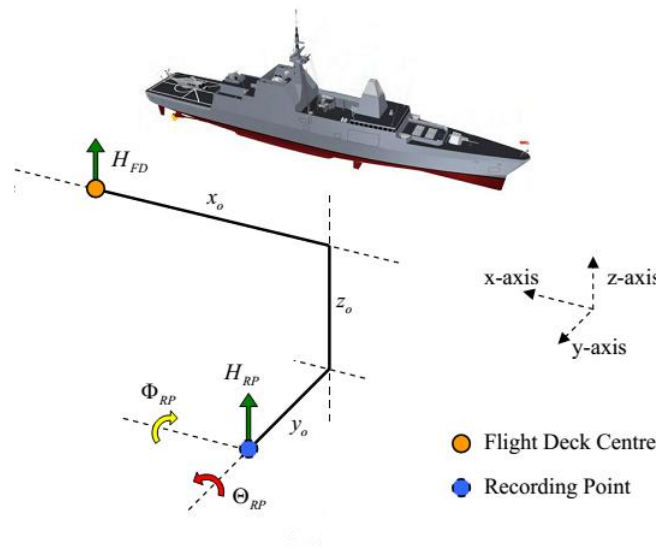


Figure A.8 - Ship axis system [7]

The inertial down component of vector \mathbf{o} is required. Therefore the vector must be transformed to the NED frame. The following direction cosine matrix (DCM) is suitable for the transformation from the NED frame to the ship's body frame using the axis definitions given in Figure A.8 and the Euler 3-2-1 angle sequence:

$$DCM(-\Phi, \theta, -\Psi) = \begin{bmatrix} \cos \theta \cos(-\Psi) & \cos \theta \sin(-\Psi) & -\sin \theta \\ \sin(-\Phi) \sin \theta \cos(-\Psi) - \cos(-\Phi) \sin(-\Psi) & \sin(-\Phi) \sin \theta \sin(-\Psi) - \cos(-\Phi) \cos(-\Psi) & \sin(-\Phi) \cos \theta \\ \cos(-\Phi) \sin \theta \cos(-\Psi) - \sin(-\Phi) \sin(-\Psi) & \cos(-\Phi) \sin \theta \sin(-\Psi) - \sin(-\Phi) \cos(-\Psi) & \cos(-\Phi) \cos \theta \end{bmatrix} \quad (\text{A.2}).$$

The inverse DCM must be used for the transformation from the ship's body frame to the NED frame:

$$\begin{bmatrix} N_{FD} \\ E_{FD} \\ H_{FD} \end{bmatrix} = DCM^{-1} \begin{bmatrix} x_o \\ y_o \\ z_o \end{bmatrix} + \begin{bmatrix} N_{RP} \\ E_{RP} \\ H_{RP} \end{bmatrix} \quad (\text{A.3}).$$

H_{FD} , the heave position at the ship's flight deck, is required. As the ship's roll, pitch and heading angles are known, the DCM is known. As vector \mathbf{o} is known in the ship's body frame, x_o , y_o and z_o are known. Finally, the inertial position of the recording point and therefore N_{RP} , E_{RP} and H_{RP} are known. The last row of equation (A.3) is considered separately:

$$H_{FD} = x_o[DCM^{-1}]_{3,1} + y_o[DCM^{-1}]_{3,2} + z_o[DCM^{-1}]_{3,3} + H_{RP} \quad (\text{A.4}).$$

As DCM is orthogonal its inverse is equal to its transpose. Therefore equation (A.4) can be rewritten as

$$H_{FD} = -x_o \sin \Theta + y_o \sin(-\Phi) \cos \Theta + z_o \cos(-\Phi) \cos \Theta + H_{RP} \quad (\text{A.5})$$

or, taking into account the signs of the angles,

$$H_{FD} = -x_o \sin \Theta - y_o \sin \Phi \cos \Theta + z_o \cos \Phi \cos \Theta + H_{RP} \quad (\text{A.6}).$$

\dot{H}_{FD} , the heave rate at the ship's flight deck can be found by taking the total derivative of equation (A.6):

$$\begin{aligned} \dot{H}_{FD} = & -x_o \dot{\Theta} \cos \Theta - y_o \dot{\Phi} \cos \Phi \cos \Theta + y_o \dot{\Theta} \sin \Phi \sin \Theta \\ & - z_o \dot{\Phi} \sin \Phi \cos \Theta - z_o \dot{\Theta} \cos \Phi \sin \Theta + \dot{H}_{RP} \end{aligned} \quad (\text{A.7}).$$

A.3.3.2 SHIP-PISTON-SHIP CONVERSION FUNCTION

The functions for the conversion of ship motion to piston motion and vice-versa provided by Smit [7] need to be revised as the piston numbering used in the conversion functions differs from the piston numbering in the actual assembled system:

- Piston 1 in the functions (p_1) is piston 2 in the actual assembled system (P_2)
- Piston 2 in the functions (p_2) is piston 3 in the actual assembled system (P_3)
- Piston 3 in the functions (p_3) is piston 1 in the actual assembled system (P_1)

The functions are modified to work with the actual assembled system. The outputs of the conversions from ship motion to piston motion (f_*) are swapped as shown in equations (A.8), (A.9) and (A.10). The inputs of the conversions from piston motion to ship motion (g_*) are swapped as shown in equations (A.11), (A.12) and (A.13).

$$P_1 = p_3 = f_3(h, \theta, \phi) \quad (\text{A.8})$$

$$P_2 = p_1 = f_1(h, \theta, \emptyset) \quad (\text{A.9})$$

$$P_3 = p_2 = f_2(h, \theta, \emptyset) \quad (\text{A.10})$$

$$h = g_h(p_1 = P_2, p_2 = P_3, p_3 = P_1) \quad (\text{A.11})$$

$$\theta = g_\theta(p_1 = P_2, p_2 = P_3, p_3 = P_1) \quad (\text{A.12})$$

$$\emptyset = g_\emptyset(p_1 = P_2, p_2 = P_3, p_3 = P_1) \quad (\text{A.13})$$

A.3.3.3 REFERENCE DELIVERY

In the original system the means of providing reference inputs to the microcontrollers is problematic. The Borland C++ application from which the references are sent to the microcontrollers is Windows-based. Windows is not a real-time operating system and can therefore not offer predictable timing accuracy [70]. High performance Windows-based timers frequently vary by 20 ms or more from one time step to the next. For the 100Hz control system in question, this is not acceptable.

The control reference timing issue was addressed by introducing an additional microprocessor which can read references from data files stored on a memory card [De Jager]. The additional microprocessor is also attached to the CAN bus. It becomes the master node and the old master becomes a slave. A suitable MATLAB-based data file creation script was also developed for the conversion of ship motion measurements into a data files suitable for use with the platform.

A.3.4 GROUND STATION

A.3.4.1 DEVELOPMENT ENVIRONMENT

The platform's Borland C++ ground station software was migrated to a Qt based application, the new standard platform for the ESL's ground station software [De Jager]. In addition to the base ground station software, real-time plots of the system output were implemented via QWT [52], an extension for Qt. These plots simplify system performance monitoring and therefore also simplify the calibration process.

A.3.4.2 INTERFACING

The 3-DOF platform system must be able to send the platform's current motion states to other systems. The original system does not have interfaces suitable for communications with other systems and the only sensors available are the encoders on the pistons. The combined output of the sensors can provide local heave position and roll and pitch angles. While heave velocity

and acceleration and roll and pitch rates can be found approximately by taking the discrete derivatives of the respective positions and angles, such derivatives tend to be noisy. Additionally, the position states are not inertial.

In order to address the matter of a lack of direct access to angular rate and heave acceleration measurements, the fitting of an inertial measurement unit (IMU) to the platform is considered. Unfortunately the platform sometimes exhibits a jerky motion making for very noisy IMU measurements. Fortunately, because the commanded references are directly available, an alternative solution is available. The master node sends the current data file time stamp to the ground station at 10 Hz. This data is used to read the current references from a local copy of the data file. These references are shifted slightly to match the current measurements. Assuming that the measurements match the shifted references well, the shifted references essentially become clean measurements. The difference between the true measurements and the shifted references is monitored throughout system operation and an error indication is given if significant deviations occur.

Various solutions to the problem of a lack of inertial position states are considered. The differential GPS system currently in use by the ESL allows for its base station to be configured to operate as a moving base station [55]. The position information obtained from the base station in this mode provides the desired inertial states. One drawback of this approach is that it requires the expensive base station to be positioned close to the platform with its antenna mounted on the moving platform. This exposes the equipment to various risks and adds an additional obstacle for the landing helicopter to avoid. An alternative is to equip the platform with a roving GPS unit like the unit used on the helicopter. The roving unit is cheaper and its antenna smaller, addressing the problems identified with using the base station. The drawback of this approach is that the helicopter project then requires two roving units when only three are currently available in the ESL. An alternative solution is available via a modified version of the above mentioned method of shifting references. Before flight the helicopter is placed on the platform with its GPS antenna aligned with the platform's *zero point* and its inertial position is captured. The inertial position of the *zero point* is added to the shifted position references mentioned above to obtain the platform's current inertial position. The decision was made to use this approach.

A TCP server and a UDP interface were added to the ground station software to allow for communication with other systems. Platform status, reference source information, current time and all motion states are made available at 5 Hz via these interfaces. A MATLAB Simulink block was implemented which interfaces with the platform ground station software via its UDP interface.

A.3.4.3 SIMULATION MODE

It is impractical to assemble the entire 3-DOF platform system for initial software testing. While a hardware-in-the-loop (HIL) simulation is not available, a simulation mode is added where encoder measurements are simply replaced by the received references on the slave microprocessors. As far as the platform control system is concerned, it controls the system perfectly in this mode. While this is not useful for platform control performance analysis simulations, it is useful for initial software tests.

A.4 TESTING

The performance of the modified platform system was determined by practical testing. For the tests the entire platform system was assembled. The same valves and pistons were always paired to ease the calibration process executed at the beginning of every test [Beeton, Alberts]. The system was commanded to follow a 0.2 Hz, 0.8 m peak-to-peak sinusoidal heave reference. The heave, pitch and roll responses are shown in Figure A.9, Figure A.10 and Figure A.11 respectively.

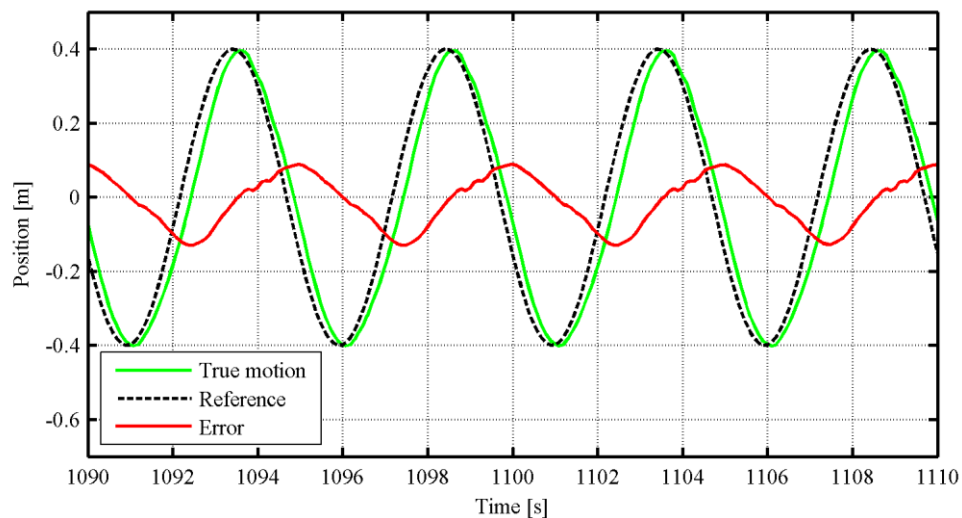


Figure A.9 - Platform heave response

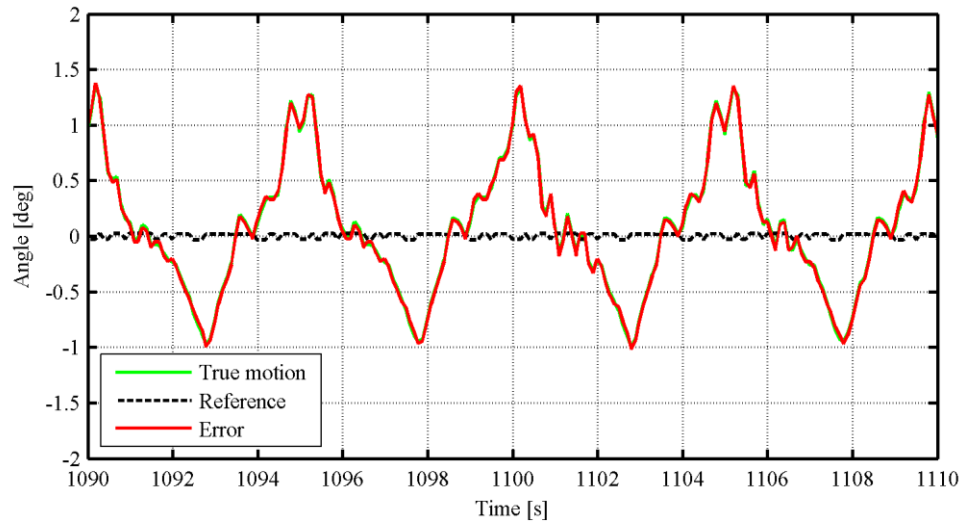


Figure A.10 - Platform pitch response

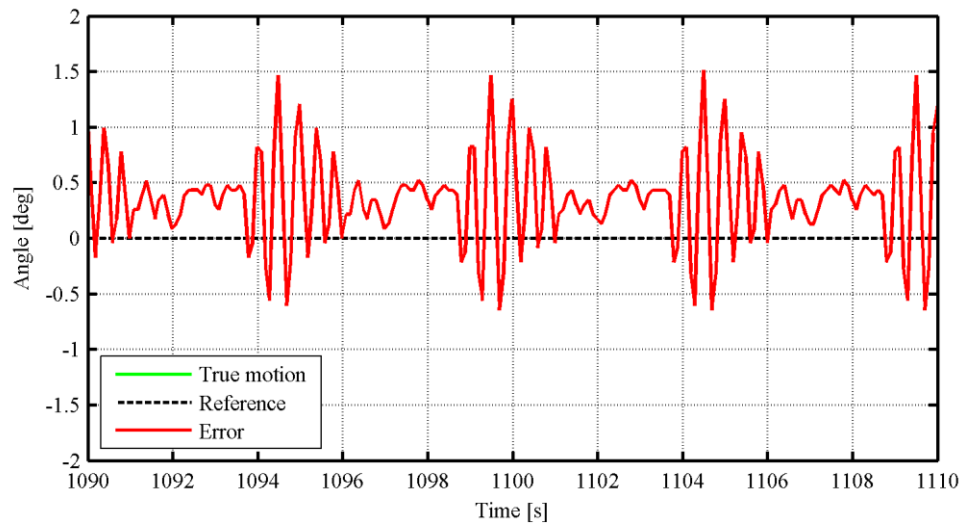


Figure A.11 - Platform roll response

From Figure A.9 it is clear that the heave response lags behind the references which results in errors of up to 130 mm. Jerky platform roll and pitch responses were observed during the test as illustrated in Figure A.10 and Figure A.11. These motions occur as the friction experienced by each piston differs slightly and because of the coupling between the pistons in the assembled system. Full performance details are detailed in Table A.4.

	Frequency (Hz)	Amplitude (peak-to-peak)	RMS error	Maximum error (+/-)
Heave	0.2	800 mm	71 mm	130 mm
Pitch	0.0	0°	0.61°	1.38°
Roll	0.0	0°	0.53°	1.51°

Table A.4 – Modified platform performance indicators

It is important to note that the errors were calculated without shifting the references to be in phase with the measurements as Smit did [7]. In order to compare the performance of the modified system with the original system the references were shifted to be in phase with the measurements as shown in Figure A.12. As roll and pitch references are zero throughout, the roll and pitch error is not affected by shifting the references.

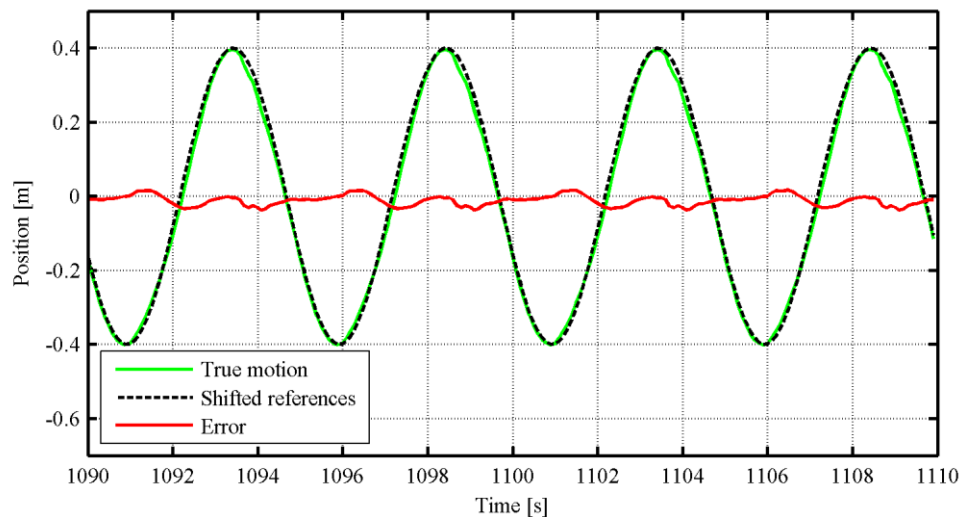


Figure A.12 - Platform heave response (time shifted 0.2 Hz references)

In order to determine if the phase lag of the platform varies in the 0.1 Hz to 0.2 Hz range, a 0.1 Hz heave reference was also tracked and its response was compared with references shifted by the same amount as the 0.2 Hz references were shifted above. The resulting response is shown in Figure A.13.

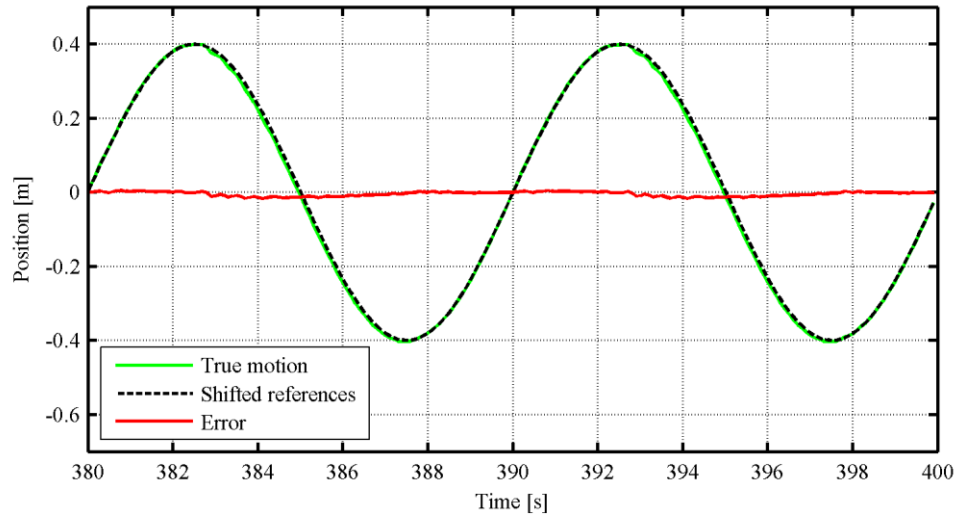


Figure A.13 - Platform heave response (time shifted 0.1 Hz references)

The performance observed during the tests is detailed in Table A.5.

Frequency (Hz)	Amplitude (peak-to-peak)	RMS error	Maximum error (+/-)
0.1	800 mm	8 mm	17 mm
0.2	800 mm	18 mm	39 mm

Table A.5 - Modified platform performance indicators (time shifted references)

While larger heave reference amplitudes were used for these tests than the tests which Smit performed, the errors observed were much larger than those observed by Smit. The tests performed by Smit must have been performed under ideal conditions. Despite the performance discrepancy, the errors observed are acceptable for the current application.

Further tests were attempted with varying roll and pitch references. In these tests the performance of the platform deteriorated drastically as the jerky motion referred to above was amplified. The system is therefore only suitable for the simulation of platform heave motions. The addition of another compressor to the system may reduce the effect of piston friction differences greatly enough to improve roll and pitch tracking performance to an acceptable level [Beeton, Alberts].

A.5 SUMMARY

The modified 3-DOF platform:

- is able to simulate the heave motion typically experienced on a ship's flight deck accurately and safely
- provides a landing surface suitable for helicopter landings
- includes a landing arrestor system
- makes accurate platform motion states available via TCP and UDP

The addition of another compressor to the system is believed to improve its ability to simulate roll and pitch motions.

B. SEA STATES

Table B.1 shows wind and wave data for various sea states for the North Atlantic as published in NATO Standard Agreement (STAGNAG) number 4194 [22].

Sea State No.	Significant Wave Height (m)		Sustained Wind Speed (kt)*		Percentage Probability of Sea State	Modal Wave Period (s)	
	Range	Mean	Range	Mean		Range **	Most Probable ***
0-1	0-0.1	0.05	0-6	3	0.70	-	-
2	0.1-0.6	0.3	7-10	8.5	6.80	3.3-12.8	7.5
3	0.5-1.25	0.88	11-16	13.5	23.70	5.0-14.8	7.5
4	1.25-2.5	1.88	17-21	19	27.80	6.1-15.2	8.8
5	2.5-4	3.25	22-27	24.5	20.64	8.3-15.5	9.7
6	4-6	5	28-47	37.5	13.15	9.8-16.2	12.4
7	6-9	7.5	48-56	51.5	6.06	11.8-18.5	15
8	9-14	11.5	56-63	59.5	1.11	14.2-18.6	16.4
>8	>14	>14	>63	>63	0.06	18.0-23.7	20

Table B.1 - NATO North Atlantic Sea State Definitions [22]

* Ambient wind sustained at 19.5 m above surface to generate fully-developed seas. To convert to another altitude, $H2$, apply $V2 \left(\frac{H2}{7(19.5)} \right)$

** Minimum is 5 percentile and maximum is 95 percentile for periods given wave height range.

*** Based on periods associated with central frequencies included in Hindcast Climatology.

C. LATERAL, LONGITUDINAL & HEADING CONTROL

C.1 INITIAL CONTROLLER TUNING TESTS

The lateral and longitudinal controllers were tuned in an attempt to improve their position holding abilities. The heading controller was tested to determine its accuracy. The same system configuration and general procedure was used as in Section 9.2.

C.1.1 FLIGHT 2: HEADING CONTROLLER VERIFICATION (2013-02-22)

C.1.1.1 AIM

The purpose of this flight test was to verify that the heading controller is able to maintain a fixed heading within 4° .

C.1.1.2 SYSTEM

The heading controller of the original helicopter system, as described in Section 6.6, was used for this flight test. For convenience, the block diagram of the heading controller is presented again in Figure C.1.

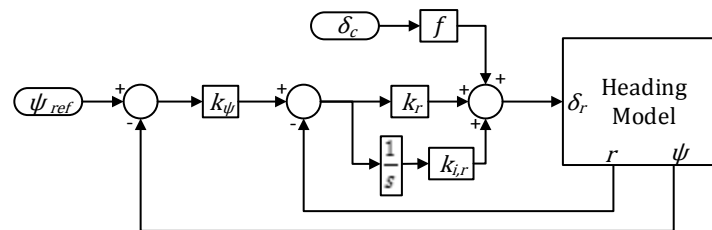


Figure C.1 - Block diagram of heading controller

The original heading controller gains, shown in Table C.1, were used for this flight test.

	k_ψ	k_r	$k_{i,r}$	f
G1	1	0.1	0.02	1

Table C.1 - Heading control gains for tuning flight

C.1.1.3 PROCEDURE

A 30° positive heading angle step manoeuvre was performed and the response was analysed.

C.1.1.4 RESULTS

The tail rotor command response to the heading step is provided in Figure C.2. The step was performed at 2 s. The commands were quite noisy because they were output by the yaw rate controller which is dependent on noisy gyro measurements. The dotted red lines are the command limits. The given commands were well within the limits.

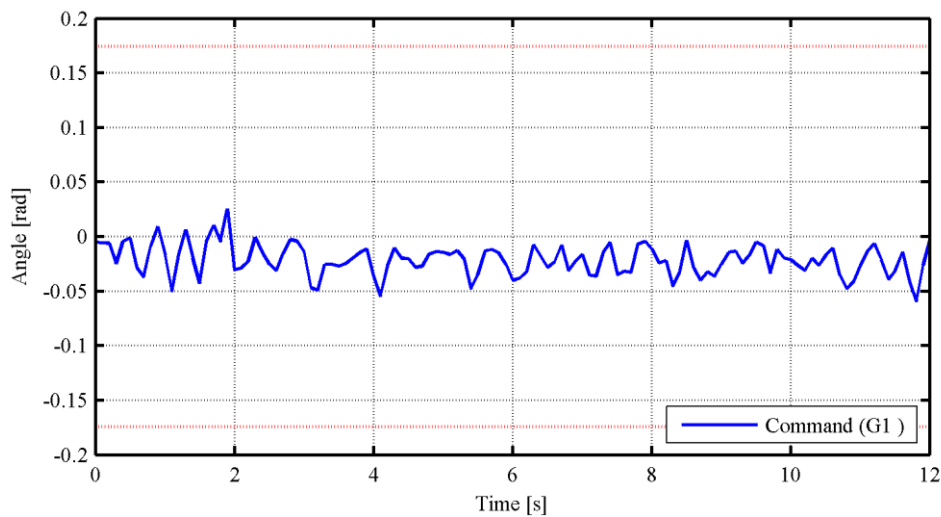


Figure C.2 - Tail rotor pitch command response

The yaw rate response to the heading step is provided in Figure C.3. Despite the large amount of noise present in the gyro measurements, the approximate average of the measurements followed the references well. The dotted red line is the yaw rate reference limit. It was not exceeded during the heading step.

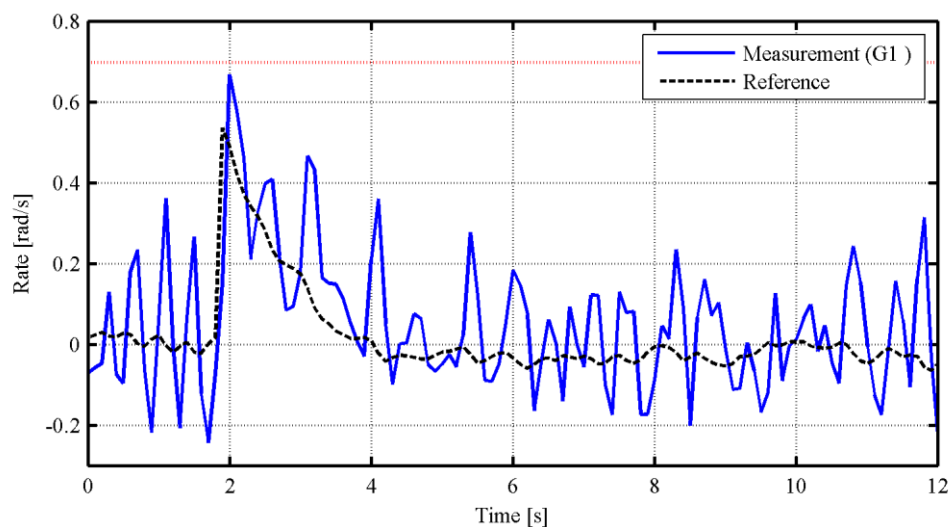


Figure C.3 - Yaw rate response

The heading angle response to the heading step is provided in Figure C.4. The heading angle error at steady state was a maximum of 3.8° or 0.066 rad.

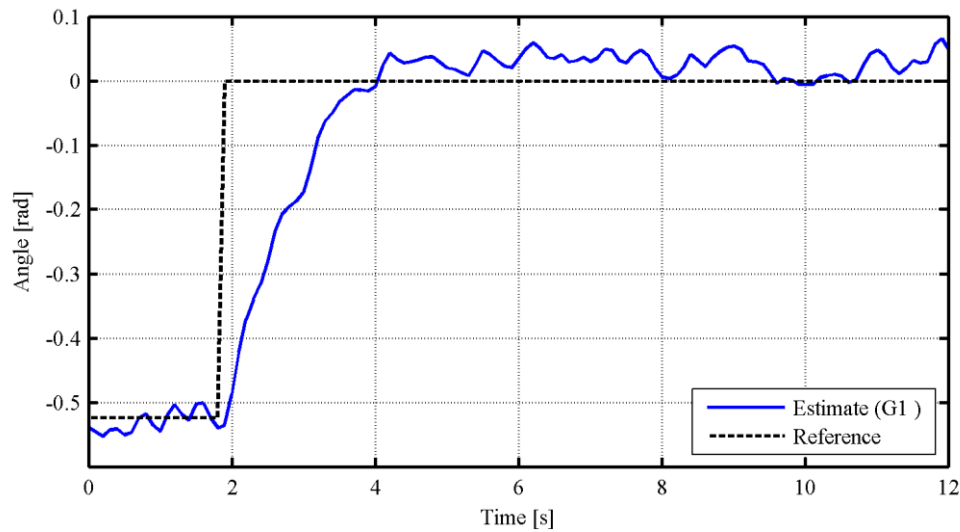


Figure C.4 - Heading angle response

C.1.1.5 CONCLUSION

The heading controller can maintain a fixed heading to within 4° or 0.07 rad and therefore meets its requirements.

C.1.2 FLIGHT 3: INERTIAL EAST & LATERAL CONTROLLERS TUNING (2013-02-22)

C.1.2.1 AIM

The purpose of this flight test was to tune the inertial east position, lateral velocity, roll angle and roll rate controllers to improve the inertial east position holding error of the controllers to 1.25 m.

C.1.2.2 SYSTEM

With a near-north heading the transformation matrix discussed in Section 6.2.1 maps the east component of an inertial vector almost directly to the lateral body axis. Therefore, in order to combine inertial east position controller tuning and lateral controller tuning in the same test, the test was performed with a near-north heading. The original helicopter system's inertial east position controller and lateral controllers were used in this test. A block diagram of the resulting combined controller is presented in Figure C.5.

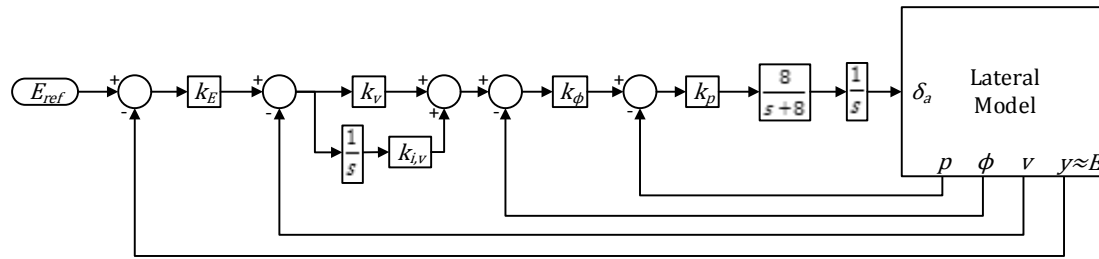


Figure C.5 - Block diagram of combined inertial east and lateral controller during near-north heading flight

In the block diagram, E is the inertial east position in metres, approximately equal to y , the lateral position, when a near-north heading is held. Additionally, v is the lateral velocity in metres per second, ϕ is the roll angle in radians, p is the roll rate in radians per second and δ_a is the lateral cyclic command in radians.

C.1.2.3 PROCEDURE

Controller tuning started with a slightly modified version (GIA in Table C.2) of the original control gains (GI): the ratio between the proportional and integral velocity gains was changed from 25:1 to 15:1. From near-north heading hover flight, position step commands were given: -5 m and +5 m in the lateral direction in the body frame. The response was observed from the ground. As none of the gain adjustment continuation criteria were violated, further gain adjustments were made.

The roll rate loop is the innermost loop and was therefore tuned first. The proportional roll rate control gain was increased by 30% (GIB in Table C.2). The same position step commands were given and the response did not violate the gain adjustment continuation criteria. This process was repeated with the proportional roll rate control gain at 70% greater than its original value (GIC).

As the controller was designed by a successive loop closure approach, the outer loop control gains could be increased by a smaller or equal percentage than the inner loop control gain while maintaining sufficient timescale separation. Accordingly, the control gains of the inertial east position, lateral velocity and roll angle loops were increased by 70% from their GIA values. Additionally, the proportional control gain of the roll rate loop was increased to a value 90% greater than its original value. This set of gains is referred to as GID . When step commands were given with these gains a control limit was hit. The gain adjustment continuation criteria were therefore violated and the gain adjustments for the lateral controller were brought to an end.

As small undesired roll oscillations were observed during the last position step the control gains were modified slightly post flight. The gains of the inertial east position, lateral velocity

and roll angle loops were decreased to values 60% greater than their *G1A* values. The new set of gains is referred to as *G2*.

	k_E	k_v	$k_{i,v}$	k_ϕ	k_p
G1	0.250	0.050	0.0020	1.40	0.50
G1A			0.0033		
G1B					0.85
G1C					
G1D	0.425	0.085	0.0057	2.38	0.95
G2	0.400	0.080	0.0053	2.24	

Table C.2 – Inertial east and lateral control gains for initial tuning flight

C.1.2.4 RESULTS

The lateral cyclic command responses to the positive position step manoeuvres are given in Figure C.6. An approximately 0.75 Hz command oscillation was introduced with the first increase of the inner loop control gain (*G1C*). The oscillation was more pronounced when the outer loop gains were also increased (*G1D*).

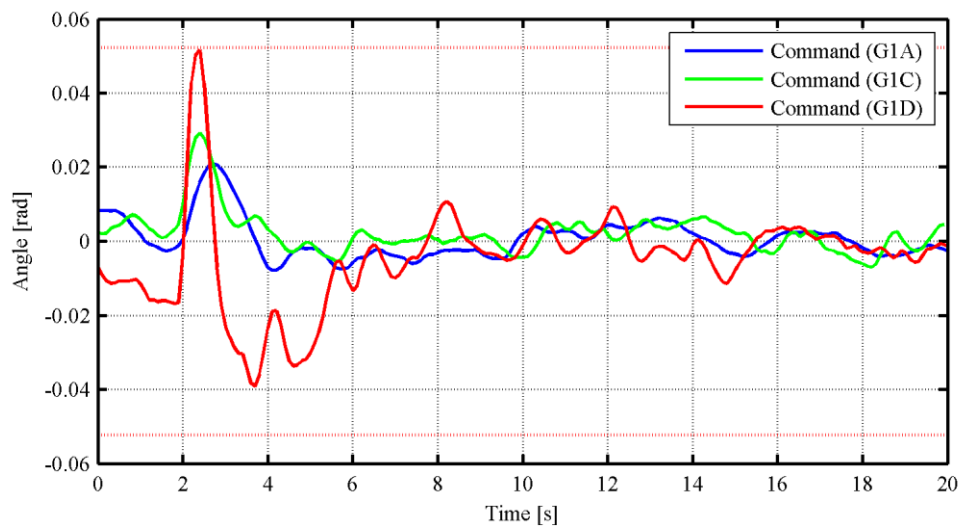


Figure C.6 - Lateral cyclic command

The roll rate responses to the positive position step manoeuvres are provided in Figure C.7. The roll rate controller followed the roll rate references well with the *G1C* and *G1D* controller gains. The oscillatory nature of the pitch rate response with *G1D* controller gains was likely

due to the high roll rate control gain which already introduced command oscillations with the *GIC* gains. The timescale separation between outer loops should be sufficient as the outer loop control gains were all increased by the same percentage.

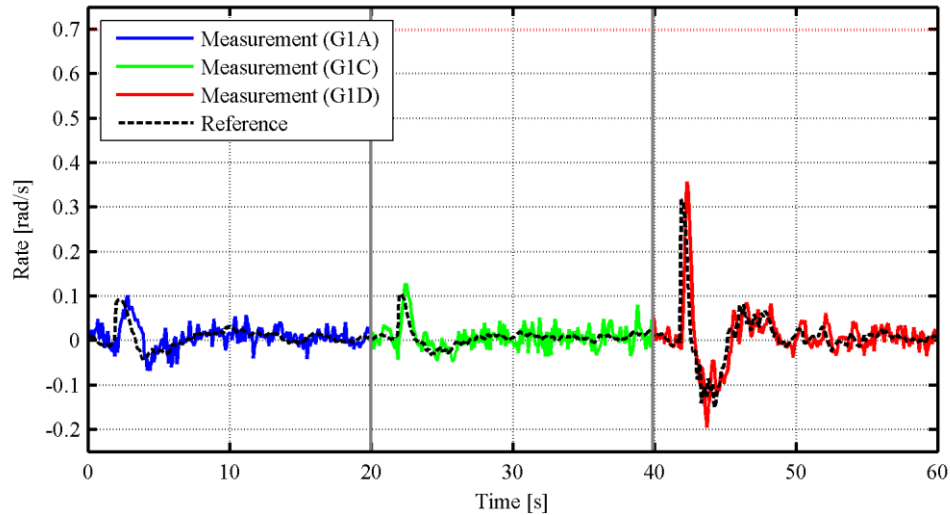


Figure C.7 - Roll rate response

The roll angle responses to the positive position steps are provided in Figure C.8. The roll angle controller followed the roll angle reference very well with the *GID* controller gains. With the *GID* gains an oscillatory motion was visible in the roll angle response.

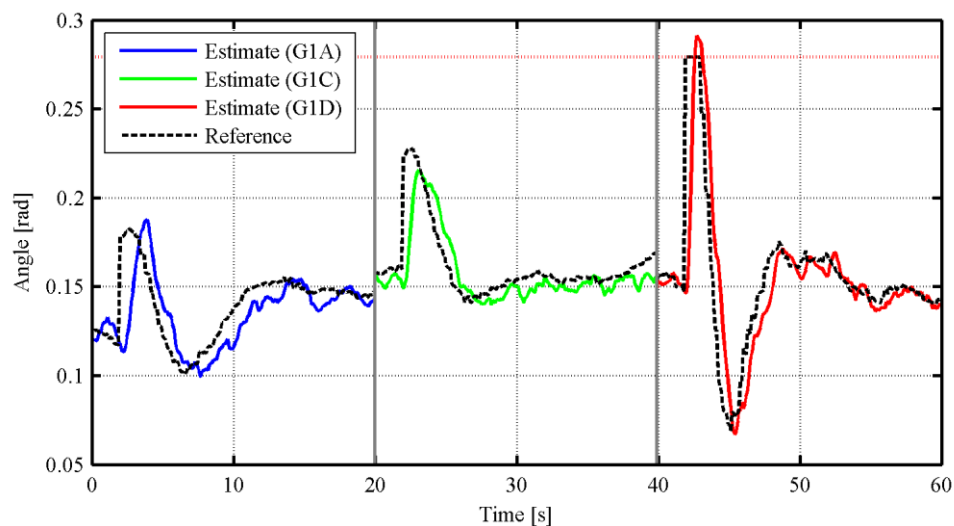


Figure C.8 - Roll angle response

The lateral velocity responses to the positive position steps are provided in Figure C.9. Marked improvements in velocity control were seen from the first gain change.

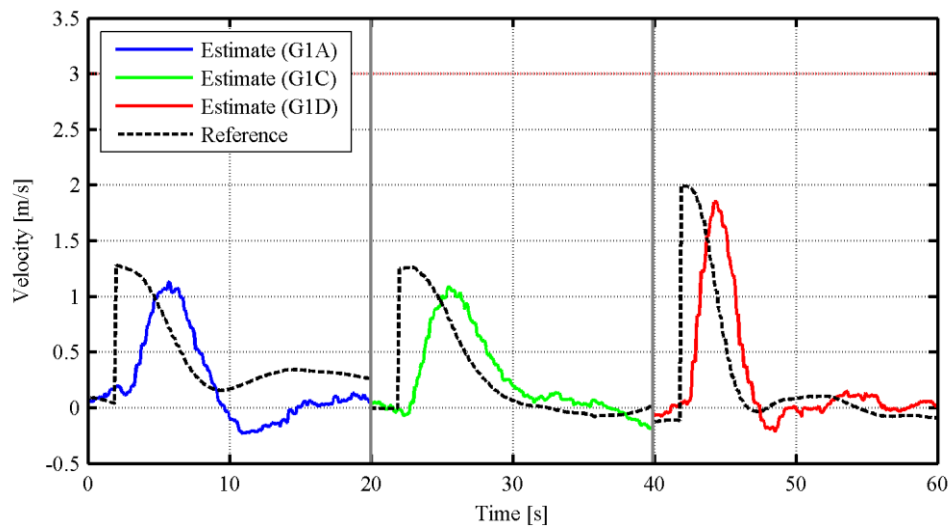


Figure C.9 - Lateral velocity response

The position responses to the positive position step manoeuvres are provided in Figure C.10. The position response of the controller with *G1A* gains was very slow and showed large errors 18 s after the step manoeuvre was performed. The controller with *G1C* had a similarly slow rise time but maintained a position error of less than 0.4 m from about 10 s after the position step was executed. The controller with *G1D* gains performed much faster than with the other gains and had a similar error as the controller with *G1C* gains 6 s after the position step was executed.

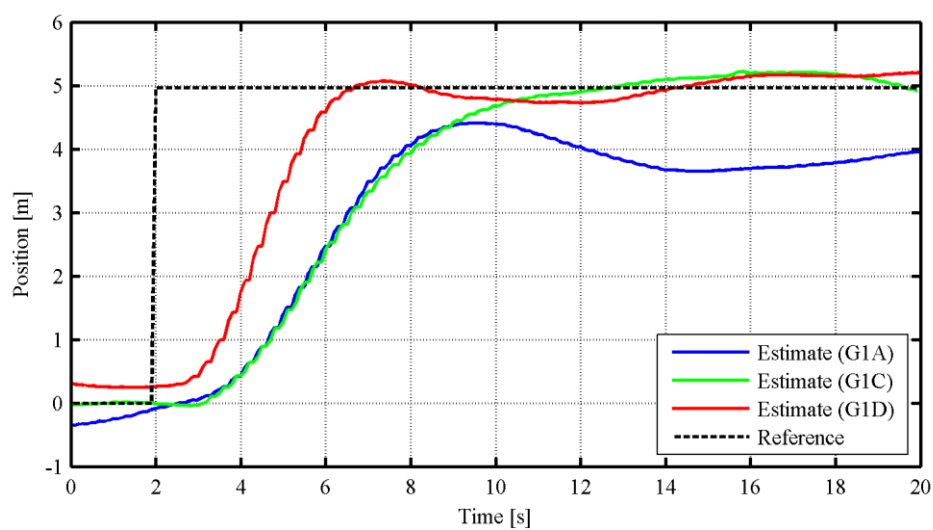


Figure C.10 - East position response

The lateral cyclic command, roll rate, roll angle, lateral velocity and inertial east position responses to the negative position steps performed are provided in Appendix D.2.1.

C.1.2.5 CONCLUSION

The inertial east position, lateral velocity, roll angle and roll rate controllers equipped with the *GIC* or *GID* gains of this section can hold a position to within 0.4 m. The faster response with the *GID* gains is preferred, but the roll oscillations present in the response is not desired. The *G2* gains chosen post flight but before the above analysis were chosen based on the assumption that the oscillations were due to a timescale separation issue between the roll rate loop and the roll angle loop. The analysis shows that the oscillations likely stem from a too high roll rate control gain. Further testing of this controller is required. Such testing and tuning was performed as discussed in Section C.2.

C.1.3 FLIGHT 4: INERTIAL NORTH & LONGITUDINAL CONTROLLERS TUNING (2013-02-22)

C.1.3.1 AIM

The aim of this flight test was to tune the inertial north position, longitudinal velocity, pitch angle and pitch rate controllers in order to hold a position within 1.25 m.

C.1.3.2 SYSTEM

With a near-north heading the transformation matrix discussed in Section 6.2.1 maps the north component of an inertial vector almost directly to the longitudinal body axis. Therefore, in order to include inertial north position controller tuning and longitudinal controller tuning in the same test, the test was performed with a near-north heading. The controllers of the original helicopter system were used. A block diagram of the resulting combined longitudinal controller is presented in Figure C.11.

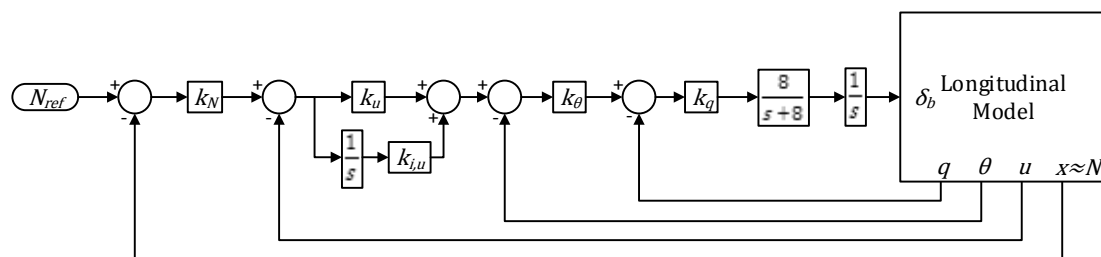


Figure C.11 - Block diagram of combined inertial north and longitudinal controller during near-north heading flight

In the block diagram, N is inertial north position in metres, approximately equal to x , the longitudinal position, when a near-north heading is held. Additionally, u is longitudinal

velocity in metres per second, θ is pitch angle in radians, q is pitch rate in radians per second and δ_b is the longitudinal cyclic command in radians.

C.1.3.3 PROCEDURE

Controller tuning started with a modified version (*GIA* in Table C.3) of the original control gains (*GI*): the ratio between the proportional and integral velocity gains was changed from 25:1 to 15:1 and the proportional pitch rate gain was increased by 100%. From near-north heading hover flight, position step commands were given: -5 m and +5 m in the longitudinal direction in the body frame. The response was observed from the ground. As none of the gain adjustment continuation criteria were violated, further gain adjustments were made.

As the controller was designed by a successive loop closure approach, the outer loop control gains could be increased by a smaller or equal percentage than the inner loop control gain while maintaining sufficient timescale separation. Accordingly, the control gains of the inertial north position, longitudinal velocity and pitch angle loops were increased by 70% from their *GIA* values. The proportional control gain of the pitch rate loop was retained. This set of gains is referred to as *G2*. When step commands were given with these gains a control limit was hit. The gain adjustment continuation criteria were therefore violated and the gain adjustments for the lateral controller were brought to an end.

	k_N	k_u	$k_{i,u}$	k_θ	k_q
G1	0.250	0.050	0.0020	1.40	0.50
G1A			0.0033		1.00
G2	0.400	0.080	0.0053	2.24	

Table C.3 – Inertial north and longitudinal control gains for initial tuning flight

C.1.3.4 RESULTS

The longitudinal cyclic command responses to the negative position step manoeuvres are shown in Figure C.12. Command oscillations with a frequency of approximately 0.75 Hz were introduced with the first gain change (*GIA*) where only pitch rate gains were adjusted. Assuming that the original gains (*GI*) did not result in oscillatory commands, this suggests that the *GIA* rate gains are too high.

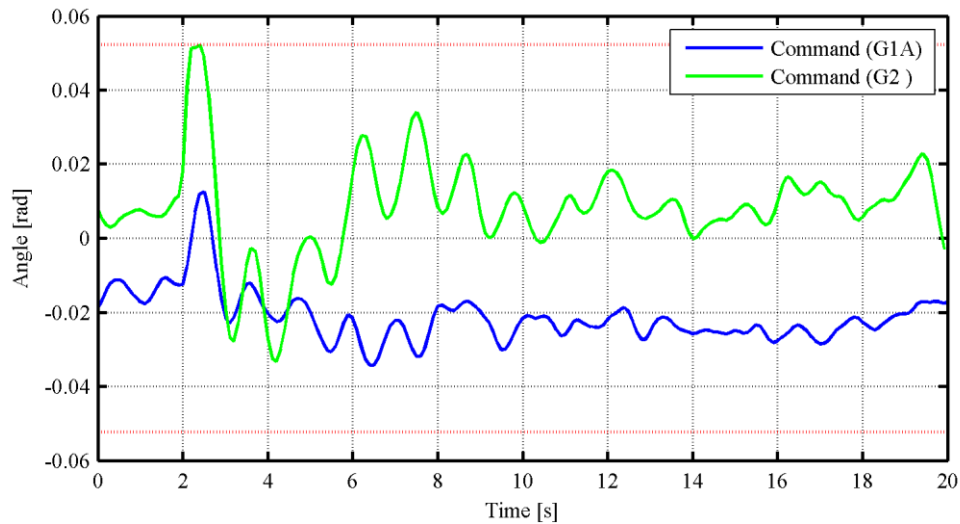


Figure C.12 - Longitudinal cyclic command response

The pitch rate responses to the negative position steps are provided in Figure C.13. The oscillatory nature of the pitch rate responses likely stemmed from the too high pitch rate control gain.

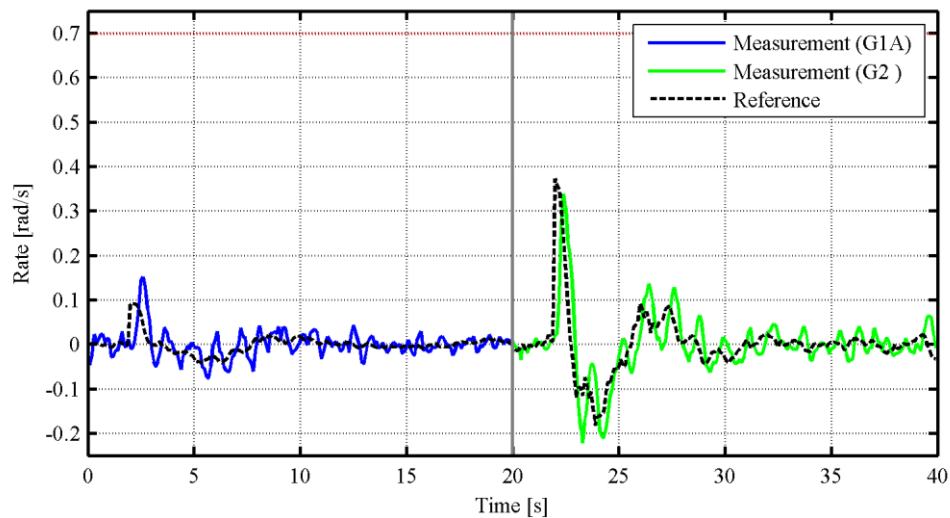


Figure C.13 - Pitch rate response

The pitch angle responses to the negative position steps are provided in Figure C.14. The oscillatory nature of the pitch angle responses was most likely also a result of the high pitch rate control gain.

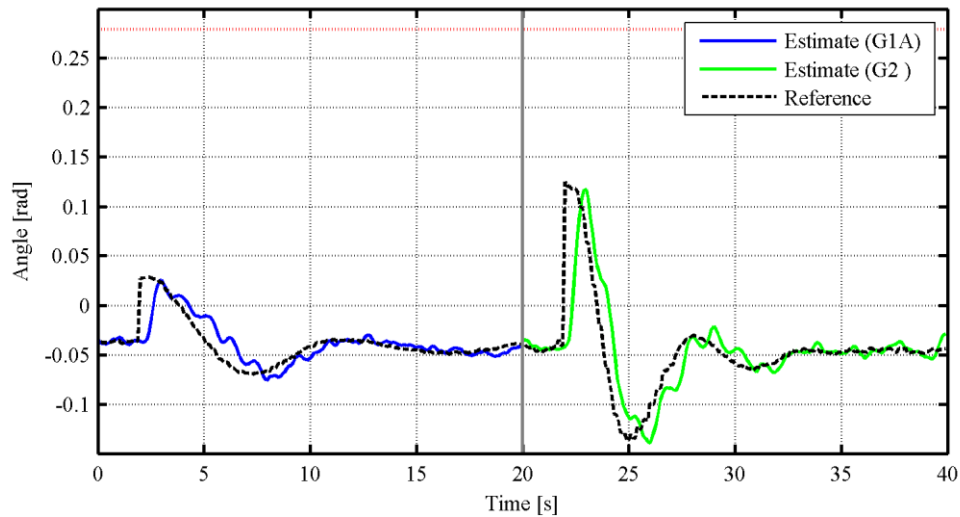


Figure C.14 - Pitch angle response

The longitudinal velocity responses to the negative position steps are given in Figure C.15. The response with $G2$ gains was much faster than the response with $G1A$ gains.

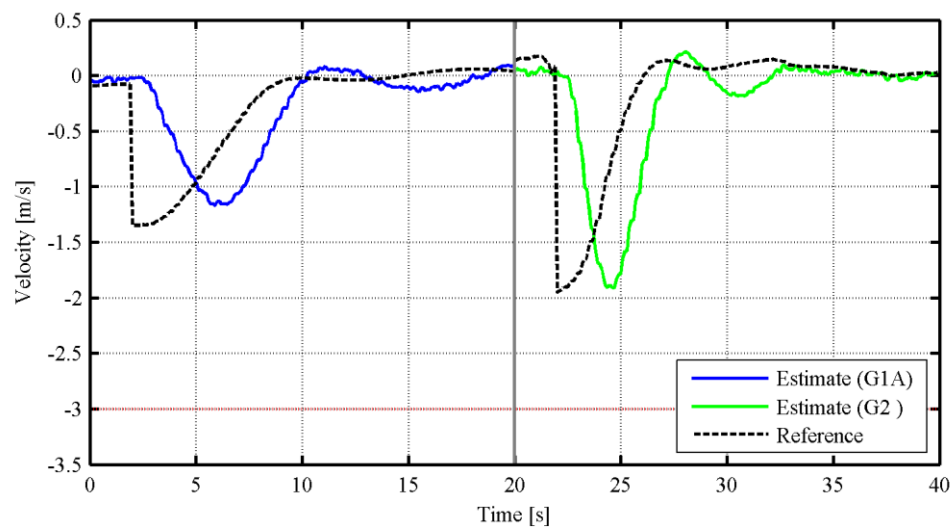


Figure C.15 - Longitudinal velocity response

The inertial north position responses to the negative position steps are provided in Figure C.16. The controller with $G1A$ gains holds the reference inertial north position to within approximately 0.3 m from about 7 s after the position step was commanded. The controller with $G2$ gains maintained the reference position to within a similar error from about 3.5 s after the position step was executed.

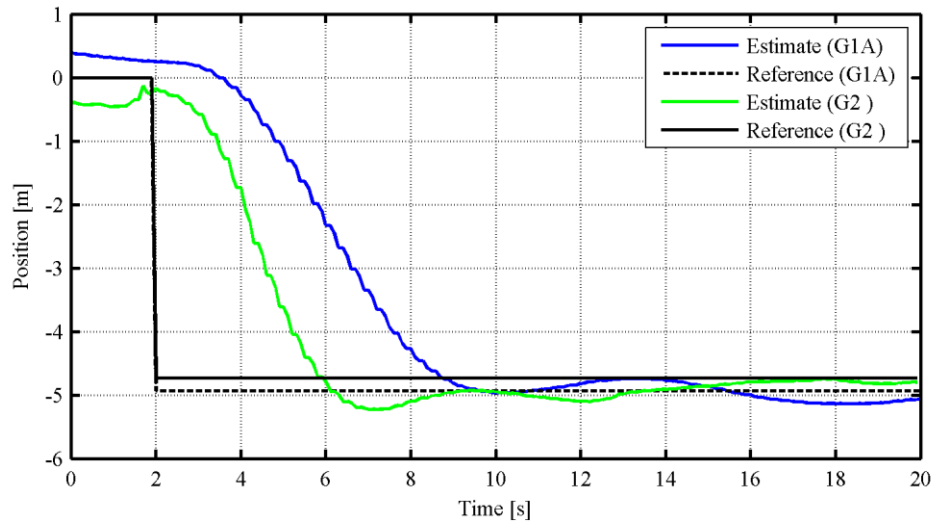


Figure C.16 - North position response

The longitudinal cyclic command, pitch rate, pitch angle, longitudinal velocity and inertial north position responses to the positive position steps performed are provided in Appendix D.3.1.

C.1.3.5 CONCLUSION

With the newly determined control gains the combination of the inertial north position, longitudinal velocity, pitch angle and pitch rate controllers can hold an inertial north position to within 0.3 m. The oscillatory pitch motions, likely stemming from a too high pitch rate control gain, are concerning and justify further controller tuning. Such tuning is described in Section C.2.

C.2 FURTHER CONTROLLER TUNING TESTS

The pitch and roll oscillations mentioned above justified further lateral and longitudinal controller tuning. As lateral and longitudinal controller tuning is not the focus of this project and due to the limited amount of practical flight testing time available the manoeuvres performed for this section were integrated into other flight tests. The tests were therefore spread across a number of flight test occasions.

C.2.1 FLIGHTS (2013-11-05; 2014-01-29; 2014-04-17)

C.2.1.1 AIM

The purpose of these flight tests was to reduce the pitch and roll oscillations mentioned above and to check the position hold capabilities of the adjusted controllers.

C.2.1.2 SYSTEM

The helicopter system was equipped with the newly calibrated magnetometer of Section 9.3.3. The control gains were changed to a more conservative set, $G3$, compared with the $G2$ gains in Table C.4. The new gains increase the timescale separation between successive control loops.

C.2.1.3 PROCEDURE

As the pitch oscillation was more pronounced than the roll oscillation, the longitudinal controller was tuned. Its pitch rate control gain was reduced by 15% ($G4$ in Table C.4), a longitudinal position step was commanded and its response was analysed. As the pitch oscillation remained the pitch angle control gain was reduced by 15% ($G5$ in Table C.4) to increase the timescale separation between the pitch angle and pitch rate controllers and the test was repeated. Unfortunately the flight testing opportunities for this project expired before the lateral controller could be tuned, but its performance with the $G3/G4/G5$ gains was analysed.

	N	Longitudinal				E	Lateral			
	k_N	k_u	$k_{i,u}$	k_θ	k_q	k_E	k_v	$k_{i,v}$	k_ϕ	k_p
G1D						0.425	0.085	0.0057	2.38	
G2	0.400	0.080	0.0053	2.24	1.00	0.400	0.080	0.0053	2.24	0.95
G3	0.25	0.07	0.0046		0.85	0.25	0.07	0.0046		
G4										
G5						1.9				

Table C.4 – Inertial, lateral and longitudinal control gains for verification flight 1

C.2.1.4 RESULTS

The longitudinal cyclic command responses to the negative longitudinal position steps are provided in Figure C.17. Despite the reduced outer loop gains of the $G3$ set of controller gains, the command oscillations previously observed with the $G2$ gains were much more pronounced with the $G3$ gains. Limits were frequently enforced on the commands. The increased oscillations were likely the result of more challenging wind conditions during the flight test with $G3$ controller gains. There was almost no wind during the flight test with $G2$ gains and wind speeds were on the limit of the acceptable flight testing envelope during the

flight test with $G3$ gains. After the pitch rate and pitch angle gains were reduced by 15% ($G5$), the oscillations were greatly reduced.

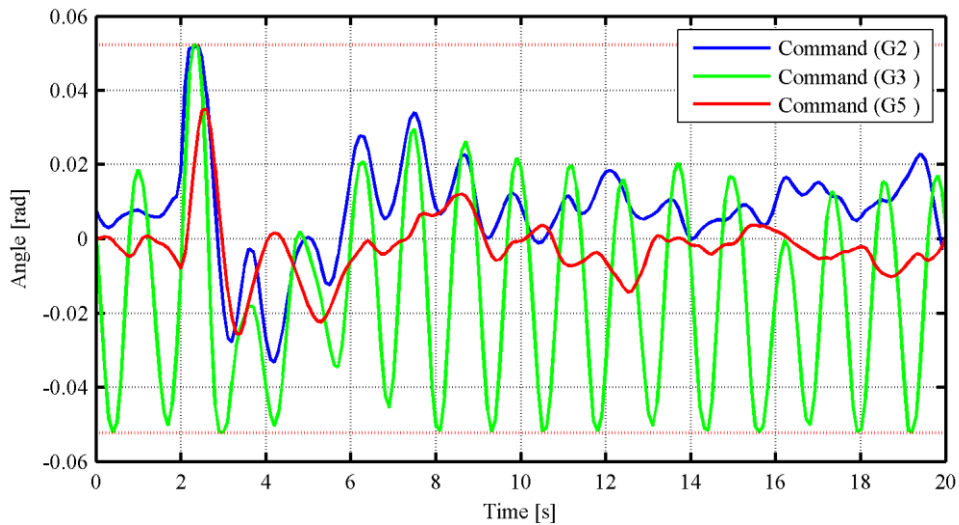


Figure C.17 - Longitudinal cyclic command response

The pitch rate responses to the negative longitudinal position steps are shown in Figure C.18. The pitch rate oscillations with the $G2$ gains were much more pronounced with the $G3$ gains. The $G5$ gains showed negligible oscillations.

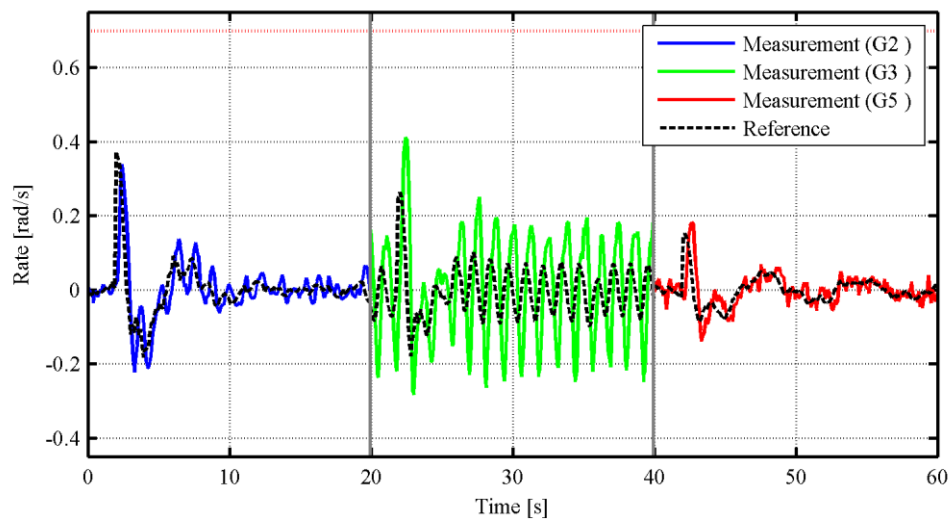


Figure C.18 - Pitch rate response

The pitch angle responses to the negative longitudinal position step manoeuvres are shown in Figure C.19. The pitch angle oscillations present with the $G2$ and $G3$ gains were greatly reduced with the $G5$ gains.

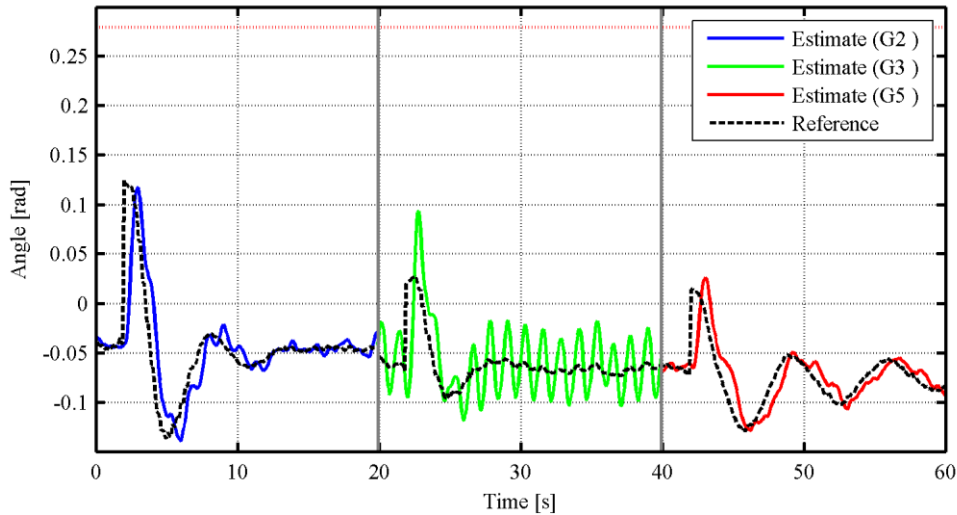


Figure C.19 - Pitch angle response

The longitudinal velocity responses to the negative longitudinal position steps which were executed are shown in Figure C.20. The longitudinal velocity controller followed velocity references better with the $G2$ and $G3$ gains than with the $G5$ gains.

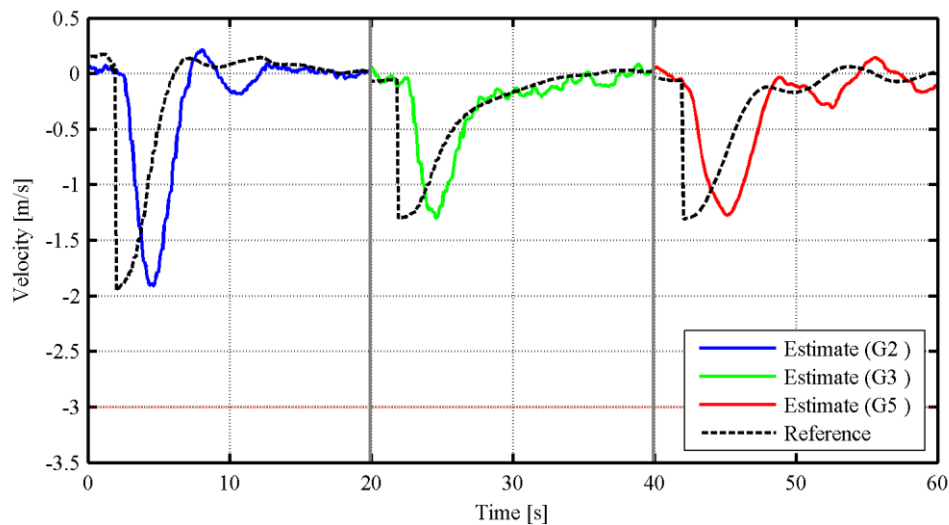


Figure C.20 – Longitudinal velocity response

The longitudinal position responses to the negative position steps are shown in Figure C.21. The controller with the $G2$ and $G3$ gains offers better position holding capabilities than the controller with $G5$ gains, but the controller with $G5$ gains can maintain a position to within approximately 0.5 m.

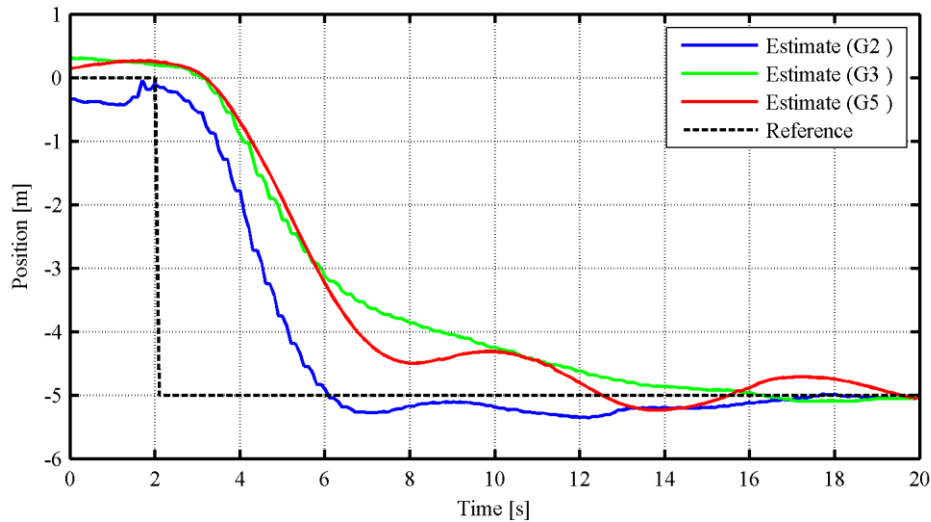


Figure C.21 - Longitudinal position response

The longitudinal cyclic command, pitch rate, pitch angle, longitudinal velocity and inertial north position responses to the positive position steps performed are provided in Appendix D.3.2.

While no further adjustments were made to the lateral control gains after the $G3$ control gains were set in Section 9.3, the responses with the $G3/G4/G5$ control gains are compared with the previous set of longitudinal responses which was analysed, the set obtained with $G1D$ gains. The lateral cyclic control, roll rate, roll angle, lateral velocity, and lateral position responses to the positive lateral position step manoeuvres are provided in Figure C.22, Figure C.23, Figure C.24, Figure C.25 and Figure C.26 respectively. The command, rate and angle responses with $G1D$ and $G3/G4/G5$ control gains were similarly oscillatory. The position holding performance was degraded with the $G5$ gains, but positions can still be held to within 0.5 m.

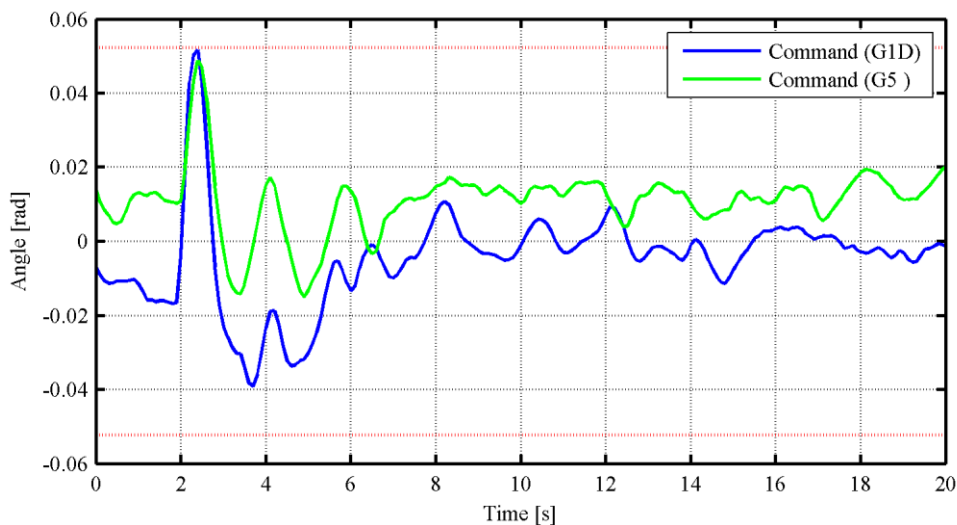


Figure C.22 - Lateral cyclic command response

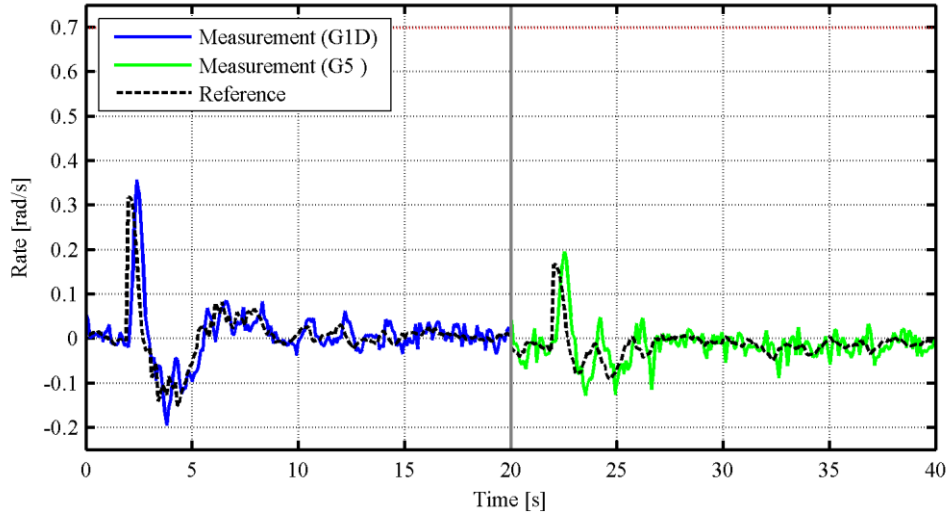


Figure C.23 - Roll rate response

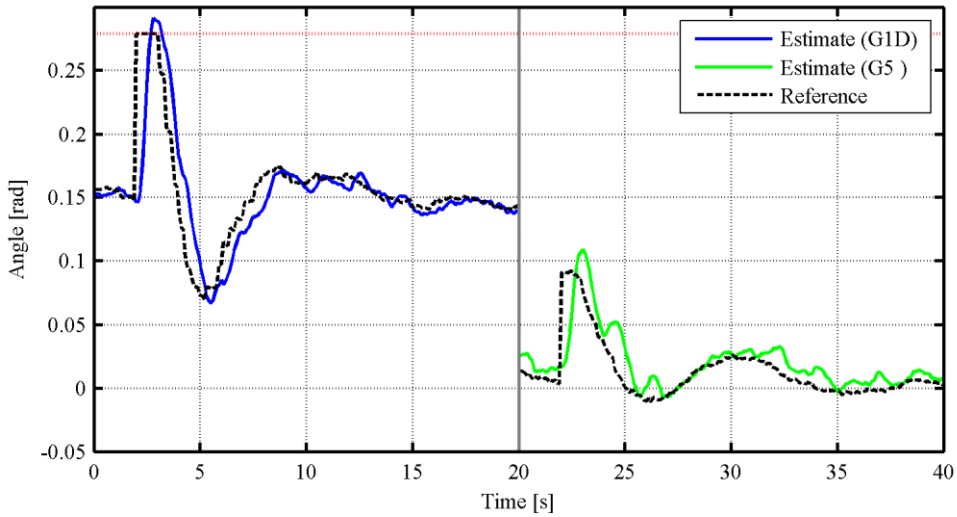


Figure C.24 - Roll angle response

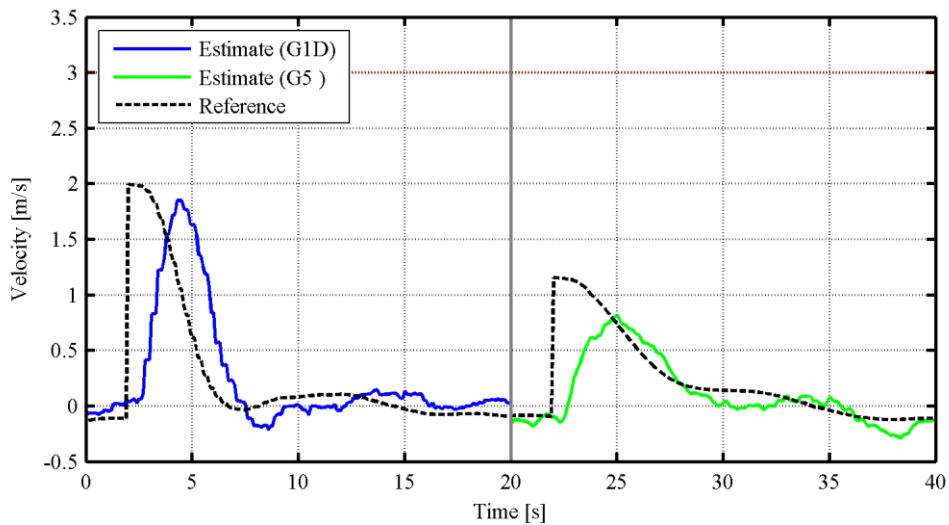


Figure C.25 - Lateral velocity response

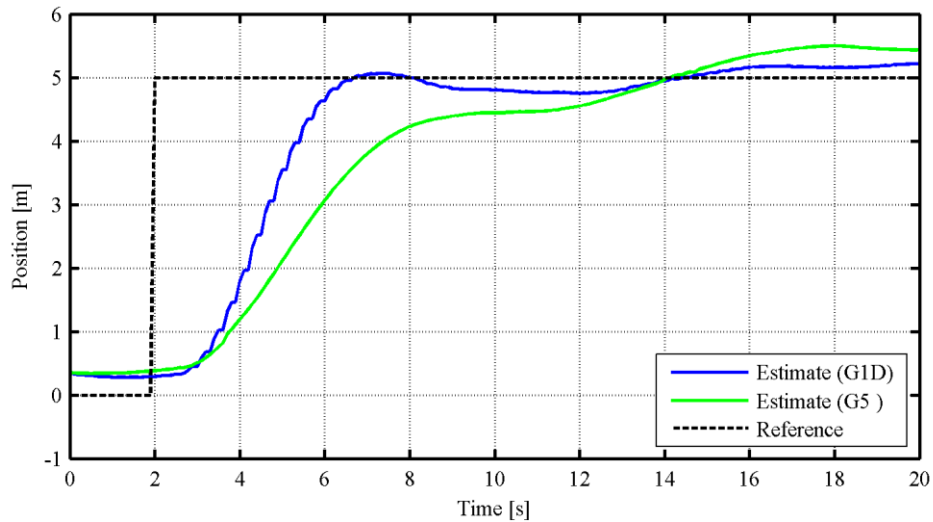


Figure C.26 - Lateral position response

The lateral cyclic command, roll rate, roll angle, lateral velocity and inertial east position responses to the negative position steps performed are provided in Appendix D.2.2.

C.2.1.5 CONCLUSION

The pitch rate oscillation problem was addressed with the *G5* control gains. Due to the limited flight testing time available and due to the small magnitude of the roll oscillations when compared with the previously experienced pitch oscillations, the lateral controller gains were not modified. Instead the *G3* gains were transferred directly to the *G4* and *G5* gains. The controllers with *G5* gains can hold a position to within 0.5 m.

D. ADDITIONAL CONTROL TUNING DATA

D.1 HEAVE

D.1.1 INITIAL TUNING

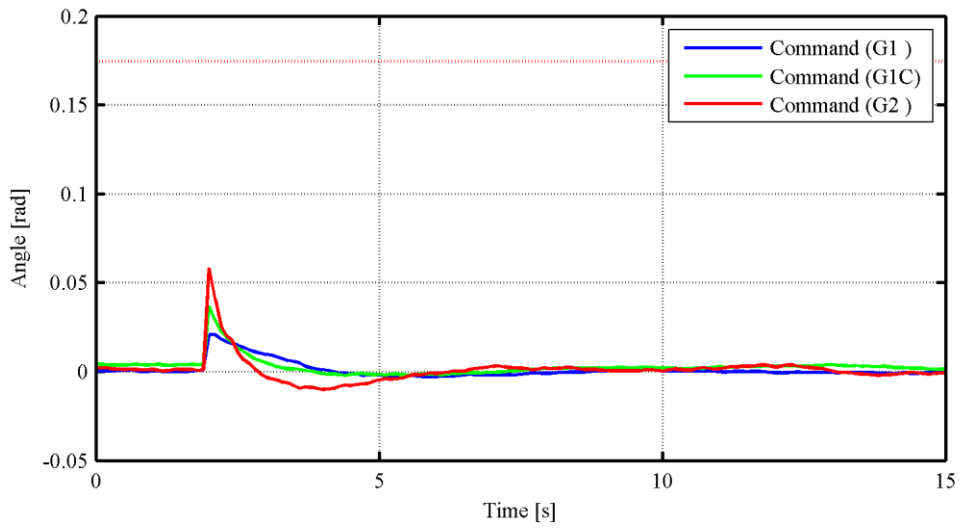


Figure D.1 - Collective command response

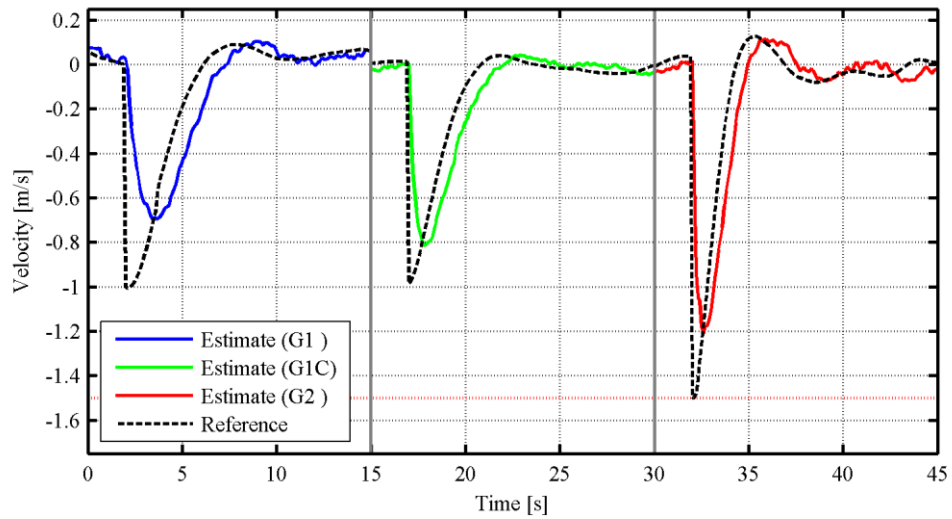


Figure D.2 - Heave velocity response

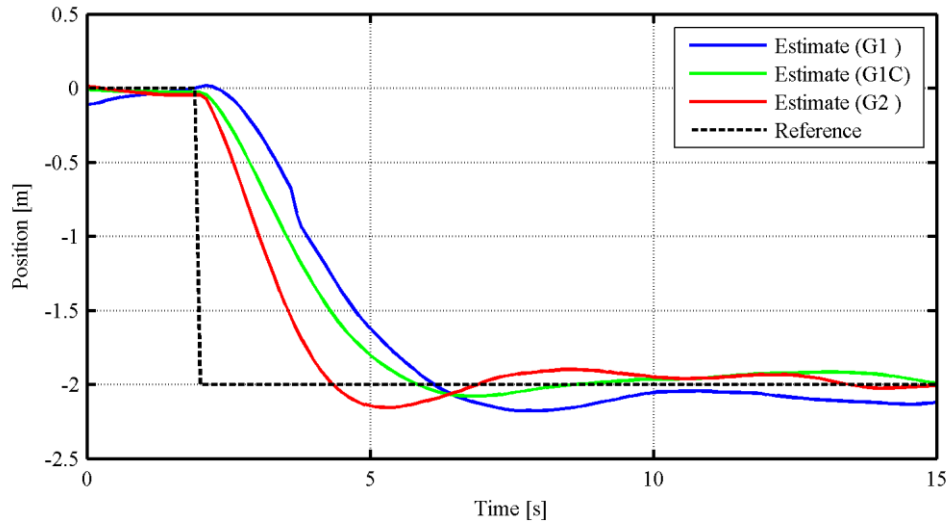


Figure D.3 - Down position response

D.1.2 TUNING VERIFICATION

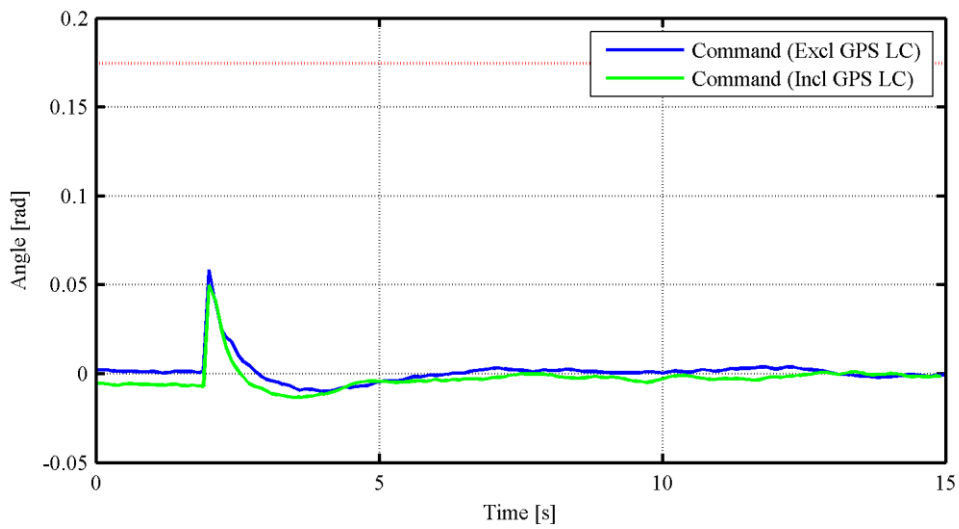


Figure D.4 - Collective command response

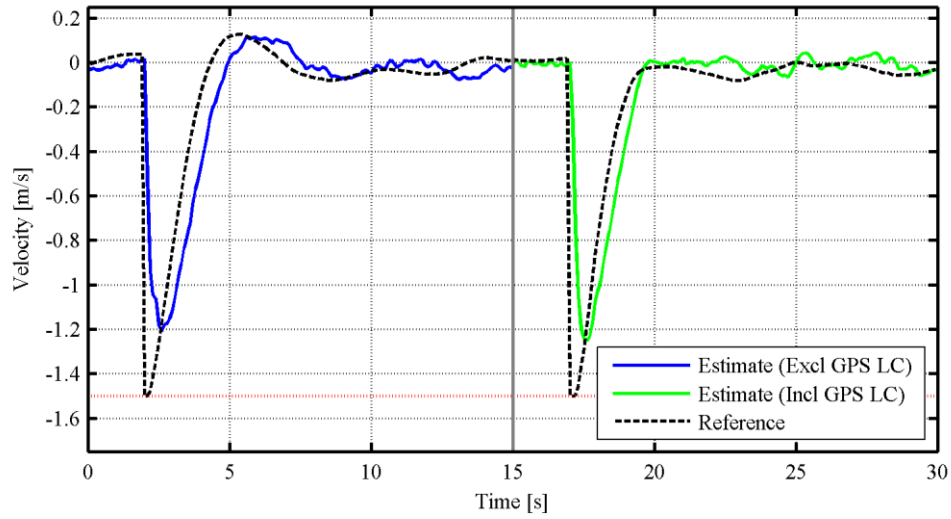


Figure D.5 - Heave velocity response

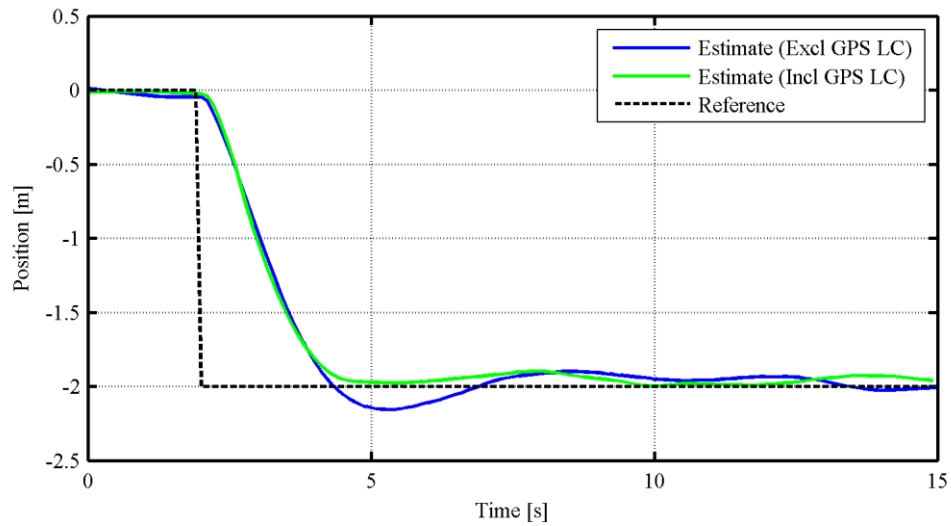
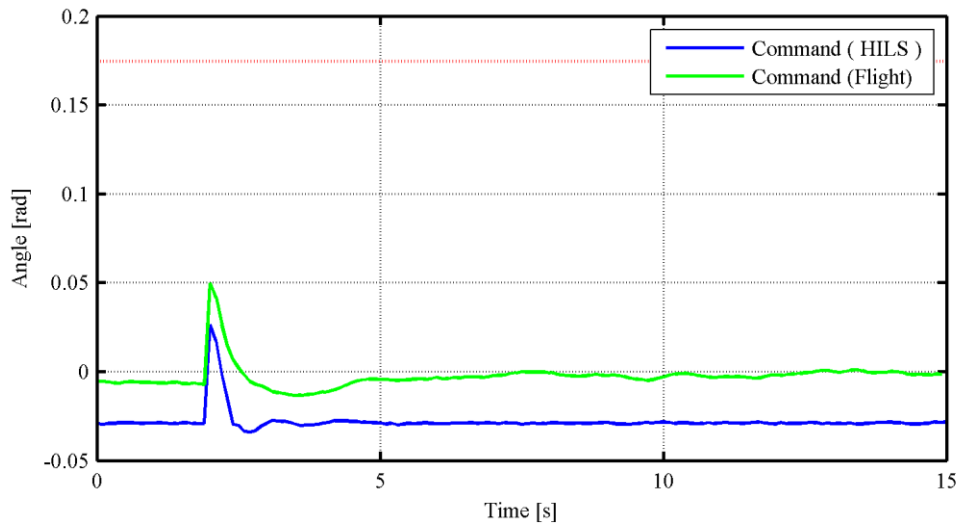
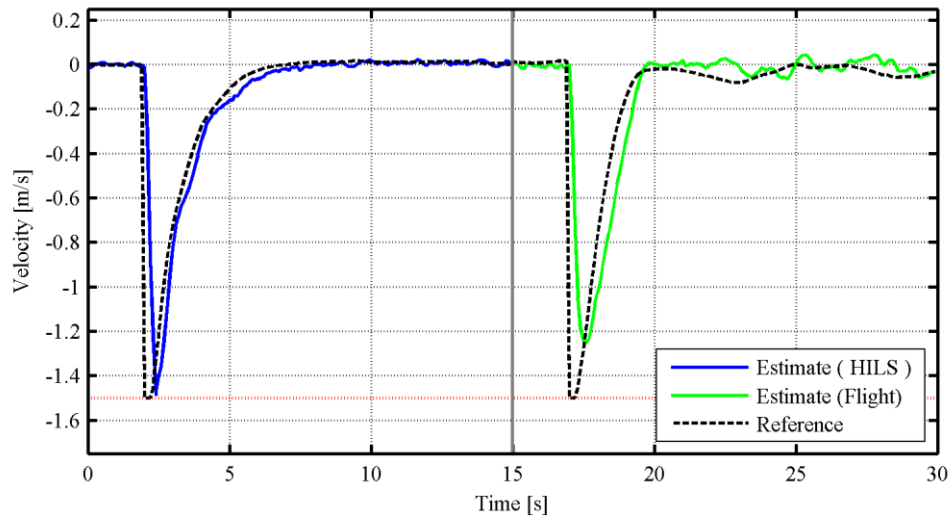


Figure D.6 - Down position response

D.1.3 HIL COMPARISON**Figure D.7** - Collective command response**Figure D.8** - Heave velocity response

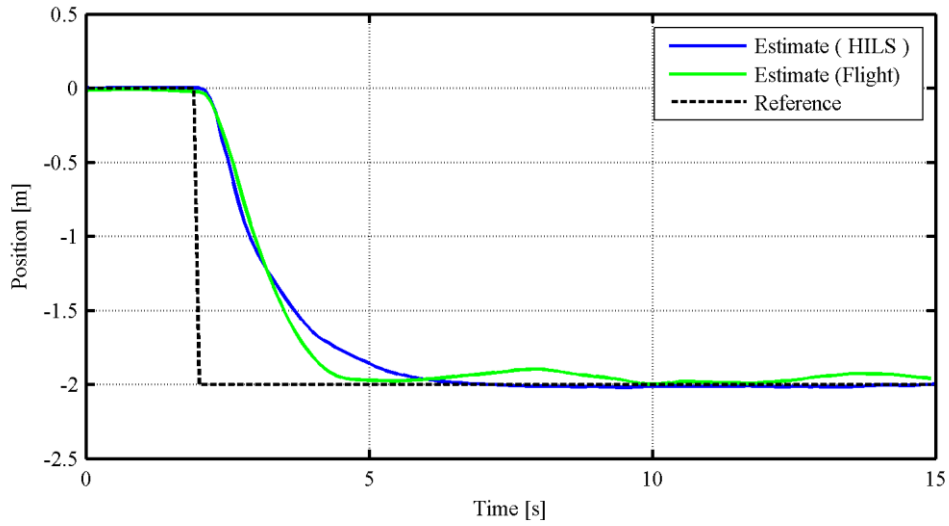


Figure D.9 - Down position response

D.2 LATERAL

D.2.1 INITIAL TUNING

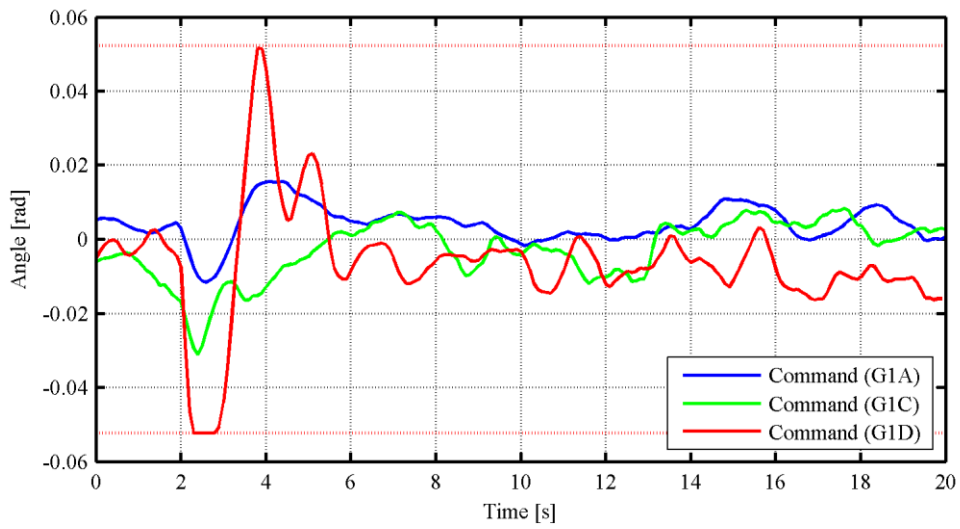
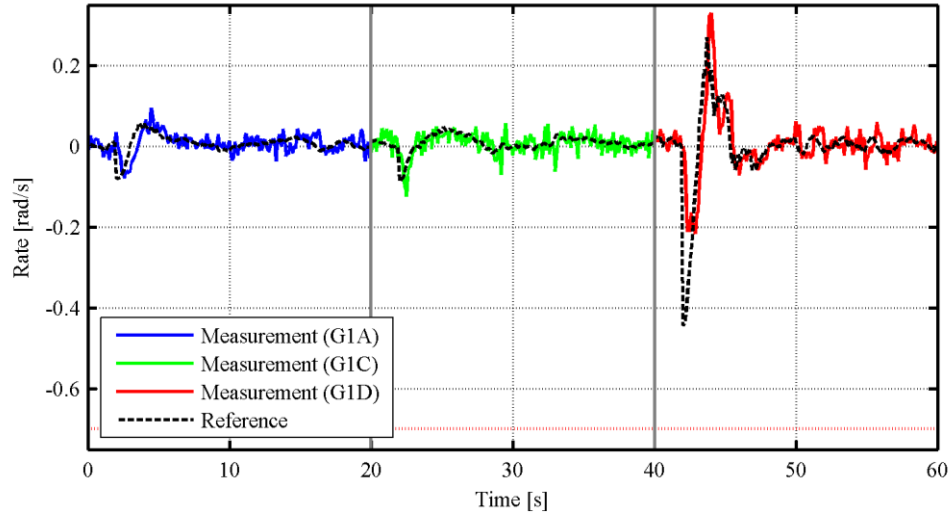
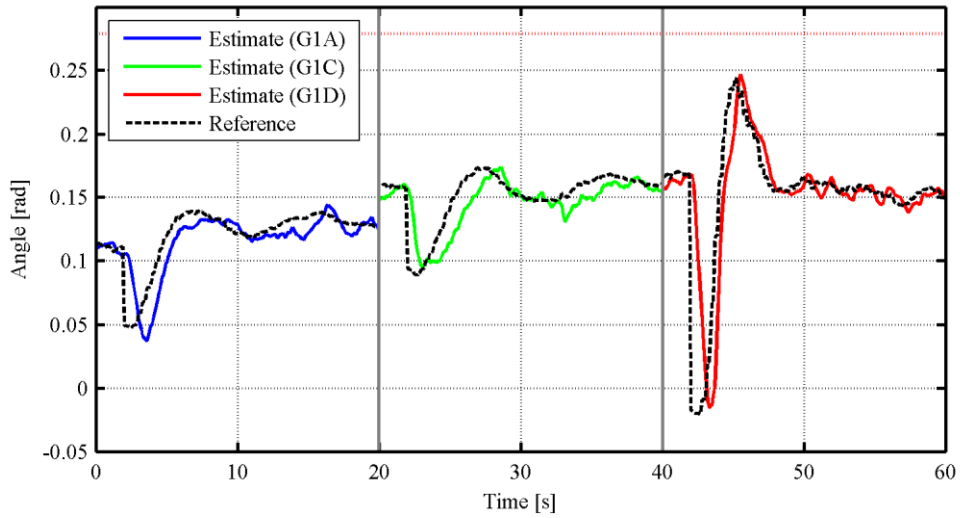


Figure D.10 - Lateral cyclic command response

**Figure D.11** - Roll rate response**Figure D.12** - Roll angle response

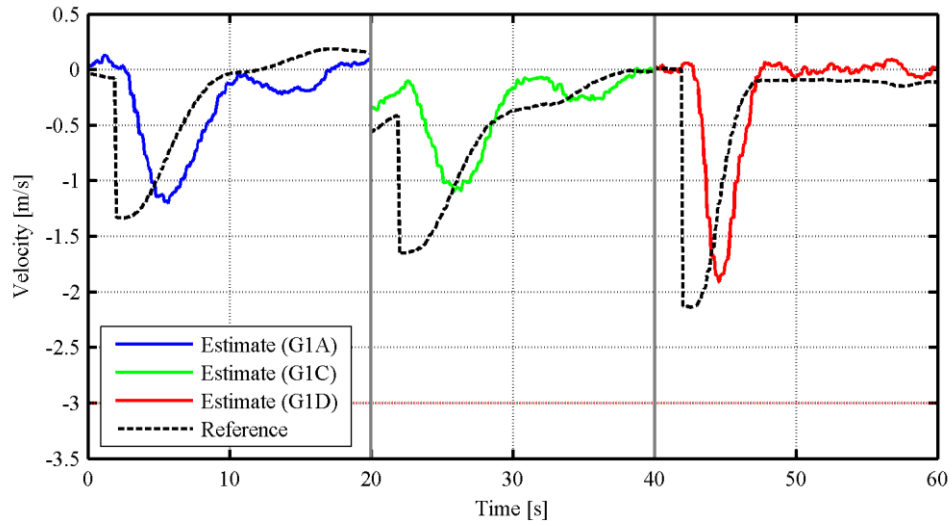


Figure D.13 - Lateral velocity response

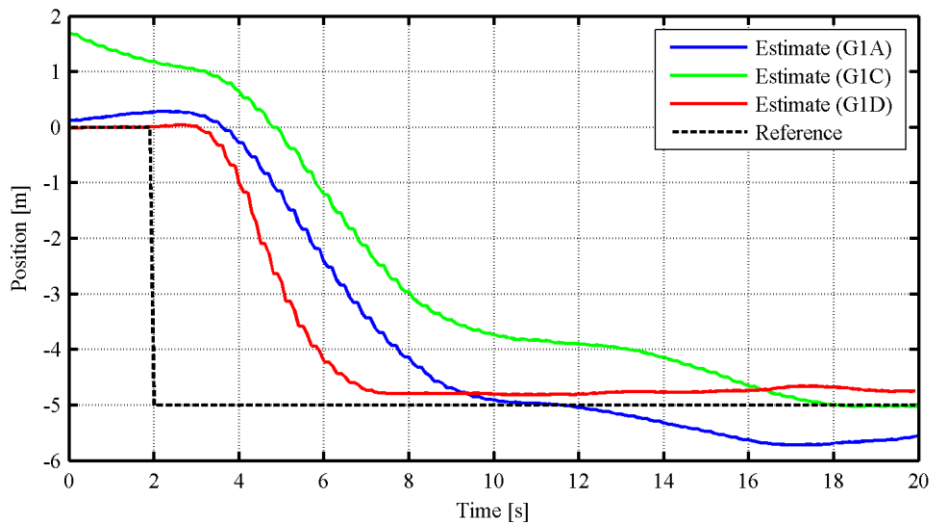


Figure D.14 - East position response

D.2.2 FURTHER TUNING

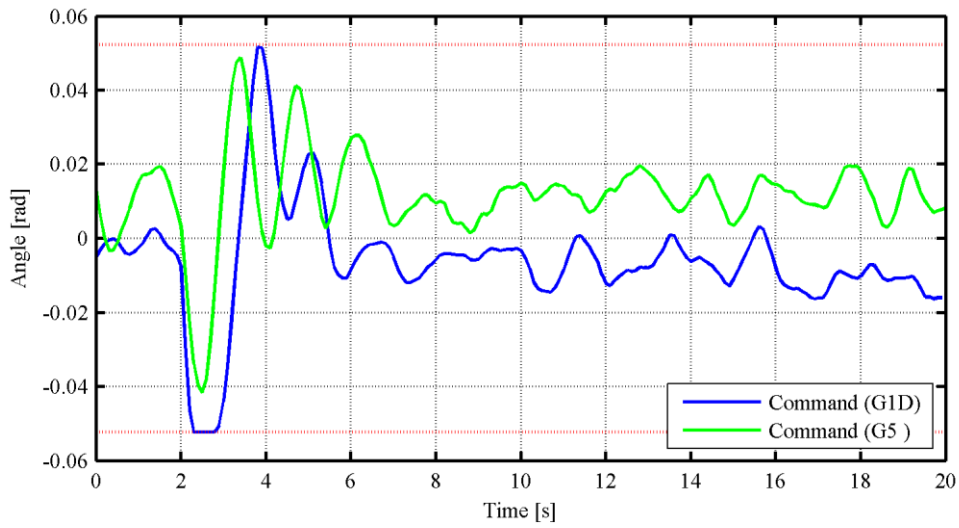


Figure D.15 - Lateral cyclic command response

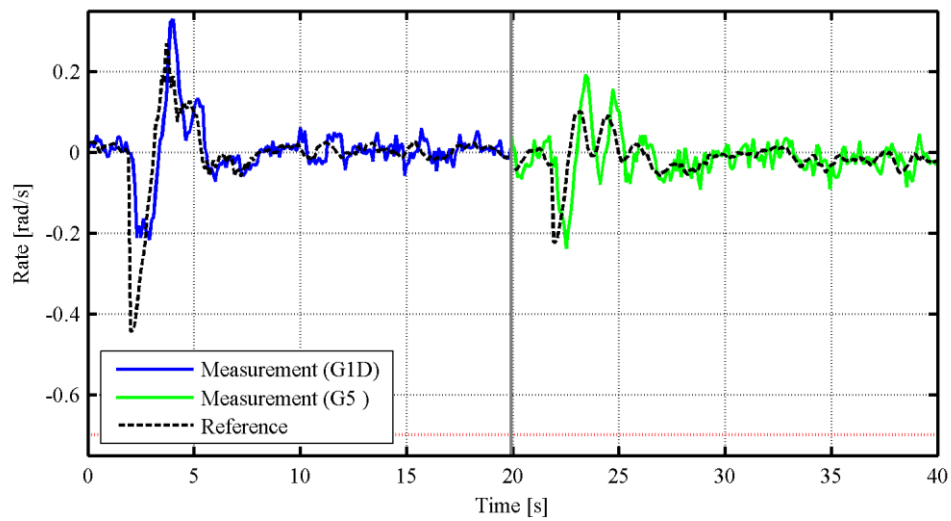


Figure D.16 - Roll rate response

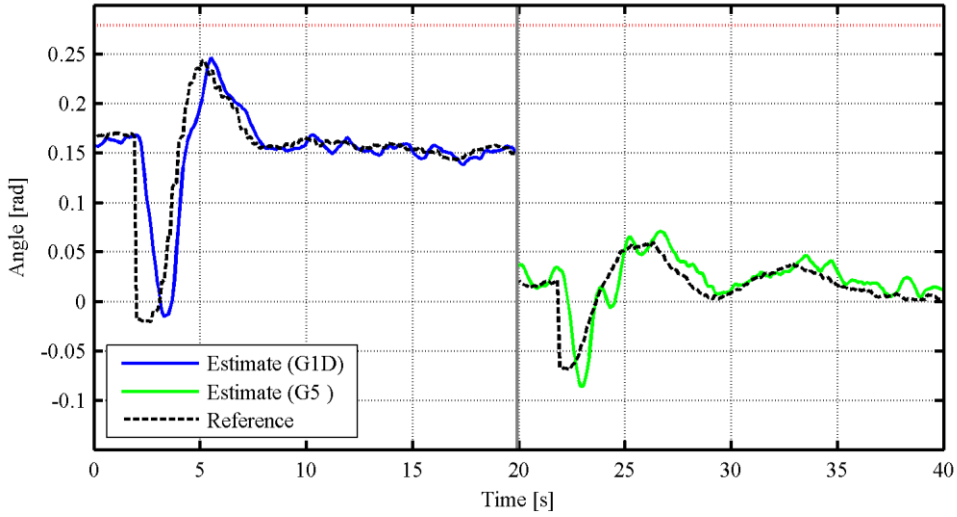


Figure D.17 - Roll angle response

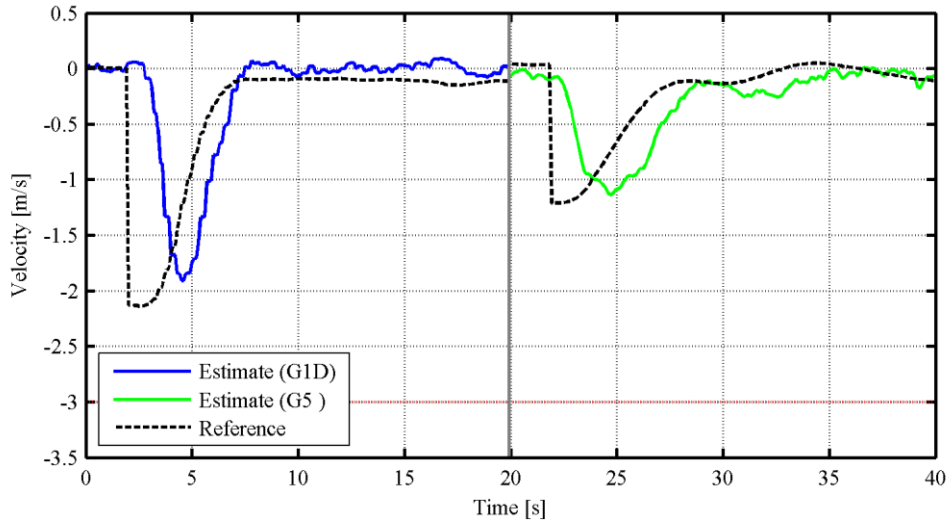


Figure D.18 - Lateral velocity response

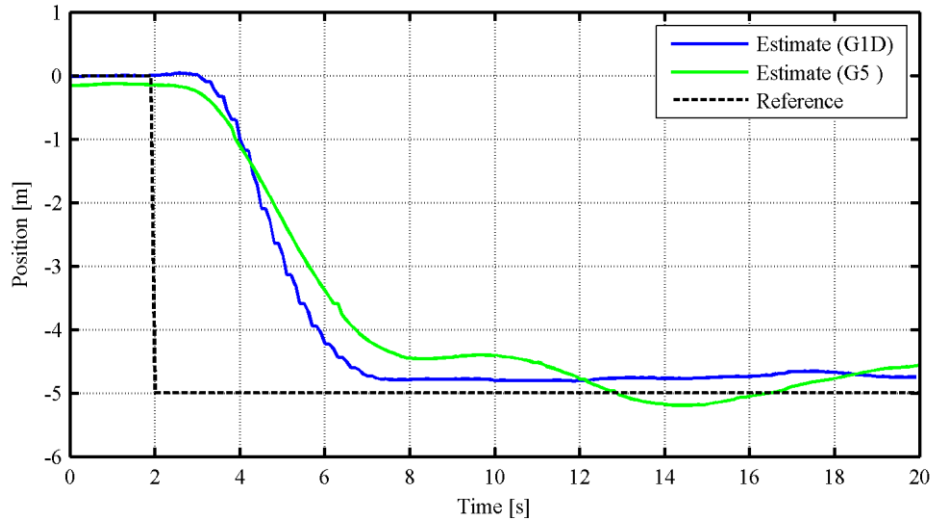


Figure D.19 - Lateral position response

D.3 LONGITUDINAL

D.3.1 INITIAL TUNING

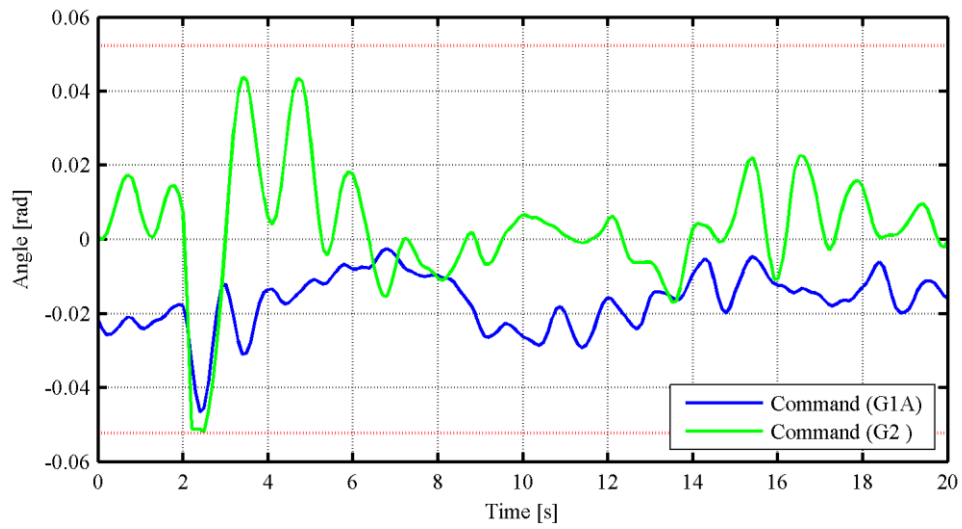
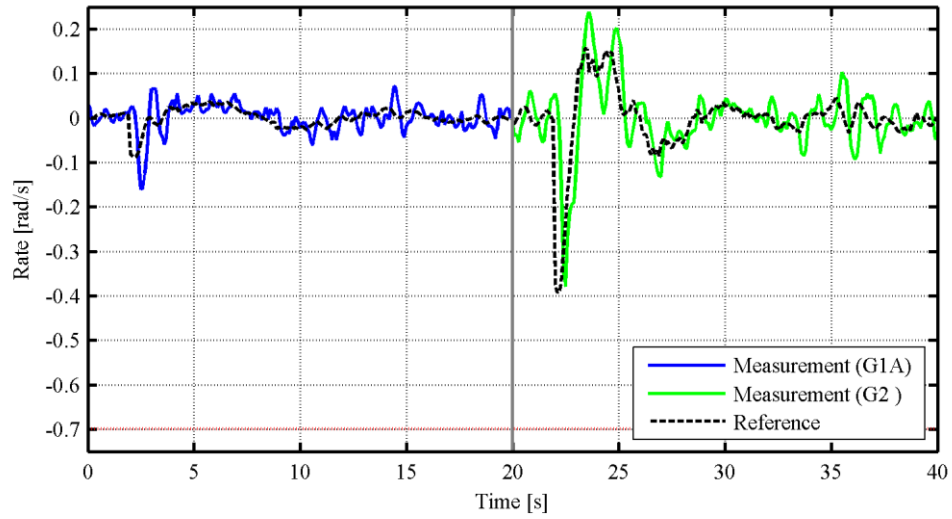
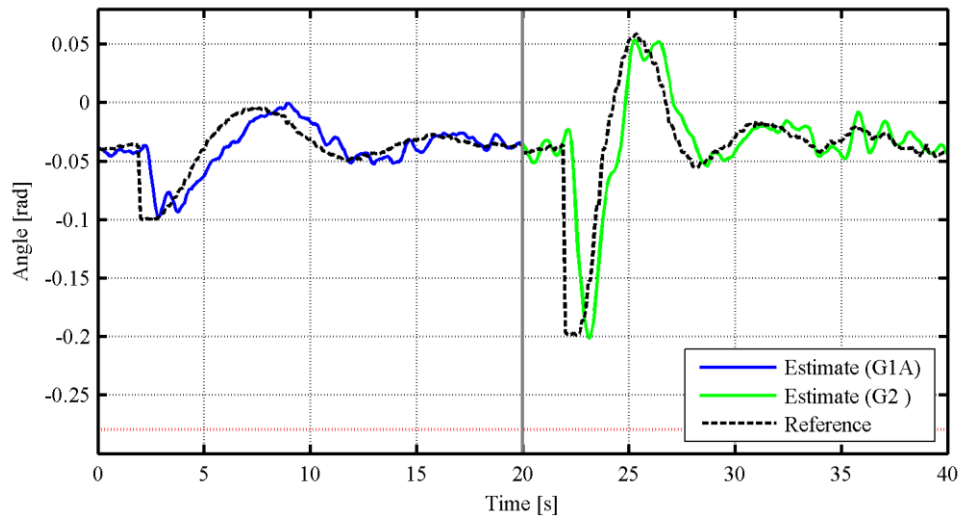


Figure D.20 - Longitudinal cyclic command response

**Figure D.21** - Pitch rate response**Figure D.22** - Pitch angle response

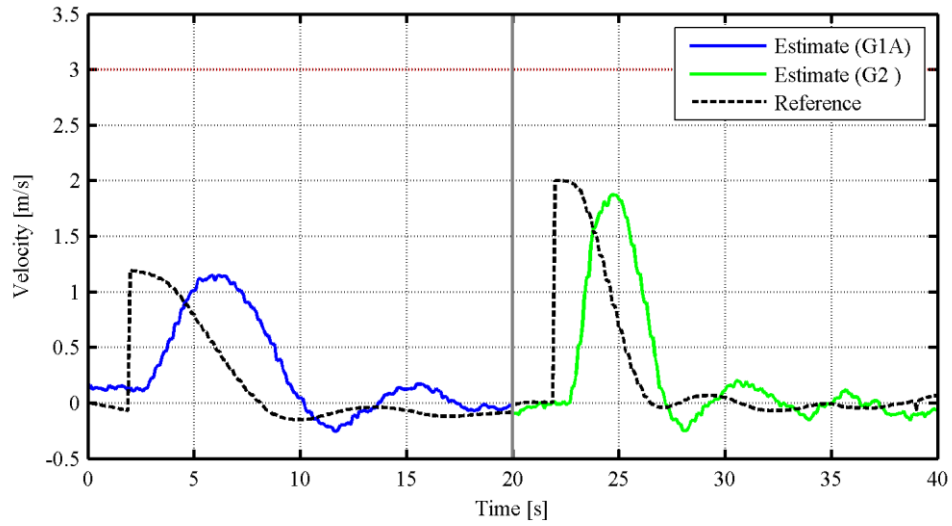


Figure D.23 - Longitudinal velocity command

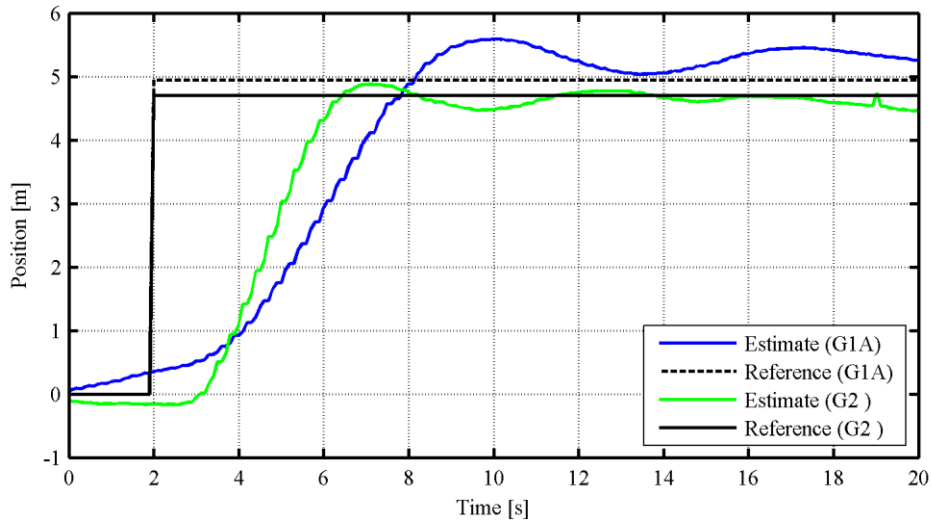
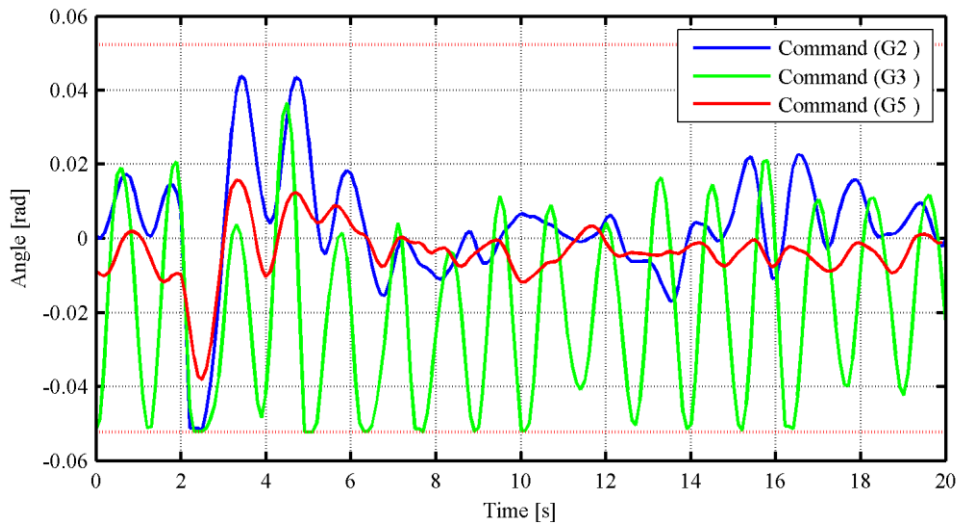
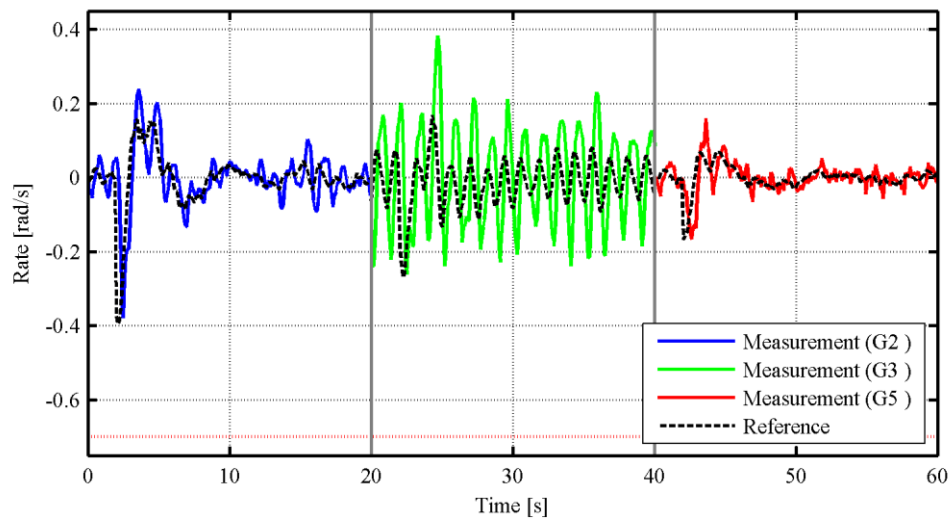


Figure D.24 - North position response

D.3.2 FURTHER TUNING**Figure D.25** - Longitudinal cyclic command response**Figure D.26** - Pitch rate response

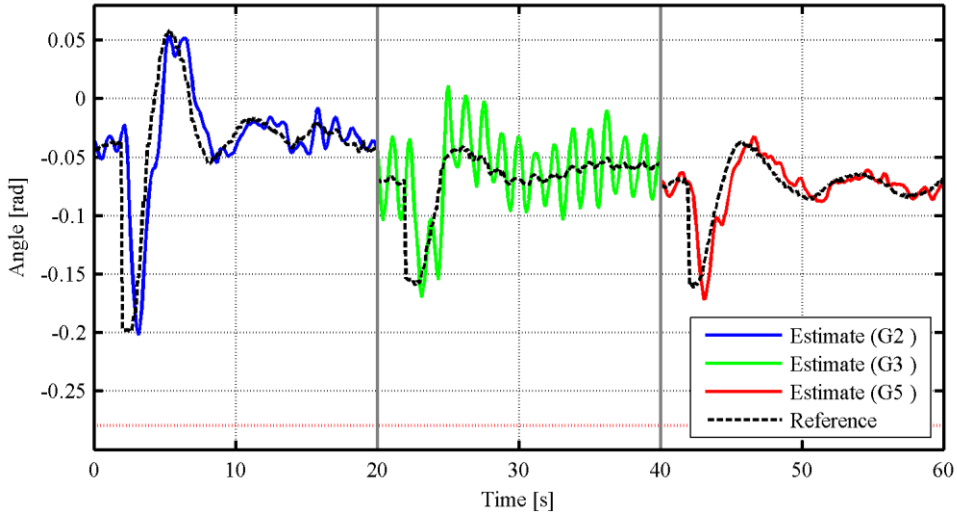


Figure D.27 - Pitch angle response

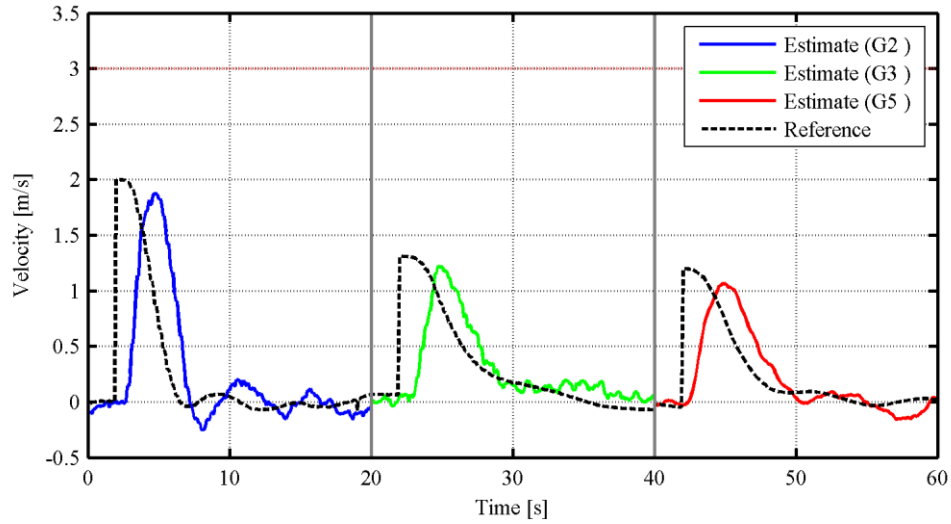


Figure D.28 - Longitudinal velocity response

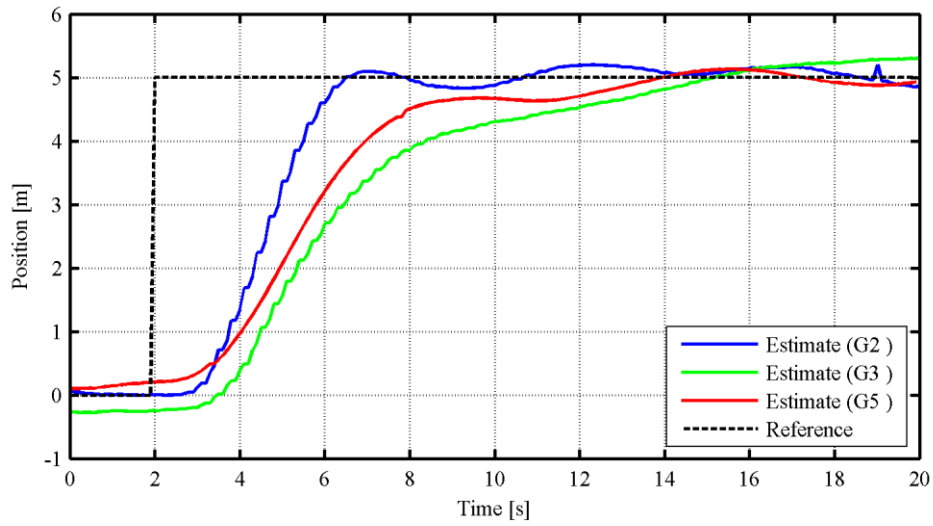


Figure D.29 - Longitudinal position response

BIBLIOGRAPHY

- [1] N. Carstens, “Development of a Low-Cost, Low-Weight Flight Control System for an Electrically Powered Model Helicopter,” Stellenbosch University, Stellenbosch, 2005.
- [2] S. Groenewald, “Development of a Rotary-Wing Test Bed for Autonomous Flight,” Stellenbosch University, Stellenbosch, 2005.
- [3] L.-E. Rossouw, “Autonomous Flight of an Unmanned Helicopter,” 2008.
- [4] C. Van Schalkwyk, “Full State Control of a Fury X-Cell Unmanned Helicopter,” 2008.
- [5] A. M. De Jager, “The design and implementation of vision-based autonomous rotorcraft landing,” 2011.
- [6] A. D. Swart, “Monocular Vision Assisted Autonomous Landing of a Helicopter on a Moving Deck,” Stellenbosch University, Stellenbosch, 2013.
- [7] P. E. Smit, “Development of a 3-DOF Motion Simulation Platform,” Stellenbosch, 2010.
- [8] F. Saghafi and S. M. Esmailifar, “Automatic Landing of Small Helicopters on 4DOF Moving Platforms,” *Journal of Aerospace Science and Technology*, vol. 4, no. 4, pp. 37-46, 2007.
- [9] W. Kong, D. Zhou, D. Zhang and J. Zhang, “Vision-based Autonomous Landing System for Unmanned Aerial Vehicle: A Survey,” in *IEEE International Conference on Multisensor Fusion and Integration for Intelligent Systems (MFI)*, Beijing, China, 2014.
- [10] J. G. Leishman, *Principles of Helicopter Aerodynamics*, Cambridge University Press, 2006.
- [11] C. H. Kääriä, “Investigating the Impact of Ship Superstructure Aerodynamics on Maritime Helicopter Operations,” 2012.
- [12] G. D. Carico, R. Fang, R. S. Finch, W. P. Geyer, H. W. Krijns and K. Long, “Helicopter/Ship Qualification Testing,” Research and Technology Organisation/North Atlantic Treaty Organisation, 2003.
- [13] B. W. Sherman, “The Examination and Evaluation of Dynamic Ship Quiescence Prediction

- and Detection Methods for Application in the Ship-Helicopter Dynamic Interface,” 2007.
- [14] P. J. From, J. T. Gravdahl and P. Abbeel, “On the Influence of Ship Motion Prediction Accuracy on Motion Planning and Control of Robotic Manipulators on Seaborne Platforms,” in *International Conference on Robotics and Automation*, Anchorage, Alaska, 2010.
- [15] J. Dannenberg, K. Hessner, P. Naaijen, H. van den Boom and K. Reichert, “The On Board Wave and Motion Estimator OWME,” in *The Proceedings of The Twentieth (2010) International Offshore and Polar Engineering Conference*, Beijing, 2010.
- [16] X. Zhao, R. Xu and C. Kwan, “Ship-Motion Prediction: Algorithms and Simulation Results,” in *International Conference on Acoustics, Speech, and Signal Processing*, Montreal, 2004.
- [17] X. Yang, “Automatic Landing of a Rotary-Wing UAV,” University of New South Wales, 2011.
- [18] X. Yang, “Displacement Motion Prediction of a Landing Deck for Recovery Operations of Rotary UAVs,” *International Journal of Control, Automation, and Systems*, vol. 11, no. 1, pp. 58-64, 2013.
- [19] X. Yang, H. Pota, M. Garratt and V. Ugrinovskii, “Ship Motion Prediction for Maritime Flight Operations,” in *Proceedings of the 17th World Congress of the International Federation of Automatic Control*, Seoul, South Korea, 2008.
- [20] American Meteorological Society, “Glossary of Meteorology,” [Online]. Available: http://glossary.ametsoc.org/wiki/Sea_state. [Accessed 10 September 2014].
- [21] Met Office, “National Meteorological Library and Archive Fact Sheet 6 - The Beaufort Scale,” Met Office, 2010, 2010.
- [22] J. M. Ross, *Human Factors for Naval Marine Vehicle Design and Operation*, Ashgate Publishing Company, 2009.
- [23] J. C. Chung, Z. Bien and Y. S. Kim, “A Note on Ship-Motion Prediction Based on Wave-Excitation Input Estimation,” *IEEE Journal of Oceanic Engineering*, vol. 15, no. 3, pp. 244-250, 1990.

- [24] "HMAS Kanimbla (II)," Royal Australian Navy, [Online]. Available: <http://www.navy.gov.au/hmas-kanimbla-ii>. [Accessed 31 August 2014].
- [25] A. Khan, C. Bil and K. E. Marion, "Real Time Prediction of Ship Motion for the Aid of Helicopter and Aircraft Deployment and Recovery," in *International Congress of the Aeronautical Sciences*, Hamburg, 2006.
- [26] A. Khan, C. Bil and K. E. Marion, "Ship motion prediction for launch and recovery of air vehicles," in *OCEANS*, Washington, D.C., 2005.
- [27] Department of the Navy, United States of America, "United States Navy Fact File," 15 November 2013. [Online]. Available: http://www.navy.mil/navydata/fact_display.asp?cid=4200&tid=900&ct=4. [Accessed 10 September 2014].
- [28] N. Mok, "Ship Motion Prediction Using Minor Component Analysis," Defence Technology Agency, Auckland, New Zealand, 2011.
- [29] R. Fang and P. J. A. Booij, "Helicopter-ship qualification testing - The Dutch clearance process," National Aerospace Laboratory NLR, 2006.
- [30] J. L. Colwell, "Flight Deck Motion System (FDMS): Operating Concepts and System Description," Defence Research and Development Canada - Atlantic, 2004.
- [31] J. McCallum, "Extending UAV Operating Envelopes," in *Launch & Recovery of Manned and Unmanned Vehicles from Surface Platforms*, Linthicum, 2012.
- [32] United States Coast Guard, Shipboard-Helicopter Operating Procedures Manual, Washington, 2011.
- [33] B. Ferrier and J. Duncan, "UAV Deck Recovery Stability Analysis," in *American Society of Naval Engineers Day*, Arlington, VA, 2012.
- [34] B. Ferrier and T. Manning, "Simulation and Testing of the Landing Period Designator (LPD) Helicopter Recovery Aid," *Naval Engineers Journal*, vol. 110, no. 1, pp. 189-205, 1998.
- [35] B. Ferrier, A. E. Baitis and A. Manning, "Evolution of the Landing Period Designator (LPD) for Shipboard Air Operations," *Naval Engineers Journal*, vol. 112, no. 4, pp. 297-

315, 2000.

- [36] Transportation Safety Board of Canada, "Aviation Investigation Report A09P0249," 2010.
- [37] P. Cantrell, "Settling with Power," All Star Helicopters, [Online]. Available: <http://www.copters.com/aero/settling.html>. [Accessed 6 October 2014].
- [38] J. L. Colwell, "Real Time Ship Motion Criteria for Maritime Helicopter Operations," in *23rd International Congress of Aeronautical Sciences*, Toronto, ON, 2002.
- [39] H. Shin, D. You and D. H. Shim, "An Autonomous Shipboard Landing Algorithm for Unmanned Helicopters," in *2013 International Conference on Unmanned Aircraft Systems (ICUAS)*, Atlanta, GA, 2013.
- [40] H. Shin, D. You and D. H. Shim, "Autonomous Shipboard Landing Algorithm for Unmanned Helicopters in Crosswind," *Journal of Intelligent and Robotic Systems*, vol. 74, no. 1-2, pp. 347-361, 2014.
- [41] C. Wu, D. Song, J. Qi and J. Han, "Autonomous Landing of an Unmanned Helicopter on a Moving Platform based on LP Path Planning," in *Proceedings of the 8th International Conference On Intelligent Unmanned Systems (ICIUS 2012)*, Singapore, 2012.
- [42] L. Marconi, A. Isidori and A. Serrani, "Autonomous vertical landing on an oscillating platform: an internal-model based approach," *Automatica*, vol. 38, no. 1, pp. 21-32, 2002.
- [43] S. M. Esmailifar and F. Saghafi, "Autonomous Unmanned Helicopter Landing System Design for Safe Touchdown on 6DOF Moving Platform," in *2009. ICAS '09. Fifth International Conference on Autonomic and Autonomous Systems*, Valencia, Spain, 2009.
- [44] C. K. Tan and J. Wang, "Ship Deck Landing of a Quadrotor using the Invariant Ellipsoid Technique," in *SICE Annual Conference*, Sapporo, Japan, 2014.
- [45] L. A. Sandino, M. Bejar and A. Ollero, "On the applicability of linear control techniques for autonomous landing of helicopters on the deck of a ship," in *2011 IEEE International Conference on Mechatronics (ICM)*, Istanbul, Turkey, 2011.
- [46] Northrop Grumman Aerospace Systems, "MQ-8B Fire Scout Vertical Takeoff and Landing Tactical Unmanned Aerial Vehicle System," Northrop Grumman Systems Corporation, 2012.

- [47] M. Gopal, *Control Systems Principles and Design*, New Delhi: McGraw-Hill, 2003.
- [48] F. Pozzi, T. Di Matteo and T. Aste, "Exponential Smoothing Weighted Correlations," *The European Physical Journal B*, vol. 85, no. 175, pp. 1-21, 2012.
- [49] Qt Project, "Supported Platforms | QtDoc 5.3," Digia Plc, 2014. [Online]. Available: <http://qt-project.org/doc/qt-5/supported-platforms.html>. [Accessed 18 November 2014].
- [50] OpenCV, "OpenCV Change Logs," OpenCV, June 2011. [Online]. Available: <http://code.opencv.org/projects/opencv/wiki/ChangeLog#23-beta>. [Accessed 18 November 2014].
- [51] "jcastastny", "Significant slow down of SVD in OpenCV 2.3 (Bug #1498)," OpenCV, 1 December 2011. [Online]. Available: <http://code.opencv.org/issues/1498>. [Accessed 18 November 2014].
- [52] U. Rathmann and J. Wilgen, "Qwt User's Guide," [Online]. Available: <http://qwt.sourceforge.net/>. [Accessed 9 October 2014].
- [53] L. Engelbrecht, "Fact file: Valour-class small guided missile frigates," *defenceWeb*, 8 February 2010. [Online]. Available: http://www.defenceweb.co.za/index.php?option=com_content&view=article&id=6524:fact-file-valour-class-small-guided-missile-frigates-&catid=79:fact-files. [Accessed 31 August 2014].
- [54] W. T. Higgins, "A Comparison of Complementary and Kalman Filtering," *IEEE Transactions on Aerospace and Electronic Systems*, Vols. AES-11, no. 3, pp. 321-325, 1975.
- [55] NovAtel Inc., "OEMV® Family Firmware Reference Manual OM-20000094 Rev 8," 2010.
- [56] C. Jeffery, *An Introduction to GNSS*, Calgary, AB: NovAtel Inc., 2010.
- [57] R. van der Merwe and E. A. Wan, "Sigma-Point Kalman Filters for Nonlinear Estimation and Sensor-Fusion: Applications to Integrated Navigation," in *AIAA Guidance, Navigation, and Control Conference and Exhibit*, Providence, Rhode Island, 2004.
- [58] P. D. Solomon, J. Wang and C. Rizos, "Latency Determination and Compensation in Real-Time GNSS/INS Integrated Navigation," in *Proceedings of the International Conference*

on Unmanned Aerial Vehicle in Geomatics (UAV-g), Zurich, Switzerland, 2011.

- [59] D. Simon, *Optimal State Estimation: Kalman, H ∞ , and Nonlinear Approaches*, Cleveland: John Wiley & Sons, Inc., 2006.
- [60] M. J. Caruso, "Applications of Magnetoresistive Sensors in Navigation Systems," Honeywell Inc., Plymouth, MN.
- [61] V. Grygorenko, "Sensing – Magnetic Compass with Tilt Compensation," Cypress Semiconductor Corp., San Jose, CA.
- [62] T. Ozyagcilar, "Layout Recommendations for PCBs Using a Magnetometer Sensor," Freescale Semiconductor, 2012.
- [63] T. Ozyagcilar, "Calibrating an eCompass in the Presence of Hard and Soft-Iron Interference," Freescale Semiconductor, 2013.
- [64] E. Rossouw, "Magnetometer Calibration Object," Stellenbosch University, Stellenbosch, 2007.
- [65] R. W. Beard and T. W. McLain, *Small Unmanned Aircraft: Theory and Practice*, Princeton University Press, 2012.
- [66] RC Helicopter Wiki, "Revolution mix," [Online]. Available: http://www.rcheliwiki.com/Revolution_mix. [Accessed 9 October 2014].
- [67] E. Brosh, S. A. Baset, V. Misra, D. Rubenstein and H. Schulzrinne, "The Delay-Friendliness of TCP," *IEEE/ACM Transactions on Networking*, vol. 18, no. 5, pp. 1478-1491, 2010.
- [68] J. Nagle, "Congestion control in IP/TCP internetworks," *ACM SIGCOMM Computer Communication Review*, pp. 11-17, October 1984.
- [69] Microsoft, "Design issues - Sending small data segments over TCP with Winsock," Microsoft, 22 June 2014. [Online]. Available: <http://support.microsoft.com/KB/214397>. [Accessed 1 December 2014].
- [70] A. S. Tanenbaum, *Modern Operating Systems*, Prentice Hall, 2007.
- [71] MaxStream, Inc., "XStream™ OEM RF Module," Lindon, UT, 2006.

- [72] Aalco Metals Limited, "Aluminium Alloy - General Information - Introduction to Aluminium and its alloys," Aalco Metals Limited, 7 November 2013. [Online]. Available: http://www.aalco.co.uk/datasheets/Aluminium-Alloy_Introduction-to-Aluminium-and-its-alloys_9.ashx. [Accessed 1 December 2014].
- [73] Adendorff Machinery Mart, "MAC-AFRIC™ 70 Liter Petrol Belt Drive Compressor 6.5HP," [Online]. Available: <http://www.adendorff.co.za/ProductDetails.aspx?id=219>. [Accessed 9 October 2014].
- [74] C. E. Shannon, "Communication in the Presence of Noise," *Proceedings of the IRE*, vol. 37, no. 1, pp. 10-21, 1949.
- [75] J. L. Knight, "Manual Control and Tracking," in *Handbook of Human Factors*, New York, John Wiley & Sons, 1987, pp. 182-218.